ISSN 0368-0797
eISSN 2410-2091

МИСИС
УНИВЕРСИТЕТ
НАУКИ И ТЕХНОЛОГИЙ

СибГИУ
Сибирский государственный
индустриальный университет

ИЗВЕСТИЯ
ВЫСШИХ УЧЕБНЫХ ЗАВЕДЕНИЙ
ЧЕРНАЯ МЕТАЛЛУРГИЯ

IZVESTIYA. FERROUS METALLURGY

fermet.misis.ru

2023 Том Vol. 66 № No. 1

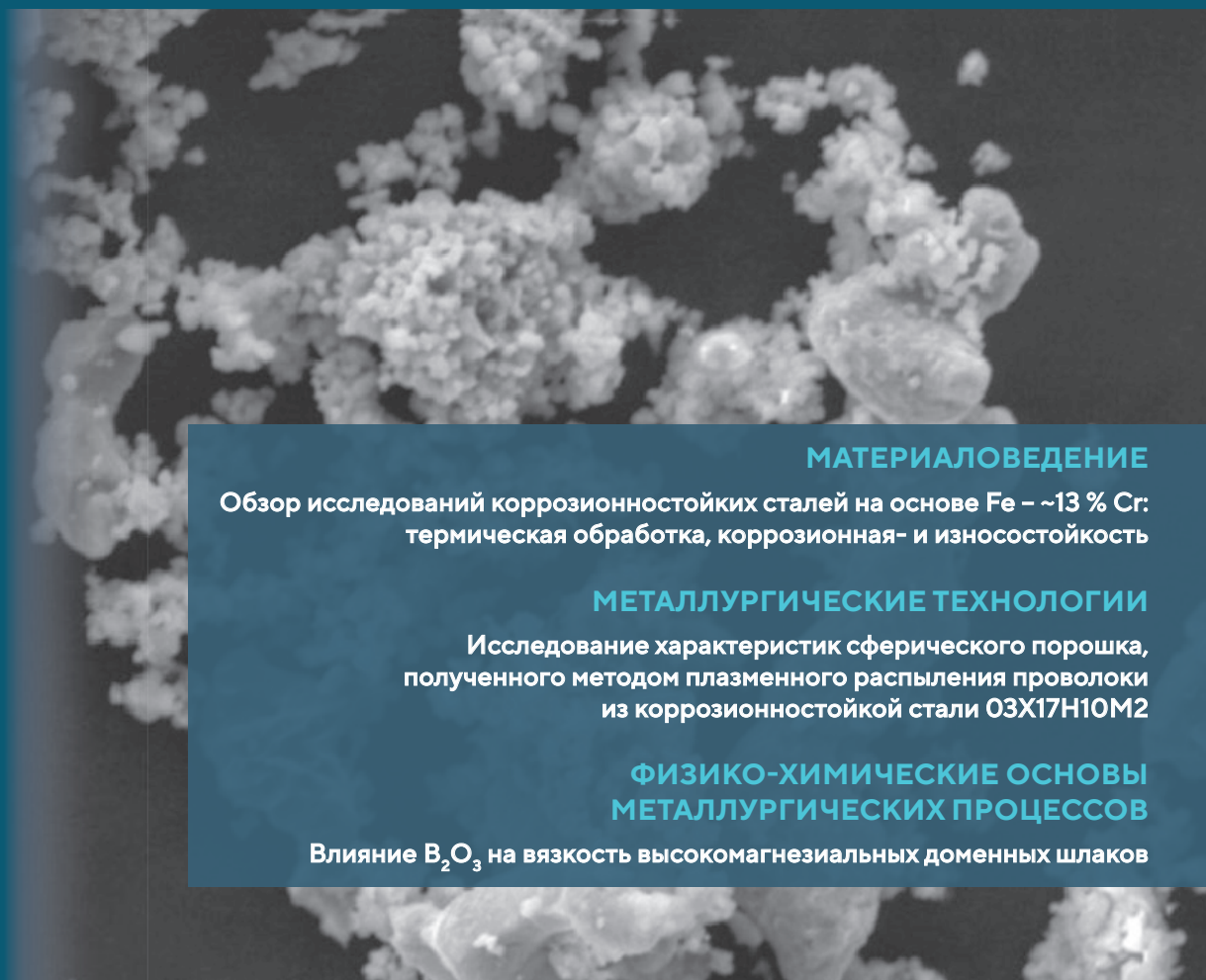

МАТЕРИАЛОВЕДЕНИЕ

Обзор исследований коррозионностойких сталей на основе Fe – ~13 % Cr: термическая обработка, коррозионная- и износостойкость

МЕТАЛЛУРГИЧЕСКИЕ ТЕХНОЛОГИИ

Исследование характеристик сферического порошка, полученного методом плазменного распыления проволоки из коррозионностойкой стали 03Х17Н10М2

ФИЗИКО-ХИМИЧЕСКИЕ ОСНОВЫ МЕТАЛЛУРГИЧЕСКИХ ПРОЦЕССОВ

Влияние B_2O_3 на вязкость высокомагнезиальных доменных шлаков

MISIS UNIVERSITY
SibSIU Siberian State Industrial University

ISSN 0368-0797
eISSN 2410-2091

IZVESTIYA FERROUS METALLURGY

Scientific and Technical Journal

Published since January 1958. Issued monthly

2023 Vol. Том 66 No. № 1

ИЗВЕСТИЯ ВЫСШИХ УЧЕБНЫХ ЗАВЕДЕНИЙ ЧЕРНАЯ МЕТАЛЛУРГИЯ

Научно-технический журнал

Издается с января 1958 г. ежемесячно

IZVESTIYA FERROUS METALLURGY

www.fermet.misis.ru

ISSN 0368-0797 *(Print)* ISSN 2410-2091 *(Online)*

Alternative title:

Izvestiya vuzov. Chernaya metallurgiya
Izvestiya. Ferrous Metallurgy

Founders:

MISIS
UNIVERSITY OF SCIENCE AND TECHNOLOGY

SibSIU
Siberian State Industrial University

Editorial Addresses:

4 Leninskii Ave., Moscow 119049, Russian Federation
National University of Science and Technology "MISIS"
Tel.: +7 (495) 638-44-11
E-mail: fermet.misis@mail.ru, ferrous@misis.ru

42 Kirova Str., Novokuznetsk, Kemerovo Region – Kuzbass
654007, Russian Federation
Siberian State Industrial University
Tel.: +7 (3843) 74-86-28
E-mail: redjizvz@sibsiu.ru

Editorial Board:

Journal "Izvestiya. Ferrous metallurgy" is included in the "List of the leading peer-reviewed scientific journals and publications, in which should be published major scientific results of dissertations for the degree of doctor and candidate of sciences" by the decision of the Higher Attestation Commission.

Indexed: Scopus, Russian Science Citation Index (RSCI), Research Bible, Chemical Abstracts, OCLC and Google Scholar

Registered in Federal Service for Supervision in the Sphere of Mass Communications **PI number FS77-35456**.

ИЗВЕСТИЯ
ВЫСШИХ УЧЕБНЫХ ЗАВЕДЕНИЙ
ЧЕРНАЯ МЕТАЛЛУРГИЯ

www.fermet.misis.ru

ISSN 0368-0797 *(Print)* ISSN 2410-2091 *(Online)*

Варианты названия:

Известия вузов. Черная металлургия
Izvestiya. Ferrous Metallurgy

Учредители:

МИСИС
УНИВЕРСИТЕТ НАУКИ И ТЕХНОЛОГИЙ

СибГИУ
Сибирский государственный индустриальный университет

Адреса редакций:

Россия, 119049, Москва, Ленинский просп., д. 4, стр. 1
Национальный исследовательский технологический университет «МИСИС»,
Тел.: +7 (495) 638-44-11
E-mail: fermet.misis@mail.ru, ferrous@misis.ru

Россия, 654007, Новокузнецк,
Кемеровская обл. – Кузбасс, ул. Кирова, зд. 42
Сибирский государственный индустриальный университет,
Тел.: +7 (3843) 74-86-28
E-mail: redjizvz@sibsiu.ru

По решению ВАК журнал «Известия вузов. Черная металлургия» входит в «Перечень ведущих рецензируемых научных журналов и изданий, в которых должны быть опубликованы основные научные результаты диссертаций на соискание ученой степени доктора и кандидата наук».

Индексирование: Scopus, Russian Science Citation Index (RSCI), Research Bible, Chemical Abstracts, OCLC и Google Scholar

Зарегистрирован Федеральной службой по надзору в сфере связи и массовых коммуникаций **ПИ № ФС77-35456**.

Izvestiya. Ferrous Metallurgy.
2023; 66(1)

Известия вузов. Черная металлургия.
2023; 66(1)

CONTENTS / СОДЕРЖАНИЕ

MATERIAL SCIENCE

Kostina M.V., Rigina L.G., Kostina V.S., Kudryashov A.E., Fedortsov R.S. Corrosion-resistant steels based on Fe – ~13 % Cr: Heat treatment, corrosion- and wear resistance 8

Goshkoderya M.E., Bobkova T.I., Bogdanov S.P., Krasikov A.V., Staritsyn M.V., Kashirina A.A. Spraying of TiB_2/Ti and HfB_2/Ti composite powder wear-resistant coatings 27

Pyshmintsev I.Yu., Gizatullin A.B., Devyaterikova N.A., Laev K.A., Tsvetkov A.S., Al'khimenko A.A., Shaposhnikov N.O., Kurakin M.K. Preliminary assessment of X52 large-diameter pipes suitability for transportation of pressurized pure gaseous hydrogen 35

Goikhenberg Yu.N., Polukhin D.S., Zherebtsov D.A., Bodrov E.G. Influence of silicon carbides on the structure and properties of nickel-phosphorus composite coatings 43

Gromov V.E., Aksenova K.V., Ivanov Yu.F., Kuznetsov R.V., Kormyshev V.E. Transformation of fine structure of lamellar pearlite under deformation of rail steel 50

Akimov K.O., Ivanov K.V., Figurko M.G., Ovcharenko V.E. Grain structure formation and microhardness of Ni_3Al intermetallic compound fabricated by SHS extrusion 57

Trishkina L.I., Klopotov A.A., Potekaev A.I., Cherkasova T.V., Borodin V.I. Parameters of substructure in wrought Cu – Mn alloys with FCC lattice 62

METALLURGICAL TECHNOLOGIES

Zinyagin A.G., Muntin A.V., Kryuchkova M.O. Using machine learning tools to study flow stress of tube steels under laboratory conditions and according to industrial rolling data 70

Kaplan M.A., Gorbenko A.D., Ivannikov A.Yu., Konushkin S.V., Mikhailova A.V., Kirsankin A.A., Baikin A.S., Sergienko K.V., Nasakina E.O., Kolmakov A.G., Sevost'yanov M.A. Properties of spherical metal powder manufactured by plasma spraying of 03Cr17Ni10Mo2 stainless steel wire 80

Babailov N.A., Loginov Yu.N., Polyanskii L.I. Cracking in MgO briquettes 86

МАТЕРИАЛОВЕДЕНИЕ

Костина М.В., Ригина Л.Г., Костина В.С., Кудряшов А.Э., Федорцов Р.С. Обзор исследований коррозионностойких сталей на основе Fe – ~13 % Cr: термическая обработка, коррозионная- и износостойкость 8

Гошкодеря М.Е., Бобкова Т.И., Богданов С.П., Красиков А.В., Старицын М.В., Каширина А.А. Напыление износостойких покрытий из плакированных порошков TiB_2/Ti и HfB_2/Ti 27

Пышминцев И.Ю., Гизатуллин А.Б., Девятерикова Н.А., Лаев К.А., Цветков А.С., Альхименко А.А., Шапошников Н.О., Куракин М.К. Предварительная оценка возможности использования труб большого диаметра из стали Х52 для транспортировки чистого газообразного водорода под давлением 35

Гойхенберг Ю.Н., Полухин Д.С., Жеребцов Д.А., Бодров Е.Г. Влияние карбидов кремния на структуру и свойства композитного никель-фосфорного покрытия 43

Громов В.Е., Аксёнова К.В., Иванов Ю.Ф., Кузнецов Р.В., Кормышев В.Е. Трансформация тонкой структуры пластинчатого перлита при деформации рельсовой стали 50

Акимов К.О., Иванов К.В., Фигурко М.Г., Овчаренко В.Е. Формирование зеренной структуры и микротвердости интерметаллического соединения Ni_3Al в результате СВС-экструзии 57

Тришкина Л.И., Клопотов А.А., Потекаев А.И., Черкасова Т.В., Бородин В.И. Параметры субструктуры в деформированных сплавах Cu – Mn с ГЦК решеткой 62

МЕТАЛЛУРГИЧЕСКИЕ ТЕХНОЛОГИИ

Зинягин А.Г., Мунтин А.В., Крючкова М.О. Исследование сопротивления деформации трубных сталей в лабораторных условиях и по данным промышленных прокаток с использованием инструментов машинного обучения 70

Каплан М.А., Горбенко А.Д., Иванников А.Ю., Конушкин С.В., Михайлова А.В., Кирсанкин А.А., Баикин А.С., Сергиенко К.В., Насакина Е.О., Колмаков А.Г., Севостьянов М.А. Исследование характеристик сферического порошка, полученного методом плазменного распыления проволоки из коррозионностойкой стали 03Х17Н10М2 80

Бабайлов Н.А., Логинов Ю.Н., Полянский Л.И. Трещинообразование в брикетах из оксида магния 86

CONTENTS (Continuation) СОДЕРЖАНИЕ (продолжение)

PHYSICO-CHEMICAL BASICS OF METALLURGICAL PROCESSES

Vusikhis A.S., Leont'ev L.I., Gulyaeva R.I., Sergeeva S.V., Tyushnyakov S.N. Effect of B_2O_3 on viscosity of high-magnesia blast furnace slag 89

Materials of the International Scientific Conference "PHYSICO-CHEMICAL FOUNDATIONS OF METALLURGICAL PROCESSES" named after Academician A.M. Samarin, Vyksa, October 10 – 14, 2022

Bakin I.V., Shapovalov A.N., Kalyaskin A.V., Kuznetsov M.S. Influence of barium and strontium on calcium recovery degree upon ladle treatment of steel by complex modifiers with alkaline earth metals 97

Vorozheva E.L., Smetanin K.S., Kislitsa V.V., Kudashov D.V. Metallographic analysis of structural peculiarities of thin slab and rolled products manufactured thereof 105

INFORMATION TECHNOLOGIES AND AUTOMATIC CONTROL IN FERROUS METALLURGY

Abdukodirov I.B., Vargin A.V., Levitskii I.A. Mathematical model of slab heating in a furnace with walking beams 112

Leont'ev A.S., Rybenko I.A. Mathematical modelling system for metallurgical enterprise: Operation and usability enhancement 119

IN THE ORDER OF DISCUSSION

Bahfie F., Manaf A., Astuti W., Nurjaman F., Suharto S., Herlina U., Adi W.A., Manawan M. Composition of tailings after selective reduction of laterite 127

ФИЗИКО-ХИМИЧЕСКИЕ ОСНОВЫ МЕТАЛЛУРГИЧЕСКИХ ПРОЦЕССОВ

Вусихис А.С., Леонтьев Л.И., Гуляева Р.И., Сергеева С.В., Тюшняков С.Н. Влияние B_2O_3 на вязкость высокомагнезиальных доменных шлаков 89

По материалам Международной научной конференции «ФИЗИКО-ХИМИЧЕСКИЕ ОСНОВЫ МЕТАЛЛУРГИЧЕСКИХ ПРОЦЕССОВ» им. академика А.М. Самарина, Выкса, 10 – 14 октября 2022 г.

Бакин И.В., Шаповалов А.Н., Каляскин А.В., Кузнецов М.С. Влияние бария и стронция на степень усвоения кальция при внепечной обработке стали комплексными модификаторами с щелочноземельными металлами 97

Ворожева Е.Л., Сметанин К.С., Кислица В.В., Кудашов Д.В. Металлографическое исследование особенностей строения тонкого сляба и произведенного из него проката 105

ИНФОРМАЦИОННЫЕ ТЕХНОЛОГИИ И АВТОМАТИЗАЦИЯ В ЧЕРНОЙ МЕТАЛЛУРГИИ

Абдукодиров И.Б., Варгин А.В., Левицкий И.А. Математическая модель нагрева сляба в печи с шагающими балками 112

Леонтьев А.С., Рыбенко И.А. Опыт использования и повышения юзабилити системы математического моделирования производства на металлургическом предприятии 119

В ПОРЯДКЕ ДИСКУССИИ

Бахфи Ф., Манаф А., Астути В., Нурджаман Ф., Сухарто С., Херлина У., Ади В.А., Манаван М. Состав хвостов при избирательном восстановлении латерита 127

MATERIAL SCIENCE / МАТЕРИАЛОВЕДЕНИЕ

UDC 669.018.8
DOI 10.17073/0368-0797-2023-1-8-26
https://fermet.misis.ru/jour/article/view/2474

Review article
Обзорная статья

Corrosion-resistant steels based on Fe – ~13 % Cr: Heat treatment, corrosion- and wear resistance. Review

M. V. Kostina [1], L. G. Rigina [1, 2], V. S. Kostina [1], A. E. Kudryashov [1], R. S. Fedortsov [1]

[1] **Baikov Institute of Metallurgy and Materials Science, Russian Academy of Sciences** (49 Leninskii Ave., Moscow 119991, Russian Federation)
[2] **JSC Russian State Research Center "CNIITMASH"** (4 Sharikopodshipnikovskaya Str., Moscow 115088, Russian Federation)

mvk@imet.ac.ru

Abstract. Martensitic stainless steels with 13 % Cr are widely used in many industries due to their high level of mechanical properties and acceptable corrosion resistance. The paper consolidates information on the guaranteed level of properties and heat treatment conditions required for its implementation. The properties after treatments proposed by researchers are compared with those known for industrial metal. The dependences of the hardness of 13Cr type hardened steels with 0.20 – 0.50 % C on the austenitization temperature and the accompanying changes in structure have been analyzed. The temperatures providing maximum hardening and the temperatures at which the steel ceases to harden have been revealed. The effect of the duration of austenitization, heating and cooling rates on the properties of steels has been considered. The mechanical properties and corrosion resistance after quenching, quenching and tempering in relation to structural-phase states of steels are considered. It is discussed in detail how the type of secondary phases during tempering, their amount, and distribution affect the corrosion resistance of steels with 13 % Cr. It increases with increasing heating temperature during austenitization and decreases with increasing tempering temperature due to the precipitation of $Cr_{23}C_6$ carbides and depletion of the matrix in chromium to the concentrations below 12 %. The tempering temperature of 500 – 550 °C is recognized as the worst: due to intensive precipitation of carbides the steel is not passive, and the corrosion rate is maximum. Quenching with low tempering is recommended for 20Cr13 steels (to combine high strength, good corrosion resistance and satisfactory plasticity), or, more often, quenching with high tempering is recommended at ~(650 – 700) °C (good plasticity, satisfactory corrosion resistance). For steels of 40Cr13 type the temperature of ~700 °C is not recommended because of the increased concentration of carbides and insufficient corrosion resistance. Examples of increasing the wear resistance properties of 40Cr13 steels due to surface treatments, from nitriding to laser and plasma surface quenching, are presented.

Keywords: steel, chromium, alloying, carbides, martensite, austenite, quenching, annealing, mechanical properties, corrosion resistance, wear resistance

Acknowledgements: The study was supported by the Russian Science Foundation, grant No. 22-23-01036.

For citation: Kostina M.V., Rigina L.G., Kostina V.S., Kudryashov A.E., Fedortsov R.S. Corrosion-resistant steels based on Fe – ~13 % Cr: Heat treatment, corrosion- and wear resistance. Review. *Izvestiya. Ferrous Metallurgy*. 2023; 66(1): 8–26.
https://doi.org/10.17073/0368-0797-2023-1-8-26

Обзор исследований коррозионностойких сталей на основе Fe – ~13 % Cr: термическая обработка, коррозионная- и износостойкость

М. В. Костина [1], Л. Г. Ригина [1, 2], В. С. Костина [1], А. Э. Кудряшов [1], Р. С. Федорцов [1]

[1] **Институт металлургии и материаловедения им. А.А. Байкова РАН** (Россия, 119991, Москва, Ленинский пр., 49)
[2] **Центральный научно-исследовательский институт технологии машиностроения, ОАО НПО «ЦНИИТМАШ»** (Россия, 115088, Москва, Шарикоподшипниковская ул., 4)

mvk@imet.ac.ru

Аннотация. Мартенситные нержавеющие стали с 13 % Cr широко используются во многих отраслях промышленности благодаря высокому уровню механических свойств и приемлемой коррозионной стойкости. В работе консолидирована информация о гарантированном уровне свойств и условиях термической обработки, необходимых для его реализации. Сопоставлены свойства после предлагаемых

исследователями обработок с известными для промышленного металла. Проанализированы зависимости твердости закаленных сталей типа 13Cr с 0,20 – 0,50 % C от температуры аустенитизации и сопутствующих изменений структуры. Выявлены температуры, обеспечивающие максимальное упрочнение и температуры, при которых сталь перестает упрочняться. Рассмотрено влияние длительности аустенитизации, скоростей нагрева и охлаждения на свойства сталей. Рассмотрены механические свойства и коррозионная стойкость после закалки, закалки и отпуска во взаимосвязи со структурно-фазовыми состояниями сталей. Подробно рассмотрено, как вид вторичных фаз при отпуске, их количество, распределение влияют на коррозионную стойкость сталей с 13 % Cr. Она повышается с ростом температуры нагрева при аустенитизации и снижается с ростом температуры отпуска вследствие выделения карбидов $Cr_{23}C_6$ и обеднения матрицы хромом до концентраций ниже 12 %. Температура отпуска 500 – 550 °C признана наихудшей: из-за интенсивного выделения карбидов сталь не пассивируется, скорость коррозии максимальна. Для сталей типа 20Х13 рекомендуются закалка с низким отпуском (для сочетания высокой прочности, хорошей коррозионной стойкости и удовлетворительной пластичности), либо, чаще, закалка с высоким отпуском при ~(650 – 700) °C (хорошая пластичность, удовлетворительная коррозионная стойкость). Для сталей типа 40Х13 температура ~700 °C не рекомендуется из-за повышенной концентрации карбидов и недостаточной коррозионной стойкости. Приведены примеры повышения износостойкости сталей типа 40Х13 за счет поверхностных обработок, от азотирования до лазерной и плазменной поверхностной закалки.

Ключевые слова: сталь, хром, легирование, карбиды, мартенсит, аустенит, закалка, отжиг, механические свойства, коррозионная стойкость

Благодарности: Исследование выполнено при поддержке гранта Российского научного фонда № 22-23-01036.

Для цитирования: Костина М.В., Ригина Л.Г., Костина В.С., Кудряшов А.Э., Федорцов Р.С. Обзор исследований коррозионностойких сталей на основе Fe – ~13 % Cr: термическая обработка, коррозионная- и износостойкость. *Известия вузов. Черная металлургия*. 2023; 66(1): 9–26. https://doi.org/10.17073/0368-0797-2023-1-8-26

Introduction

Medium-carbon high-strength martensitic steels with 0.20 – 0.40 % C and 12 – 14 % Cr are a widely demanded constructional material, which is the most inexpensive among corrosion-resistant steels. They are used in the manufacture of loaded parts, friction pairs and metal seals, pressure vessels, hydraulic units, casings for the oil and gas industry, and steam turbine blades. Although they are not a new material, there are many publications dedicated to them in the scientific literature. These works are aimed at:

– modifying the surface of (20–40)Cr13 steels to increase their strength and wear resistance properties, studying their corrosion resistance;

– forming the structure and phase composition of similar steels, providing high strength while maintaining the process ductility and ensuring corrosion resistance due to variations in the chemical composition and heat treatment modes.

In this review article:

– information on the structure and guaranteed level of properties currently achievable in industrial steels with 0.20 – 0.40 % C and 12 – 14 % Cr is provided;

– the structure and mechanical properties of steels of this type, obtained as a result of modern studies of the effect of different variants for traditional heat treatment of such steels – martensite quenching and different types of tempering (annealing) – are considered;

– information on the results of studies of corrosion resistance of these steels is given.

Properties of industrial steels with ≤0.20 – 0.40 % C and 12 – 14 % Cr

When heated above 800 °C, austenite appears in steels with 13 % Cr. The carbon concentration increase contributes to the expansion of the γ-region[1] [1]. Dissolution of carbide phase particles (primary carbides) occurs during high-temperature annealing. Cooling from the austenitic region fixes the martensitic structure in the steel. Depending on the quenching heating temperature and steel composition, some carbide, ferrite or residual austenite particles may be present in it. During the tempering process, depending on the temperature and duration of the process, there may be a return, polygonization, recrystallization, nucleation of secondary dispersed carbides in martensite, their growth and coagulation. In this way, it is possible to obtain a structure consisting of tempered martensite with carbides, or to bring the process to the decomposition of martensite into a ferrite-nitride mixture.

Table 1 provides standard grade chemical compositions of common industrial steel grades with <0.20 – 0.40 % C and 12 – 14 % Cr. In Russia these are steel grades 20Cr13, 30Cr13 and 40Cr13, differing in carbon content only. According to standard GOST RF 5632-2014, they do not contain other metallic alloying elements except chromium (and up to 0.8 % Mn, see Table 1). Such steels are also known to be supplied with up to 0.6 % Ni, up to 0.2 % Ti, and up to 0.3 % Cu[2]. Steel AISI 420 is an analogue of all the mentioned Cr13 grades with 0.2 – 0.4 % C, because its carbon content is limited to the lower limit of 0.15 %, but the upper limit is not specified[3] (see Table 1).

Using reference resources[2 – 8], the authors summarized the information on industrial steels of Cr13 type (13Cr are foreign grades):

[1] Phase diagram of Fe-Cr-0.2%C. *Wikimedia Commons*. URL: https://upload.wikimedia.org/wikipedia/commons/thumb/3/3c/Phase_diagram_of_Fe-Cr-0.2%25C.svg/1024px-Phase_diagram_of_Fe-Cr-0.2%25C.svg.png

[2] Steel grades and alloys. *Central Metal Portal*. URL: https://metallicheckiy-portal.ru/marki_metallov

[3] *Standard specification for stainless steel bars and shapes. Contractors Materials Company*. URL: https://cmcmmi.com/wp-content/uploads/ASTM-A276.pdf

Table 1

Chemical composition, % (wt.), of Russian and foreign steel grades with 0.20 – 0.40 % C and 12 – 14 % Cr (iron is the basis) according to GOST RF 5632-2014 and Contractors Materials Company [3]

Таблица 1. **Химический состав, % (по массе), российских и зарубежных марок сталей с 0,20 – 0,40 % C и 12 – 14 % Cr (железо – основа) согласно ГОСТ РФ 5632-2014 и Contractors Materials Company [3]**

Steel grade	Standard	C	N	Mn	Si	Cr	Mo	Ni	S	P	Other
20Cr13	GOST 5632-2014	0.16 – 0.25	–	<0.8	<0.8	12.0 – 14.0	–	–	<0.025	<0.030	–
30Cr13		0.26 – 0.35	–								
40Cr13		0.36 – 0.45	–								
AISI 420*	ASTM A276	0.15 min	–	<1.0	<1.0	12.0 – 14.0	–	–	<0.030	<0.040	–

* In the USA these are the AISI 420 grades, in Germany – 1.4031, 1.4034, X38Cr13, X39Cr13, X40Cr13, X42Cr13, X46CM3, X46Cr13; in Japan – SUS420J2; in France – X40Cr14, Z33C13, Z38C13M, Z40C13, Z40C14, Z44C14, Z50C14; in the European Union – 1. 4031, 1.4034, X39Cr13, X40Cr13, X41Cr13; and in China – X40Cr14, X41Cr13KU, X46Cr13

– critical points, treatment modes and structure (Table 2);

– impact of the tempering temperature after quenching on their mechanical properties (Table 3);

– mechanical properties of semiproducts from these steels, giving the idea of their guaranteed level of properties, which modern researchers try to surpass (Table 4).

Table 3 shows that high annealing (tempering) at 700 °C causes increased ductility and impact strength, because at this temperature martensite in steel is converted to ferrite and carbides (see Table 2). The yield strength of rods and forgings varies depending on the section and carbon concentration from 440 to 635 MPa, the tensile strength from 510 to 830 MPa, and the ductility from 12 to 16 %. After quenching and low tempering at 200 to 300 °C, these steels have high strength and low ductility (see Table 3). Therefore, for Russian industrial semiproducts after such treatment only hardness values are given (see Table 4), and for semiproducts made of AISI 420 steel the data of tensile tests are also given. Table 4 shows that for semiproducts from Cr13 type steel the main type of heat treatment is quenching from 1000 – 1050 °C and tempering, mainly high, at temperatures in the range of 600 – 770 °C.

Studies of the impact of quenching and tempering (aging) processes on the structure and properties of Cr13 type steels

At the end of this section summary Table 5 is presented with the chemical composition of all steels considered here.

Hardness measurements are most often used to evaluate the mechanical properties of Cr13 type steels, since it correlates with strength. Few tensile and impact bending test results given in the literature are collected in separate summary Table 6 at the end of this section.

Heating temperature for quenching (austenitizing)

It is known that hardening during martensite quenching of steels is caused by several factors and primarily high dislocation density and presence of carbon in the solid solution. The results of studies [2 – 5] on the effect of austenitizing temperatures of Cr13 type steels with 0.14 – 0.45 % C before quenching on their hardness and phase composition are presented in Figure 1. After holding at 800 °C [2] or rolling at 850 °C [4] and quenching in oil, the steel has a structure consisting of ferrite and finely dispersed $Cr_{23}C_6$ carbides (F + C) and is characterized by minimum hardness. Increasing the heating temperature for quenching to $t \geq 850$ °C causes partial dissolution of carbides and fixation of martensitic structure (M(α)) in the steel during quenching [2]. As the austenitizing temperature increases due to the intensification of carbide dissolution, the hardness of martensite-quenched steel increases. This is due to a significant increase in the degree of tetragonality (c/a) of the martensite crystal lattice, described by dependence [6]

$$c/a = 0.45[C] + 1.00. \quad (1)$$

[4] Index of steel. *Lasmet – Laboratory of Special Metallurgy*. URL: http://www.lasmet.ru/steel

[5] Critical points of steel. *HeatTreatment.ru – Equipment and Technologies for Heat Treatment of Metals*. URL: https://heattreatment.ru/kriticheskie-tochki-stali

[6] 40X13. *MarkMet – Education, Profession, Business*. URL: https://markmet.ru/encyclopedia/40x13

[7] Stainless steel 420 grade data sheet. *Atlas Steels – Australia's largest supplier of stainless steel, aluminium and specialty steel products*. URL: https://atlassteels.com.au/wp-content/uploads/2021/06/Stainless-Steel-420-Grade-Data-Sheet-28-04-21.pdf

[8] SS420 grade AISI 420 stainless steel properties, heat treatment, hardness, magnetic. *The World Material*. URL: https://www.theworldmaterial.com/ss420-astm-aisi-420-stainless-steel-grade/

Table 2

Process parameters and structure of steels 20Cr13, 30Cr13, 40Cr13 (according to [2, 4, 5])

Таблица 2. **Технологические параметры и структура сталей 20Х13, 30Х13, 40Х13 (по данным [2, 4, 5])**

Feature			20Cr13	30Cr13	40Cr13
Critical points, °C	Temperature of the beginning of austenite formation during heating	Ac_1	810[5]; 820[2, 4]	810[2, 5]; 820[4]	800[2]; 810[5]; 820[4]
	Temperature of the beginning of austenite transformation during cooling	Ar_1	780[2]	710[2]	780[2]
	Temperature of the end of ferrite dissolution during heating	Ac_3	900[5]; 950[2, 4]	860[2, 5]; 860 – 880[4]	860[5]
	Temperature at the beginning of ferrite precipitation during cooling	Ar_3	660[2]	660[2]	–
	Temperature of the beginning of martensite transformation	M_n	320[5]	240[2, 5]; 270[4]	240[5]; 270[4]
Deformation temperatures, heating and cooling conditions			1100 – 875 – 950 °C	1100 – 850 °C	
			Heating to deformation is carried out slowly to a temperature of		
			780 °C	830 °C	
			After deformation, slowed cooling in sand or a furnace		
Annealing after deformation			750 – 800 °C, cooling with a furnace to 500 °C	740 – 800 °C, cooling at 25 – 50 °C/h to 600 °C	
Final treatment – quenching and tempering to the required hardness and corrosion resistance			Quenching at 950 – 1000°C with cooling in oil or air + tempering	Quenching at 950 – 1050 °C with cooling in oil or air + tempering. Medical steel: interrupted quenching from 1020 °C to 1040 °C, cooling in alkali at 350 °C	
Microstructure after quenching			Martensite and carbides of $Me_{23}C_6$ type	Martensite, carbides of $Me_{23}C_6$ type have a small amount of residual austenite. Its amount increases as the quenching temperature increases above ≥1050 °C	
Microstructure after annealing			Mixture of high-chromium ferrite and carbide of $Me_{23}C_6$ type	Ferrite-carbide mixture	
Effect of tempering temperature			With an increase of t_{opt} ≥450 °C the ductility increases, and the strength and corrosion resistance decrease significantly	In the tempering temperature range of 450 – 550 °C, the secondary hardness effect related to the precipitation of dispersed carbides is observed	

Herewith, in Cr13 steels parameter *c*/*a* with increasing carbon content increases 2.5 times more intensively than in similar unalloyed steels [2].

The maximum values of HV 540 – 570 for 20Cr13 type steels are achieved after quenching from the temperatures of 1000 – 1050 °C [2 – 4]. For steel with 0.45 % C, the maximum HV level of 696 – 710 is achieved after quenching from 1110 – 1130 °C [5] (see Figure 1). Large-needle martensite is noted in the samples quenched from 1000 °C [2]. When comparing the *X*-ray diffraction spectra of annealed (α-Fe) and austenitized and martensite-quenched (M(α)) samples, expansion and shifting of peaks are clearly visible, which is due to the stress state of the martensitic lattice due to its saturation with carbon [3]. Peak shifting increases with increasing quenching temperature, which indicates greater dissociation of chromium carbides with temperature and increased saturation of martensite with carbon.

The noticeable effect of hardness reduction after reaching its maximum during further increase of the heating temperature over 1000 °C, recorded for 20Cr13 steel with 0.08 % N (420U6) [4], 45Cr13 and 50Cr13 steels during heating at 1100 °C and above [5, 7] is explained by the following:

Table 3

Mechanical properties at 20 °C of 20Cr13 and 40Cr13[6] and AISI 420[7] steels after quenching and annealing at temperatures from 200 to 700 °C

Таблица 3. **Механические свойства при 20 °С сталей 20Х13 и 40Х13[6] и стали AISI 420[7] после закалки и отжига при температурах от 200 до 700 °С**

Steel	Tempering temperature, °C	$\sigma_{0.2}$, MPa	σ_v, MPa	δ_5, %	ψ, %	KCU, J/cm^2 (KCV, J)	HRC (HB)
Quenching:	Quenching at 1050 °C, air						
20Cr13 (billet with 14 mm section)	200	1300	1600	13	50	81	46
	300	1270	1460	14	57	98	42
	400	1330	1510	15	57	71	45
	500	1300	1510	19	54	75	46
	600	920	1020	14	60	71	29
	700	650	780	18	64	102	20
Quenching:	Quenching at 1000 °C, oil						
40X13	200	1620	1840	1	2	19	52
	350	1450	1710	11	22	25	50
	500	1390	1680	7	9	19	51
	700	500	780	35	59	71	(217)
Quenching:	Quenching at 980–1035 °C, oil or air[7]						
AISI 420 (UNS S42000)	Annealed	345	655	25	–	–	(255 max)
	204	1360	1600	12	–	(20)	(444)
	316	1365	1580	14	–	(19)	(444)
	427	1420	1620	10	–	#	(461)
	538	1095	1305	15	–	#	(375)
	593	810	1035	18	–	(22)	(302)
	650	680	895	20	–	(42)	(262)
# This steel shall not be quenched in the range from 425 to 600 °C due to induced low impact strength.							

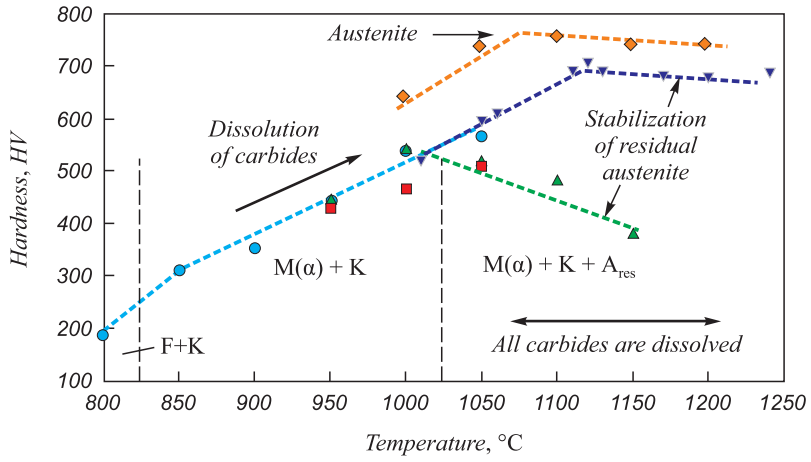

Fig. 1. Effect of austenitization temperature[9] before quenching on hardness[10] and phase composition of Cr13 steels with 0.14 – 0.45 % C: ● – steel 20Cr13 [2]; ■ – steel 20Cr13 [3]; ▲ – steel 20Cr13 + 0.008 N [4]; ▼ – steel 45Cr13 [5]; ◆ – steel 50Cr13 [7]

Рис. 1. Влияние температуры аустенитизации[9] перед закалкой на твердость[10] и фазовый состав сталей Х13 с 0,14 – 0,45 % С: ● – сталь 20Х13 [2]; ■ – сталь 20Х13 [3]; ▲ – сталь 20Х13 + 0,008 N [4]; ▼ – сталь 45Х13 [5]; ◆ – сталь 50Х13 [7]

[9] Выдержки при нагреве, охлаждение: [2, 3] – 30 мин, закалка в масло; [5] – 60 с, охлаждение со скоростью 2 °С/с.

[10] Значения измерений в единицах HRC из работ [2, 4] переведены в значения твердости HV по шкале пересчета, приведенной в работе [8].

Table 4

Mechanical properties of semiproducts from 4Cr13 type steels according to the RF standards and AISI 420[8] steel

Таблица 4. **Механические свойства полуфабрикатов из сталей типа 4Х13 по стандартам РФ и стали AISI 420[8]**

GOST	Type of semiproduct, heat treatment mode	Section, mm	$\sigma_{0.2}$, MPa	σ_v, MPa	δ_5, %	Ψ, %	KCU, kJ/m^2	HB (HRC$_o$, max)
Mechanical properties of 20Cr13 steel								
GOST 5949-75	Rods. Quenching at 1000 – 1050 °C, air or oil. Tempering at 600 – 700 °C, air or oil	60	635	830	10	50	59	–
	Rods. Quenching at 1000 – 1050 °C, air or oil. Tempering at 660 – 700 °C, air, oil or water	60	440	650	16	55	78	–
GOST 18907-73	Ground rods, machined to the specified strength	1 – 30	–	510 – 780	14	–	–	–
GOST 7350-77	Hot- or cold-rolled sheets. Quenching at 1000 – 1050 °C, air. Tempering at 680 – 780 °C, air or furnace (transverse specimens)	Over 4	372	509	20	–	–	–
GOST 25054-81	Forgings. Quenching at 1000 – 1050 °C, air or oil. Tempering at 660 – 770 °C, air	1000	441	588	14	40	39	–
GOST 4986-79	Cold-rolled strip. Annealing or tempering at 740 – 800 °C	Up 0.2	–	500	8	–	–	–
		0.2 – 2.0	–	500	16	–	–	–
GOST 18143-72	Heat-treated wire	1.0 – 6.0	–	490 – 780	14	–	–	–
Mechanical properties of 30Cr13 steel								
GOST 5949-75	Quenching at 950 – 1020 °C, oil. Tempering at 200 – 300 °C, air or oil	Speci-mens	–	–	–	–	–	(50)
GOST 18907-73	Ground rods machined to the specified strength	1 – 30	–	530 –780	12	–	–	–
GOST 25054-81	Forgings. Quenching at 1000 – 1050 °C, oil. Tempering at 700 – 750 °C, air	Up to 1000	588	735	14	40	29	Surfaces 235 – 277
GOST 18143-72	Heat-treated wire	1.0 – 6.0	–	490 – 830	12	–	–	–
GOST 5582-75	Thin sheet, annealing or tempering at 740 – 800 °C	–	–	490	15	–	–	–
Mechanical properties of 40Cr13 steel								
GOST 5949-75	Rods. Quenching at 1000 – 1050 °C, oil. Quenching at 200 – 300 °C, cooling in the air or in oil	Speci-mens	–	–	–	–	–	(≥52)
GOST 18907-73	Rods:							
	– ground, machined to the specified strength;	1 – 30	–	590 – 810	10	–	–	–
	– annealed	Over 5	–	–	–	–	–	143 – 229
GOST 5582-75	Thin, hot-rolled or cold-rolled sheets. Annealing or tempering at 740 – 800 °C (transverse samples)	Up 3.9	–	550	15	–	–	–
GOST 18143-72	Heat-treated wire	1.0 – 6.0	–	590 – 810	10	–	–	–
Mechanical properties of AISI 420 steel (UNS S42000)[8]								
ASTM AISI and SAE Standards	Quenching from 1038 °C in oil. Quenching at 316 °C	–	1482	1724	8	25	20 J	(≥52)
	Annealed rod	–	345	655	25	55	–	195
	Annealing, drawing	–	690	760	14	40	–	228

– in the structure of these steels due to the intensification of carbides and carbonitrides dissolution the concentration of austenite-forming elements (carbon [5, 6], carbon and nitrogen [4]) is achieved and increases, contributing to the formation of residual austenite and increasing its quantity after quenching (Fig. 1);

– growth of the austenite grain [7].

It is noteworthy that in the 20Cr13 steel, in the absence of nitrogen in its composition, stabilization of austenite after holding at 1050 °C did not occur [2, 3] in contrast to the 20Cr13 steel with 0.08 % N [4] (Fig. 1). It should be noted that in the 50Cr13 steel, which is on the modified Schaeffler–Delong diagram in the martensite-austenite region near the boundary with the austenite region, the amount of austenite after austenitization at temperatures in the range of 1000 – 1200 °C and quenching increases from 97.5 to 100 % [7].

Grain-boundary carbides not dissolved during thermal soaking inhibit grain growth during heating. Increasing the austenitizing temperature of the 20Cr13 steel with 0.08 % N from 950 to 1100 °C (holding during 30 min) leads to an order decrease in carbide density from ~0.053 to ~0.004 1/μm^2, and their average diameter decrease from 0.57 to 0.26 μm (Fig. 2, *a*) [4]. Further increase in the annealing temperature to 1150 °C no longer contributed to significant changes in the particle density and size. Increasing the austenitizing temperature from 950 to 1000 °C did not cause the grain growth during holding for 30 and 60 min at those temperatures, and the grain size remained equal to 15 – 18 μm. Increasing the heating temperatures above 1000 °C led to significant grain growth (Fig. 2, *b*). Obviously, decrease in the carbide density and increase in the grain size also contribute to the decrease in hardness of this steel quenched from temperatures above 1000 °C.

Only weak grain growth from 10 to 20 μm was observed for the 45Cr13 steel with higher carbon content [5] in the heating tempering range for quenching of 1000 – 1120 °C; austenitization at 1170 and 1240 °C resulted in the grain growth to 47 and 65 μm respectively. For steel X46Cr13 (1.4034) it was noted [9] that austenitizing at temperatures above 1100 °C causes complete dissolution of carbides in X46Cr13 and optimum distribution of chromium and carbon in the mixed crystal. The elimination of the blocking effect of carbides and the higher diffusion rate lead to significant grain enlargement. Decreasing the austenitizing temperature below 1100 °C leaves mixed chromium and iron carbides in the structure, which reduce hardness and corrosion resistance.

Duration of heating during austenitization (during heating for quenching)

The effect of duration of annealing (~950 – 1200 °C, 30, 60 and 120 min) of the 20Cr13 steel with 0.08 % N on the structure and hardness has been studied [4]. It is shown that the longer the holding time at a given temperature, the coarser the grain size, and this effect is more significant the higher the heating temperature (Fig. 2, *b*). At low temperatures (960 and 1000 °C), the holding time had little effect and the grain growth from the 15 – 20 μm level was practically not registered. At 1200 °C such holding led to the grain growth up to 87 – 142 μm. With all holding times, the hardness maximum was observed when the austenitization temperature increased to 1000 °C, and

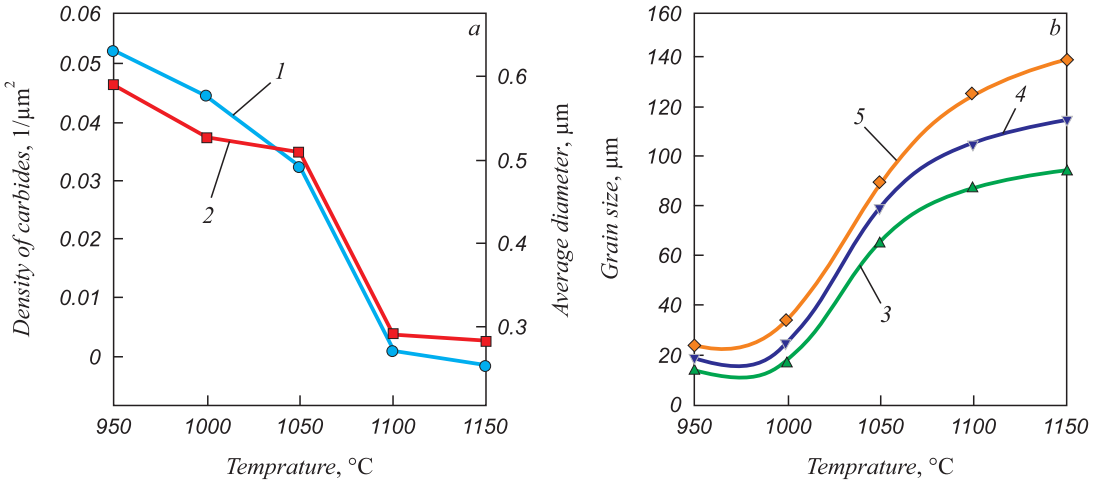

Fig. 2. Effect of austenitization temperature of 20Cr13 steel with 0.08 % N on density (*1*) and average size of carbide particles (*2*) during holding for 30 min (*a*) and martensite grain size (*b*) during soaking for:
3 – 30 min; *4* – 60 min; *5* – 120 min [4]

Рис. 2. Влияние температуры аустенитизации стали 20Х13 с 0,08 % N на плотность (*1*) и средний размер карбидных частиц (*2*) при выдержке 30 мин (*a*) и размер зерна мартенсита (*b*) при выдержке:
3 – 30 мин; *4* – 60 мин; *5* – 120 мин [4]

Table 5

Chemical composition of 13Cr steels under study

Таблица 5. **Химический состав рассмотренных сталей 13Cr**

Source	C	N	Mn	Si	Cr	Mo	Ni	S	P	Other components
[2]	0.16 – 0.25	–	≤0.800	≤0.800	12.00 – 14.00	–	≤0.600	≤0.025	≤0.0300	Cu ≤0.3, Ti ≤0.2
[3]	0.17	–	0.700	0.500	12.20	–	–	0.030	0.2300	–
[4]	0.14	0.085	0.590	0.380	13.78	–		0.006	0.0270	–
[5]	0.45	–	0.440	0.320	13.00	–	0.380	0.016	0.0300	–
[9]	0.42	–	0.530	0.400	13.92	0.030	0.310	–	–	Cu = 0.15
[10]	0.45	–	0.440	0.320	13.00	–	0.380	0.016	0.0300	–
[11]	0.43	–	0.600	0.560	13.00	–	–	–	–	–
	0.19	–	0.640	–	12.77	–	–	–	–	–
[12]	<0.2	<0.020	0.500	0.310	12.78	<0.050	0.130	0.016	0.0010	Nb + V + Ti = 0.064, Cu <1.0
[11]	0.26 – 0.35	–	≤1.500	≤1.000	12.00 – 14.00	–	–	≤0.030	≤0.0400	Cu ≤0.3, Ti ≤0.2
[13]	0.15	–	1.160	1.060	12.08	0.131	0.952	0.030	0.0400	–
[16]	0.38	–	0.600	0.900	13.60	–	–	–	–	V = 0.30
[17]	0.18	–	0.850	0.300	12.90	–	–	0.002	0.0200	–
[18]	0.347	–	0.332	0.422	14.11	–	–	0.030	0.0156	–

then it decreased with increasing temperature. The longer the holding time in the range of 1050 – 1150 °C, the more residual austenite was in the steel and the lower the hardness was achieved during subsequent quenching. Treatment at 1000 °C for 30 min was chosen as optimal, as it provided maximum hardness while maintaining a relatively fine grain size.

Thus, the maximum effective temperature of austenitization before quenching, which provides high hardness, is 1000 – 1020 °C for steel type 20Cr13 and 1100 – 1120 °C for steel type 45Cr13.

Heating rate during austenitization and cooling rate during quenching

When quenching carbon-containing steels, martensitic transformation occurs in a shear manner. However, this does not exclude the possibility of diffusive redistribution of carbon in austenite during cooling to the temperature of the beginning of martensitic transformation (M_n) and further in the formed martensite when cooling from M_n to the room temperature [6].

The study [10] conducted on steel with 0.45 % C and 13Cr (45Cr13) showed that the temperature required to achieve complete dissolution of $Me_{23}C_6$ carbides in the austenitic phase increases with the increasing heating rate from 0.05 to 10 K/s, changing from 1353 to 1448 K (1080 – 1175 °C). For a given heating rate and holding time (60 s), the amount of carbide in the quenched microstructure of this steel decreases with increasing temperature. Carbide precipitation was found during quenching from 1393 K (1120 °C) and slower cooling rates than 20 K/s. For these cooling rates, the amount of carbide precipitation increased with the decreasing cooling rate. With continuous cooling at any quenching rate from 1333 K (1060 °C) no significant carbide precipitation is observed. After annealing at optimum temperatures, starting from the cooling rate of 1 °C/s, the hardness of martensite microstructures is very close to the maximum. The hardness obtained by quenching from their respective optimum temperatures reaches the values between 700 and 710 HV_5 when cooling at 1 °C/s. For X45Cr13 steel heated to 1120 °C, the percentage of the carbide area in the final microstructure after quenching at a cooling rate of 1 °C/s is 3.2 %, whereas when quenched from 1060 °C at a cooling rate of more than 25 °C/s it is 6 % [10].

High-rate heating (50 °C/s) by the method of current transmission through the specimen was carried out on steel 20Cr13 specimens (length of 100 mm, diameter of 10 mm), after which they were quenched in oil [2]. The obtained properties were compared with the results of metal heated in the furnace and similarly quenched metal. The maximum value of the tensile strength of 1530 MPa when heated in the furnace was achieved after quenching from 950 °C, and the relative elongation did not exceed 4.7 %. During high-rate heating the same strength was obtained after quenching from a temperature of 1020 °C, and the relative elongation in this case did not

[11] X30Cr13 – Nr. 1.4028. Rodacciai. URL: https://www.rodacciai.com/UPLOAD/datasheets/420B_X30Cr13-Nr.1.4028-ENG.pdf

Table 6

Mechanical properties of 13Cr steels after various heat treatments

Таблица 6. **Механические свойства сталей 13 Cr после различных термических обработок**

Source	% C in steel	Heat treatment (temperature in °C)		Treatment number	$\sigma_{0.2}$, MPa	σ_v, MPa	δ_5, %	Ψ, %	Hardness		Impact energy, J
[13]	0.15	Quenching from 1000 + tempering for 2 h at temperatures:	200 + 200	1	780	1720	–	–	HRC	52	80
			450 + 450	2	736	1605	–	–		51	87
[17]	0.18	Quenching from 980	710 + 680	3	570	712	20	64	BHN	212	18*
		Quenching from 1040		4	640	780	26	66		232	13*
		Quenching from 1040 + 980		5	620	752	27	66		227	29*
[11]	0.19	Quenching at 1050, 240 s + tempering for 375, 375 s		6	–	1515	7.5	–	–	–	–
[2]	0.16 – 0.25	Quenching	800	7	–	579	29	–	HRC	14	–
			950	8	–	1530	4.7	–		45	–
		Quenching from 850 + tempering for 2 h at temperatures:	500	9	–	–	–	–		34	–
			600	10	–	–	–	–		17	–
			700	11	–	–	–	–		12	–
		Quenching from 1000 + tempering for 2 h at temperatures:	500	12	990	1010	1	4		43	–
			600	13	730	855	16	55		33	–
			650	14	–	–	10	30		–	–
			700	15	560	700	17	57		19	–
[18]	0.347	Annealing for 15 min, cooling with a furnace	850	16	265	530	14	–	HV	200	–
		Annealing at 850 + quenching from 1000, 15 min, air cooling + tempering at temperatures	200	17	755	989	15	–		310	–
			500	18	630	880	19	–		400	–
		Annealing + quenching + cryogenic treatment + tempering at temperatures	200	19	440	664	15	–		250	–
			500	20	650	933	40	–		260	–
[11]	0.43	Quenching at 1100, 300 s + tempering for 400, 300 s		21	–	1800	11	–	–	–	–

* Charpy samples, tests at –10 °C

exceed 6.5 %. After a series of experiments in [2] it was concluded that high-rate heating leads to a shift of hardening curves by 40 – 60 °C up the temperature scale compared to the curves obtained during furnace heating.

The effect of different cooling rates (from 3 to 100 K/s) during hot forging of X46Cr13 steel on the hardness, strength and ductility of steel after quenching (1100 °C, 300 s) and after additional tempering (1100 °C, 300 s) was studied [11]. This factor was shown to have no effect on hardness: it is at a level of about 700 HV_{10} after quenching and 580 HV_{10} after tempering. During the study of the effect on strength and ductility, the steel sheets were cooled to the room temperature at a rate of 3 to 140 K/s, caused by different surface pressures in the tool and outside the cooling medium. No significant effect on the tensile strength was found, whereas the relative tensile elongation could decrease from 11 to 6 % with the increasing cooling rate. The best properties (strength of 1800 MPa and relative elongation of 11 %) were obtained after a low surface pressure of 1 MPa and a cooling rate of 30 K/s.

Effect of tempering modes after quenching from different temperatures

Tempering of quenched laboratory steels 20Cr13 [2], AISI 420 with 0.17 % C [3] and <0.20 % C [12] causes their hardness reduction especially significant in the temperature range from 400 to 780 °C (Fig. 3, *a*). In the tempering temperature range up to ~600 °C higher hardness values are inherent in steels quenched from higher temperatures, which have higher supersaturation of austenite with carbon during quenching (this shows a significant difference in hardness values for the same tempering temperature obtained in different studies). The results of the study of properties after quenching and tempering over the widest temperature range are given for the X30Cr13 steel (1.4028) with a grade content of 0.26 – 0.35 % C and up to 1 % Si (Fig. 3, *b*)[11].

The annealing temperature range of 710 – 780 °C was studied in [12] due to the fact that the 13Cr steel casings are used in the condition after quenching and tempering at 680 – 780 °C (API-5CT). After quenching from 975 °C, the steel was characterized by the presence of lath martensite and hardness of 525 HV. Holding of such martensite for 20 min at 710, 730, 750, 770, 780 °C showed that tempering at ~(710 – 730) °C leads to martensite enlargement. It becomes equiaxial, and in its structure there are $Cr_{23}C_6$ carbides in the form of spheres/rods and needle Cr_7C_3 carbides (~100 nm). Tempering at 770 °C causes dissolution of Cr7C3 carbides and enlargement of spherical $Cr_{23}C_6$ carbides, and recrystallization occurs. Hardness at such high tempering decreases (Fig. 3, *a*).

Hardness of the X30Cr13 steel weakly decreases in the temperature range up to 300 °C, then a plateau is observed up to 500 °C, after which, in the range of 500 – 600 °C, there is a sharp decrease in hardness (Fig. 3, *b*). The strength properties change in a similar way, including the ultimate strength decreasing from 1600 to 900 MPa for anneals between 500 and 700 °C. The ductility and impact strength change mirror-like, and when annealed at temperatures above 500 °C they increase significantly. The manufacturer recommends[11] the following temperatures for this steel: 900 – 1100 °C for hot deformation, 745 – 825 °C for annealing with cooling in the air, 950 – 1050 °C for quenching in oil or air, and 625 – 675 °C for annealing (after quenching from 850 °C).

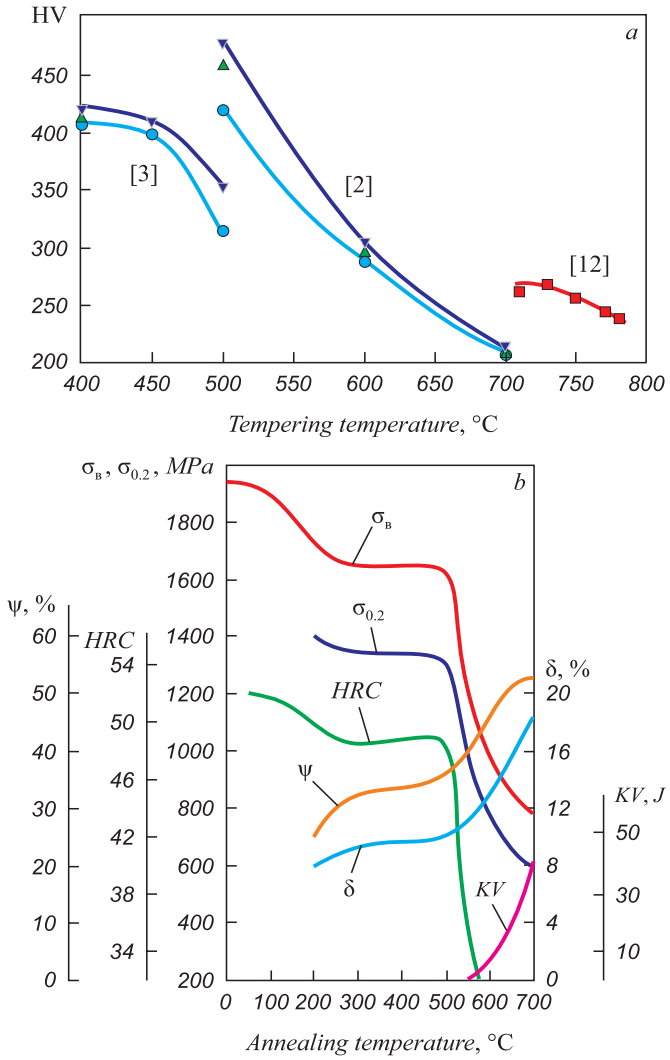

Fig. 3. Effect of annealing temperature:
a – on hardness of laboratory steels of 20Cr13 type after quenching from different temperatures [2, 3, 12] (● – 950, ■ – 975, ▲ – 1000 and ▼ – 1050 °C);
b – on hardness, strength, ductility and impact energy of industrial steel X30Cr13 – Nr. 1.4028 (30Kh13)[11]

Рис. 3. Влияние температуры отжига:
a – на твердость лабораторных сталей типа 20Х13 после закалки от разных температур [2, 3, 12] (● – 950, ■ – 975, ▲ – 1000 и ▼ – 1050 °C);
b – на твердость, прочность, пластичность и энергию ударного разрушения промышленной стали Х30Cr13 – Nr. 1.4028 (30Х13)[11]

The effect of isothermal holding of steel quenched from 975 °C at 750 °C for 5 – 60 min on the carbide formation processes was studied [12]. After isothermal treatment for 5 min, $Cr_{23}C_6$ carbides were formed mainly at the grain and lath boundaries, and Cr_7C_3 carbides were formed inside the laths. Further increase in the time of isothermal annealing led to dissolution of Cr_7C_3 carbides and enlargement of $Cr_{23}C_6$ carbides. Accordingly, after holding for 5 and 15 min, the return processes were observed, and after longer holding recrystallization and grain growth processes took place. The return and recrystallization during tempering reduce the hardness of steels up to 250 HV. Minimum hardness at 750 °C is achieved during 15 min holding, at which time it decreases from 550 to 275 HV. Further heating at 750 °C (up to 60 min) does not lead to changes in hardness. In this case, the average particle size increases from ~45 to ~130 nm, and their density decreases compared to the maximum one by a factor of 3. The density of the particles is maximum after holding for 5 min; and during this time about 50 % of the total amount of the carbide phase is precipitated for 60 min, estimated by the "area fraction, %" parameter.

In [11] the heating temperatures for quenching of the X20Cr13 steel varied from 950 to 1150 °C and the tempering temperatures were 225, 375 and 525 °C. The holding times during such treatments were 240 and 480 s. The strength of the steel in this case ranged from 1310 to 1660 MPa, and the ductility varied from 3.5 to 7.5 %. The best combination of these characteristics, 1515 MPa strength and 7.5 % elongation, was achieved after quenching from 1050 °C (240 s) and tempering at 375 °C (420 s).

In this section only the effect of tempering on the structure and mechanical properties of steels is considered; below, in a separate section, attention is paid to the effect of this treatment on the corrosion resistance of steels with 13 % Cr.

Use of complex heat treatments: repeated austenitization, double annealing, cooldown

The effect of double annealing on the structure, hardness, strength and impact strength of AISI 410 steel was studied [13]. In the initial state the steel had a structure consisting of ferrite and chromium-rich carbides $Me_{23}C_6$ after annealing at 750 °C for 2 h followed by slow cooling inside the furnace to a temperature of 25 °C for 20 h in order to obtain maximum softness for molding [13, 14]. Such samples were heated in the range of 900 and 1100 °C (30 min) and quenched in oil, followed by double annealing at temperatures between 200 and 700 °C (steel was cooled after annealing and then annealed again at the same temperature). The purpose of repeated annealing was to promote the transformation of residual austenite into martensite, since, according to [15], residual austenite is almost completely transformed as a result of double tempering at high temperature.

It was shown [13] that chromium carbides $Me_{23}C_6$ dissolve in the temperature range from 950 °C. Varying the tempering temperature of steel samples austenitized at 900 °C does not effectively change the microstructure or cause hardening (Fig. 4, *a*), as $Me_{23}C_6$ carbides are not precipitated, martensite and ferrite become softer and ductility increases. The structure after this treatment is ferrite in a matrix of lath-tempered martensite with $Me_{23}C_6$ chromium carbide particles (primary and small particles of secondary). The highest values of hardness as well as the yield strength and tensile strength are achieved after quenching from higher $T_A = 1050$ °C and tempering at 200 °C (Fig. 4, *a* – *c*).

The microstructure after tempering at 200 – 650 °C consists of ferrite islands and small spheroidal particles of secondary chromium carbide $Me_{23}C_6$ in a matrix of coarse-grained lath-tempered martensite. Tempering at $t \geq 550$ °C leads to an increase in the number of precipitations along grain boundaries. A satisfactory combination of hardness, strength and impact energy is achieved by double tempering of steel at 200 and 450 °C after quenching from 1050 °C (Fig. 4, Table 6) [22]. In general, double tempering did not result in a significant change in mechanical properties for any of the tested specimens; the microstructure after it still contained a significant amount of residual austenite. During conventional austenitizing treatment, carbide dissolution and grain size growth intensified with increasing austenitizing temperature, while double tempering treatment promoted carbide formation with a slight increase in the grain size. For comparison, in the 40Cr13 type steel (with 0.38 % C and 0.3 % V, i.e., in which the number of carbide particles must be much larger) the precipitations in the samples after single tempering at 300, 500 and 650 °C are nanosized ε-Me_3C carbides, chromium-rich nanosized $Me_{23}C_6$ carbides and micron or submicron $Me_{23}C_6$ carbides, respectively [16].

The effect of treatment with double quenching and double annealing (710 °C + 680 °C) on the microstructure, hardness, and mechanical properties of 13Cr hot-rolled steel with 0.2 % C was studied [17]. Austenitizing followed by quenching (duration of 3 h 15 min) was carried out according to the following modes: 980 °C, quenching + 1040 °C, quenching; 1040 °C, quenching + 980 °C, quenching. Cooling during quenching and after tempering was carried out in oil. Both in the case of single quenching at 980 °C and double quenching (1040 °C + 980 °C), there was no delta-ferrite in the tempered martensite microstructure. After single heat treatment, the structure contained carbides along the grain boundaries, and very fine distribution of ferrite was observed. During single quenching, continuous carbide chains along the grain boundaries of the former austenite contributed

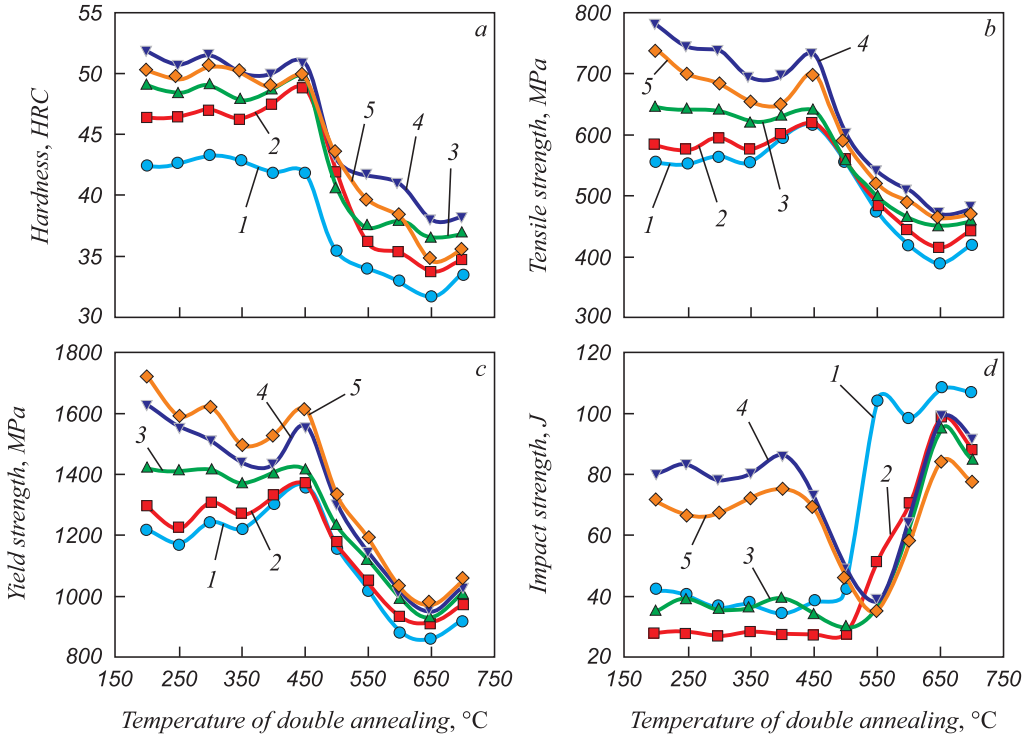

Fig. 4. Effect of double annealing temperature on hardness (*a*), yield strength (*b*), tensile strength (*c*), impact strength (*d*) of AISI 410 steel after quenching from austenitization temperatures (T_A), °C [13]: *1* – 900; *2* – 950; *3* – 1000; *4* – 1050; *5* – 1100

Рис. 4. Влияние температуры двойного отжига на твердость (*a*), предел текучести (*b*), предел прочности (*c*) и ударную вязкость (*d*) стали AISI 410 после закалки от температур аустенитизации (T_A), °C [13]: *1* – 900; *2* – 950; *3* – 1000; *4* – 1050; *5* – 1100

to the reduction of the impact strength, and its values did not meet the specification requirements. When this steel with the initial martensite microstructure obtained during the first quench from 1040 °C was subjected to secondary austenitizing at 980 °C, recrystallization of the grain structure from the defective matrix of martensitic laths obtained during the first quench occurred. The modified heat treatment with double quenching at 1040 °C + 980 °C provided a finer grain size along with a higher degree of carbon dissolution in the austenitic matrix. During tempering, very fine carbides (having a much smaller size compared to the single heat treatment process) formed in small numbers at low-angle and high-angle boundaries. This resulted in the increased strength and impact strength after tempering, compared to single quenching from 980 °C (Table 2).

In [18] the effect of conventional heat treatment and cryogenic treatment on the mechanical properties of AISI 420 steel was compared. Cryogenic treatment was carried out by a gradual decrease in temperature to avoid the thermal shock: –20 °C, 4 h; –70 °C, 5 h; –196 °C, 24 h. Subsequent heating occurred in the reverse sequence. In the initial state (annealing at 850 °C and cooling with a furnace) the steel had a ferrite-carbide structure with low mechanical properties. Quenching to martensite from 1000 °C followed by tempering at 200 °C provided a martensite structure with residual austenite and undissolved dispersed carbides, and a combination of strength of 989 MPa with ductility of 15 %. Increasing the tempering temperature to 500 °C resulted in coarsening of Me_7C_3 carbides and partial transformation to $Me_{23}C_6$ carbides, some reduction in strength and increase in ductility. Conducting a stepwise cryogenic treatment before tempering at 500 °C increased the strength properties to 933 MPa and the relative elongation to 40 % (Table 6) due to the precipitation of finely dispersed carbides. The combination of strength and plastic properties thus obtained for this steel is a good result, but the disadvantage of such treatment is the complexity of cryogenic treatment using long periods of holding in a refrigerator, dry ice and liquid nitrogen and subsequent heating in the reverse sequence.

Suggested heat treatment options and mechanical properties

Data on the chemical composition of 13Cr type steels discussed above are given in Table 5. The mechanical properties obtained by researchers for 13Cr steels when varying both conventional quenching and tempering modes and dual heat treatments are given in Table 6. Comparison of the properties of treatments No. 1 – 21 from

Table 6 with the properties of industrial steels of the 13Cr group (Table 3) shows that treatments No. 1 and 2 for 20Cr13 type steels and treatment No. 21 for the 40Cr13 steel achieved a higher level of strength than that specified in the known reference materials for these steels. After treatments No. 4 and 5, the 20Cr13 type steel had a level of strength close to that of this steel after tempering at 700 °C in Table 3, but a higher ductility was achieved in this case. The results of treatments No. 16 – 20 are new, and in the reference literature there is no such data for the 30Cr13 steel.

The publications dedicated to the study of corrosion resistance and the possibilities to increase the wear resistance of steels of the Cr13 group are considered below.

Studies of wear resistance of steels with 13 % Cr

In the Russian scientific segment, a number of publications have been found that consider the prospect of increasing the wear resistance of 40Cr13 steel due to surface treatments. In addition, a significant place is given to the surface layer saturation with nitrogen during the following treatments:

– nitrocementation [19];

– ion-plasma nitriding [20, 21], including thermal-cycle [20];

– nitriding combined with heat treatment [22].

It is demonstrated that diffusion layers on the cutting surfaces of 40Cr13 steel, saturated with large amounts of carbonitrides during nitrocementation, provide high cutting ability, self-sharpening and wear resistance [19]. Ion-plasma thermal-cycle nitriding made it possible to obtain hardened wear-resistant surfaces, which have a complex of specific physical, mechanical and operational properties [20]. It has been established that during high-frequency nitriding of 40Cr13 steel in inductively coupled plasma of the argon, hydrogen and nitrogen mixture a three-layer structure is formed in the near-surface layer. Its wear rate is the lower the higher the amplitude of the displacement potential [21]. A study of the wear mechanism of ion-modified nitrogen in 40Cr13 steel subjected to various modes of pretreatment has shown that the nitrated layer is an α-Fe matrix phase with chromium nitrides CrN. In the process of friction of nitrogen-modified 40Cr13 steel, accelerated wear of the nitrided layer is registered as its thickness decreases to a certain critical value. As the hardness of the substrate increases, the critical thickness of the nitrided layer decreases from 11 – 12 to 9 – 10 μm [22].

The possibilities of hardening the 40Cr13 steel by surface laser and plasma quenching have been studied [23, 24]. The possibility of effective surface hardening of products using laser heating is also considered. The influence of arising thermal stresses on the temperature interval of austenitic transformation is taken into account, and the dependences of hardness on density, power and treatment rate are analyzed. The work showed that high hardness is achieved when heating to a temperature of 150 – 200 K below the melting temperature [23]. The technology of plasma surface hardening of products made of high-alloy corrosion-resistant steel 40Cr13 allows obtaining a hardened martensitic layer more than 4 mm deep on its surface [24]. The feature of the technology is the microhardness values evenly distributed over the section, the absence of changes in the geometric shape and structure of the 40Cr13 steel part core. In the hardening zone from the solid phase a spectrum of structures is observed – from the martensitic type structure on the boundary with the melting zone with the transition to the martensitic type structure with carbides precipitation (both in the grain body and on the grain boundaries). In the transition zone (thermal impact zone) the structure has the form of a ferrite-carbide mixture of sorbitic type of different dispersion. Such a distribution of microstructures in zones is characteristic of the traditional hardening of 40Cr13 steel products for maximum hardness with preservation of corrosion resistance properties.

Complex treatment of the 40Cr13 steel consisting of heat and mechanical treatments, high-vacuum annealing and diffusion siliconizing has been proposed [25]. It provides the possibility of hardening to a depth of 4.2 mm. Tests of fracture and wear resistance, evaluation of the hardness and microgeometry of the surface layer of samples showed that this treatment can increase the durability of parts.

The use of the 40Cr13 steel as a coating on steel 45 to increase the wear resistance of the material is of interest [26]. Gas-thermal coating of 40Cr13 wire steel was applied to steel 45 plates by high-speed metallization. Additionally, the coating was treated with nitrogen ions. Ion-beam treatment increases the microhardness of coatings to the values of 1000 – 1450 $HV_{0.025}$ and their wear resistance under friction in the I-20 lubricant medium by 1.7 times. Based on the results obtained, the temperature mode of ion-beam nitriding with the highest tribotechnical properties has been selected.

Studies of corrosion resistance of steels with 13 % Cr

It is known that heat treatment is an important factor influencing the tendency of alloys to corrosion. Stainless steels are most resistant to corrosion effects in the state of treatment for a solid solution. Tempering in the temperature range of excess phases (carbides, carbonitrides, nitrides) reduces the resistance of steel to intergranular and pitting corrosion. This is due to the emergence around the carbides of zones depleted in chromium, with reduced

corrosion resistance. The less (negative) the pitting corrosion potential of an alloy, the greater its tendency to pitting. The value of the pitting potential is a measure of the tendency of metals to pitting.

The works [7, 9, 16, 27 – 31] are dedicated to the studies of the effect of heat treatment on corrosion resistance of steels with 13 % Cr.

In [7] the object of the studies was steel with 13.7 % Cr with increased carbon content (0.497 %), high-purity due to vacuum melting. The effect of microstructure changes at different austenitizing (T_A) temperatures on various corrosion mechanisms was studied. Polarization scanning was carried out in the 0.1 M NaCl + 0.1 M phosphate buffer solution (pH = 7.5). It is demonstrated that the resistance against general corrosion increases with increasing T_A up to 1100 °C due to dissolution of carbides and the associated increase in the chromium content of the alloy matrix. This also leads to better passivation and a thicker internal passive layer rich in chromium. A further increase in T_A does not increase the chromium content and resistance to general corrosion, since all carbides are dissolved. On the other hand, with increasing T_A up to 1100 °C, the carbon content increases, which increases the internal lattice stress and leads to a more defective passive layer, causing a decrease in the resistance to pitting. A further increase in T_A, without affecting the carbon content, increases the grain size. The density of lattice defects in the bulk material decreases, reducing the defectiveness of the passive layer and increasing the resistance to pitting. In contrast, the critical potential shows a contradictory course, increasing up to 1100 °C and decreasing at lower temperatures. A higher pitting potential means less susceptibility to pitting, while a higher critical pitting potential means slower pitting, if any. The authors of [7] note that:

– the research can show that there is not one corrosion resistance, but several different corrosion mechanisms, which are influenced by different microstructure properties;

– the amount of carbon is a critical factor for the pitting corrosion potential;

– alloys with a lower carbon content exhibit different pitting behavior and, given this, the seemingly contradictory results simply refer to different phenomena and are not a contradiction.

A similar study to evaluate the effect of austenitizing temperature and cooling rate (water/air) on corrosion resistance was also conducted on high carbon steel with 13.92 % Cr, 0.42 % C (X46Cr13 (1.4034)) under potentiodynamic polarization in 0.1 M H_2SO_4 [9]. Heating followed by cooling in water was performed at temperatures: 850 °C (72 h), 900 °C (9 h), 950 °C (90 min), 1000 °C (30 min), 1050, 1100, 1150 °C (15 min), and 1200 °C (10 min). Heating followed by air cooling was performed at 1000 °C (30 min), 1050 and 1100 °C (15 min). It was also noted, as in [7], that austenitization at temperatures of 1100 °C and above leads to a complete dissolution of carbides. The optimal distribution of chromium and carbon in the mixed crystal is ensured. The elimination of the blocking effect of carbides and the higher diffusion rate lead to significant grain enlargement. Decreasing the austenitizing temperature below 1100 °C leaves mixed chromium and iron carbides in the structure, which reduce hardness and corrosion resistance. Temperature-dependent diffusion processes occur during slow air cooling. New carbides form during cooling at the grain boundaries or in the grains themselves and locally remove chromium from the matrix. Second, iron is precipitated from the remaining mixed chromium and iron carbides as solubility drops sharply with temperature. Both processes lead to chromium depletion during air cooling, which is localized mainly on carbides at 1100 °C and on carbides and grain boundaries at 1000 and 1050 °C. Depletion of the chromium content locally worsens the stability of the passive layer, and the resistance to pitting decreases significantly.

In works [16, 27 – 29] the effect of tempering modes on electrochemical corrosion in aqueous NaCl solutions of 13Cr steels with different carbon content was studied.

Experiments on the potentiodynamic polarization in the 3.5 % aqueous NaCl solution of low carbon steel with 0.03 % C and 12.8 % Cr (AISI 410) were performed after quenching from the temperatures in the range from 950 to 1100 °C and quenching from 1050 °C with tempering at 300 – 700 °C [27]. The corrosion rate of AISI 410 steel decreases as the austenitizing temperature increases. The microstructure after austenitizing and tempering is represented by tempered martensite, residual austenite and carbides. The lowest corrosion current density was obtained after tempering at 300 and 400 °C, and the lowest corrosion rate after austenitizing at 1050 °C, quenching and tempering at 600 °C.

The effect of heat treatment on the corrosion behavior of AISI 420 steel (12.10 % Cr, 0.23 % C) in 0.5 M NaCl with pH = 6.26 and electrical conductivity of 49.9 mS/cm was studied on samples in four structural states [28]. In the initial state (*A*), a continuously cast calibrated rod was considered. Treatment *B* was annealing at 770 °C for 20 min and cooling with a furnace. Treatment *C* was 1000 °C, 30 min, martensite quenching in water. Treatment *D* was tempering at 700 °C, 60 min, cooling in air. The order of samples by corrosion resistance value from higher to lower was established: $B > C > D > A$. Sample AISI 420 (*B*) is the most resistant to corrosion, and sample *A* is the most susceptible to corrosion. Sample *C* also showed high polarization resistance.

The results of studies [16, 29] of steels close in the chemical composition of the studied steels, heat treatment modes and conclusions made are summarized in Table 7.

The peculiarity of research [30] is that the evolution of microstructure and corrosion behavior of martensitic stainless steel of type 420 with increased carbon content (13.7 % Cr, 0.46 % C, 0.47 % Si, 0.39 % Mn) was studied, tempering of which after austenitizing (950 °C, 1 h, water) was carried out not only at 550 and 700 °C, but also at lower temperatures of 250 and 400 °C (1 h, air), and the potentiodynamic polarization test was conducted not in salt solution, but in the 0.1 M HCl solution at 20 °C. After austenitization and quenching, the metal had a martensitic structure and most of the $Cr_{23}C_6$ carbides dissolved. After tempering at 250 °C some amount of $Cr_{23}C_6$ carbides was found on the grain boundaries. After tempering at 400 °C they were larger and more abundant, and after tempering at 550 °C precipitation of CrC, Cr_7C_3 and an even greater number of $Cr_{23}C_6$ particles, also at the grain boundaries, were found. After tempering at 700 °C only $Cr_{23}C_6$ carbides were observed, with local corrosion and nucleation of pits near carbides. After all tempering temperatures, pitting corrosion was observed, with the specimen tempered at 250 °C having the highest corrosion resistance and a hardness value of well above 500 HV, and after treatment at 550 °C, general and intergranular corrosion was also observed. The concentration of chromium in the solid solution after different treatments was: 200, 400 °C – >12 %, 550 °C – 10.5 %, 700 °C – ≈11.5 %, i.e. after the last two treatments it was below the critical level. Thus, in contrast to works [16, 29] (see Table 7), a different order of carbide occurrence during tempering can be noted for the studied steel. The temperature of 250 °C is specified as the best choice of tempering temperature, which provides the highest corrosion resistance (high kinetics Epit and low pit growth kinetics). Tempering modes at 550 and 700 °C should be avoided because corrosion resistance reduced due to a large amount of large-size chromium carbides formed at these tempering temperatures.

Since the AISI 420 martensitic stainless steel is quenched and tempered or double tempered at temperatures up to 250 °C for tableware applications, corrosion resistance was also compared for steel with 12.1 % Cr and 0.19 % C after single and double tempering at 180 °C (2 h, air) after austenitizing at 1050 °C (5 min, air) [31]. The potentiodynamic polarization test was performed in aerated 3.5 % NaCl (pH = 6.0). Single tempering showed a hardness close to air quenching and did not degrade the pitting corrosion resistance. Double tempering did not improve the resistance to pitting corrosion, and hardness decreased afterwards. Only single tempering is recommended.

Conclusions

The properties of steels with 12 – 14 % Cr and $0.2 \le$ % C ≥ 0.4: industrial steels produced with heat treatment according to the standards and known from reference literature, as well as metal properties of laboratory melts treated by various modes of austenitizing and tempering are considered.

In these steels initially annealed at ~800 °C with the formation of the ferrite-carbide structure, with their heating from 800 to 1240 °C, the dissolution of carbides of $Me_{23}C_6$ type occurs, which causes the formation of austenite at 810 – 820 °C with the fixation during quenching of the martensite-carbide structure. Depending on the concentration of carbon in these steels, carbide dissolution in them ends at 950 – 1050 °C. Dissolution of carbides is accompanied by the growth of the austenite grain and preservation of residual austenite after quenching in the structure. Therefore, as the austenitization temperature increases, the quenched steels first show a linear increase in martensite hardness due to carbide hardening ($c/a = 0.45[C] + 1.00$). And then, when the maximum degree of carbide dissolution is achieved, the steels hardness decreases with further heating, which is associated with the formation of residual austenite and growth of the austenite grain. The maximum effective austenitizing temperature before quenching, which provides high hardness, is 1000 – 1020 °C (HV ~550) for 20Cr13 steels and 1100 – 1120 °C (HV 700 – 750) for 45Cr13 steels.

The grain size during austenitization is the coarser the longer the holding time at a given temperature, and this effect is the more significant the higher the heating temperature. The longer the holding time in the temperature range above the maximum effective austenitizing temperature, the greater the residual austenite in the steel and the lower the hardness after hardening.

The temperature required to achieve complete dissolution of $Me_{23}C_6$ carbides in the austenitic phase increases with the increasing heating rate. High-rate heating leads to a shift of hardening curves after quenching by 40 – 60 °C up the temperature scale compared to the curves obtained during furnace heating.

Quenching not in water at slower cooling rates than 20 K/s (including air) causes precipitation of some carbides.

Hardened steels 20Cr13 – 40Cr13 are characterized by high strength, hardness, and low ductility, especially high-carbon steels. Tempering of hardened laboratory steels in the range up to 400 °C causes a slight decrease in martensite hardness and strength (a small amount of carbides precipitates in martensite, and it becomes unstable). In the interval of 400 – 500 °C a slight increase in hardness and strength due to the effect of dispersion hardening is possible. Then, in the range of 500 – 780 °C, there

Table 7

Effect of tempering at 300, 500-550 and 650 – 700 °C on corrosion resistance of steels with 13 % Cr and 0.31 – 0.38 % C

Таблица 7. **Влияние отпуска при 300, 500 – 550 и 650 – 700 °C на коррозионную стойкость сталей с 13 % Cr и 0,31– 0,38 % C**

Main provisions of the paper	Source [29]	Source [16]
Steel	13.3 % Cr, 0.31 % C, 0.04 % V, 0.48 % Cu	13 % Cr, 0.38 % C, 0.3 % V
Quenching mode	1020 °C (30 min, quenching in oil)	1030 °C (45 min, quenching in oil)
Tempering mode	300, 550 and 700 °C (2.5 h, cooling in air)	300, 500 °C and 650 °C (2 h, cooling in air)
Type of tests	Potentiostatic polarization tests	
Test medium	0.1 M NaCl solution	3.5 % NaCl aqueous solution
Precipitation in steels during tempering	300 °C – nanosized ε-Me_3C carbides; 500 – 550 °C – nanosized $Me_{23}C_6$ carbides; 650 – 700 °C – micron or submicron $Me_{23}C_6$ carbides	
Structure after austenitizing	Austenitizing at 1020 – 1030 °C did not lead to the complete dissolution of carbides	
	Fine-lath martensite with residual austenite interlayers at the lath boundaries, $Cr_{23}C_6$ carbides	Martensite and $Cr_{23}C_6$ carbides
	The share of residual austenite decreases with tempering temperature, and after tempering at 550 and 700 °C residual austenite is not observed	Residual austenite is observed only after tempering at 300 °C, and there is no residual austenite after tempering at 500 and 650 °C
Effect of austenitizing and tempering at 300 °C on corrosion resistance	In the austenitized state a passive film enriched with chromium is formed. The sample austenitized and tempered at 300 °C shows less current transients, and no sustained pitting corrosion is observed in the 3 h test	Pitting corrosion potential Epit of hardened steel is higher than that of tempered steel and decreases with increasing tempering temperature. Relatively low-temperature tempering (300 °C) slightly reduced corrosion resistance compared to steel after quenching
Corrosion after tempering at 500 – 550 °C	Tempering reduced the pitting potential and increased the metastable pitting. Tempering at 550 °C made the steel highly prone to pitting. Pitting occurred at the carbide-matrix interface due to the presence of chromium depletion areas associated with the massive precipitation of chromium-rich carbide. The passive film formed at corrosion potential was enriched with iron particles. It was less protective than the film after austenitization and increased the corrosion current density at corrosion potential and showed no passivity in the 0.1 M NaCl solution above the corrosion potential	The sample after tempering at 500 °C exhibits active corrosion behavior without passivation. This is explained by the precipitation of a large number of chromium-rich nanosized $Me_{23}C_6$ carbides. The large carbide/matrix interface, as pitting occurred, prevented the formation of a protective passive film on the steel surface due to the small distance between the carbides
Comparison of the corrosion behavior after tempering at 500 – 550 and 660 – 700 °C and final conclusion	The Epit value is higher for the sample tempered at 700 °C compared to the sample tempered at 550 °C. A possible reason is the repeated diffusion of Cr from the matrix into the depleted regions, which minimizes the discontinuity of the interfacial regions. The above results confirm the assumption that tempering of steel with 13 % Cr should be carried out at 700 °C because it also provides resistance to pitting.	The sample 1030-650 showed better corrosion resistance than sample 1030-500, even though the Cr content of the matrix was slightly lower than that of sample 1030-500. The tempering temperature for the 13 % Cr steels should be much lower or higher than 500 °C to avoid the massive precipitation of nanosized $Me_{23}C_6$ carbides. Steels with 13 % Cr, tempered at 300 °C, show a combination of high relative hardness and high corrosion resistance.

is a significant decline in these characteristics (intensive precipitation of carbides → decomposition of martensite into ferrite and carbides → coagulation of carbides and their partial dissolution, recrystallization). The plasticity and impact strength increase symmetrically.

The heat treatment with double quenching at 1040 °C + 980 °C provided a finer grain size along with a higher degree of carbon dissolution in the austenitic matrix. During tempering (double at 710 °C + 680 °C), very fine carbides (having a much smaller size compared to the single heat treatment process) formed in small numbers at low-angle and high-angle boundaries. This resulted in increased strength and impact strength after tempering, compared to single quenching from 980 °C.

Corrosion resistance increases with increasing austenitizing heating temperature and decreases with increasing tempering temperature, at which pitting and intergranular corrosion are added to general corrosion, which is associated with the precipitation of $Cr_{23}C_6$ carbides and depletion of the matrix in chromium to the concentrations below 12 %. The recommended heat treatments for 20Cr13 steels are quenching with low tempering at 200 – 300 °C (combination of high strength, good corrosion resistance and satisfactory plasticity), or quenching with high tempering at ~700 °C (good plasticity, satisfactory corrosion resistance). For steels of 40Cr13 type the temperature of ~700 °C is not recommended. The worst tempering temperature is 500 – 550 °C because of the maximum precipitation of ultradispersed carbides.

The possibility of ensuring increased wear resistance of 40Cr13 steels by saturating the surface layer with nitrogen (nitrocementation, ion-plasma nitriding, nitriding and heat treatment), surface laser and plasma quenching, a combination of heat and mechanical treatments, high-vacuum annealing and diffusion siliconizing is demonstrated.

Список литературы / References

1. *Metals Handbook. Vol. 8: Metallography, Structures and Phase Diagrams*. 8th ed. American Society for Metals; 1973: 465.
2. Ivashko V.V. Influence of heating modes on the structure and properties of stainless steel 20Kh13. *Vestnik BarGU. Seriya: Tekhnicheskie nauki*. 2015; (3): 45–48. (In Russ.).

   Ивашко В.В. Исследование влияния режимов нагрева на структуру и свойства нержавеющей стали 20Х13. *Вестник БарГУ. Серия: Технические науки.* 2015; (3): 45–48.
3. Scheuer C.J., Fraga R.A., Cardoso R.P., Brunatto S.F. Effects of heat treatment conditions on microstructure and mechanical properties of AISI 420 steel. In: *21 CBECIMAT – Congresso Brasileiro de Engenharia e Ciência dos Materiais 9 a 13 de Novembro de 2014, Cuiabá, MT, Brasil*. 2014: 5857–5867.
4. Xiao Li, Yinghui Wei. Effect of austenitising heat treatment on microstructure and properties of a nitrogen bearing martensitic stainless steel. *Open Physics*. 2019; 17(1): 601–606. https://doi.org/10.1515/phys-2019-0061
5. Garcia de Andrés C., Álvarez L.F., López V. Effects of carbide-forming elements on the response to thermal treatment of the X45Cr13 martensitic stainless steel. *Journal of Materials Science*. 1998; 33: 4095–4100. https://doi.org/10.1023/A:1004424329556
6. Grinberg E.M., Goncharov S.S., Mova D.A., Kondaurova E. Yu., Surovtseva E.A. Effect of cooling rate during quenching on the structure and hardness of Kh13 steels with different carbon content. *Izvestiya TulGU. Tekhnicheskie nauki* 2009; (3): 1–11. (In Russ.).

   Гринберг Е.М., Гончаров С.С., Мова Д.А., Кондаурова Е.Ю., Суровцева Е.А. Влияние скорости охлаждения при закалке на структуру и твердость сталей типа Х13 с различным содержанием углерода. *Известия ТулГУ. Технические науки*. 2009; (3): 1–11.
7. Bösing I., Cramer L., Steinbacher M., Werner Zoch H., Thöming J., Baune M. Influence of heat treatment on the microstructure and corrosion resistance of martensitic stainless steel. *AIP Advances*. 2019; 9(6): 065317. https://doi.org/10.1063/1.5094615
8. Zubchenko A.S., Koloskov M.M., Kashirskii Yu.V., etc. *Grader of Steels and Alloys*. Moscow: Mashinostroenie; 2003: 784. (In Russ.).

   Зубченко А.С., Колосков М.М., Каширский Ю.В. и др. *Марочник сталей и сплавов*. М.: Машиностроение; 2003: 784.
9. Rosemann P., Müller C., Kauss N., Halle T. Einfluss der Wärmebehandlung auf Mikrostruktur und Korrosions- verhalten kohlenstoffhaltiger nichtrostender Stähle. *Werkstofftechnischen Kolloquium (Chemnitz)*, September, 2014: 10.
10. Garcia de Andrés C., Caruana G., Alvarez L.F. Control of $M_{23}C_6$ carbides in 0.45C–13Cr martensitic stainless steel by means of three representative heat treatment parameters. *Materials Science and Engineering: A*. 1998; 241(1–2): 211–215. https://doi.org/10.1016/S0921-5093(97)00491-7
11. Behrens B.-A., Hübner S., Sunderkötter C., Gebel L., Gnaß S., Berndt G., Trimborn C., Pfeffer C. Influence of process parameters on the hot stamping of carbon-martensitic chromium steel sheets. *IOP Conference Series: Materials Science and Engineering*. 2018; 418: 012007. https://doi.org/10.1088/1757-899X/418/1/012007
12. Ma Hou-Yu, He Yin-Sheng, Lee Kwon-Yeong, Shin Keesam. Effect of heat treatment on microstructural evolution of 13Cr martensitic stainless steel. *Key Engineering Materials*. 2016; 727: 29–35. https://doi.org/10.4028/www.scientific.net/KEM.727.29
13. Abdul Kareem F. Hassan, Qahtan Adnan Jawad. Investigation of the effect of austenitizing temperature and multiple tempering on the mechanical properties of AISI 410 martensitic stainless steel. *The Iraqi Journal for Mechanical and Material Engineering. Special Vol. Babylon First Int. Engineering Conf.* 2016; C: 411– 435.
14. Abdul Kareem F. Hassan, Qahtan Adnan Jawad. Estimation of austenitizing and multiple tempering temperatures from the mechanical properties of AISI 410 using artificial neural network. *International Journal of Engineering & Technology*. 2018; 7(4.19): 778–787. https://doi.org/10.14419/ijet.v7i4.19.27997

15. Balan K.P., Venugopal Reddy A., Sarma D.S. Effect of single and double austenitization treatments on the microstructure and mechanical properties of 16Cr-2Ni steel. *Journal of Materials Engineering and Performance*. 1999; 8(3): 385–393. https://doi.org/10.1361/105994999770346963

16. Lu S.-Y., Yao K.-F., Chen Y.-B., Wang M.-H., Liu X., Ge X. The effect of tempering temperature on the microstructure and electrochemical properties of a 13 wt.% Cr-type martensitic stainless steel. *Electrochimica Acta.* 2015; 165: 45–55. https://doi.org/10.1016/j.electacta.2015.02.038

17. Kulkarni S., Srinivas P., Biswal P.K., Balachandran G., Balasubramanian V. Improvement in mechanical properties of 13Cr martensitic stainless steels using modified heat treatments. In: *Proceedings of the 28th ASM Heat Treating Society Conference. Detroit*, 2015: 335–341.

18. Mohameda Hareer S., Ataiwib Ali H., Dawood Jamal J. Mechanical properties of martensitic stainless steel (AISI420) subjected to conventional and cryogenic treatments. *Engineering and Technology Journal*. 2020; 38 A(8): 1096–1105. https://doi.org/10.30684/etj.v38i8A.517

19. Romanenko D.N., Nikulin A.A., Gadalov V.N., etc. Prospects for the use of stainless steel 40Kh13 for knives of meat-grinding equipment. *Konstruktsii iz kompozitsionnykh materialov*. 2011; (4): 59–63. (In Russ.).

Романенко Д.Н., Никулин А.А., Гадалов В.Н. и др. Перспективы использования нержавеющей стали 40Х13 для ножей мясоизмельчающего оборудования. *Конструкции из композиционных материалов*. 2011; (4): 59–63.

20. Rutkovskii A.V. Kumurzhi A.Yu. Wear resistance of 40Kh13 steel after hardening by thermal cyclic ion-plasma nitriding under abrasive wear. *Problems of Friction and Wear*. 2012; 57: 240–250. (In Russ.).
https://doi.org/10.18372/0370-2197.57.3607

Рутковский А.В. Кумуржи А.Ю. Износостойкость стали 40Х13 после упрочнения методом термоциклического ионно-плазменного азотирования в условиях абразивного изнашивания. *Вопросы трения и износа*. 2012; 57: 240–250. https://doi.org/10.18372/0370-2197.57.3607

21. Sidelev D.V., Voronina E.D., Kozhina O.I., Grudinin V.A., Stolbovskaya G.N. Nitriding of 40H13 steel in inductively coupled plasma: Role of a bias potential. *Prikladnaya fizika*. 2022; (2): 16–23. (In Russ.).

Сиделев Д.В., Воронина Е.Д., Кожина О.И., Грудинин В.А., Столбовская Г.Н. Азотирование стали 40х13 в индуктивно-связанной плазме: влияние потенциала смещения образца. *Прикладная физика*. 2022; (2): 16–23. https://doi.org/10.51368/1996-0948-2022-2-16-23

22. Kukareko V.A., Kushnerov A.V. Influence of pre-heat treatment on wear resistance of 40Kh13 steel modified with nitrogen ions. *Uprochnyayushchie tekhnologii i pokrytiya*. 2022; 18(2(206)): 61–65. (In Russ.).
https://doi.org/10.36652/1813-1336-2022-18-2-61-65

Кукареко В.А., Кушнеров А.В. Влияние предварительной термической обработки на износостойкость стали 40Х13, модифицированной ионами азота. *Упрочняющие технологии и покрытия*. 2022; 18(2): 61–65.
https://doi.org/10.36652/1813-1336-2022-18-2-61-65

23. Korostelev V.F., Kirilina A.N. Analysis of hardening of blade tools from steel 40Kh13 due to laser heating. *Metallovedenie i termicheskaya obrabotka metallov*. 2011; (3(669)): 38–41. (In Russ.).

Коростелев В.Ф., Кирилина А.Н. Анализ упрочнения лезвийного инструмента из стали 40Х13 в условиях лазерного нагрева. *Металловедение и термическая обработка металлов*. 2011; (3(669)): 38–41.

24. Belinin D.S., Shchitsyn Yu.D. Features of structure formation during plasma surface hardening to a great depth of products from steel 40Kh13. *Izvestiya Samarskogo nauchnogo tsentra Rossiiskoi akademii nauk*. 2012; 14(4-5): 1202–1205. (In Russ.).

Белинин Д.С., Щицын Ю.Д. Особенности структурообразования при плазменной поверхностной закалке на большую глубину изделий из стали 40Х13. *Известия Самарского научного центра Российской академии наук*. 2012; 14(4–5): 1202–1205.

25. Suslov A.G., Shalygin M.G. Comprehensive technological increase in wear resistance and static strength of parts made of steel 40Kh13. *Naukoemkie tekhnologii v mashinostroenii*. 2018; (1(79)): 19–21. (In Russ.).

Суслов А.Г., Шалыгин М.Г. Комплексное технологическое повышение износостойкости и статической прочности деталей из стали 40Х13. *Наукоемкие технологии в машиностроении*. 2018; (1(79)): 19–21.

26. Grigorchik A.N., Belotserkovskii M.A., Kukareko V.A. Wear resistance of an ion-nitrided gas-thermal coating of martensitic steel 40Kh13. In: *Abstracts of the Int. Sci. and Tech.Conf. "POLIKOMTRIB-2017", Gomel', 27–30.06.2017*: 130. (In Russ.).

Григорчик А.Н., Белоцерковский М.А., Кукареко В.А. Износостойкость подвергнутого ионному азотированию газотермического покрытия из мартенситной стали 40Х13. В кн.: *Полимерные композиты и трибология (ПОЛИКОМТРИБ-2017): Тезисы докладов международной научно-технической конференции, Гомель, Беларусь, 27–30 июня 2017 года. Гомель, Беларусь: Институт механики металлополимерных систем имени В.А. Белого НАН Беларуси*, 2017: 130.

27. Rizky D., Syaiful A.M., Rusnaldy, Mabruri E. Effect of heat treatment of AISI 410 martensitic stainless steel on microstructure and corrosion resistance. *Metalurgi (Indonesia)*. 2018; 33(1): 18–24.

28. Minciuna M.G., Achitei D.C., Vizureanu P., Benchea M., Sandu A.V. The effect of heat treatment and corrosion behavior of AISI 420. *IOP Conference Series: Materials Science and Engineering.* 2018; 374: 012039.
https://doi.org/10.1088/1757-899X/374/1/012039

29. Bonagani S.K., Bathula V., Kain V. Influence of tempering treatment on microstructure and pitting corrosion of 13 wt.% Cr martensitic stainless steel. *Corrosion Science*. 2018; 131: 340–354.
https://doi.org/10.1016/j.corsci.2017.12.012

30. Zhou Y., Engelberg D.L. Accessing the full spectrum of corrosion behaviour of tempered type 420 stainless steel. *Materials and Corrosion*. 2021; 72(11): 1718–1729.
https://doi.org/10.1002/maco.202112442

31. De Alcântara C.M., de Moura A.N., D'Azeredo Orlando M.T., da Silva Labiapari W., da Cunha M.A., de Oliveira T.R., Lopes Buono V.T. Microstructure and pitting corrosion resistance of quenched, single tempered and double tempered AISI 420 martensitic stainless steel. *Materials Research*. 2021; 24(6): 20210093.
https://doi.org/10.1590/1980-5373-MR-2021-0093

Information about the Authors

Mariya V. Kostina, *Dr. Sci. (Eng.), Assist. Prof., Senior Researcher, Head of the Laboratory "Physicochemistry and Mechanics of Metallic Materials",* Baikov Institute of Metallurgy and Materials Science, Russian Academy of Sciences
ORCID: 0000-0002-2136-5792
E-mail: mvk@imet.ac.ru

Lyudmila G. Rigina, *Cand. Sci. (Eng.), Leading Researcher,* Baikov Institute of Metallurgy and Materials Science, Russian Academy of Sciences; JSC Russian State Research Center "CNIITMASH"
E-mail: LGRigina@cniitmash.com

Valentina S. Kostina, *Cand. Sci. (Eng.), Junior Researcher of the Laboratory "Physicochemistry and Mechanics of Metallic Materials",* Baikov Institute of Metallurgy and Materials Science, Russian Academy of Sciences
ORCID: 0000-0001-7956-499X
E-mail: vskostina@yandex.ru

Aleksandr E. Kudryashov, *Research Engineer,* Baikov Institute of Metallurgy and Materials Science, Russian Academy of Sciences
E-mail: al.kudriashov@mail.ru

Ruslan S. Fedortsov, *Research Engineer,* Baikov Institute of Metallurgy and Materials Science, Russian Academy of Sciences
ORCID: 0000-0002-5359-1161
E-mail: mvk@imet.ac.ru

Сведения об авторах

Мария Владимировна Костина, *д.т.н., доцент, ведущий научный сотрудник, заведующий лабораторией физикохимии и механики металлических материалов,* Институт металлургии и материаловедения им. А.А. Байкова РАН
ORCID: 0000-0002-2136-5792
E-mail: mvk@imet.ac.ru

Людмила Георгиевна Ригина, *к.т.н., ведущий научный сотрудник,* Институт металлургии и материаловедения им. А.А. Байкова РАН; Центральный научно-исследовательский институт технологии машиностроения, ОАО НПО «ЦНИИТМАШ»
E-mail: LGRigina@cniitmash.com

Валентина Сергеевна Костина, *к.т.н., младший научный сотрудник лаборатории физикохимии и механики металлических материалов,* Институт металлургии и материаловедения им. А.А. Байкова РАН
ORCID: 0000-0001-7956-499X
E-mail: vskostina@yandex.ru

Александр Эдуардович Кудряшов, *инженер-исследователь,* Институт металлургии и материаловедения им. А.А. Байкова РАН
E-mail: al.kudriashov@mail.ru

Руслан Сергеевич Федорцов, *инженер-исследователь,* Институт металлургии и материаловедения им. А.А. Байкова РАН
ORCID: 0000-0002-5359-1161
E-mail: mvk@imet.ac.ru

Contribution of the Authors

M. V. Kostina – formation of the article main idea, processing and analysis of literary data, writing the text.
L. G. Rigina – search and analysis of literary data on heat treatment, translation, participation in writing a section on heat treatment.

V. S. Kostina – search for literary data on corrosion resistance, translation, participation in writing a section on corrosion.
A. E. Kudryashov – search and translation of literary data on wear resistance, participation in writing a section on wear resistance.
R. S. Fedortsov – search and analysis of literary data, translation, work with the list of references, preparation of drawings.

Вклад авторов

М. В. Костина – идея статьи, обработка и анализ литературных данных, написание статьи.
Л. Г. Ригина – поиск и анализ литературных данных по термической обработке, перевод, участие в написании раздела по термической обработке.
В. С. Костина – поиск литературных данных по коррозионной стойкости, перевод, участие в написании раздела по коррозии.
А. Э. Кудряшов – поиск и перевод литературных данных по износостойкости, участие в написании раздела по износостойкости.
Р. С. Федорцов – поиск и анализ литературных данных, перевод, работа со списком литературы, подготовка рисунков.

Received 11.11.2022
Revised 05.12.2022
Accepted 26.12.2022

Поступила в редакцию 11.11.2022
После доработки 05.12.2022
Принята к публикации 26.12.2022

MATERIAL SCIENCE / МАТЕРИАЛОВЕДЕНИЕ

UDC 621.793.7:621.762
DOI 10.17073/0368-0797-2023-1-27-34

Original article
Оригинальная статья

Spraying of TiB_2/Ti and HfB_2/Ti composite powder wear-resistant coatings

M. E. Goshkoderya [1], T. I. Bobkova [1], S. P. Bogdanov [2], A. V. Krasikov [1], M. V. Staritsyn [1], A. A. Kashirina [1]

[1] **Academician I.V. Gorynin Central Research Institute of Structural Materials "Prometey", National Research Center "Kurchatov Institute"** (49 Shpalernaya Str., St. Petersburg 191015, Russian Federation)
[2] **St. Petersburg State Institute of Technology** (24-26/49 Moskovskii Ave., St. Petersburg 190013, Russian Federation)

gosmike@yandex.ru

Abstract. In this paper we studied the synthesis of composite core – shell powders sprayed as wear-resistant metal-ceramic coatings. High-hardness TiB_2 and HfB_2 powders form the core, and the shell is made of titanium. The cladding was applied by iodide transport technology. This cladding method involves deposition by gas transport with iodine as an agent. The TiB_2/Ti and HfB_2/Ti composite powders were sprayed using microplasma technology. In contrast to conventional plasma spraying, it minimizes the phase transformations in the composite powders induced by heating. Analysis of the final coating on polished cross sections revealed that during microplasma spraying, the titanium is oxygenated and it produces a titanium dioxide phase. As a result, the TiB_2/Ti and HfB_2/Ti composite powders are transformed into TiB_2 (TiB)/Ti(TiO_2) and HfB_2/Ti(TiO_2) coatings. We also studied the distribution of the components across the coating. The hardness measurements showed that the titanium diboride coatings obtain microhardness of 1300 HV. The microhardness of the hafnium diboride coatings is about 1600 HV. For abrasion testing of the TiB_2(TiB)/Ti(TiO_2) and HfB_2/Ti(TiO_2)) coatings we used uncoated alloyed 45Kh steel (similar to EU grade: 41Cr4) and the specified coatings as an abradant material. Despite their lower microhardness, the TiB_2(TiB)/Ti(TiO_2) coating showed the highest abrasion resistance.

Keywords: wear-resistant coatings, clad composite powders, titanium diboride/titanium, hafnium diboride/titanium, microplasma spraying, protective and restorative coatings

Acknowledgements: The work was carried out as part of the Project No. 21-73-30019 supported by the Russian Science Foundation.
Experimental studies were carried out on the equipment of the Center for Collective Use "Composition, Structure and Properties of Structural and Functional Materials" of the NRC "Kurchatov Institute" – CRISM "Prometey" with the financial support of the Ministry of Education and Science of the Russian Federation under agreement No. 13.CKP.21.0014, unique identifier RF-2296.61321X0014.

For citation: Goshkoderya M.E., Bobkova T.I., Bogdanov S.P., Krasikov A.V., Staritsyn M.V., Kashirina A.A. Spraying of TiB_2/Ti and HfB_2/Ti composite powder wear-resistant coatings. *Izvestiya. Ferrous Metallurgy*. 2023; 66(1): 27–34.
https://doi.org/10.17073/0368-0797-2023-1-27-34

Напыление износостойких покрытий из плакированных порошков TiB_2/Ti и HfB_2/Ti

М. Е. Гошкодеря [1], Т. И. Бобкова [1], С. П. Богданов [2], А. В. Красиков [1], М. В. Старицын [1], А. А. Каширина [1]

[1] **ЦНИИ КМ «Прометей» имени академика И.В. Горынина НИЦ «Курчатовский институт»** (Россия, 191015, Санкт-Петербург, ул. Шпалерная, 49)
[2] **Санкт-Петербургский государственный технологический институт (технический университет)** (Россия, 190013, Санкт-Петербург, Московский пр., 24-26/49)

gosmike@yandex.ru

Аннотация. В представленной работе приведены результаты по синтезу композиционных плакированных порошковых систем с типом строения «ядро–оболочка» для напыления износостойких металлокерамических покрытий. Для синтеза композиционного порошка в качестве ядра использованы порошки высокотвердых боридов TiB_2 и HfB_2, а для создания оболочки на их поверхности – титан.

Синтез плакирующего слоя осуществляли йодотранспортным методом. Плакирование порошка используемым методом подразумевает осаждение одного компонента на другой посредством газотранспорта, агентом которого выступает йод. Напыление композиционных плакированных порошков систем TiB_2/Ti и HfB_2/Ti осуществляли микроплазменным методом, который, в отличие от классического плазменного напыления, позволяет минимизировать фазовые превращения в композиционных порошках из-за термического воздействия. При исследовании поперечных микрошлифов напыленных покрытий определено, что в процессе микроплазменного напыления титан насыщается кислородом, образуя фазу диоксида титана. В результате плакированные композиционные порошки систем TiB_2/Ti и HfB_2/Ti превращаются в покрытия из систем TiB_2(TiB)/Ti(TiO_2) и HfB_2/Ti(TiO_2). Выявлены особенности распределения компонентов по толщине покрытия. Исследования твердости показали, что у покрытий на основе диборида титана интегральное значение микротвердости составляет 1300 HV. У покрытий на основе диборида гафния интегральная микротвердость составила порядка 1600 HV. При исследовании износостойкости пары с покрытиями TiB_2(TiB)/Ti(TiO_2) и HfB_2/Ti(TiO_2) сопрягались с контртелом образца из стали 45Х без покрытия и совместно друг с другом. Несмотря на менее высокую микротвердость, наиболее износостойким является покрытие системы TiB_2(TiB)/Ti(TiO_2).

Ключевые слова: износостойкие покрытия, плакированные композиционные порошки, диборид титана/титан, диборид гафния/титан, микроплазменное напыление, защитные и восстановительные покрытия

Благодарности: Исследование выполнено за счет гранта Российского научного фонда, проект № 21-73-30019.
Экспериментальные исследования проводились на оборудовании Центра коллективного пользования «Состав, структура и свойства конструкционных и функциональных материалов» НИЦ «Курчатовский институт» – ЦНИИ КМ «Прометей» при финансовой поддержке Министерства образования и науки Российской Федерации по соглашению № 13.ЦКП.21.0014, уникальный идентификатор RF-2296 .61321X0014.

Для цитирования: Гошкодеря М.Е., Бобкова Т.И., Богданов С.П., Красиков А.В., Старицын М.В., Каширина А.А. Напыление износостойких покрытий из плакированных порошков TiB_2/Ti и HfB_2/Ti. *Известия вузов. Черная металлургия*. 2023; 66(1): 28–34.
https://doi.org/10.17073/0368-0797-2023-1-27-34

Introduction

New structural materials and coatings are developed to offer better performance and reliability. New composites extend the service life of products operating at high rates under elevated temperatures, mechanical loads or exposed to aggressive environments.

Borides of transition metals, such as TiB_2 and HfB_2 are promising ones since they have a high level of hardness, heat, wear and corrosion resistance [1 – 5]. There are few boride coating application technologies. Jayaraman S. et al. [6] produced HfB_2 and Hf – B – N coatings by chemical vapor deposition (CVD). The hardness of the coatings is up to 40 GPa. The CVD technology is also used to apply ultra-high-temperature transition metal boride coatings onto porous substrates. The application technology for such coatings consist of thermal gas-phase decomposition of titanium, zirconium and hafnium borohydride solutions in high-boiling saturated hydrocarbons as borohydride and solvent vapor are passed through porous materials preheated to 250 °C, and then placed in a tubular reactor under vacuum (Dugin S.N. et al. [7]).

Composite HfB2/SiC coatings protect from oxidation in various aggressive environments [8 – 12] and are therefore of a great interest. Silicon carbide alloying with hafnium diboride significantly increases the structural strength at high temperatures, thermal conductivity and heat resistance while reducing the thermal expansion coefficient. Such coatings are extensively used under high temperatures and contact loads, e.g. in solid-propellant rocket engine components [13].

Spark plasma sintering (SPS) is used for sintering ceramic powders. This technology produces ultra-high-temperature and high-strength ceramics [14 – 16]. The standard temperature of HfB_2 – SiC spark plasma sintering is 1800 – 2100 °C [17].

Despite their excellent performance and physical/structural properties, such coatings are not widely used due to their high brittleness and the lack of direct application technologies. Therefore, it is advisable to use boride composites with binding metals.

Gas cladding is an efficient technology for making highly dispersed composite powders; one component is converted into a gas phase and then deposited on the surface of the other component. Iodine is used as a transport agent. Bogdanov S.P. [18; 19] studied the iodine transport of cladding components in detail.

As components operated under high contact loads are restored a layer up to 1 mm thick [20] is mostly applied.

Thermal spraying is considered a suitable technology for making coatings of such thicknesses [21]. In particular, the microplasma technology can spray composite powders while maintaining their high physical and structural properties. 20 – 300 μm thick coatings are applied with a single pass.

The above-mentioned composite powders can be used as protective and repair coatings for mechanical parts exposed to high contact loads, variable temperatures and aggressive or corrosive environments in heat exchangers, steam generators, pipelines, valves and jet engines.

The purpose of this study is to apply the iodine transport technology to TiB_2/Ti and HfB_2/Ti composite pow-

Table 1

Chemical composition of PTOM-1 powder

Таблица 1. **Химический состав порошка марки ПТОМ-1**

Powder grade	Titanium	Wt. % (max)					
		nitrogen	carbon	hydrogen	iron + nickel	silicon	calcium
PTOM-1	Core	0.08	0.05	0.40	0.40	0.10	0.08

ders, fine-tune the microplasma spraying process, and estimate the properties of the resulting coatings.

Materials and Methods

We used the following materials:

– PTOM-1 titanium powder, 10 – 100 μm grade from POLEMA, AO (see Table 1 for the chemical composition);

– titanium diboride powder, 1 – 4 μm grade (the chemical composition is: 68.3 % titanium; 30.2 % boron; 0.1 % carbon; 0.05 % iron).

– HfB_2 hafnium diboride powder, 3 – 12 μm grade, 99.8 % purity (the chemical composition is: boron 29 %; the rest is hafnium).

Fig. 1 shows the SEM images of the powders. The powders were mechanically mixed. The MeB_2:Ti mass equivalent ratio was 50:50 %, where *Me* is Ti or Hf. The mixtures were then synthesized by the iodine transport technology. The titanium was converted into a gas phase by a chemical reaction with iodine vapor and carried to the surface of ceramic particles. The mass transfer intensity depends on the temperature and the holding time. The temperature was 700 °C, and the holding time was 3 h. The resulting TiB_2/Ti and HfB_2/Ti composite powders, 20 to 80 μm grade were deposited with the microplasma technology on UGNP-7/2250 machine equipped with Kawasaki FS003N robot manipulator. The plasma generator power reached 2.8 kW and the arc current was 35 to 40 A at 40 V. Argon (2 l/min flow rate) served as the transport agent and plasma gas.

We studied the structure of the powders and the polished cross-sections of the coatings on Tescan Vega 3 scanning electron microscope (SEM). PMT-3 microhardness tester was used for the coating microhardness testing by Vickers method.

The 2168 UMT abrasion testing machine performed accelerated wear resistance tests. It is a general-purpose machine with replaceable friction pairs and multiple available motions in a wide range of rpm and loads. Lubricants can be delivered to the friction area. The samples had coating sprayed on their ends. They were arranged as a ring-on-ring friction pair with continuous water cooling. The independent variables were the normal load applied to the ring, the ring rpm and the test time. All the samples were examined under the 0.5 MPa load at 100 rpm for 5 h.

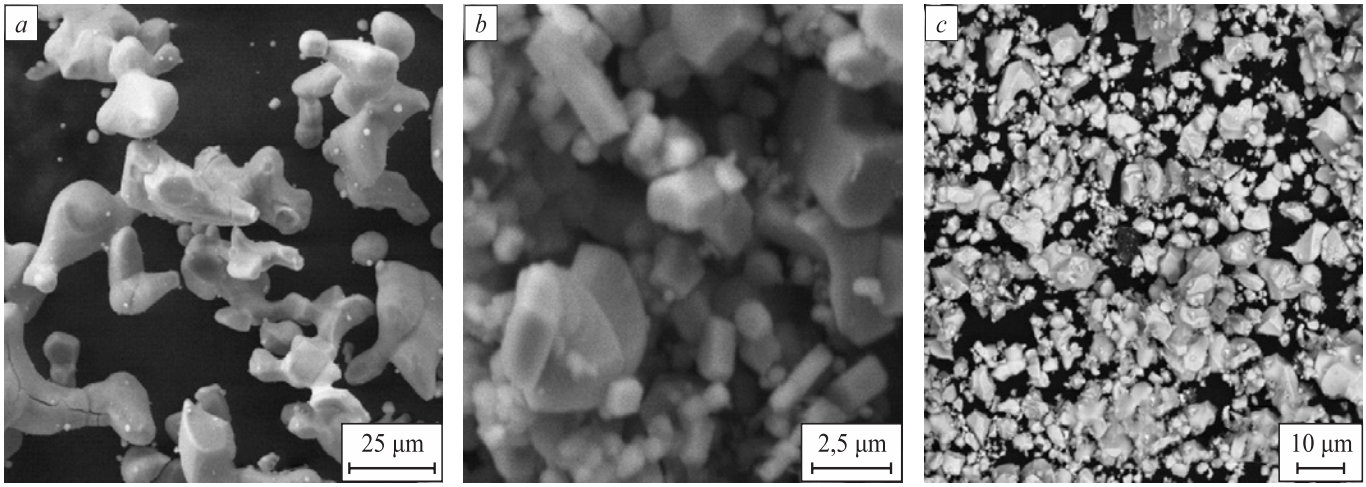

Fig. 1. SEM micrographs of the powders:
a – PTOM-1, *b* – TiB_2, *c* – HfB_2

Рис. 1. РЭМ-микрофотографии исходных порошков:
a – ПТОМ-1; *b* – TiB_2; *c* – HfB_2

Results and Discussion

We examined the structure of the TiB_2/Ti and HfB_2/Ti composite powders processed by the iodine transport technology. The typical structure is shown in Fig. 2.

The composite particles mostly inherit the shape of the original ceramic components, while some of the particles remain unclad and they are merged in agglomerates.

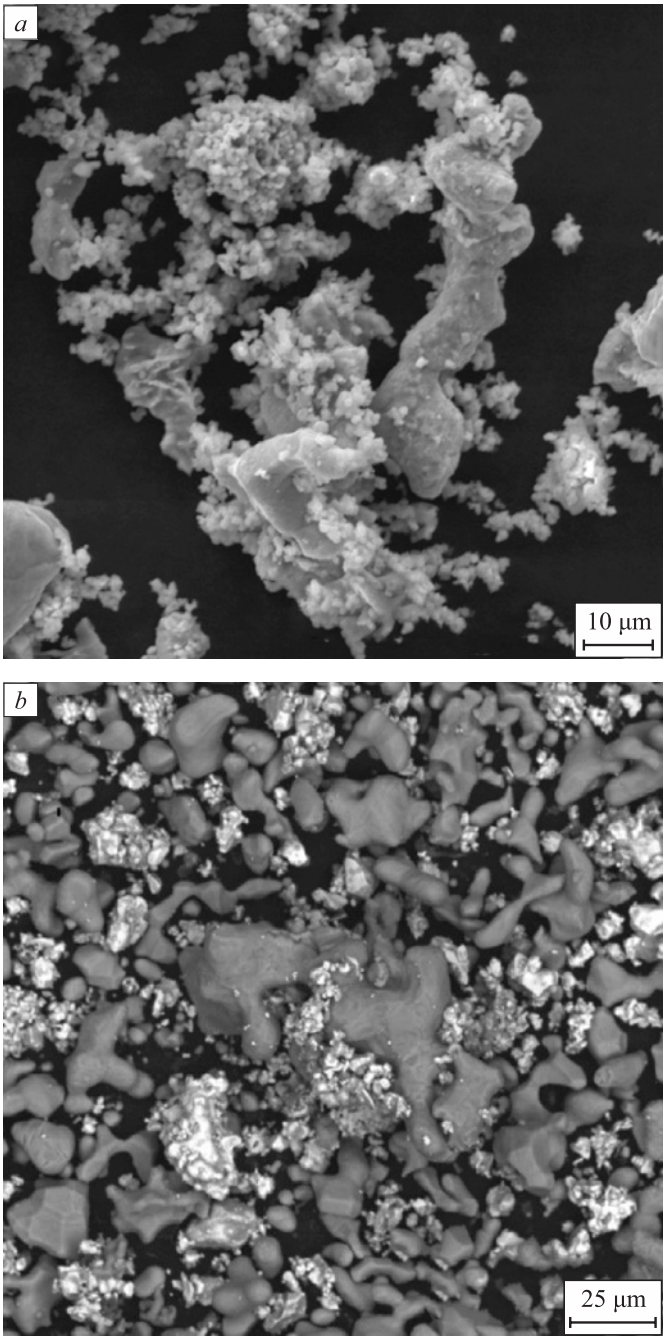

Fig. 2. SEM images of the clad powders:
a – TiB_2/Ti, *b* – HfB_2/Ti

Рис. 2. РЭМ-микрофотографии плакированных порошков:
a – TiB_2/Ti; *b* – HfB_2/Ti

Fig. 3 and 4 show the SEM images of the TiB_2/Ti and HfB_2/Ti composite powder coating polished cross-sections respectively.

The images in Fig. 3 and 4 indicate that the coatings have clear interfaces with the substrate, without through pores. The dark and bright areas in the backscattered electron SEM images indicate that the titanium diboride and hafnium diboride particles are preserved in the coating. Fig. 3 shows that the light areas are titanium and the dark areas are titanium diboride. In the SEM images of the coatings (Fig. 4) the darker areas are rich in titanium and the lighter areas are rich in hafnium, due to the higher atomic number of the latter. The titanium diboride coating changes its phase composition during spraying. The diboride is partially converted into titanium monoboride. A similar effect was given in [22; 23]. The hafnium diboride powder coating does not feature such transformations. Besides, the titanium dioxide phase is formed in the coatings due to the oxygen diffusion during spraying. It can be identified as the areas with an intermediate contrast between the areas containing the ceramic and the binder.

We examined the microhardness of the polished cross-sections of the coatings. The hardness of TiB_2(TiB)/Ti(TiO_2) coating is 1320 HV under 100 g load and 1.0 rms deviation. The hardness of HfB_2/Ti(TiO_2) is 1654 HV under 200 g load and 3.2 rms deviation.

The results indicate high hardness values of the ceramic components in the coatings. HfB_2/Ti has higher hardness because the ceramic component does not have a phase transition. As mentioned above, the titanium diboride is saturated with titanium at spraying, which resulted in monoboride formation. It slightly decreases the final hardness, since the hardness of the titanium diboride reaches 35 GPa, while that of the titanium monoboride is 28 GPa [24; 25] only.

We also tested the sprayed coatings for abrasion resistance. First, we used 41Cr4 steel as an abradant material (Table 2, tests *1* and *2*). Then we tested the abrasion resistance of two samples with two types of coatings (Table 2, test *3*). Table 2 shows the weight changes, weight wear and wear rates for each friction pair.

The weight wear of TiB_2(TiB)/Ti(TiO_2) coating is 28 %, which is less than that of the steel part. The mass losses of the sample and the abradant materials were low. The similar test with a friction pair of a hafnium diboride coating sample and 41Cr4 abradant material showed that the sample mass loss increases while the steel body wear is 690 % higher than that of the coated sample. The reason is the higher hardness of HfB_2/Ti(TiO_2) coatings.

Abrasion tests of TiB_2(TiB)/Ti(TiO_2) and HfB_2/Ti(TiO_2) coatings showed that the titanium diboride coating had higher wear resistance.

The weight wear of HfB_2/Ti(TiO_2) coating is 290 % higher than that of TiB_2 (TiB)/Ti(TiO_2) coating despite its higher microhardness. This can be explained by better elasticity of titanium diboride coatings, since spraying forms titanium monoboride. The substance creates a chemical bond between crystal lattices of initial phases, which prevents the ceramic component removal by friction. The hafnium diboride coating lacks such a bond. As a result, HfB_2/Ti(TiO_2) coating wear rate is higher than that of TiB_2 (TiB)/Ti(TiO_2) coating under identical contact loads.

Conclusions

We synthesized TiB_2/Ti and HfB_2/Ti metal-ceramic powders. The initial mass ratio of the components in the mixture was 50:50 %. The synthesis lasted for 3 h at 700 °C.

We studied the properties of TiB_2/Ti and HfB_2/Ti composite powder coatings applied with the microplasma technology.

The structural examination showed that the particles of ceramic components are fixed in the matrix without any through pores. During spraying the energy input changes the phase composition of titanium diboride composite powders from TiB_2/Ti to TiB_2 (TiB)/Ti(TiO_2).

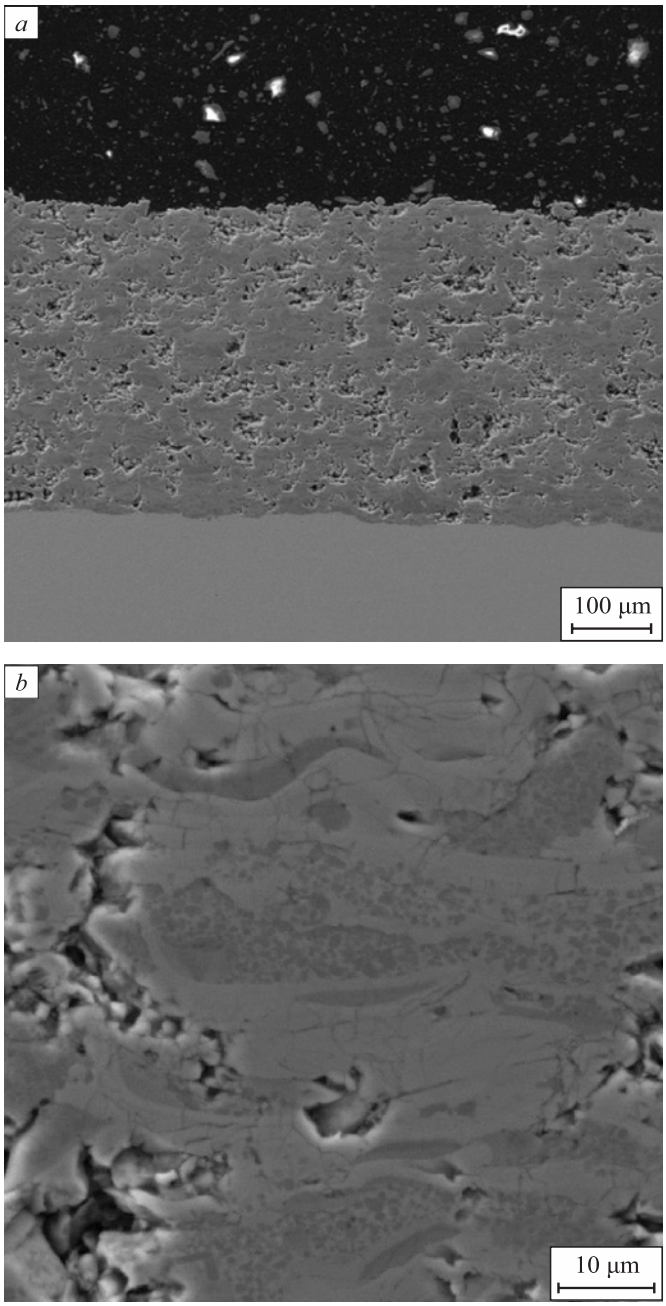

Fig. 3. Backscattered electron SEM images of TiB_2/Ti coating polished cross-section: *a* – ×300, *b* – ×3600

Рис. 3. РЭМ-микрофотография в отраженных электронах поперечного микрошлифа покрытия из TiB_2/Ti: *a* – ×300; *b* – ×3600

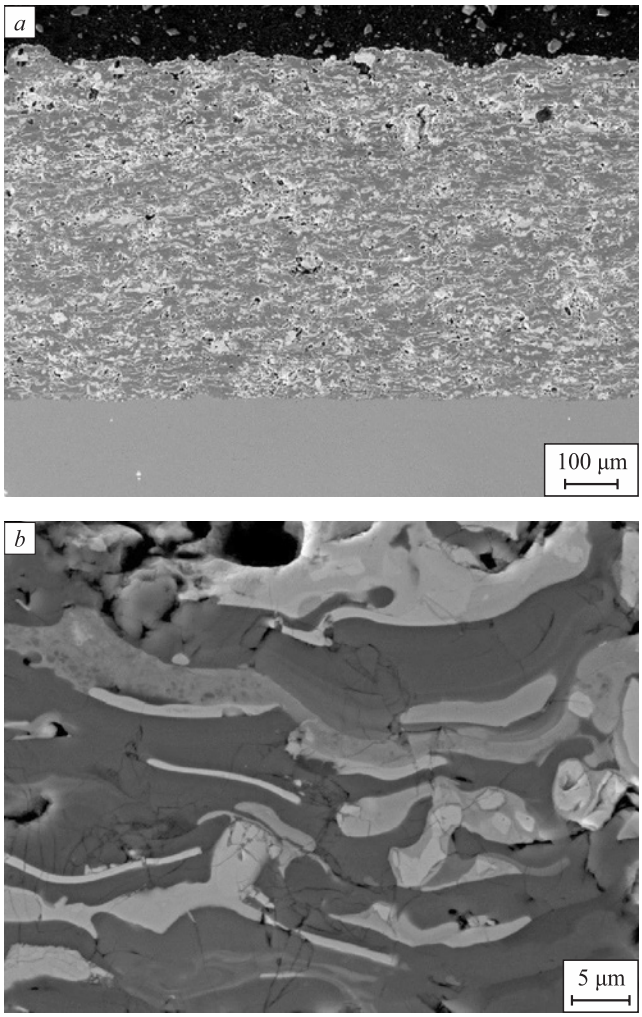

Fig. 4. Backscattered electron SEM images of HfB_2/Ti coating polished cross-section: *a* – ×300, *b* – ×3600

Рис. 4. РЭМ-микрофотография в отраженных электронах поперечного микрошлифа покрытия из HfB_2/Ti: *a* – ×300; *b* – ×3600

Table 2

Wear resistance properties of the coatings

Таблица 2. **Показатели износостойкости исследуемых систем материалов**

Test number	Friction pair	Sample weight, g			Weight wear, g/km	Wear rate, g/h
		before testing	after testing	Δm		
1	45H	37.4536	37.4522	0.0014	0.000619250	0.00028
	TiB_2(TiB)/Ti(TiO_2)	36.9823	36.9813	0.0010	0.000442321	0.00020
2	45H	37.4775	37.4632	0.0143	0.006325195	0.00286
	HfB_2/Ti(TiO_2)	37.3925	37.3907	0.0018	0.000796178	0.00036
3	TiB_2(TiB)/Ti(TiO_2)	37.0552	37.0451	0.0101	0.004467445	0.00202
	HfB_2/Ti(TiO_2)	37.6530	37.6130	0.0400	0.017692852	0.00800

Hardness of TiB_2 (TiB)/Ti(TiO_2) coating is 1320 HV and the hardness of HfB_2/Ti(TiO_2) coating is 1654 HV. The abrasion tests indicated that for the steel grade 45H abradant material, the weight wear of the coatings is 28 % less than the wear of the steel body. TiB_2 (TiB)/Ti coating offers the best performance with the lowest wear under a contact load with a steel body.

References / Список литературы

1. Gerasimova N.S. *The Main Types of Composite Materials and Ceramics: Manual*. Bauman Moscow State Technical University; 2019: 32. (In Russ.).

   Герасимова Н.С. *Основные виды композиционных материалов и керамики: Учебное пособие*. Москва: МГТУ им. Н.Э. Баумана; 2019: 32.
2. Ivantsov A.E., Rozhkova G.A. *Borides: Methodical instruction*. Kazan: Kazan State Technol. University; 2006: 19. (In Russ.).

   Иванцов А.Е., Рожкова Г.А. *Бориды: Методическое указание*. Казань: Казанский государственный технологический университет; 2006: 19.
3. Goncharov A.A., Dub S.N., Agulov A.V., Petukhov V.V. Structure, composition, and mechanical properties of thin films of transition metals diborides. *Journal of Superhard Materials*. 2015; 37(6): 422–428. https://doi.org/10.3103/S1063457615060076
4. Liang R., Shiota T., Omiya Y., Fujii M. Dry friction and wear behavior of various boride hard coating films. *The Proceedings of Conference of Chugoku-Shikoku Branch*. 2021; 59: 05b1. https://doi.org/10.1299/jsmecs.2021.59.05b1
5. Portnova E.N. *Production of ultra-high-temperature ceramic materials based on zirconium and hafnium diborides: Cand. Tech. Sci. Diss.* Perm National Research Polytechnic University; 2016: 137. (In Russ.).

   Портнова Е.Н. *Получение ультравысокотемпературных керамических материалов на основе диборидов циркония и гафния. Диссертация … кандидата технических наук.* Пермь: Пермский национальный исследовательский политехнический университет; 2016: 137.
6. Jayaraman S., Gerbiac J.E., Yangac Y., Kimbc D.Y., Chatterjeeac A., Bellonac P., Girolamibc G.S., Chevalierd J.P., Abelsonac J.R. HfB_2 and Hf–B–N hard coatings by chemical vapor deposition. *Surface and Coatings Technology*. 2006; 200 (22–23): 6629–6633. https://doi.org/10.1016/j.surfcoat.2005.11.040
7. Dugin S.N., Grebennikov A.V., Bogachev E.A., Gurkova E.L., Storozhenko P.A., Kolomiitsev I.A., Stepanov G.V. *Method of applying oxidation-resistant and ultra-high-temperature coatings of titanium, zirconium and hafnium diborides to composite material*. Patent RF no. 2 675 618. Publ. 20.12.2018 (In Russ.).

   Дугин С.Н., Гребенников А.В., Богачев Е.А., Гуркова Э.Л., Стороженко П.А., Коломийцев И.А., Степанов Г.В. *Способ нанесения окислительностойких и ультравысокотемпературных покрытий из диборидов титана, циркония и гафния на композиционные материалы*. Патент РФ № 2 675 618. Опубл. 20.12.2018.
8. Pavese M., Fino P., Badini C., Ortona A., Marino G. HfB_2/SiC as a protective coating for 2D Cf/SiC composites: Effect of high temperature oxidation on mechanical properties. *Surface and Coatings Technology*. 2008; 202 (10): 2059–2067. https://doi.org/10.1016/j.surfcoat.2007.08.037
9. Ren X., Li H., Chu Y., Fu Q., Li K. Ultra-high-temperature ceramic HfB_2-SiC coating for oxidation protection of SiC-coated carbon/carbon composites. *International Journal of Applied Ceramic Technology*. 2015; 12 (3): 560–567. https://doi.org/10.1111/ijac.12241
10. Zhou L., Zhang J., Hu D., Fu Q., Ding W., Hou J., Liu B., Tong M. High temperature oxidation and ablation behaviors of HfB_2-SiC/SiC coatings for carbon/carbon composites fabricated by dipping-carbonization assisted pack cementation. *Journal of Materials Science & Technology*. 2022; 111: 88–98. https://doi.org/10.1016/j.jmst.2021.08.092
11. Zhang P., Fu Q., Cheng C., Sun J., Zhang J., Xu M., Zhu X. Microstructure evolution of in-situ SiC-HfB2-Si ternary coating and its corrosion behaviors at ultra-high temperatures. *Journal of the European Ceramic Society*. 2021; 41(13): 6223–6237. https://doi.org/10.1016/j.jeurceramsoc.2021.05.058
12. Potanin A.Yu., Pogozhev Yu.S., Rupasov S.I., Shvyndina N.V., Levashov E.A. Obtaining SHS-ceramics HfB_2-SiC for high-temperature applications. In: *New Materials and Technologies: Powder Metallurgy, Composite Materials,*

Protective Coatings, Welding: Materials of the 14th Int. Sci. and Tech.Conf. Dedicated to the 60th Anniversary of Powder Metallurgy of Belarus, Minsk, September 9–11, 2020. Minsk: Belorusskaya nauka; 2020: 409–414. (In Russ.).

Потанин А.Ю., Погожев Ю.С., Рупасов С.И., Швындина Н.В., Левашов Е.А. Получение СВС-керамики HfB_2-SiC для высокотемпературных областей применения. В кн.: *Новые материалы и технологии: порошковая металлургия, композиционные материалы, защитные покрытия, сварка: Материалы 14-й Международной научно-технической конференции, посвященной 60-летию порошковой металлургии Беларуси, Минск, 9–11 сентября 2020 года*. Минск: ИД «Белорусская наука»; 2020: 409–414.

13. Shvaleva N.A., Ivanov M.E. Improving the design and manufacturing technology of the RTTT glass. *Aktual'nye problemy aviatsii i kosmonavtiki*. 2017; 1(13): 47–49. (In Russ.).

Швалева Н.А., Иванов М.Е. Совершенствование конструкции и технологии изготовления стакана РДТТ. *Актуальные проблемы авиации и космонавтики*. 2017; 1(13): 47–49.

14. Nisar A., Balani K. Phase and microstructural correlation of spark plasma sintered HfB_2-ZrB_2 based ultra-high temperature ceramic composites. *Coatings*. 2017; 7(8): 110. https://doi.org/10.3390/coatings7080110

15. Monteverde F. Ultra-high temperature HfB_2–SiC ceramics consolidated by hot-pressing and spark plasma sintering. *Journal of Alloys and Compounds*. 2007; 428(1–2): 197–205. https://doi.org/10.1016/j.jallcom.2006.01.107

16. Zapata-Solvas E., Jayaseelan D.D., Lin H.T., Brown P., Lee W.E. Mechanical properties of ZrB_2-and HfB_2-based ultra-high temperature ceramics fabricated by spark plasma sintering. *Journal of the European Ceramic Society*. 2013; 33(7): 1373–1386. https://doi.org/10.1016/j.jeurceramsoc.2012.12.009

17. Grashchenkov D.V., Sorokin O.Yu., Lebedeva Yu.E., Vaganova M.L. Specific features of sintering of HfB_2-based refractory ceramic by hybrid spark plasma sintering. *Russian Journal of Applied Chemistry*. 2015; 88(3): 379–386. https://doi.org/10.1134/S1070427215030040

Гращенков Д.В., Сорокин О.Ю., Лебедева Ю.Е., Ваганова М.Л. Особенности спекания тугоплавкой керамики на основе HfB_2 методом гибридного искрового плазменного спекания. Журнал прикладной химии. 2015; 88(3): 379–386.

18. Bogdanov S.P. Preparation of coatings on powders by the iodide transport method. *Glass Physics and Chemistry*. 2011; 37(2): 172. https://doi.org/10.1134/S1087659611020040

Богданов С.П. Получение покрытий на порошках методом йодного транспорта. *Физика и химия стекла*. 2011; 37(2): 229–237.

19. Bogdanov S.P. Iodotransport method of obtaining coatings on powders. *Izvestiya Sankt-Peterburgskogo gosudarstvennogo tekhnologicheskogo instituta. Khimiya i khimicheskaya tekhnologiya. Tekhnologiya neorganicheskikh veshchestv*. 2012;16 (42): 24–28. (In Russ.).

Богданов С.П. Йодотранспортный метод получения покрытий на порошках. *Известия Санкт-Петербургского государственного технологического института. Химия и химическая технология. Технология неорганических веществ*. 2012; 16(42): 24–28.

20. Kornev A.B., Kulik Yu.G., Funtikova E.V. On the strategy for restoring parts by gas–thermal spraying. In: *Sudostroenie i remont. Vestnik Volzhskogo gosudarstvennogo universiteta vodnogo transporta*. 2004: 166–174. (In Russ.).

Корнев А.Б., Кулик Ю.Г., Фунтикова Е.В. К вопросу стратегии восстановления деталей газотермическим напылением. *Судостроение и ремонт. Вестник Волжского государственного университета водного транспорта*. 2004: 166–174.

21. Kalita V.I., Komlev D.I. *Plasma Coatings with Nanocrystalline and Amorphous Structure: Monograph*. Moscow: Lider M; 2008: 388. (In Russ.).

Калита В.И., Комлев Д.И. *Плазменные покрытия с нанокристаллической и аморфной структурой*. Москва: Лидер М; 2008: 388.

22. Goshkoderya M.E., Bobkova T.I. Development of new composite materials of volumetrically reinforced configuration based on the Ti/TiB_2 system for spraying wear-resistant coatings effective under negative temperatures. In: *Coll. of Abstracts of the VIII All-Russ. Youth Sci. Forum "OpenScience 2021", Gatchina, November 17–19, 2021*: 105–106. (In Russ.).

Гошкодеря М.Е., Бобкова Т.И. Разработка новых композиционных материалов объемноармированной конфигурации на основе системы Ti/TiB_2 для напыления износостойких покрытий, эффективных при воздействии отрицательных температур. В кн.: *Сборник тезисов VIII Всероссийского молодежного научного форума «OpenScience 2021», Гатчина, 17–19 ноября 2021*: 105–106.

23. Goshkoderya M.E., Bobkova T.I., Staritsyn M.V. Investigation of Ti/TiB_2 system composite coatings sprayed by microplasma method. *Journal of Physics: Conference Series*. 2022; 2182(1): 012073.

24. Krutskii Yu.L., Cherkasova N.Yu., Gudyma T.S., Netskina O.V., Krutskaya T.M. Diborides of transition metals: Properties, application and production. Review. Part 1. Titanium and vanadium diborides. *Izvestiya. Ferrous Metallurgy*. 2021; 64(2): 149–164. https://doi.org/10.17073/0368-0797-2021-2-149-164

Крутский Ю.Л., Черкасова Н.Ю., Гудыма Т.С., Нецкина О.В., Крутская Т.М. Бориды некоторых переходных металлов: свойства, области применения и методы получения. Часть 1. Бориды титана и ванадия (обзор). *Известия вузов. Черная металлургия.* 2021; 64(2): 149–164. https://doi.org/10.17073/0368-0797-2021-2-149-164

25. Samsonov G.V., Vinitskii I.M. *Refractory Compounds (Handbook)*. Moscow: Metallurgy; 1976: 500. (In Russ.).

Самсонов Г.В., Виницкий И.М. *Тугоплавкие соединения: Справочник*. Москва: Металлургия; 1976: 500.

Information about the Authors

Mikhail E. Goshkoderya, *Cand. Sci. (Eng.), Engineer,* Academician I.V. Gorynin Central Research Institute of Structural Materials "Prometey" National Research Center "Kurchatov Institute"
E-mail: gosmike@yandex.ru

Tat'yana I. Bobkova, *Cand. Sci. (Eng.), Head of the Laboratory,* Academician I.V. Gorynin Central Research Institute of Structural Materials "Prometey" National Research Center "Kurchatov Institute"
E-mail: mail@crism.ru

Sergei P. Bogdanov, *Cand. Sci. (Eng.), Assist. Prof.,* St. Petersburg State Institute of Technology
E-mail: BogdanovSP@mail.ru

Aleksei V. Krasikov, *Cand. Sci. (Chem.), Deputy Head of Research Department,* Academician I.V. Gorynin Central Research Institute of Structural Materials "Prometey" National Research Center "Kurchatov Institute"
E-mail: mail@crism.ru

Mikhail V. Staritsyn, *Engineer,* Academician I.V. Gorynin Central Research Institute of Structural Materials "Prometey" National Research Center "Kurchatov Institute"
E-mail: mail@crism.ru

Anastasiya A. Kashirina, *Engineer,* Academician I.V. Gorynin Central Research Institute of Structural Materials "Prometey" National Research Center "Kurchatov Institute"
E-mail: mail@crism.ru

Сведения об авторах

Михаил Евгеньевич Гошкодеря, *инженер,* ЦНИИ КМ «Прометей» имени академика И.В. Горынина НИЦ «Курчатовский институт»
E-mail: gosmike@yandex.ru

Татьяна Игоревна Бобкова, *к.т.н., начальник лаборатории,* ЦНИИ КМ «Прометей» имени академика И.В. Горынина НИЦ «Курчатовский институт»
E-mail: mail@crism.ru

Сергей Павлович Богданов, *к.т.н., доцент,* Санкт-Петербургский государственный технологический институт (технический университет)
E-mail: BogdanovSP@mail.ru

Алексей Владимирович Красиков, *к.х.н., заместитель начальника,* ЦНИИ КМ «Прометей» имени академика И.В. Горынина НИЦ «Курчатовский институт»
E-mail: mail@crism.ru

Михаил Владимирович Старицын, *инженер,* ЦНИИ КМ «Прометей» имени академика И.В. Горынина НИЦ «Курчатовский институт»
E-mail: mail@crism.ru

Анастасия Анверовна Каширина, *инженер,* ЦНИИ КМ «Прометей» имени академика И.В. Горынина НИЦ «Курчатовский институт»
E-mail: mail@crism.ru

Contribution of the Authors

M. E. Goshkoderya – preparation of source materials; participation in synthesis of composite clad powders; participation in the study of powders/coatings morphology; spraying by microplasma method; determination of indicators of hardness and wear resistance.

T. I. Bobkova – deposition by microplasma method; determination of indicators of hardness and wear resistance.
S. P. Bogdanov – synthesis of composite clad powders of the studied systems.
A. V. Krasikov – participation in tests to determine wear resistance.

M. V. Staritsyn – study of materials on a scanning electron microscope.
A. A. Kashirina – study of materials on a scanning electron microscope.

Вклад авторов

М. Е. Гошкодеря – подготовка исходных материалов, участие в синтезе композиционных плакированных порошков, участие в исследовании морфологии порошков/покрытий, напыление микроплазменным методом, определение показателей твердости и износостойкости.
Т. И. Бобкова – напыление микроплазменным методом, определение показателей твердости и износостойкости.
С. П. Богданов – синтез композиционных плакированных порошков исследуемых систем.
А. В. Красиков – участие в испытаниях по определению износостойкости.
М. В. Старицын – исследование материалов на растровом электронном микроскопе.
А. А. Каширина – исследование материалов на растровом электронном микроскопе.

Received 18.08.2022
Revised 27.11.2022
Accepted 05.01.2023

Поступила в редакцию 18.08.2022
После доработки 27.11.2022
Принята к публикации 05.01.2023

MATERIAL SCIENCE / МАТЕРИАЛОВЕДЕНИЕ

UDC 621.774:622.691.4
DOI 10.17073/0368-0797-2023-1-35-42

Original article
Оригинальная статья

Preliminary assessment of X52 large-diameter pipes suitability for transportation of pressurized pure gaseous hydrogen

I. Yu. Pyshmintsev [1], A. B. Gizatullin [1], N. A. Devyaterikova [1], K. A. Laev [1], A. S. Tsvetkov [2], A. A. Alkhimenko [2], N. O. Shaposhnikov [2], M. K. Kurakin [2]

[1] **JSC "TMK"** (40/2a Pokrovka Str., Moscow 101000, Russian Federation)
[2] **Peter the Great St. Petersburg Polytechnic University** (29 Politekhnicheskaya Str., St. Petersburg 195251, Russian Federation)

PyshmintsevIU@tmk-group.com

Abstract. In order to assess the resistance to hydrogen embrittlement caused by the presence of hydrogen in the transported product, and, accordingly, the suitability of pipes for transporting hydrogen, we studied the metal of large-diameter X52 strength class pipes manufactured by JSC "ChelPipe" (a TMK Group company). The work included the study of pure gaseous hydrogen effect under pressure up to 10 MPa on change in mechanical characteristics of the base metal of large-diameter pipes (LDP) during preliminary hydrogen charging for various periods in a stationary autoclave under pressure, and during simultaneous loading with a slow strain rate (SSRT) under expected operating conditions. Results of the X52 LDP metal study show that there is no significant impact on the effect of gaseous hydrogen under pressure for up to 144 hours on mechanical characteristics of the base metal determined by static uniaxial tension (decrease in ductile characteristics does not exceed 9 %). During SSRT at a rate of not more than $1 \cdot 10^{-6}$ s^{-1} in a pure gaseous hydrogen environment under a pressure of 10 MPa, the change in strength and ductile characteristics does not exceed 13 % in comparison with the reference tests in a nitrogen environment under the same pressure. The results obtained allow us to consider that the base metal of low-alloy pipe steel with ferrite-perlite microstructure of X52 strength class is sufficiently resistant to hydrogen embrittlement. Final confirmation of the possibility of using LDP made from steel under study will be the results of further qualification tests, including the study of the weld metal and heat-affected zone properties.

Keywords: pipeline steel, hydrogen embrittlement, slow strain rate test, hydrogen transport, large diameter pipeline, X52 steel, tensile tests, autoclave for testing in a hydrogen environment

Acknowledgements: The research was supported by the Ministry of Science and Higher Education of the Russian Federation as part of the World-Class Research Center program: Advanced Digital Technologies (contract No. 075-15-2022-311 dated 20 April 2022).

For citation: Pyshmintsev I.Yu., Gizatullin A.B., Devyaterikova N.A., Laev K.A., Tsvetkov A.S., Alkhimenko A.A., Shaposhnikov N.O., Kurakin M.K. Preliminary assessment of X52 large-diameter pipes suitability for transportation of pressurized pure gaseous hydrogen. *Izvestiya. Ferrous Metallurgy*. 2023; 66(1): 35–42. https://doi.org/10.17073/0368-0797-2023-1-35-42

Предварительная оценка возможности использования труб большого диаметра из стали X52 для транспортировки чистого газообразного водорода под давлением

И. Ю. Пышминцев [1], А. Б. Гизатуллин [1], Н. А. Девятерикова [1], К. А. Лаев [1], А. С. Цветков [2], А. А. Альхименко [2], Н. О. Шапошников [2], М. К. Куракин [2]

[1] **ПАО «Трубная металлургическая компания»** (Россия, 101000, Москва, ул. Покровка, 40, стр. 2А)
[2] **Санкт-Петербургский политехнический университет Петра Великого** (Россия, 195251, Санкт-Петербург, ул. Политехническая, 29)

PyshmintsevIU@tmk-group.com

Аннотация. Для оценки стойкости к водородному охрупчиванию, вызванному присутствием водорода в транспортируемом продукте, и, соответственно, пригодности труб для транспортировки водорода был исследован основной металл труб большого диаметра класса

прочности Х52 производства АО «Челябинский трубопрокатный завод» (входит в группу компаний ПАО «Трубная металлургическая компания»). В работе изучено влияние чистого газообразного водорода под давлением до 10 МПа на изменение механических характеристик основного металла труб большого диаметра (ТБД). Исследование проводилось при предварительном наводороживании в стационарном автоклаве под давлением, а также при одновременном нагружении с малой скоростью деформации (SSRT) в ожидаемых условиях эксплуатации. Результаты исследования металла ТБД Х52 показывают отсутствие существенного влияния воздействия газообразного водорода под давлением в течение 24 – 144 ч на механические характеристики основного металла, определяемые при статическом одноосном растяжении (снижение пластических характеристик не превышает 9 %). При испытании SSRT со скоростью не более $1 \cdot 10^{-6}$ $с^{-1}$ в среде чистого газообразного водорода под давлением 10 МПа изменение прочностных и пластических характеристик не превышает 13 % в сравнении с контрольными испытаниями в среде азота под тем же давлением. Полученные результаты позволяют считать основной металл низколегированной трубной стали с феррито-перлитной микроструктурой класса прочности Х52 достаточно устойчивым к водородному охрупчиванию. Окончательным подтверждением возможности применения ТБД из исследуемой стали будут служить результаты дальнейших квалификационных испытаний, включающих изучение свойств металла шва и зоны термического влияния.

Ключевые слова: сталь трубопроводная, водородное охрупчивание, испытания при малой скорости деформации, транспорт водорода, трубопровод большого диаметра, Х52, испытания на растяжение, автоклав для испытаний в среде водорода

Благодарности: Исследование выполнено при поддержке ПАО «ТМК» и Министерства науки и высшего образования Российской Федерации (контракт № 075-15-2022-311).

Для цитирования: Пышминцев И.Ю., Гизатуллин А.Б., Девятерикова Н.А., Лаев К.А., Цветков А.С., Альхименко А.А., Шапошников Н.О., Куракин М.К. Предварительная оценка возможности использования труб большого диаметра из стали Х52 для транспортировки чистого газообразного водорода под давлением. *Известия вузов. Черная металлургия*. 2023; 66(1): 36–42.
https://doi.org/10.17073/0368-0797-2023-1-35-42

Introduction

One of the current challenges is the transition to hydrogen energy. There is extensive research to support the development of hydrogen transportation and storage infrastructure and the use of existing gas pipeline grids to deliver hydrogen. One important issue is the properties of materials which come into contact with pure gaseous hydrogen under pressure[1] [1].

For this reason, the Scientific and Technological Complex «New Technologies and Materials» at St. Petersburg Peter the Great Polytechnic University initiated a project to study the changes in structure and properties of pipe steel grades after hydrogen charging in a pure gaseous hydrogen environment under pressure [2 – 5]. According to several studies [6 – 10], the advanced steel grades used in main pipelines are promising for hydrogen transportation.

The structural strength, microstructure, and other properties may vary greatly in hydrogen, air, or inert environments. As indicated by tensile tests with standard and extremely slow strain rates, the elasticity is affected the most when the fracture pattern is changed. The purpose of this study is to estimate the degradation of the large-diameter pipe (LDP) material properties. The pipes are made of ferrite-perlite plate steel when exposed to gaseous hydrogen at high pressure equal to the operating pressure in today's long-distance gas transportation grids.

[1] Hydrogen Certified Pipes. A new era for hydrogen transportation. Available at URL: https://www.cpw.gr/userfiles/news/2020/CPW-H2-CPW-newsletter-final.pdf. (Accessed 01.09.2022)

Material Properties

We studied the samples of LDP (diameter: 1420 mm; wall thickness: 14 mm) 17G1S-U low-alloy tube steel grade (GOST 19281, X52 strength class). The EU analog is Fe52CFN. The chemical composition (as indicated in the quality certificate) in % is as follows:

C	Mn	Si	Cr	Cu	Ni	P	S
0.110	1.460	0.490	0.040	0.040	0.010	0.010	0.001
V	Nb	Al	Ti	Nb + V + Ti		S + P	
0.006	0.032	0.031	0.017	0.055		0.011	

Metallographic analysis showed that the steel has a ferrite-perlite structure. The average grain diameter is 7.61 μm (Fig. 1).

The pipe was manufactured from hot-rolled plates after controlled rolling. The pipe is made by cold gradual forming of rolled plates with a press. The pipe has one longitudinal double-sided (outer and inner) weld made by the automated flux-cored arc welding process. The pipe quality is compliant with the pipe specifications.

Test Methods

In order to evaluate the changes in the mechanical properties after preliminary hydrogen charging, the samples were kept for 72 and 144 h in pure hydrogen gas in in a stationary autoclave with a working part volume of 0.5 liters (Fig. 2, *a*).

Before the test, the autoclave was repeatedly purged with helium and then with hydrogen. After the pure gase-

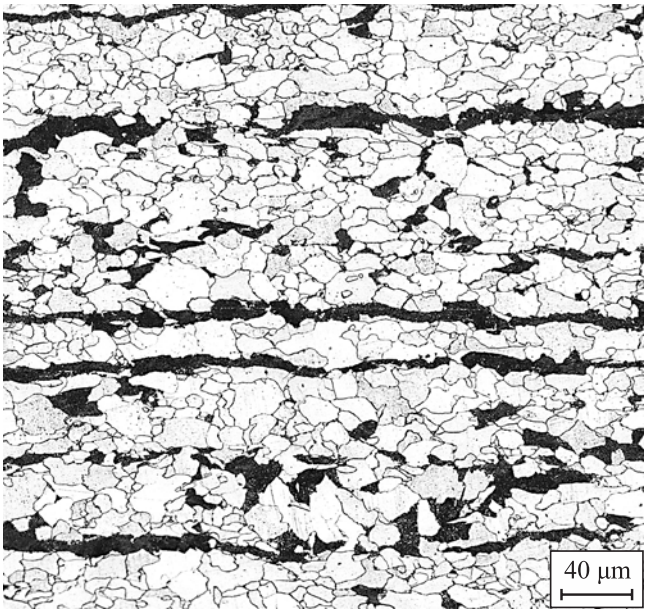

Fig. 1. Microstructure of base metal of the studied steel, ×500

Рис. 1. Микроструктура основного металла исследуемой стали, ×500

ous hydrogen pressure reached 10 MPa, the samples were held for the required period. Then for 10 – 15 min, they were tested for uniaxial tension with an Instron testing machine.

The smooth cylindrical samples 6 mm dia. were tested for static uniaxial tension according to GOST 1497 and ASTM G142. The samples were cut along the main direction of strain. Two samples for each holding time were used. We compared the tested mechanical properties with that of the reference samples.

The slow strain rate testing (SSRT) complied with ASTM G129 and NACE TM0198 using a UME-10T tensile testing machine: a customized autoclave that can apply loads to the sample in a gaseous environment pressure (Fig. 2, *b*). The tests were performed in pure gaseous hydrogen and nitrogen (for the reference samples) at a slow strain rate of $8.5 \cdot 10^{-7}$ s^{-1}. It complies with the NACE TM0198 requirement that the strain rate should be less or equal to $1 \cdot 10^{-6}$ s^{-1}. The samples were smooth cylinders 6.35 mm dia. cut in the longitudinal direction. Two samples were used for each environment. After placing the samples, the autoclave was repeatedly purged with helium and then with hydrogen (for the hydrogen environment tests) or nitrogen (for the reference sample tests). The gas pressure was raised to the required value (10 MPa), and the strain was applied at the specified rate.

We evaluated the tensile test results (also for the SSRT) by analyzing the average values of the measured structural strength and elasticity. The property changes were expressed as a percentage [6 – 8]. The strength and elasticity ratios are the ratios of the property values in a pure

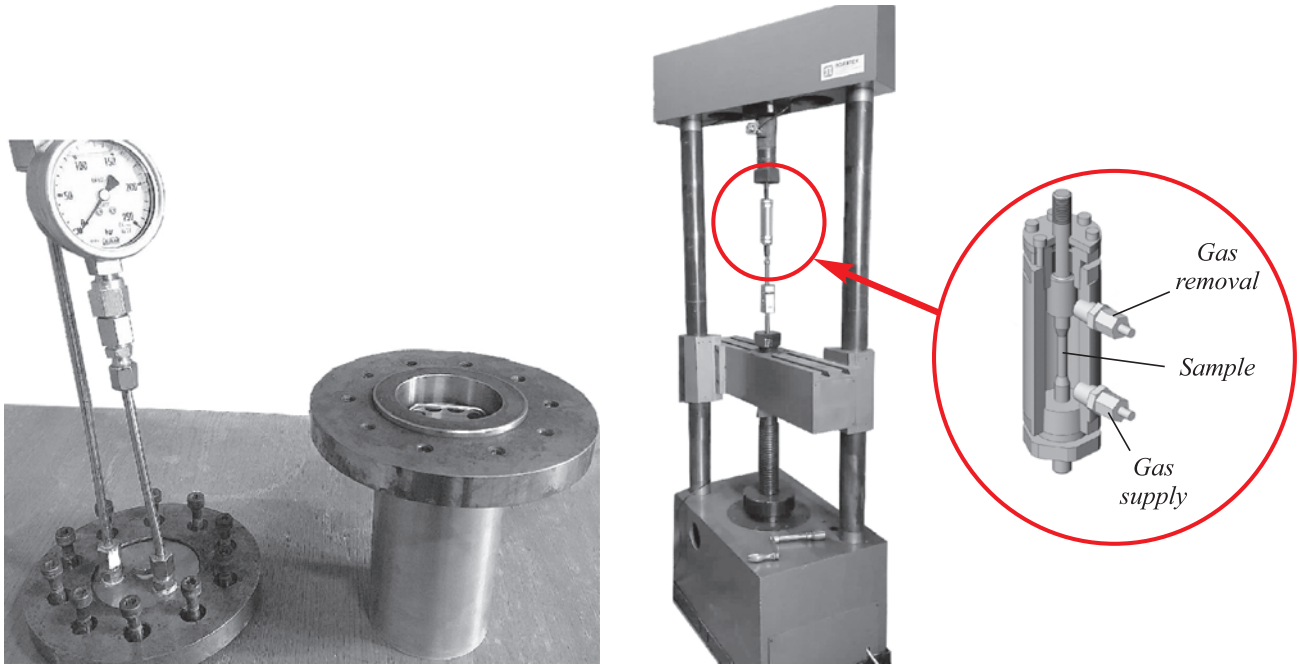

a *b*

Fig. 2. Autoclaves used: stationary autoclave with the possibility to control and regulate pressure (*a*); tensile testing machine with an installed autoclave for tensile test of the samples in a gaseous environment (*b*)

Рис. 2. Используемые автоклавы: стационарный автоклав с возможностью контроля и регулирования давления (*a*); машина для испытания на растяжение с установленным автоклавом для растяжения образцов в газообразной среде (*b*)

hydrogen environment to the property values of the reference samples.

The changes in the strength and elasticity ratios were expressed as the decrease in value relative to 100 %. When a value is close to 100 %, we may claim that the respective material property is not affected by hydrogen under the test conditions. The lower the strength and elasticity ratios, the greater the effect of the holding time in pure hydrogen at 10 MPa on the metal's mechanical properties.

We examined the fracture surface of the samples using a Tescan MIRA3 scanning electron microscope.

Test Results

The static uniaxial tension tests of the hydrogen charged samples show a weak effect of the hydrogen charging conditions used on the elasticity properties (Fig. 3, *a*). The decrease in the plasticity ratios does not exceed 9 %. No significant degradation of the structural strength after such tests was found (the strength ratios are about 100 %). According to Tröger M. et al. [7], elasticity ratios above 80 % indicate high resistance to hydrogen embrittlement.

As the results show, longer exposure to gaseous hydrogen leads to a slight decrease in the elasticity properties of the metal. This has also been reported in many studies [6; 9 – 11]. Despite this trend, the key properties of the sample metal after holding it in pure hydrogen gas for 72 and 144 h changed insignificantly relative to the reference samples.

The fracture surfaces of the samples have pits. The surface pattern does not change significantly after hydrogen charging (Fig. 4, *a*, *b*).

All of the above indicates no significant effect of pure gaseous hydrogen at 10 MPa, a well as the high resistance (no changes in the strength and elasticity) of the studied metal during pre- hydrogen charging at up to 144 h holding time.

When testing the X52 pressure rating steel at slow strain rates in a hydrogen environment, there is a slight decrease in the strength and elasticity compared to the reference tests in a nitrogen environment. The changes in strength and elasticity of the samples tested in a hydrogen environment relative to that of the reference samples in a nitrogen environment under identical conditions do not exceed 13 %. The strength and elasticity ratios are above 80 %, which indicates the resistance of the investigated steel to loads applied in a hydrogen environment [7].

The results are consistent with other SSRT studies of hydrogen embrittlement in pipe steels in a hydrogen environment [6; 12; 13]. The tensile curves for the tested samples are shown in Fig. 3, *b*.

The SSRT samples tested in a nitrogen environment showed a viscous fracture pattern. The fracture surface has pits (Fig. 4, *c*). The slow strain rate tests in pure gaseous hydrogen produced microcracks and brittle frac-

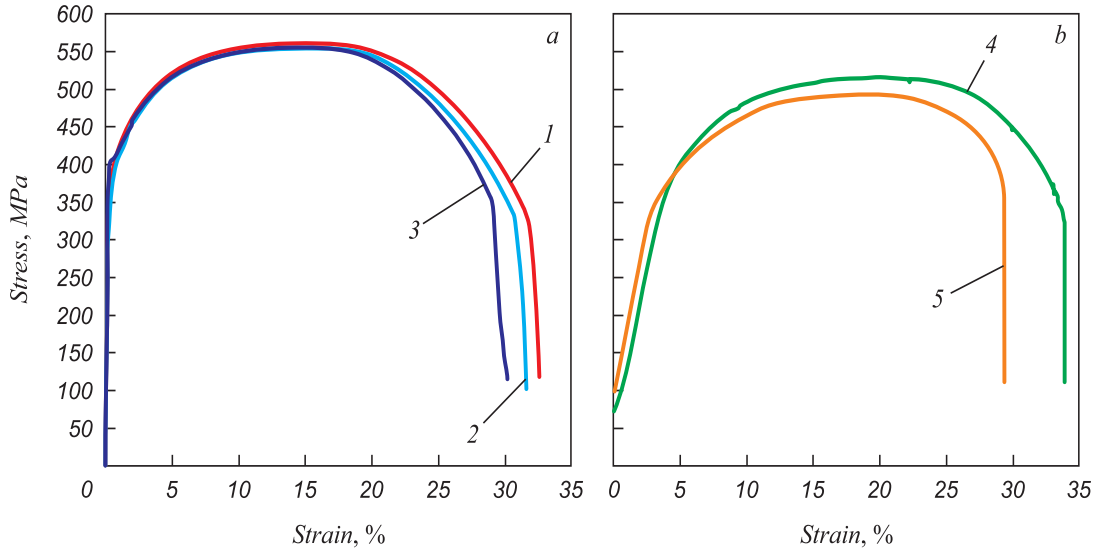

Fig. 3. Tensile test diagrams of the samples at a strain rate of 10^{-2} s^{-1} (*a*) and 10^{-6} s^{-1} (*b*):
1 – reference tests; *2* – test after preliminary exposure to hydrogen for 72 h (E_{pr} = 95.23 %);
3 – test after preliminary exposure to hydrogen for 144 h (E_{pr} = 91.09 %); *4* – SSRT in nitrogen environment;
5 – SSRT in gaseous hydrogen environment (E_{pr} = 86.59 %)

Рис. 3. Диаграммы растяжения образцов со скоростью 10^{-2} $с^{-1}$ (*a*) и 10^{-6} $с^{-1}$ (*b*):
1 – контрольные испытания; *2* – испытание после предварительной выдержки в водороде в течение 72 ч ($E_{пр}$ = 95,23 %);
3 – испытание после предварительной выдержки в водороде в течение 144 ч ($E_{пр}$ = 91,09 %);
4 – SSRT испытание в среде азота; *5* – SSRT испытание в среде газообразного водорода ($E_{пр}$ = 86,59 %)

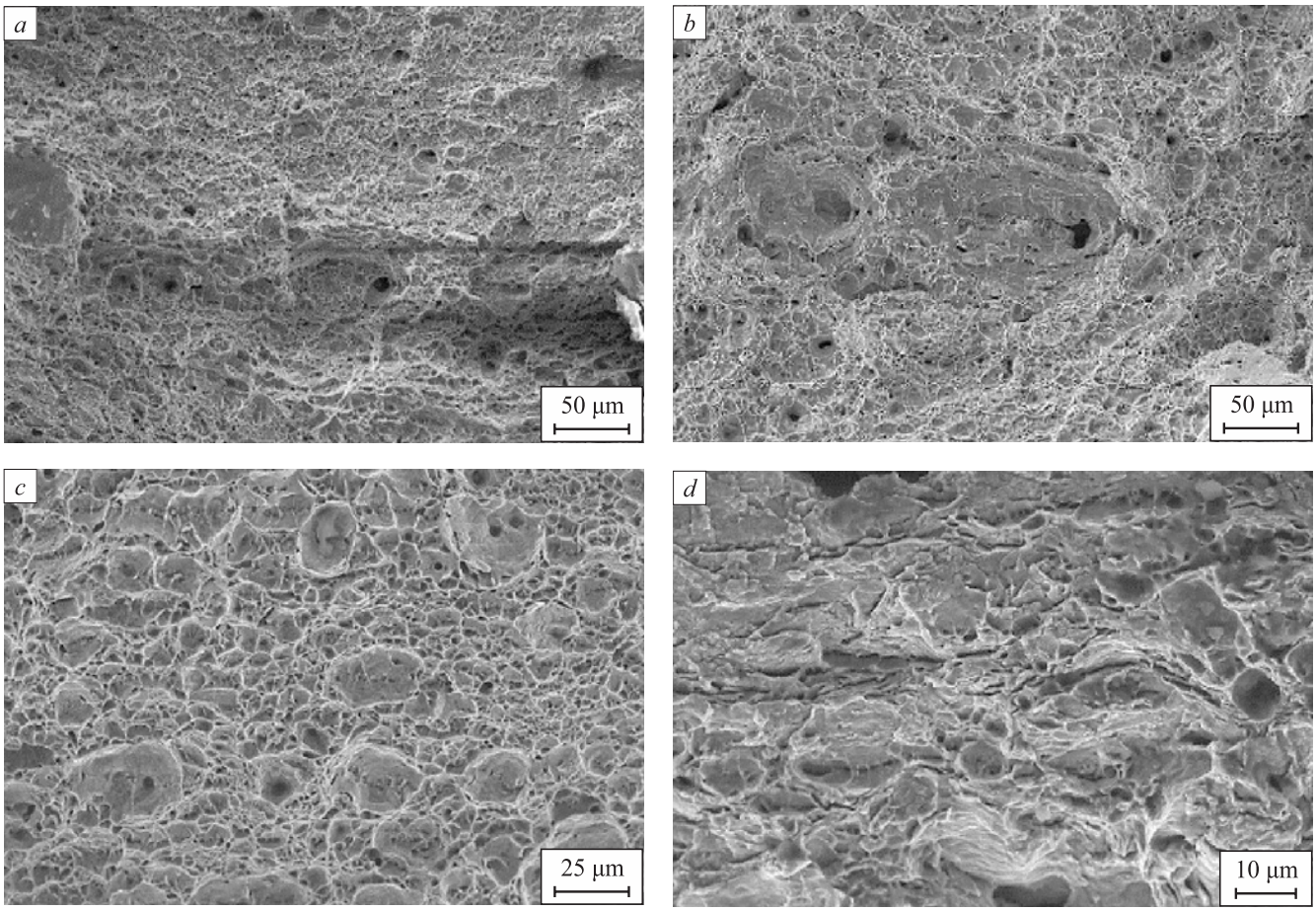

Fig. 4. Appearance of fracture surface of the tested samples:
tensile behavior at a strain rate of 10^{-2} s^{-1} of the reference samples (*a*);
tensile behavior at a strain rate of 10^{-2} s^{-1} of the samples exposed to hydrogen for 144 h (*b*);
tensile behavior at a strain rate of 10^{-6} s^{-1} in a nitrogen environment (*c*);
tensile behavior at a strain rate of 10^{-6} s^{-1} in hydrogen at 10 MPa (*d*)

Рис. 4. Внешний вид поверхности разрушения испытанных образцов:
растяжение со скоростью 10^{-2} $с^{-1}$ контрольных образцов (*a*);
растяжение со скоростью 10^{-2} $с^{-1}$ образцов после выдержки в среде водорода в течение 144 ч (*b*);
растяжение со скоростью 10^{-6} $с^{-1}$ в среде азота (*c*);
растяжение со скоростью 10^{-6} $с^{-1}$ в среде водорода при давлении 10 МПа (*d*)

ture areas (Fig. 4, *d*).The results we obtained are similar to the fractography results presented in [11; 14; 15]. The fracturing is attributed to the accumulation of hydrogen in defects both in the surface layer of the metal and below. This can lead to high internal stress at the hydrogen concentration areas and the formation of micro- and macro-cracks. Hydrogen embrittlement requires the continuous diffusion of hydrogen from inside the metal to its surface. Thus any factors which contribute to the increase of the hydrogen volume diffusing to the crack intensify hydrogen embrittlement [16]. With a significantly lower strain rate, hydrogen has enough time to diffuse into the sample material and redistribute at the critical points of the microstructure (e.g., at the tops of cracks formed during testing) [8]. It facilitates the formation of embrittlement areas and leads to small cracks during testing (Fig. 4, *d*).

A decrease in the strain rate from ~10^{-2} s^{-1} (for the hydrogen charged sample testing according to GOST 1497) to ~10^{-6} s^{-1} (for SSRT in hydrogen) leads to a more noticeable, but not critical change in the plasticity ratios from 95 to 85 % on average. A similar decrease in elasticity with virtually unchanged strength was found in gaseous hydrogen SSRT tests of X80 pressure rating pipe steel [6; 11], while the loss of elasticity increases with decreasing the strain rate.

Despite the changes observed in the mechanical properties when we tested the samples after preliminary hydrogen charging and by loading in a gaseous hydrogen environment, the properties of X52 pipe steel remain within the specifications for pipes. They are consistent with the test results presented in [6 – 15] where metal embrittlement in pure hydrogen gas environment under pressure is evaluated.

Conclusions

We studied the resistance of typical low-alloy pipe steel, moderate X52 strength class rating to hydrogen embrittlement. We found no significant changes in strength and elasticity after exposure to gaseous hydrogen at 10 MPa and room temperature for 24 – 144 h. The reduction of elasticity in the samples does not exceed 10 %.

The SSRT tests (strain rate not exceeding $1 \cdot 10^{-6}$ s^{-1}) showed a decrease in elasticity not exceeding 20 %. The greater loss of elasticity compared to the tests of pre-hydrogen charged samples is caused by the possible diffusion of hydrogen near the stress concentrators and the tops of cracks with the strain rate decrease.

Regardless of the test conditions, the key structural strength properties of the metal remain within the specifications.

Therefore, the tests (under the above conditions) indicate that the ferrite-perlite pipe steel, X52 strength class, shows good resistance to hydrogen embrittlement. Our results are in good agreement with the published results of similar tests of low-alloy plate and pipe steel grades.

The final confirmation of the X52 strength class pipe steel suitability for operations in gaseous hydrogen at pressures up to 10 MPa will be the qualification tests pursuant to ASME B 31.12[2] [17; 18] and ASME BPVC [19], as well as studies of the hydrogen effects on the weld metal and heat affected zone.

References / Список литературы

1. Chugunov A.V. Bebeshko I.G., Semenov A.M., Becker W., Fenin C., Hoecher T. Experimental research in the influence of a mixture of methane and oxygen gases uponstructural and mechanical properties of several steel grades. *Gazovaya promyshlennost'*. 2016; 10: 82–89. (In Russ.).

   Чугунов А.В., Бебешко И.Г., Семенов А.М., Беккер В., Фенин К., Хечер Т. Экспериментальное исследование воздействия смеси газов метана и водорода на структурно-механические свойства некоторых марок стали. *Газовая промышленность*. 2016; 10: 82–89.
2. Kolesov S., Alekseeva E. Evaluation of the stress-strain state in alloy 718 after hydrogen charging. In: *Proceedings of the 9th Int. Symp. on Superalloy 718 & Derivatives: Energy, Aerospace, and Industrial Applications. The Minerals, Metals & Materials Series.* 2018: 553–563. https://doi.org/10.1007/978-3-319-89480-5_36
3. Kolesov S., Badrak R., Shakhmatov A. Hydrogen influence on crack propagation and stress-strain evolution of alloy 718. In: *Proceedings of the 9th Int. Symp. on Superalloy 718 & Derivatives: Energy, Aerospace, and Industrial Applications. The Minerals, Metals & Materials Series.* 2018: 209–218. https://doi.org/10.1007/978-3-319-89480-5_12
4. Frolova K., Vilchevskaya E., Polyanskiy V., Alekseeva E. Modelling of a hydrogen saturated layer within the micropolar approach. *New Achievements in Continuum Mechanics and Thermodynamics*. 2019; 108: 117–128. https://doi.org/10.1007/978-3-030-13307-8_9
5. Polyanskiy V.A., Belyaev A.K., Alekseeva E.L., Tretyakov D.A., Yakovlev Y.A. Phenomenon of skin effect in metals due to hydrogen absorption. *Continuum Mechanics and Thermodynamics*. 2019; 31: 1961–1975. https://doi.org/10.1007/s00161-019-00839-2
6. Nanninga N.E., Levy Y.S., Drexler E.S., Condon R.T., Stevenson A.E., Slifka A.J. Comparison of hydrogen embrittlement in three pipeline steels in high pressure gaseous hydrogen environments. *Corrosion Science*. 2012; 59: 1–9. https://doi.org/10.1016/j.corsci.2012.01.028
7. Tröger M., Bosch C., Wiart J.-N., Meuser H., Knoop F.M., Brauer H., Schröder J. Investigations on hydrogen assisted cracking of welded high-strength pipes in gaseous hydrogen. *Steely Hydrogen Conf. Proceedings – 2014*. 2014: 491–501.
8. Brauer H., Simm M., Wanzenberg E., Henel M., Huising O.J. Energy transition with hydrogen pipes: Mannesmann "H2 ready" and the changeover. *Pipeline Technology*. 2020; 1: 16–29.
9. Meng B., Gu C., Zhang L., Zhou C., Li X., Zhao Y., Zheng J., Chen X., Han Y. Hydrogen effects on X80 pipeline steel in high-pressure natural gas/hydrogen mixtures. *International Journal of Hydrogen Energy*. 2017; 42(11): 7404–7412. https://doi.org/10.1016/J.IJHYDENE.2016.05.145
10. Zhou D., Li T., Huang D., Wu Y., Huang Z., Xiao W., Wang Q., Wang X. The experiment study to assess the impact of hydrogen blended natural gas on the tensile properties and damage mechanism of X80 pipeline steel. *International Journal of Hydrogen Energy*. 2021; 46(10): 7402–7414. https://doi.org/10.1016/j.ijhydene.2020.11.267
11. Briottet L., Moro I., Lemoine P. Quantifying the hydrogen embrittlement of pipeline steels for safety considerations. *International Journal of Hydrogen Energy*. 2012; 37(22): 17616–17623. https://doi.org/10.1016/j.ijhydene.2012.05.143
12. Somerday B.P. *Technical reference on hydrogen compatibility of materials. Plain carbon ferritic steels: C-Mn alloys (code 1100).* URL: https://www.sandia.gov/app/uploads/sites/158/2021/12/1100TechRef_FeCMn.pdf (Accessed 13.01.2023).
13. Bolobov V.I., Latipov I.U., Popov G.G., Buslaev G.V., Martynenko Ya.V. Estimation of the influence of compressed hydrogen on the mechanical properties of pipeline steels. *Energies*. 2021; 14(19): 6085. https://doi.org/10.3390/en14196085
14. Nguyen T.T., Park J., Kim W.S., Nahm S.H., Baek U.B. Effect of low partial hydrogen in a mixture with methane on the mechanical properties of X70 pipeline steel. *International Journal of Hydrogen Energy*. 2020; 45(3): 2368–2381. https://doi.org/10.1016/j.ijhydene.2019.11.013
15. Joseph A., Ronevich J.A., Song E.J., Somerday B.P., San Marchi C.W. Hydrogen-assisted fracture resistance of pipeline welds in gaseous hydrogen. *International Journal of Hydrogen Energy*. 2021; 46(10): 7601–7614. https://doi.org/10.1016/j.ijhydene.2020.11.239

[2] Hydrogen certified pipes: X70M high-grade HFW pipes succeed in qualification tests for hydrogen (ASME CODE). URL: https://www.cpw.gr/en/media-center/news-events/newsevent-hydrogen-certified-pipes-x70m-high-grade-hfw-pipes-succeed-in-qualification-tests-for-hydrogen-asme-code (Accessed 13.01.2023).

16. Kolachev B.A. *Hydrogen Brittleness of Metals*. Moscow: Metallurgiya; 1985: 216. (In Russ.).

Колачев Б.А. *Водородная хрупкость металлов*. М.: Металлургия; 1985: 216.

17. Martin M.L., Connolly M., Buck Z.N., Bradley P.E., Lauria D., Slifka A.J. Evaluating a natural gas pipeline steel for blended hydrogen service. *Journal of Natural Gas Science and Engineering*. 2022; 101: 104529. https://doi.org/10.1016/j.jngse.2022.104529

18. *ASME B31.12-2019. Hydrogen Piping and Pipelines*. USA, ASME; 2020: 280.

19. *ASME BPVC. VIII. 3 – 2017. Boiler & Pressure Vessel Code. Division 3 Alternative Rules for Construction of High Pressure Vessels*. USA, ASME; 2017: 407.

Information about the Authors / Сведения об авторах

Igor' Yu. Pyshmintsev, *Dr. Sci. (Eng.), Prof., Director for Research,* JSC "TMK", *General Director,* LLC "Research and Development Centre TMK", *General Director,* Russian Scientific Research Institute of the Pipe Industry
E-mail: PyshmintsevIU@tmk-group.com

Anton B. Gizatullin, *Deputy Director for Research,* JSC "TMK"
E-mail: Anton.Gizatullin@chelpipegroup.com

Natal'ya A. Devyaterikova, *Chief Specialist of Industrial Pipe Center,* JSC "TMK"
E-mail: n.devyaterikova@chelpipegroup.com

Konstantin A. Laev, *Cand. Sci. (Eng.), Chief Specialist of Industrial Pipe Center,* JSC "TMK"
E-mail: Konstantin.Laev@chelpipegroup.com

Anton S. Tsvetkov, *Cand. Sci. (Eng.), Engineer, Deputy Head of the Experimental Laboratory of the Scientific and Technical Complex "New Technologies and Materials" of the Center for Scientific and Technical Research,* Peter the Great St. Petersburg Polytechnic University
E-mail: tsvetkov_as@spbstu.ru

Alexei A. Alkhimenko, *Director of the Scientific and Technological Complex "New Technologies and Materials",* Peter the Great St. Petersburg Polytechnic University
ORCID: 0000-0001-6701-1765
E-mail: a.alkhimenko@spbstu.ru

Nikita O. Shaposhnikov, *Executive Director of the Scientific and Technological Complex "New Technologies and Materials",* Peter the Great St. Petersburg Polytechnic University
E-mail: shaposhnikovno@gmail.com

Maksim K. Kurakin, *Engineer, Project Manager of the Scientific and Technical Complex "New Technologies and Materials" of the Center for Scientific and Technical Research,* Peter the Great St. Petersburg Polytechnic University
E-mail: maksim_kurakin@mail.ru

Игорь Юрьевич Пышминцев, *д.т.н., профессор, директор по научной работе,* ПАО «Трубная металлургическая компания», *генеральный директор,* ООО «ТМК НТЦ», *генеральный директор,* АО «РусНИТИ»
E-mail: PyshmintsevIU@tmk-group.com

Антон Бильгуварович Гизатуллин, *заместитель директора по научной работе,* ПАО «Трубная металлургическая компания»
E-mail: Anton.Gizatullin@chelpipegroup.com

Наталья Анатольевна Девятерикова, *главный специалист Центра труб промышленного назначения,* ПАО «Трубная металлургическая компания»
E-mail: n.devyaterikova@chelpipegroup.com

Константин Анатольевич Лаев, *к.т.н., главный специалист отдела труб инфраструктурных проектов Центра труб промышленного назначения,* ПАО «Трубная металлургическая компания»
E-mail: Konstantin.Laev@chelpipegroup.com

Антон Сергеевич Цветков, *к.т.н., инженер, заместитель заведующего испытательной лаборатории НТК «Новые технологии и материалы» центра НТИ,* Санкт-Петербургский политехнический университет Петра Великого
E-mail: tsvetkov_as@spbstu.ru

Алексей Александрович Альхименко, *директор НТК «Новые технологии и материалы»,* Санкт-Петербургский политехнический университет Петра Великого
ORCID: 0000-0001-6701-1765
E-mail: a.alkhimenko@spbstu.ru

Никита Олегович Шапошников, *исполнительный директор НТК «Новые технологии и материалы» центра НТИ,* Санкт-Петербургский политехнический университет Петра Великого
E-mail: shaposhnikovno@gmail.com

Максим Константинович Куракин, *инженер, руководитель проектов НТК «Новые технологии и материалы» центра НТИ,* Санкт-Петербургский политехнический университет Петра Великого
E-mail: maksim_kurakin@mail.ru

Contribution of the Authors / Вклад авторов

I. Yu. Pyshmintsev – formation of the article main concept and goals, scientific guidance, analysis of the research results.

A. B. Gizatullin – LDP manufacture, preparation of metal for testing, analysis of the research results, LDP expertise.

N. A. Devyaterikova – supervising research from JSC "TMK", analysis the research results, writing the text, solving organizational issues.

K. A. Laev – analysis of the research results, expertise of the properties and metals testing.

И. Ю. Пышминцев – определение основного направления исследований и концепции статьи, научное руководство, анализ полученных результатов исследований.

А. Б. Гизатуллин – изготовление ТБД, подготовка металла для испытаний, анализ полученных результатов исследований, экспертиза ТБД.

Н. А. Девятерикова – курирование исследований от ПАО «ТМК», анализ полученных результатов исследований, написание статьи, решение организационных вопросов.

К. А. Лаев – анализ полученных результатов исследований, экспертиза свойств и испытаний металлов.

A. S. Tsvetkov – supervising research from Peter the Great St. Petersburg Polytechnic University, conducting the research, analysis of the research results, writing the text.
A. A. Alkhimenko – scientific guidance, analysis of the research results, writing the text.
N. O. Shaposhnikov – determination of the research directions, analysis of the research results, writing the text, solving organizational issues.
M. K. Kurakin – supervising research from Peter the Great St. Petersburg Polytechnic University, analysis of the research results, writing the text, solving organizational issues.

А. С. Цветков – организация проведения исследований со стороны СПбПУ, проведение исследований, анализ полученных результатов, написание статьи.
А. А. Альхименко – научное руководство, анализ полученных результатов исследований, написание статьи.
Н. О. Шапошников – определение направлений исследований, анализ полученных результатов исследований, написание статьи, решение организационных вопросов.
М. К. Куракин – курирование исследований, анализ полученных результатов исследований, написание статьи, решение организационных вопросов.

Received 19.09.2022
Revised 11.01.2023
Accepted 12.01.2023

Поступила в редакцию 19.09.2022
После доработки 11.01.2023
Принята к публикации 12.01.2023

MATERIAL SCIENCE / МАТЕРИАЛОВЕДЕНИЕ

UDC 621.793
DOI 10.17073/0368-0797-2023-1-43-49

Original article
Оригинальная статья

Influence of silicon carbides on the structure and properties of nickel-phosphorus composite coatings

Yu. N. Goikhenberg [1], D. S. Polukhin [2], D. A. Zherebtsov [1], E. G. Bodrov [2]

[1] **South Ural State University** (76 Lenina Ave., Chelyabinsk 454080, Russian Federation)
[2] **Research & Development Center KONAR, LLC** (8 Yeniseiskaya Str., Chelyabinsk 455030, Russian Federation)

goikhenbergyn@susu.ru

Abstract. The authors studied the structure, properties, and corrosion resistance in different acids of the nickel-phosphorus coatings with the dispersed silicon carbides after crystallization annealing in different modes. Crystallization onset temperatures after heating at rates of 1, 5, and 20 °C/min and the percentage of crystalline phases formed under isothermal conditions (nickel phosphide Ni_3P and nickel) were determined. It was determined that a high microhardness of more than 1000 HV is achieved in the composite nickel-phosphorus coating with dispersed particles of the silicon carbides also during prolonged low-temperature annealing, accompanied by crystallization with the formation of already insignificant (10 %) amounts of Ni_3P. The revealed dispersed Ni_3P located both inside the grains and along the boundaries of the grains make the main contribution to the increase in microhardness. Yield strength and tensile strength of coatings increase during crystallization annealing by only 12 – 15 MPa, and elongation drops to zero, due to the formation of the brittle Ni_3P compounds. Annealing with a short-term soaking at crystallization temperatures leads to the fact that the silicon carbides exhibit a barrier effect. This reduces the intensity of the formation of crystalline Ni_3P and corrosion resistance, while a long-term soaking at lower crystallization temperatures forms about 70 % Ni_3P, contributing to consistently high hardness and improved corrosion resistance. Corrosion resistance of the composite Ni-P coatings with the silicon carbides, regardless of heat treatment modes, is maximum in acetic and orthophosphoric acids at the 70 % nickel phosphide and minimum in nitric acid and its mixtures with other acids.

Keywords: amorphous coatings, nickel-phosphorus, silicon carbides, crystallization annealing, nickel phosphides, nickel, microhardness, plasticity, corrosion resistance, acids

For citation: Goikhenberg Yu.N., Polukhin D.S., Zherebtsov D.A., Bodrov E.G. Influence of silicon carbides on the structure and properties of nickel-phosphorus composite coatings. *Izvestiya. Ferrous Metallurgy*. 2023; 66(1): 43–49. https://doi.org/10.17073/0368-0797-2023-1-43-49

Влияние карбидов кремния на структуру и свойства композитного никель-фосфорного покрытия

Ю. Н. Гойхенберг [1], Д. С. Полухин [2], Д. А. Жеребцов [1], Е. Г. Бодров [2]

[1] **Южно-Уральский государственный университет** (454080, Россия, Челябинск, пр. Ленина, 76)
[2] **ООО «Научно-технический центр КОНАР»** (Россия, 454010, Челябинск, Енисейская ул., 8)

goikhenbergyn@susu.ru

Аннотация. Статья содержит исследования структуры, свойств и коррозионной стойкости в различных кислотах никель-фосфорных покрытий с дисперсными карбидами кремния после кристаллизационного отжига по различным режимам. Установлены температуры начала кристаллизации после нагрева со скоростями 1, 5, 20 °С/мин и процентное содержание образующихся в изотермических условиях кристаллических фаз (фосфида никеля Ni_3P и никеля). Определено, что высокая микротвердость более 1000 HV достигается в композитном никель-фосфорном покрытии с дисперсными частицами карбидов кремния также при длительном низкотемпературном отжиге, сопровождающемся кристаллизацией с образованием уже незначительных (10 %) количеств фосфида никеля. Выявленные дисперсные фосфиды никеля, располагающиеся как в теле, так и по границам зерен, вносят основной вклад в приращение микротвердости. Предел текучести и предел прочности покрытий увеличиваются при кристаллизационном отжиге всего на 12 – 15 МПа, а относительное удлинение падает до нуля, что обусловлено образованием хрупких соединений фосфида никеля. Отжиг с непродолжительными выдержками при температурах кристаллизации приводит к тому, что карбиды кремния проявляют барьерный эффект, снижая интенсивность образования кристаллического фосфида никеля и коррозионную стойкость, тогда как продолжительные выдержки при более низких температурах кристаллизации формируют порядка 70 % Ni_3P, способствуя стабильно высокой твердости и улучшенным показателям коррозионной стойкости. Коррозионная стойкость композитных покрытий Ni-P + карбиды кремния вне зависимости от режимов термообработки максимальная в уксусной и ортофосфорной кислотах при 70 % фосфида никеля и минимальная в азотной кислоте и ее смесях с другими кислотами.

Ключевые слова: аморфные покрытия, никель-фосфор, карбиды кремния, кристаллизационный отжиг, фосфиды никеля, никель, микротвердость, пластичность, коррозионная стойкость, кислоты

Для цитирования: Гойхенберг Ю.Н., Полухин Д.С., Жеребцов Д.А., Бодров Е.Г. Влияние карбидов кремния на структуру и свойства композитного никель-фосфорного покрытия. *Известия вузов. Черная металлургия*. 2023; 66(1): 44–49.
https://doi.org/10.17073/0368-0797-2023-1-43-49

Introduction

Chrome and nickel plating are the main types of the metal coatings. Currently, the nickel coatings occupy a leading position in the technological process of protecting components [1]. Thus, the composite nickel-phosphorus coatings have a significant wear resistance [2; 3], high corrosion resistance [4 – 7], good adhesion [8] and decorative properties [1]. A promising method of hardening and protecting components of a simple shape is the method of laser cladding of the nickel-based coatings, providing high tribological properties at high temperatures (about 1000 °C) [9; 10]. Methods of obtaining coatings by supersonic electric arc spraying are being studied and improved [11]. According to [12; 13], the most commonly used nickel-phosphorus coatings containing about 10 wt. % of phosphorus in their composition are amorphous after application. A subsequent heat treatment eventually transforms such coatings into a crystalline state which provides the necessary level of properties.

The composite nickel-phosphorus coatings usually have a layered structure, in the surface layer of which there are dispersed particles (silicon carbides, titanium, zirconium, diamond micro-powder [15 – 18]), contributing to the increase in service characteristics. Currently, in the manufacture of critical components used in transportation of oil and gas, the composite nickel-phosphorus coatings with the dispersed silicon carbides are being introduced, which increase the service life of products.

The purpose of this study was to determine the phase composition of the composite nickel-phosphorus coatings with the silicon carbide particles, which provides a high microhardness of more than 1000 HV in combination with a high corrosion resistance in different aggressive media.

Research materials and methodology

We applied a double-layer 60 μm thick nickel-phosphorus coating (Ni-P: 30 μm, Ni-P + silicon carbides: 30 μm), or a single-layer 60 μm thick Ni-P coating to a prepared 300×100 mm, 4 mm thick ground surface made of steel grade 09G2S (EU analog: MnSi5) using the electroless technology with the hypophosphite ions [19; 20]. The single-layer coating composition (% wt.) was as follows: 89.32 – 90.15 Ni; 9.71 – 10.14 P; 0.10 – 0.22 Si; 0.15 – 0.43 Cu. In addition, we also applied the coatings to 3 mm thick ground sheets made of stainless steel grade 08Cr18Ni10Ti (EU analog: X6CrNiTi18-10) in an electroless nickel plating bath. The coatings were subsequently separated by bending for further analysis.

We studied the crystallization of the separated coatings under a continuous heating in a neutral argon atmosphere at rates of 1, 5 and 20 °C/min using a Netzsch STA 449 F1 Jupiter simultaneous thermal analyzer. Then we used the curves obtained by differential scanning calorimetry (DSC) to determine crystallization onset temperatures and to evaluate thermal effects. Under isothermal conditions, the samples of the nickel coatings separated from the substrate were heat-treated according to specified conditions in a LOIP LF-15/11-G1 lab muffle furnace in an oxidizing atmosphere.

We measured the Vickers microhardness at a 100 g load applied to a polished surface of the samples by indenting a diamond indentor on a DuraScan-50 microhardness tester with the ECOS Workflow software. The test procedure was compliant with GOST R ISO 6507-1-2007 (ISO 6507-1:2005). The microhardness measurement error was ±35 HV. We produced flat 20×250×0.06 mm samples of the coating separated from the substrate for tensile testing at a 5 mm/min rate on an Instron electromechanical tensile testing machine with a force of 250 kN. Tensile strength and yield strength measurement error was ±5 MPa, and elongation measurement error was 0.1 %.

The coating resistance to extremely aggressive media was evaluated using the gravimetric method. During the test, the coating was immersed in concentrated acids or their solutions for 24 h at room temperature. Before and after the test, the samples were washed in ethyl alcohol, dried, and weighed with a VLR-200 lab scale ($0{,}25 \cdot 10^{-3}$ g error). The coating weight loss was estimated as a percentage.

The structure of the initial coatings and the coatings after different annealing modes was studied using an Olympus GX-51 inverted microscope. The surface of the prepared sections was etched for 10 s in a mixture of concentrated nitric and acetic acids using the liquid-drop method.

We used a Jeol JSM-7001F Schottky emission scanning electron microscope with an Oxford INCA X-max 80 SDD detector for electron microscopic studies of the structure. The instrument determines the chemical composition of individual structural components and draws distribution patterns of different elements in them.

For *X*-ray diffraction studies, we used a DRON-4-07 diffractometers (iron anode radiation) and Rigaku Ultima IV (copper anode radiation). We applied the Rietveld

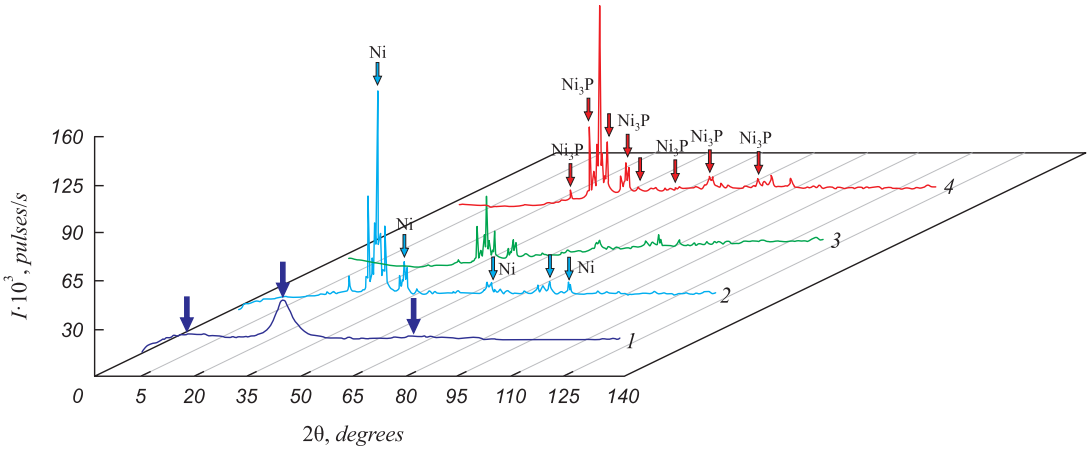

Fig. 1. *X*-ray diffractograms of the composite Ni-P coatings with the silicon carbides annealed at different temperatures and for different soaking time:
1 – without heat treatment; *2* – 450 °C (0.5 h); *3* – 420 °C (1 h); *4* – 390 °C (2 h)

Рис.1. Дифрактограммы композитных покрытий Ni-P + карбиды кремния, подвергнутых отжигу при различных температурах и времени выдержки:
1 – без т/о; *2* – 450 °C (0,5 ч); *3* – 420 °C (1 ч); *4* – 390 °C (2 ч)

method [21] for the qualitative and quantitative phase analysis after optimizing the interference peaks. The accuracy of the quantitative phase analysis was ±5 %. The sizes of the coherent scattering regions (CSRs) were determined by the Williamson–Hall and Halder–Wagner methods [22].

Research results and discussion

It was found that the coatings containing about 10 wt. % of phosphorus and about 1.0 % of the dispersed silicon carbide particles are in an amorphous state after application to steel substrates. The *X*-ray diffractograms of such coatings that were not subjected to heat treatment lack any interference peaks. There are only a few halos (marked with arrows) of different intensity in a wide range of 2θ reflection angles (Fig. 1, curve *1*).

Microhardness of the initial Ni-P coatings is about 400 HV. As 1 % of the silicon carbide particles are added to the solution, it increases to 600 HV. This is also lower than the values of 1000 HV required by the specifications [23]. After application, the strength and plasticity properties of the coatings (refer to Table 1) are low (elongation varies from 0 to 1.5 %).

Heating the nickel-phosphorus coatings leads to crystallization and microhardness increase to the required values (over 1000 HV).

Crystallization onset temperature of the composite Ni-P coating with the silicon carbide particles is above 300 °C during a continuous heating. It largely depends on the heating rate, while a significant exothermic thermal effect changes insignificantly (Fig. 2).

As the samples are heated above the crystallization temperature, the *X*-ray diffractograms show diffraction peaks (see Fig. 1), indicating the formation of crystalline phases in the coating. As our tests showed, after crystallization, in addition to the SiC and Si_5C_3 carbides, the coating contains crystallized nickel, and precipitated Ni_3P compound. The coating structure is homogeneous and fine-grained. The grain size is 6 – 14 μm, and the silicon carbide particle size is 0.5 – 1.5 μm (Fig. 3, *a*).

The crystallization of the Ni-P coating with the silicon carbides develops noticeably under isothermal conditions at a temperature lower than during a continuous heating. For example, it was found that the coatings on a steel substrate contain about 10 % of Ni_3P after 24 h of soaking at 280 °C (refer to Table 2). If the temperature or annealing time is increased, the amount of the precipitated crystalline nickel phosphide reaches almost 70 % (refer to Table 2).

Note that for the coatings containing the dispersed silicon carbide particles, the proportion of these particles did not exceed 1 %. For this reason, we ignored them in the quantitative analysis of the phase composition in the calculation.

Table 1

Mechanical properties of the Ni-P coatings with the silicon carbides separated from the substrate

Таблица 1. **Механические свойства отделенных от подложки Ni-P покрытий с карбидами кремния**

Microhardness, HV	Tensile strength, MPa	Yield strength, MPa	δ, %
before heat treatment			
600	177	172	0 – 1.5
after heat treatment			
1012 – 1080	189	187	0

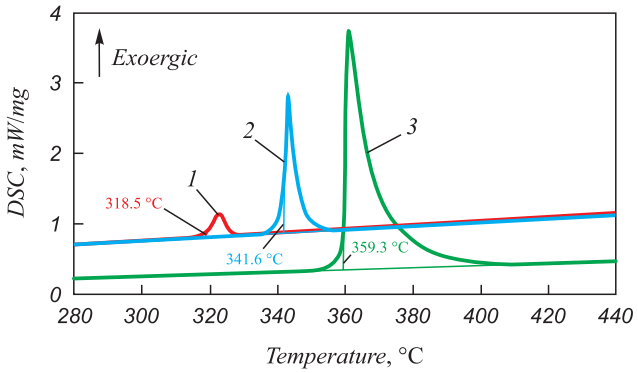

Fig. 2. DSC curves for heating in argon at the following rates: *1* – 1 °C/min (89.1 J/g); *2* – 5 °C/min (87.2 J/g); *3* – 20 °C/min (87.3 J/g)

Рис. 2. Кривые ДСК, полученные при нагреве в аргоне со скоростями: *1* – 1 °C/мин (89,1 Дж/г); *2* – 5 °C/мин (87,2 Дж/г); *3* – 20 °C/мин (87,3 Дж/г)

With the increase in the content of the nickel phosphide in the coating composition after 15 min of soaking at a temperature of 390 °C, microhardness increases from an initial 600 HV to an average of 976 HV, and to 1057 HV after 120 min of soaking, when 71 % Ni_3P is formed (refer to Table 3).

When temperature reaches 420 °C, a similar high hardness of the samples is achieved in a shorter time. For all soaking ranges at the specified temperature, hardness is ensured with consistently obtained values of more than 1000 HV.

As the annealing temperature reaches 450 °C, microhardness is at its maximum after 30 min of soaking. Then it decreases due to phase coagulation and phosphorus burnout from the surface which gets a characteristic bluish hue. For a 24 h soaking period at 280 °C, the formed structure creates the same high hardness HV_{avg} = 1016 (1033; 1004; 1023; 1033; 985) HV.

The coatings with a high microhardness after heat treatment have low yield strength and tensile strength. These values are increased by only 12 – 15 MPa. Heat treatment makes the coatings so brittle that their plasticity drops to zero. Such changes in the coating properties during heat treatment are mainly due to the formation of the brittle nickel phosphide compounds with a high microhardness.

The phosphorus microvolume distribution chart helped us to identify the locations of nickel phosphides. Phosphorus in this coating is part of the Ni_3P compund. Thus, the locations of phosphorus localization indicate that the nickel phosphides are located both inside the grains and along the grain boundaries. After annealing for 1 h at 420 °C, the nickel phosphide precipitates at all grain boundaries. The nickel phosphides inside the grains and along the grain boundaries are indicated by arrows in the electron microscope image (Fig. 3, *b*).

The fine structure of the coatings after crystallization annealing in different modes shows that the SCR sizes determined by the Williamson–Hall and Halder–Wagner methods are close. In crystalline nickel, they vary from 10 to 25 nm (refer to Table 2), while in the nickel phosphide they are slightly larger and range from 15 to 30 nm. As listed in Table 2, the lower the annealing temperature and the shorter the soaking time, the smaller the size of the SCR formed.

Corrosion resistance of the coatings to the effects of different aggressive media (acids and their solutions) is the most important quality metric along with a high hardness. It was found that the studied Ni-P coating with the silicon carbides has the highest corrosion resistance to acetic and orthophosphoric acids, regardless of heat treatment. After daily tests, the most aggressive medium for such coatings is nitric acid, its mixture with other acids, or even its solution diluted with distilled water. The coatings are completely dissolved in nitric acid and its solutions during daily tests (Fig. 4, curve *5*). On the other

Table 2

SCR size, amount of crystalline nickel (C_{Ni}), and percentage of nickel phosphide (C_{Ni_3P}) in the coating after different heat treatment modes

Таблица 2. **Размер ОКР, количество кристаллического никеля (C_{Ni}) и процентное содержание фосфида никеля (C_{Ni_3P}) в покрытии после различных режимов т/о**

Annealing mode	SCR size, nm	C_{Ni}, %	C_{Ni_3P}, %
280 °C – 24 h	13.5	89	10
390 °C – 1.0 h	20.9	75	24
390 °C – 2.0 h	18.7	28	71
420 °C – 0.5 h	16.0	78	21
420 °C – 1.0 h	15.9	34	65
420 °C – 2.0 h	25.5	32	67
450 °C – 0.5 h	18.4	68	31

Table 3

Microhardness of the Ni-P coatings with the silicon carbides after annealing at different temperatures and for different soaking time (τ)

Таблица 3. **Микротвердость покрытий Ni-P + карбиды кремния после отжига при различных температурах и времени выдержки (τ)**

τ, min	Microhardness, HV_{avg}		
	390 °C	420 °C	450 °C
15	976	1047	1002
30	989	1049	1061
60	1047	1062	1021
120	1057	1039	1018

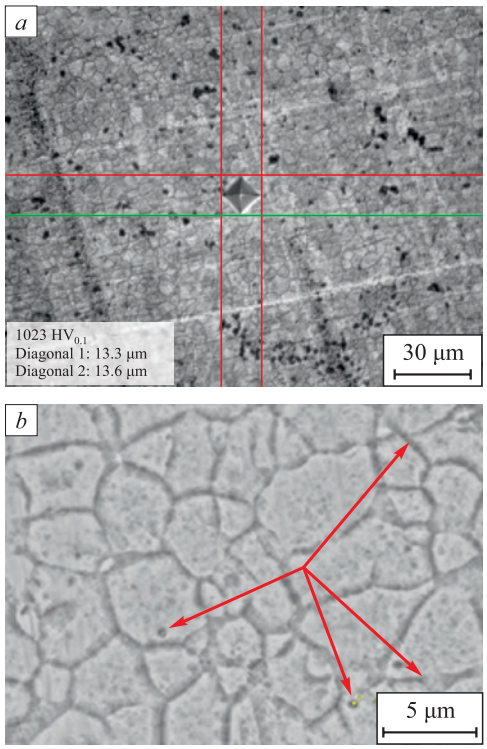

Fig. 3. Microstructure of the Ni-P coating with the silicon carbides after annealing at 420 °C for 1 h:
a – ×400; *b* – SEM, ×5000

Рис. 3. Микроструктура покрытия Ni-P + карбиды кремния после отжига при 420 °C в течение 1 ч:
a – ×400; *b* – РЭМ, ×5000

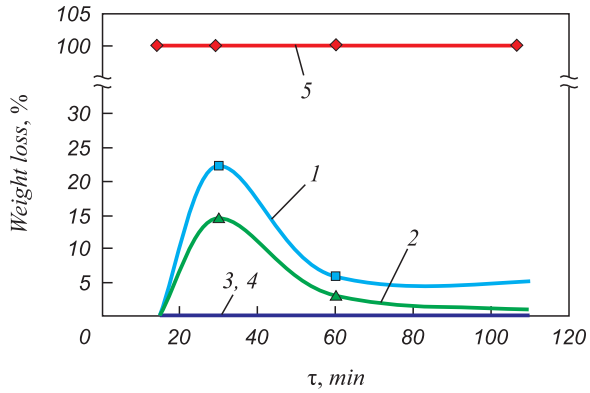

Fig. 4. Weight loss (%) vs. heat treatment period at 390 °C for the Ni-P coatings with the silicon carbides after a 24 h exposure to concentrated hydrochloric (*1*), sulfuric (*2*), acetic (*3*), orthophosphoric (*4*) and nitric (*5*) acids

Рис. 4. Потеря массы в зависимости от времени т/о при 390 °C Ni-P покрытий с карбидами кремния после их суточной выдержки в концентрированных соляной (*1*), серной (*2*), уксусной (*3*), ортофосфорной (*4*) и азотной (*5*) кислотах

hand, the max daily weight loss duting soaking in sulfuric acid is less and amounts to 5.3 %. The weight loss in hydrochloric acid is 11.2 %, which is also less than in nitric acid.

We also found a relationship between corrosion resistance of the Ni-P coatings with the silicon carbides and their quantitative phase composition. Corrosion resistance is at its maximum after 2 h of soaking at 390 °C (Fig. 4) or 1 h of soaking at 420 °C when about 70 % Ni_3P is formed. Its stability is greater than that of pure nickel or its other compounds with phosphorus. The presence of the dispersed silicon carbides decreases the weight loss of the samples compared to the pure Ni-P coating [24]. The introduction of the silicon carbide as a dispersed phase, which creates a barrier effect for the formation of the nickel phosphides, makes it possible to achieve the set goals with the use of a longer treatment at lower temperatures. This also improves main service characteristics of the coating such as a high microhardness and corrosion resistance.

Conclusions

The required 1000 HV of microhardness according to the specifications is achieved in the composite nickel-phosphorus coating with the dispersed silicon carbide particles during a long-term low-temperature annealing with crystallization and the formation of insignificant (10 %) amounts of nickel phosphide.

The revealed dispersed nickel phosphides formed during crystallization and located both inside the grains and along the grain boundaries make a main contribution to the microhardness increase.

A max corrosion resistance of the coatings to different acids combined with a high microhardness is achieved at a high (70 %) nickel phosphide content. Its amount increases with the increase in annealing temperature or time.

With a significant increase in microhardness of the coatings from the initial 600 to the required 1000 HV after crystallization annealing, yield strength and tensile strength increase by only 12 – 15 MPa, and elongation drops to zero due to the formation of brittle nickel phosphide compounds.

Heat treatment of the Ni-P coatings with the silicon carbides forms a homogeneous, fine-grained structure with a grain size of 6 – 14 μm and the SCR size of 10 – 25 nm in nickel, and 15 – 30 nm in the nickel phosphide.

References / Список литературы

1. Moskvitin G.V., Birger E.M., Polyakov A.N., Polyakova G.N. Modern reinforcing coatings of critical parts of mechanisms and tools. *Metalloobrabotka*. 2015; (2(86)): 22–27. (In Russ.).

   Москвитин Г.В., Биргер Е.М., Поляков А.Н., Полякова Г.Н. Современные упрочняющие покрытия критических деталей механизмов и инструмента. *Металлообработка*. 2015; (2(86)): 22–27.
2. Alexis J., Etcheverry B., Beguin J.D., Bonino J.P. Structure, morphology and mechanical properties of electrodeposited composite coatings Ni-P/SiC. *Materials Chemistry and Physics*. 2010; 120: 244–250.
   https://doi.org/10.1016/j.matchemphys.2009.12.013

3. Aslanyan I.R., Shuster L.Sh. Wear of electrolytic Ni-P coatings during sliding friction. *Trudy VIAM*. 2015; (3): 52–61. (In Russ.).

Асланян И.Р., Шустер Л.Ш. Изнашивание электролитических Ni-P покрытий при трении скольжения. *Труды ВИАМ*. 2015; (3): 52–61.

4. Drovosekov A.B., Ivanov M.V., Polyakova O.A., Tsupak T.E. Corrosion properties and protective power of Ni-P coatings. *Gal'vanotekhnika i obrabotka poverkhnosti*. 2011; 19(4): 41–46. (In Russ.).

Дровосеков А.Б., Иванов М.В., Полякова О.А., Цупак Т.Е. Коррозионные свойства и защитная способность химико-каталитических Ni–P покрытий. *Гальванотехника и обработка поверхности*. 2011; 19(4): 41–46.

5. Ahmadkhaniha D., Eriksson F., Leisner P., Zanella C. Effect of SiC particle size and heat-treatment on microhardness and corrosion resistance of Ni-P electrodeposited coatings. *Journal of Alloys and Compounds*. 2018; 769: 1080–1087. https://doi.org/10.1016/j.jallcom.2018.08.013

6. Bahramian A., Eyraud M., Vacandio F., Knauth P. Improving the corrosion properties of amorphous Ni-P thin films using different additives. *Surface and Coatings Technology*. 2018; 345: 40–52. https://doi.org/10.1016/j.surfcoat.2018.03.075

7. Afroukhteh S., Dehghanian C., Emamy M. Preparation of the Ni-P composite coating co-deposited by nano TiC particles and evaluation of its corrosion property. *Applied Surface Science.* 2012; 28(7): 2597–2601. https://doi.org/10.1016/j.apsusc.2011.10.101

8. Ryabchenkov A.V., Ovsyankin V.V., Zot'ev Yu.A. On the effect of heat treatment of chemically nickel-plated steel on composition and protective properties of nickel-phosphorus coatings. *Zashchita metallov*. 1969; 5: 638–642. (In Russ.).

Рябченков А.В., Овсянкин В.В., Зотьев Ю.А. О влиянии термической обработки химически никелированной стали на состав и защитные свойства никель-фосфорных покрытий. *Защита металлов*. 1969; 5: 638–642.

9. Makarov A.V., Korobov Yu.S., Soboleva N.N., Khudorozhkova Yu.V., Vopneruk A.A., Balu P., Barbosa M., Malygina I.Y., Burov S.V., Stepchenkov A.K. Wear resistant nickel-based laser clad coatings for high-temperature applications. *Letters on Materials*. 2019; 9(4): 470–474. https://doi.org/10.22226/2410-3535-2019-4-470-474

10. Makarov A.V., Soboleva N.N., Malygina I.Yu., Osintseva A.L. The formation of NICRBSI–TiC composite coating with increased abrasive wear resistance by gas powder laser cladding. *Uprochnyayushchie tekhnologii i pokrytiya*. 2013; (11): 38–44. (In Russ.).

Макаров А.В., Соболева Н.Н., Малыгина И.Ю., Осинцева А.Л. Формирование композиционного покрытия NiCrBSi–TiC с повышенной абразивной износостойкостью методом газопорошковой лазерной наплавки. *Упрочняющие технологии и покрытия*. 2013; (11): 38–44.

11. Kolomeichenko A.V., Logachev V.N., Deev V.B., Dudareva N.Yu. Properties of coatings obtained by supersonic electric arc metallization with aerosol fluxing. *Izvestiya. Ferrous Metallurgy*. 2022; 65(9): 637–643. (In Russ.). http://doi.org/10.17073/0368-0797-2022-9-637-643

Коломейченко А.В., Логачев В.Н., Деев В.Б., Дударева Н.Ю. Свойства покрытий, полученых сверхзвуковой электродуговой металлизацией с аэрозольным флюсованием. *Известия вузов. Черная металлургия.* 2022; 65(9): 637–643. http://doi.org/10.17073/0368-0797-2022-9-637-643

12. Pillai A.M., Rajendra A., Sharma A.K. Electrodeposited nickel-phosphorous (Ni – P) alloy coating: An in-depth study of its preparation, properties, and structural transitions. *Journal of Coatings Technology and Research*. 2012; 9(6): 785–797. https://doi.org/10.1007/s11998-012-9411-0

13. Buchtík M., Krystýnová M., Másilko J., Wasserbauer J. The effect of heat treatment on properties of Ni-P coatings deposited on AZ91 magnesium alloy. *Coatings*. 2019; 9(7): 461. https://doi.org/10.3390/coatings9070461

14. Gorbunova K.M., Nikiforova A.A. *Physico-Chemical Basics of Chemical Nickel Plating*. Moscow: USSR Academy of Sciences; 1960: 7–194. (In Russ.).

Горбунова К.М., Никифорова А.А. *Физико-химические основы процесса химического никелирования*. Москва: АН СССР; 1960: 7–194.

15. Sotskaya N.V., Dobrozrakova A.D., Aristov I.V., Ryabinina E.I. Features of the formation of composite coatings with inclusion of diamond micro-powder by chemical nickel plating. *Teoriya i praktika sorbtsionnykh protsessov*. 1998; (3): 114–120. (In Russ.).

Соцкая Н.В., Доброзракова А.Д., Аристов И.В., Рябинина Е.И. Особенности образования композиционных покрытий с включением алмазного микропорошка методом химического никелирования. *Теория и практика сорбционных процессов*. 1998; (3): 114–120.

16. Mainier F., Fonseca M.C., Tavares S., Pardal J. Quality of electroless Ni-P coatings applied in oil production equipment with salinity. *Journal of Materials Science and Chemical Engineering*. 2013; 1(06): 1–8. https://doi.org/10.4236/msce.2013.16001

17. Joseph A., Narayanasamy M., Kirybasankar B., Angaiah S. Development of MoS_2 nanosheets embedded nickel composite coating and its mechanical properties. *ES Materials & Manufacturing*. 2018; 2: 2–8. https://www.doi.org/10.30919/esmm5f152

18. Osama F., Radwan A.B., Sliem M.H., Abdullah B.M., Hasan A., Shakoor R.A. Investigating the properties of electrodeposited of Ni-P-ZrC nanocomposite coatings. *ACS Omega*. 2021; 6: 33310–33324. https://doi.org/10.1021/acsomega.1c03117

19. Gorbunova K.M., Ivanov M.V. *Chemical Methods of Metal Deposition (Chemical Nickel Plating and Cobalting): Handbook*. Moscow: Metallurgiya; 1987: 365–401. (In Russ.).

Горбунова К.М., Иванов М.В. *Химические методы осаждения металлов (химическое никелирование и кобальтирование: Справочник*. Москва: Металлургия; 1987: 365–401.

20. Gamburg Yu.D. *Chemical Nickel Plating (Obtaining Nickel–Phosphorus Coatings by Electrocatalytic Reduction with Hypophosphite)*. Moscow: RAS; 2020: 82. (In Russ.).

Гамбург Ю.Д. *Химическое никелирование (получение никель-фосфорных покрытий путем электрокаталитического восстановления гипофосфитом)*. Москва: РАН; 2020: 82.

21. Krzhizhanovskaya M.G., Firsova V.A., Bubnova R.S. *Application of the Rietveld Method for Solving Problems of Powder Diffractometry. Manual*. St. Petersburg University; 2016: 67. (In Russ.).

Кржижановская М.Г., Фирсова В.А., Бубнова Р.С. *Применение метода Ритвельда для решения задач порошковой дифрактометрии: Учебное пособие*. Санкт-Петербургский университет; 2016: 67.

22. Izumi F., Ikeda T. Implementation of the Williamson–Hall and Halder–Wagner methods into RIETAN-FP. *Annual Report of Advanced Ceramics Research Center*. 2014; 3: 33–38.

23. Goikhenberg Yu.N., Polukhin D.S Structure, properties and quality of composite nickel-phosphorus coating applied to steel substrates of various composition. *Chernye metally*. 2022; (4): 46–49. (In Russ.).
http://doi.org/10.17580/chm.2022.04.08

Гойхенберг Ю.Н., Полухин Д.С. Структура, свойства и качество композитного никель-фосфорного покрытия, наносимого на стальные подложки различного состава. *Черные металлы*. 2022; (4): 46–49.
http://doi.org/10.17580/chm.2022.04.08

24. Polukhin D.S., Goikhenberg Yu.N., Bodrov E.G. Corrosion resistance of composite nickel-phosphorus coating in various aggressive media. *Voprosy materialovedeniya*. 2022; (3(111)): 98–108. (In Russ.).
http://doi.org/10.22349/1994-6716-2022-111-3-98-108

Полухин Д.С., Гойхенберг Ю.Н., Бодров Е.Г. Коррозионная стойкость композитного никель-фосфорного покрытия в различных агрессивных средах. *Вопросы материаловедения*. 2022; (3(111)): 98–108.
http://doi.org/10.22349/1994-6716-2022-111-3-98-108

Information about the Authors / Сведения об авторах

Yurii N. Goikhenberg, *Dr. Sci. (Eng.), Senior Researcher, Prof. of the Chair of Materials Science and Physical Chemistry of Materials,* South Ural State University
E-mail: goikhenbergyn@susu.ru

Dmitrii S. Polukhin, *Executive Director,* LLC "Scientific and Technical Centre KONAR"
E-mail: polukhin.dmitriy@konar.ru

Dmitrii A. Zherebtsov, *Dr. Sci. (Chem.), Senior Researcher of the Chair of Materials Science and Physical Chemistry of Materials,* South Ural State University
E-mail: zherebtcovda@susu.ru

Evgenii G. Bodrov, *Director,* LLC "Scientific and Technical Centre KONAR"
E-mail: bodrov.evgeniy@konar.ru

Юрий Нафтулович Гойхенберг, *д.т.н., старший научный сотрудник, профессор кафедры «Материаловедение и физико-химия материалов»,* Южно-Уральский государственный университет
E-mail: goikhenbergyn@susu.ru

Дмитрий Сергеевич Полухин, *исполнительный директор,* ООО «Научно-технический центр КОНАР»
E-mail: polukhin.dmitriy@konar.ru

Дмитрий Анатольевич Жеребцов, *д.х.н., старший научный сотрудник кафедры «Материаловедение и физико-химия материалов»,* Южно-Уральский государственный университет
E-mail: zherebtcovda@susu.ru

Евгений Геннадьевич Бодров, *директор,* ООО «Научно-технический центр КОНАР»
E-mail: bodrov.evgeniy@konar.ru

Contribution of the Authors / Вклад авторов

Yu. N. Goikhenberg – determination of the conceptual research direction, literary review, consolidation of experimental data, joint interpretation of the results, formulation of the conclusions.

D. S. Polukhin – preparation of the research material, literary review, performing studies on mechanical properties and corrosion resistance, joint interpretation of the results, formulation of the conclusions.

D. A. Zherebtsov – development and coordination of the experimental work, joint interpretation of the results, formulation of the conclusions.

E. G. Bodrov – performing X-ray diffraction and electron microscopic studies, joint interpretation of the results, formulation of the conclusions.

Ю. Н. Гойхенберг – определение концептуального направления исследования и перечня используемой литературы; консолидация экспериментальных данных; совместная интерпретация результатов и формулировка выводов.

Д. С. Полухин – подготовка материала исследования, изучение и формирование перечня цитируемой литературы; выполнение исследований по механическим свойствам и коррозионной стойкости; совместная интерпретация результатов и формулировка выводов.

Д. А. Жеребцов – разработка и согласование плана и методики выполнения экспериментальной части работы с другими участниками; совместная интерпретация результатов и формулировка выводов.

Е. Г. Бодров – выполнение рентгеноструктурных и электронно-микроскопических исследований; совместная интерпретация результатов и формулировка выводов.

Received 03.11.2022
Revised 23.12.2022
Accepted 30.12.2022

Поступила в редакцию 03.11.2022
После доработки 23.12.2022
Принята к публикации 30.12.2022

MATERIAL SCIENCE / МАТЕРИАЛОВЕДЕНИЕ

UDC 669.539.382:669.17:625.1:539.4
DOI 10.17073/0368-0797-2023-1-50-56

Original article
Оригинальная статья

TRANSFORMATION OF FINE STRUCTURE OF LAMELLAR PEARLITE UNDER DEFORMATION OF RAIL STEEL

V. E. Gromov [1], K. V. Aksenova [1] ✉, Yu. F. Ivanov [2], R. V. Kuznetsov [1], V. E. Kormyshev [1]

[1] **Siberian State Industrial University** (42 Kirova Str., Novokuznetsk, Kemerovo Region – Kuzbass 654007, Russian Federation)
[2] **Institute of High Current Electronics, Siberian Branch of the Russian Academy of Sciences** (2/3 Akademicheskii Ave., Tomsk 634055, Russian Federation)

✉ 19krestik91@mail.ru

Abstract. The defective substructure of polycrystalline bodies preconditions substructural hardening and mechanical properties. Pearlite, which is the main structural component of rails, is subjected under deformation to considerable transformation accompanied by a number of processes. In the present work, methods of the modern physical materials science were used to study and analyze the defective substructure of pearlite with lamellar morphology and properties of rail steel subjected to fracture under the conditions of uniaxial tensile strain of flat samples. It was established that the ultimate strength changes from 1247 to 1335 MPa, and the relative strain-to-fracture is from 0.69 to 0.75. The formation of three zones of the fracture surface is observed: fibrous, radial and shear zones. Their shapes and sizes have been analyzed. The deformation of rail steel is accompanied by fracture of cementite plates of pearlite colonies and re-precipitation of nanosized particles of tertiary cementite about 8.3 nm in size in the volume of ferrite plates. The main mechanisms of cementite plate fracture are cutting and dissolution. Dislocation substructure is represented by chaotic distribution of dislocations and their clusters. Scalar density of dislocations in ferrite increases from 3.2·1010 cm-2 in the initial state to $7.9 \cdot 10^{10}$ cm^{-2} at failure. Deformation is accompanied by the formation of internal stress fields which manifest themselves as bending contours of extinction. The sources of stress fields are the interfaces of cementite and ferrite plates as well as grain interfaces. Fragmentation of ferrite and cementite plates has been revealed. The average size of cementite fragments is 9.3 nm. In the fracture zone of the rail steel sample, rotation of pearlite grains has been noted, indicating the presence of a rotational mode of strain. The electron microscopic images of cementite plates show a change in the contrast, which may be related to formation of the Cottrell atmospheres.

Keywords: fine structure, perlite, strain by uniaxial tension, evolution, cementite, fragmentation

Acknowledgments: The work was supported by a grant of the Russian Foundation for Fundamental Research (project No. 19-32-60001) and the scholarship of the President of the Russian Federation for young scientists and postgraduate students carrying out promising scientific research and developments in priority areas of modernization of the Russian economy (project SP-4517.2021.1).
The authors express their gratitude to E.A. Polevoi for providing the samples of rail steel and N.A. Popova for participation in discussion of the experimental results.

For citation: Gromov V.E., Aksenova K.V., Ivanov Yu.F., Kuznetsov R.V., Kormyshev V.E. Transformation of fine structure of lamellar pearlite under deformation of rail steel. *Izvestiya. Ferrous Metallurgy*. 2023; 66(1): 50–56. https://doi.org/10.17073/0368-0797-2023-1-50-56

ТРАНСФОРМАЦИЯ ТОНКОЙ СТРУКТУРЫ ПЛАСТИНЧАТОГО ПЕРЛИТА ПРИ ДЕФОРМАЦИИ РЕЛЬСОВОЙ СТАЛИ

В. Е. Громов [1], К. В. Аксёнова [1] ✉, Ю. Ф. Иванов [2], Р. В. Кузнецов [1], В. Е. Кормышев [1]

[1] **Сибирский государственный индустриальный университет** (Россия, 654007, Кемеровская обл. – Кузбасс, Новокузнецк, ул. Кирова, 42)
[2] **Институт сильноточной электроники Сибирского отделения РАН** (Россия, 634055, Томск, пр. Академический 2/3)

✉ 19krestik91@mail.ru

Аннотация. Дефектная субструктура поликристаллических тел обуславливает субструктурное упрочнение и механические свойства. Перлит, являющийся основной структурной составляющей рельсов, при деформационном воздействии подвергается значительному преобразованию, которое сопровождается целым рядом процессов. В настоящей работе методами современного физического

материаловедения проведены исследования и анализ дефектной субструктуры перлита пластинчатой морфологии и свойств рельсовой стали, подвергнутой разрушению в условиях деформации одноосным растяжением плоских образцов. Установлено, что предел прочности изменяется от 1247 до 1335 МПа, а относительная деформация до разрушения – от 0,69 до 0,75. Наблюдается формирование трех зон поверхности разрушения: волокнистой, радиальной и зоны среза. Проанализированы их форма и размеры. Деформация рельсовой стали сопровождается разрушением пластин цементита колоний перлита и повторным выделением в объеме пластин феррита наноразмерных частиц третичного цементита размером приблизительно 8,3 нм. Основными механизмами разрушения пластин цементита являются разрезание и растворение. Дислокационная субструктура представлена хаотическим распределением дислокаций и их скоплениями. Скалярная плотность дислокаций в феррите увеличивается от $3{,}2 \cdot 10^{10}$ см$^{-2}$ в исходном состоянии до $7{,}9 \cdot 10^{10}$ см$^{-2}$ при разрушении. Деформация сопровождается формированием внутренних полей напряжений, проявляющихся в виде изгибных контуров экстинкции. Источниками полей напряжений являются границы раздела пластин цементита и феррита, а также границы зерен. Выявлена фрагментация пластин феррита и цементита. Средние размеры фрагментов цементита составляют 9,3 нм. В зоне разрушения образца рельсовой стали отмечено вращение зерен перлита, свидетельствующее о наличии ротационной моды деформации. На электронно-микроскопических изображениях пластин цементита наблюдается изменение контраста, что может быть связано с образованием атмосфер Коттрелла.

Ключевые слова: тонкая структура, перлит, деформация, эволюция, цементит, фрагментация

Благодарности: Работа выполнена при поддержке Российского фонда фундаментальных исследований (грант № 19-32-60001) и стипендии Президента Российской Федерации для молодых ученых и аспирантов, осуществляющих перспективные научные исследования и разработки по приоритетным направлениям модернизации российской экономики (проект СП-4517.2021.1).
Выражаем благодарность Е.А. Полевому за предоставленные образцы рельсовой стали и Н.А. Поповой за помощь в обсуждении результатов эксперимента.

Для цитирования: Громов В.Е., Аксёнова К.В., Иванов Ю.Ф., Кузнецов Р.В., Кормышев В.Е. Трансформация тонкой структуры пластинчатого перлита при деформации рельсовой стали. *Известия вузов. Черная металлургия*. 2023; 66(1): 51–56.
https://doi.org/10.17073/0368-0797-2023-1-50-56

Introduction

One of the basic and most general types of strengthening of polycrystalline bodies is substructural, caused by the defective substructure. This largely determines the mechanical properties of materials. The nucleation and development of microcracks in plastic materials are closely related to the substructure evolution [1, 2].

Significant increase in the intensity of railway traffic and traffic concentration requires high operational durability of rails made of pearlitic steel. During operation, rails are subjected to significant strain effects, accompanied by evolution of the structural-phase state of pearlite [3, 4]. Importance of the information in this field is determined by the depth of understanding the fundamental issues of the physical materials science, on the one hand, and the practical importance, on the other hand. The practical importance is connected with the creation of high-quality rails with high performance properties, ensuring accident-free operation with a passing tonnage of more than 2 billion tons (gross). Creation of special types of rails for high-speed railways, low-temperature reliability, and increased contact-fatigue endurance requires a study of the dependence of hardening on the structural state of rails before strain and establishing cause-effect relations between the phenomena that determine the strain behavior [3, 4].

In the initial state, rails contain about 70 % of pearlite of lamellar morphology [5 – 7], the deformation of which is accompanied by a complex transformation of ferrite and cementite [8, 9] usually observed by transmission electron microscopy. Main attention is paid to the strain-induced fracture of cementite [10 – 12] which leads to an increase in the carbon concentration in ferrite and an additional hardening mechanism [13].

The purpose of the present work was to analyze the defective substructure of pearlite of rail steel lamellar morphology, fractured under the conditions of uniaxial tensile strain of flat samples.

Research materials and methods

Samples of rail steel, the properties and elementary composition of which are regulated by GOST R 51685–2013, were used as the research material. The chemical composition of rails of DT350 category, % (wt.) was as follows: C 0.73; Mn 0.75; Si 0.58; P 0.012; S 0.007; Cr 0.42; Ni 0.07; Cu 0.13; Ti 0.003; Mo 0.006; V 0.04; Al 0.003; Ti 0.008; and the rest was iron.

Mechanical tests were performed by uniaxial tensioning of flat proportional samples in the form of double-sided blades with the dimensions of the working area of the blades of 1.5×4.45×8.0 mm. Samples were cut from the head of 100-meter differentially hardened rails of DT350 category produced by JSC “EVRAZ – Joint West Siberian Metallurgical Plant”. Uniaxial tensile strain was applied on an Instron 3369 testing machine at a loading rate of 1.2 mm/min.

The structure of the fracture surface was studied by scanning electron microscopy (SEM 515 Philips device). The steel deformed substructure in the fracture zone was studied by transmission electron diffraction microscopy (thin-foil method) (JEM-2100 JEOL device) [14 – 16]. Foil for the transmission electron microscope was made by ion thinning (Ion Slicer EM-091001S installation, thinning achieved by argon ions) of plates cut from fractured

samples on the Isomet Low Speed Saw installation perpendicular to the fracture surface. The methods for measuring the scalar and excess dislocation densities did not differ from those described in [3, 4].

Results and discussion

The tests showed that tensile strength varied in the range from 1247 to 1335 MPa, and strain of the samples at failure ranged from 0.69 to 0.75. As a rule, under tensile strain of the samples three zones are formed on the fracture surface: a fibrous zone (central part of the specimen); the radial zone following it; and the shear zone along the edge of the sample [17]. The fibrous zone is elliptical in shape with a large axis parallel to the long sides of the rectangle. The radial zone of the samples, whose width is much greater than their thickness, has a chevron or herringbone shape. Chevron patterns are often associated with unstable, relatively rapid crack propagation. The appearance of a chevron pattern is caused by the mismatch between the general direction of crack propagation and the shortest direction from the crack front to the free surface. In this case, radial scars propagate towards the free surface, forming chevron patterns [17]. The vertices of V-shaped chevrons are directed away from the fracture center.

Previously, it was shown in [2 – 4, 18] that the following components are distinguished in the structure of the steel studied according to the morphological feature: pearlite grains of lamellar morphology, grains of ferrite-carbide mixture (irregular pearlite grains) and grains of structurally free ferrite (ferrite grains with no carbide phase particles in their volume). The main type of structure of the steel under study is lamellar pearlite grains, the relative content of which in the material is 0.7. The relative content of ferrite-carbide mixture grains is 0.27; and the rest are grains of structurally free ferrite.

As a rule, the structure of lamellar pearlite is represented by alternating ferrite plates (solid solution based on iron crystal body-centered lattice) and cementite plates (iron carbide of Fe_3C composition, orthorhombic crystal lattice) [19]. Fracture of steel under uniaxial tension conditions in flat samples does not change the morphology of the material. In the fracture zone and away from it, grains with a lamellar structure characteristic of pearlite are present. Change in the steel structure is detected at the level of the defective subsystem and is accompanied by multiple pearlite transformation.

When considering the transformation of the ferrite plate structure, it was found that ferrite plates of pearlite colonies fragment, i.e., they split into the regions separated by low-angle boundaries. Deformation is accompanied by the formation of a dislocation substructure in the volume of ferrite plates (Fig. 1). Dislocations are distributed chaotically or form clusters. The scalar density of dislocations is $7.9 \cdot 10^{10}$ cm^{-2}, $3.2 \cdot 10^{10}$ cm^{-2} in the initial state.

Deformation of steel is accompanied by the formation of stress fields in the sample. When the material is studied by electron microscopy of thin foils, the internal stress fields appear as bending contours of extinction, located mainly in ferrite plates. The sources of stress fields in the surveyed steel are the interfaces of cementite and ferrite plates (Fig. 2), as well as grain interfaces. It should be noted that the tensile stress of the steel studied is accompanied by pearlite grain rotation, which is most pronounced in the fracture zone of the samples (Fig. 2). The latter suggests the presence of a rotational mode

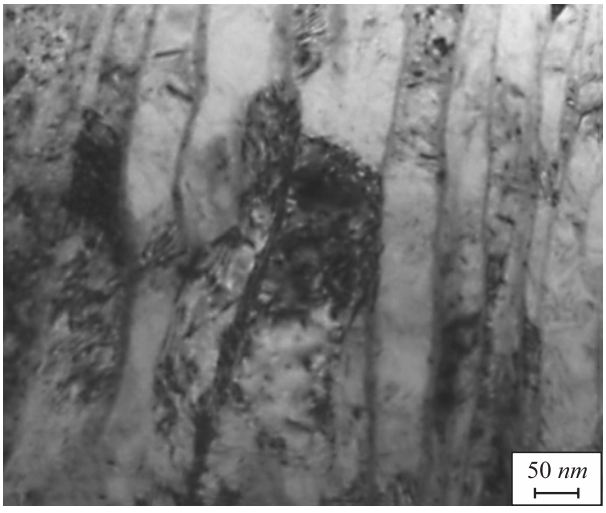

Fig. 1. Electron microscopic image of dislocation substructure of rail steel ferrite plates

Рис. 1. Электронно-микроскопическое изображение дислокационной субструктуры пластин феррита рельсовой стали

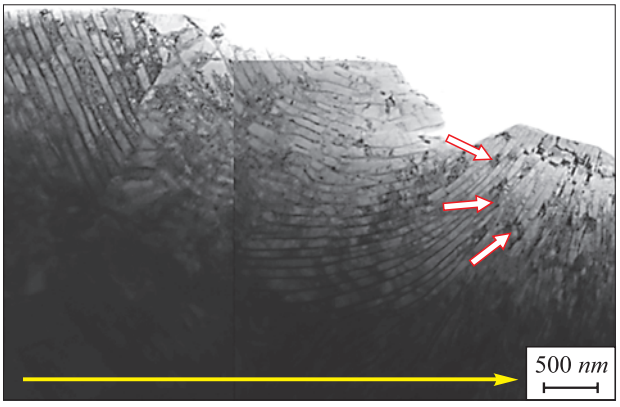

Fig. 2. Electron microscopic image of pearlite grain structure in the fracture zone; curved contours of extinction are shown with arrows (the long arrow indicates the direction of specimen stretching (longitudinal axis of the sample))

Рис. 2. Электронно-микроскопическое изображение структуры зерен перлита в зоне разрушения; стрелками указаны изгибные контуры экстинкции (длинной стрелкой обозначено направление растяжения образца (продольная ось образца))

of strain in the fracture zone of the specimen [20 – 22], associated with the formation of local lattice curvature. In this connection, it can be assumed that the development of a similar effect in rail steel makes it easier to move the carbon atoms.

Deformation of the steel under study is accompanied by the fracture of cementite plates. Two possible mechanisms of cementite plates fracture are discussed in the scientific literature: cutting and dissolution [2, 3, 13]. Dissolution of cementite plates occurs due to greater binding energy of dislocations with carbon atoms (~0.6 – 0.7 eV) compared to the binding energy of carbon atoms in the cementite lattice [23 – 25]. According to the results of [26], an increase in free energy caused by geometric thinning of cementite plates and the formation of slip bands destabilizes the cementite and ensures its fracture. A similar thermodynamic model based on the Gibbs–Thomson effect and the diffusion controlled process of dissolution is proposed in [27]. Carbon atoms are carried out by moving dislocations into the volume of ferrite plates with the subsequent formation of nanosized particles of iron carbide (Fig. 3). The average size of the particles located in the ferrite plates is 8.3 nm. Particles of this size are most clearly detected by dark-field analysis (Fig. 3, *b*).

Dissolution of cementite is accompanied by the formation of a region of material around the plates which differs from the main grain volume in contrast (Fig. 4, *a*). It can be assumed that the change in the contrast is caused by a change in the chemical composition of the material surrounding the cementite plate, namely, an increased concentration of carbon. The carbon atoms pulled out of the cementite by dislocations are capable of forming Cottrell atmospheres, leading to a change in contrast.

Along with dissolution, the plastic yield of steel is accompanied by fragmentation of cementite plates. It was found that in the fracture zone of samples the cementite plates, while retaining their original morphology, break into regions of coherent dispersion, the average size of which is 9.3 nm (Fig. 5).

Conclusion

The methods of the modern physical materials science were used to study the mechanical properties, defective substructure of pearlite with lamellar morphology, and fracture surface of rail steel subjected to fracture under the conditions of uniaxial tensile stress. It was also established that the ultimate tensile strength varies from 1247 to 1335 MPa. The fracture strain of the samples ranges from 0.69 to 0.75. The formation of three zones of the fracture surface has been detected: fibrous, radial and shear zones. It has been demonstrated that the steel strain is accompanied by fragmentation of ferrite plates with low-angle boundaries and a significant increase in the scalar dislocation density to $7.9 \cdot 10^{10}$ cm^{-2} (the scalar dislocation density of the initial steel is $3.2 \cdot 10^{10}$ cm^{-2}). The fracture of cementite plates by cutting and dissolution mechanisms was established with subsequent removal of carbon by moving dislocations to the ferrite plates volume with the formation of nanosized (8.3 nm) round-shaped tertiary cementite particles in them. Thermody-

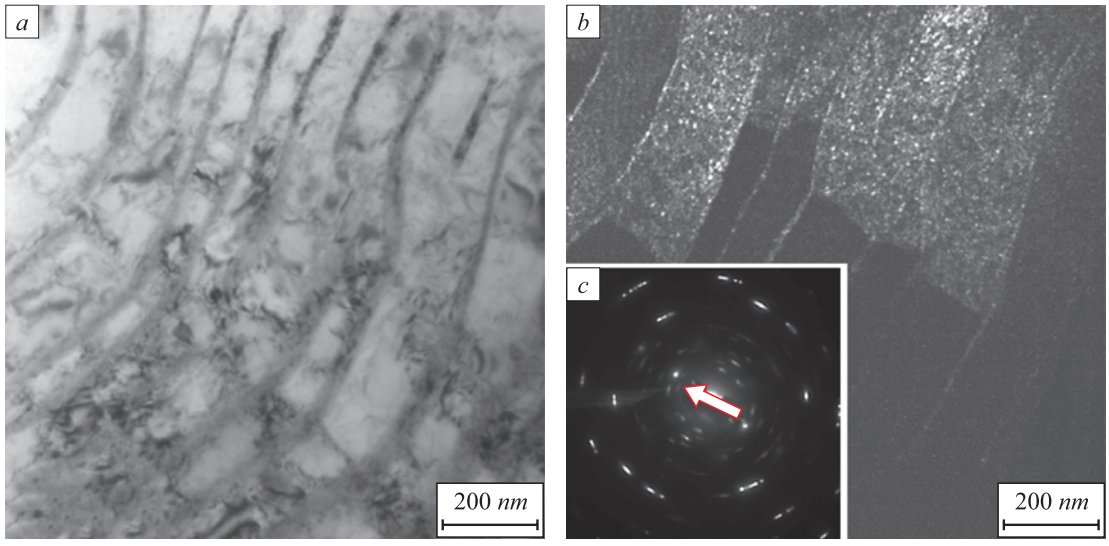

Fig. 3. Electron microscopic image of nanosized cementite particles formed in ferrite plates of rail steel:
a – light field; *b* – dark field obtained in reflex [110]α-Fe + [121]Fe_3C; *c* –micro diffraction pattern
(the arrow shows a reflex in which the dark-field image was obtained (*b*))

Рис. 3. Электронно-микроскопическое изображение наноразмерных частиц цементита, образовавшихся в пластинах феррита рельсовой стали:
a – светлое поле; *b* – темное поле, полученное в рефлексе [110]α-Fe + [121]Fe_3C; *c* – микроэлектронограмма
(стрелкой показан рефлекс, в котором получено темнопольное изображение (*b*))

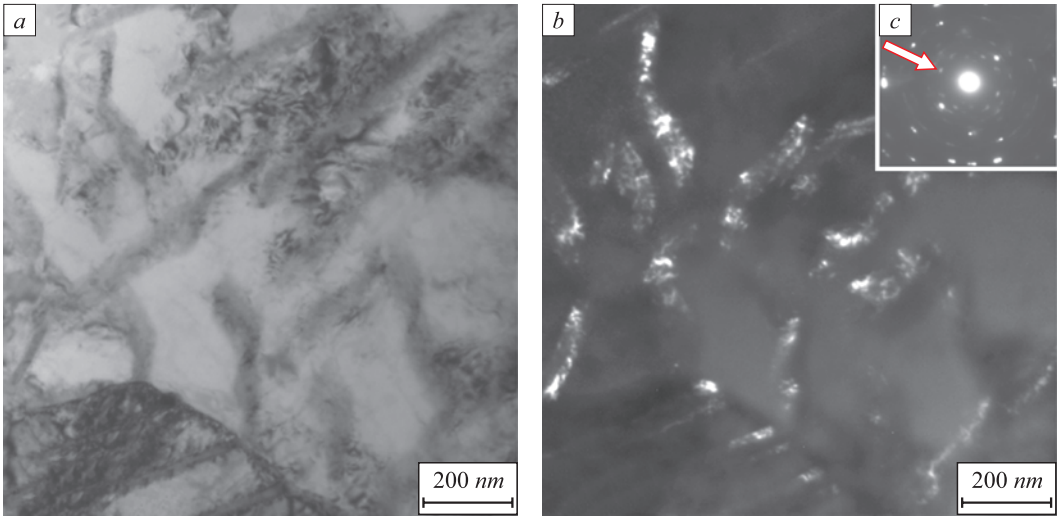

Fig. 4. Electron microscopic image of rail steel structure near cementite plates:
a – light field; *b* – dark field obtained in reflex [230]Fe_3C; *c* – micro diffraction pattern
(the arrow indicates a reflex in which the dark-field image was obtained (*b*))

Рис. 4. Электронно-микроскопическое изображение структуры рельсовой стали возле пластин цементита:
a – светлое поле; *b* – темное поле, полученное в рефлексе [230]Fe_3C; *c* – микроэлектронограмма
(стрелкой показан рефлекс, в котором получено темнопольное изображение (*b*))

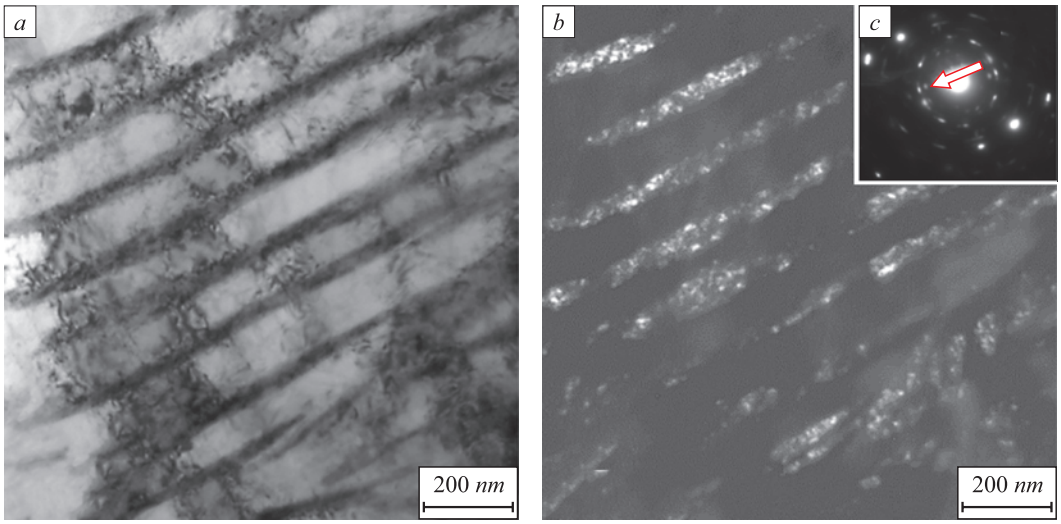

Fig. 5. Electron microscopic image of fragmented structure of cementite:
a – light field; *c* – dark field obtained in reflex [110]α-Fe + [121]Fe_3C; *c* – micro diffraction pattern
(the arrow shows a reflex in which the dark-field image was obtained (*c*))

Рис. 5. Электронно-микроскопическое изображение фрагментированной структуры цементита:
a – светлое поле; *c* – темное поле, полученное в рефлексе [110]α-Fe + [121]Fe_3C; *c* – микроэлектронограмма
(стрелкой показан рефлекс, в котором получено темнопольное изображение (*c*))

namic models of cementite fracture are discussed. It was shown that the dissolution of cementite plates is accompanied by their fragmentation (division into coherent diffusion regions with the average size of 9.3 nm).

References / Список литературы

1. Koneva N.A., Trishkina L.I., Kozlov E.V. Physics of substructural and grain-bound hardening. *Fundamental problems of modern materials science*. 2014; 11(1): 40–49. (In Russ.).

Конева Н.А., Тришкина Л.И., Козлов Э.В. Физика субструктурного и зернограничного упрочнения. *Фундаментальные проблемы современного материаловедения*. 2014; 11(1): 40–49.

2. Ivanov Yu.F., Gromov V.E., Popova N.A., Konovalov S.V., Koneva N.A. *Structural-Phase State and Mechanisms of Hardening of Deformed Steel.* Novokuznetsk: Polygraphist; 2016: 510. (In Russ.).

Структурно-фазовое состояние и механизмы упрочнения деформированной стали / Ю.Ф. Иванов, В.Е. Гро-

мов, Н.А. Попова, С.В. Коновалов, Н.А. Конева. Новокузнецк: Полиграфист; 2016: 510.

3. Yuriev A.A., Ivanov Yu.F., Gromov V.E., Rubannikova Yu.A., Starostenkov M.D., Tabakov P.Y. *Structure and Properties of Lengthy Rails after Extreme Long-Term Operation*. USA: Materials Research Forum LLC; 2021: 190.
4. Gromov V.E., Peregudov O.A., Ivanov Yu.F., Konovalov S.V., Yur'ev A.A. *Evolution of Structural-Phase States of Metal Rails during Long-Term Operation*. Novosibirsk: Publishing House of SB RAS; 2017: 164. (In Russ.).

   Эволюция структурно-фазовых состояний металла рельсов при длительной эксплуатации / В.Е. Громов, О.А. Перегудов, Ю.Ф. Иванов, С.В. Коновалов, А.А. Юрьев. Новосибирск: Изд-во СО РАН; 2017: 164.
5. Hong M.H., Reynolds W.T., Tarui T., Hono K. Atom probe and transmission electron microscopy investigations of heavily drawn pearlitic steel wire. *Metallurgical and Materials Transactions A*. 1999; 30(3): 717–727. https://doi.org/10.1007/s11661-999-1003-y
6. Hono K., Ohnuma M., Murayama M., Nishida S., Yoshie A., Takahashi T. Cementite decomposition in heavily drawn pearlite steel wire. *Scripta Materialia*. 2001; 44(6): 977–983. https://doi.org/10.1016/S1359-6462(00)00690-4
7. Taniyama A., Takayama T., Arai M., Hamada T. Structure analysis of ferrite in deformed pearlitic steel by means of X-ray diffraction method with synchrotron radiation. *Scripta Materialia*. 2004; 51(1): 53–58. https://doi.org/10.1016/j.scriptamat.2004.03.018
8. Goto S., Kirchheim R., Al-Kassab T., Borchers C. Application of cold drawn lamellar microstructure for developing ultra-high strength wires. *Transactions of Nonferrous Metals Society of China*. 2007; 17(6): 1129–1138. https://doi.org/10.1016/S1003-6326(07)60238-6
9. Borchers C., Al-Kassab T., Goto S., Kirchheim R. Partially amorphous nanocomposite obtained from heavily deformed pearlitic steel. *Materials Science and Engineering: A.* 2009; 502(1-2): 131–138. https://doi.org/10.1016/j.msea.2008.10.018
10. Read H.G., Reynolds Jr. W.T, Hono K., Tarui T. APFIM and TEM studies of drawn pearlitic wire. *Scripta Materialia*. 1997; 37(8): 1221–1230. https://doi.org/10.1016/S1359-6462(97)00223-6
11. Maruyama N., Tarui T., Tashiro H. Atom probe study on the ductility of drawn pearlitic steels. *Scripta Materialia*. 2002; 46(8): 599–603. https://doi.org/10.1016/S1359-6462(02)00037-4
12. Tarui T., Maruyama N., Takahashi J., Nishida S., Tashiro H. Microstructure control and strengthening of high-carbon steel wires. *Nippon Steel Technical Report*. 2005; 91: 56–61.
13. Danoix F., Julien D., Sauvage X., Copreaux J. Direct evidence of cementite dissolution in drawn pearlitic steels observed by tomographic atom probe. *Materials Science and Engineering: A*. 1998; 250(1): 8–13. https://doi.org/10.1016/S0921-5093(98)00529-2
14. Egerton F.R. *Physical Principles of Electron Microscopy*. Basel: Springer International Publishing; 2016: 196. https://doi.org/10.1007/978-3-319-39877-8
15. Kumar C.S.S.R. *Transmission Electron Microscopy. Characterization of Nanomaterials*. New York: Springer; 2014: 717. https://doi.org/10.1007/978-3-642-38934-4
16. Carter C.B., Williams D.B. *Transmission Electron Microscopy*. Berlin: Springer International Publishing; 2016: 518.
17. *Fractography and Atlas of Fractograms. Reference book*. Fellows J. ed. Moscow: Metallurgiya; 1982: 489. (In Russ.).

   Фрактография и атлас фрактограмм. Справ. изд. / Пер. с англ.; под ред. Дж. Феллоуза. М.: Металлургия; 1982: 489.
18. Kuznetsov R.V., Gromov V.E., Ivanov Yu.F., Kormyshev V.E., Shlyarova Yu.A., Polevoi E.V., Yur'ev A.A. Evolution of structural-phase states and properties of differentially hardened rails during extremely long-term operation. Message 4. Formation of gradients of the structural-phase state of the metal of the rail head along the central axis after the missed tonnage of 1770 million tons gross. *Problemy chernoi metallurgii i materialovedeniya*. 2021; 3: 37–46. (In Russ.).

   Кузнецов Р.В., Громов В.Е., Иванов Ю.Ф., Кормышев В.Е., Шлярова Ю.А., Полевой Е.В., Юрьев А.А. Эволюция структурно-фазовых состояний и свойств дифференцированно закаленных рельсов при экстремально длительной эксплуатации. Сообщение 4. Формирование градиентов структурно-фазового состояния металла головки рельсов по центральной оси после пропущенного тоннажа 1770 млн т брутто. *Проблемы черной металлургии и материаловедения*. 2021; 3: 37–46.
19. Schastlivtsev V.M., Mirzaev D.A., Yakovleva I.L., Okishev K.Yu., Tabatchikova T.I., Khlebnikova Yu.V. *Perlite in Carbon Steels*. Yekaterinburg: UB RAS; 2006: 312. (In Russ.).

   Перлит в углеродистых сталях / В.М. Счастливцев, Д.А. Мирзаев, И.Л. Яковлева, К.Ю. Окишев, Т.И. Табатчикова, Ю.В. Хлебникова. Екатеринбург: УрО РАН; 2006: 312.
20. Panin V.E., Egorushkin V.E., Panin A.V., Chernyavskii A.G. Plastic distortion as a fundamental mechanism in nonlinear mesomechanics of plastic deformation and fracture. *Physical Mesomechanics*. 2016; 19(3): 255–268. https://doi.org/10.1134/S1029959916030048
21. Panin V.E., Egorushkin V.E., Panin A.V. Nonlinear wave processes in a deformable solid as in a multiscale hierarchically organized system. *Uspekhi fizicheskikh nauk*. 2012; 182(12): 1351–1357. (In Russ.). https://doi.org/10.3367/UFNr.0182.201212i.1351

   Панин В.Е., Егорушкин В.Е., Панин А.В. Нелинейные волновые процессы в деформируемом твердом теле как многоуровневой иерархически организованной системе. *Успехи физических наук*. 2012; 182(12): 1351–1357. https://doi.org/10.3367/UFNr.0182.201212i.1351
22. Grigorovich K.V., Gromov V.E., Kuznetsov R.V., Ivanov Yu.F., Shlyarova Yu.A. Formation of a thin structure of pearlite steel under ultra-long plastic deformation. *Doklady Rossiiskoi akademii nauk. Fizika, tekhnicheskie nauki*. 2022; 503(41): 69–72. (In Russ.). https://doi.org/10.31857/S2686740022020079

   Григорович К.В., Громов В.Е., Кузнецов Р.В., Иванов Ю.Ф., Шлярова Ю.А. Формирование тонкой структуры перлитной стали при сверхдлительной пластической деформации. *Доклады Российской академии наук. Физика, технические науки.* 2022; 503(41): 69–72. https://doi.org/10.31857/S2686740022020079

23. Li Y.J., Choi P., Borchers C., Westerkamp S., Goto S., Raabe D., Kirchheim R. Atomic-scale mechanisms of deformation-induced cementite decomposition in pearlite. *Acta Materialia*. 2011; 59(10): 3965–3977. https://doi.org/10.1016/j.actamat.2011.03.022
24. Gavriljuk V.G. Comment on "Effect of interlamellar spacing on cementite dissolution during wire drawing of pearlitic steel wires". *Scripta Materialia*. 2001; 45(12): 1469–1472. https://doi.org/10.1016/S1359-6462(01)01185-X
25. Gavriljuk V.G. Decomposition of cementite in pearlite steel due to plastic deformation. *Materials Science and Engineering: A*. 2003; 345(1-2): 81–89. https://doi.org/10.1016/S0921-5093(02)00358-1
26. Languillaume J., Kapelski G., Baudelet B. Cementite dissolution in heavily cold drawn pearlitic steel wires. *Acta Materialia*. 1997; 45(3): 1201–1212. https://doi.org/10.1016/S1359-6454(96)00216-9
27. Sauvage X., Copreaux J., Danoix F., Blavette D. Atomic-scale observation and modelling of cementite dissolution in heavily deformed pearlitic steels. *Philosophical Magazine A*. 2000; 80(4): 781–796. https://doi.org/10.1080/01418610008212082

Information about the Authors / Сведения об авторах

Viktor E. Gromov, *Dr. Sci. (Phys.-Math.), Prof., Head of the Chair of Science named after V.M. Finkel',* Siberian State Industrial University
ORCID: 0000-0002-5147-5343
E-mail: gromov@physics.sibsiu.ru

Krestina V. Aksenova, *Cand. Sci. (Eng.), Assist. Prof. of the Chair of Science named after V.M. Finkel',* Siberian State Industrial University
ORCID: 0000-0003-4908-6776
E-mail: 19krestik91@mail.ru

Yurii F. Ivanov, *Dr. Sci. (Phys.-Math.), Prof., Chief Researcher of the Laboratory of Plasma Emission Electronics,* Institute of High-Current Electronics, Siberian Branch of the Russian Academy of Sciences
ORCID: 0000-0001-8022-7958
E-mail: yufi55@mail.ru

Roman V. Kuznetsov, *Candidates for a degree of Cand. Sci. (Eng.) of the Chair of Science named after V.M. Finkel',* Siberian State Industrial University
E-mail: mail@kuzmash.com

Vasilii E. Kormyshev, *Cand. Sci. (Eng.), Senior Researcher of Department of Scientific Researches,* Siberian State Industrial University
ORCID: 0000-0002-5147-5343
E-mail: 89236230000@mail.ru

Виктор Евгеньевич Громов, *д.ф.-м.н., профессор, заведующий кафедрой естественнонаучных дисциплин им. профессора В.М. Финкеля,* Сибирский государственный индустриальный университет
ORCID: 0000-0002-5147-5343
E-mail: gromov@physics.sibsiu.ru

Крестина Владимировна Аксёнова, *к.т.н., доцент кафедры естественнонаучных дисциплин им. профессора В.М. Финкеля,* Сибирский государственный индустриальный университет
ORCID: 0000-0003-4908-6776
E-mail: 19krestik91@mail.ru

Юрий Федорович Иванов, *д.ф.-м.н., профессор, главный научный сотрудник лаборатории плазменной эмиссионной электроники,* Институт Сильноточной электроники Сибирского отделения РАН
ORCID: 0000-0001-8022-7958
E-mail: yufi55@mail.ru

Роман Вадимович Кузнецов, *соискатель степени к.т.н. кафедры естественнонаучных дисциплин им. профессора В.М. Финкеля,* Сибирский государственный индустриальный университет
E-mail: mail@kuzmash.com

Василий Евгеньевич Кормышев, *к.т.н., старший научный сотрудник Управления научных исследований,* Сибирский государственный индустриальный университет
ORCID: 0000-0002-5147-5343
E-mail: 89236230000@mail.ru

Contribution of the Authors / Вклад авторов

V. E. Gromov – formulation of the article concept, scientific guidance, writing the text.
K.V. Aksenova – literary review, discussion of the results, editing the text.
Yu. F. Ivanov – conducting electron microscopic studies, analysis of the results.
R. V. Kuznetsov – writing the text, discussion of the results.

V. E. Kormyshev – preparation of the samples for transmission electron microscopic tests, discussion of the results.

В. Е. Громов – формулирование концепции работы, научное руководство, написание текста статьи.
К. В. Аксёнова – обзор литературы, обсуждение результатов, редактирование текста статьи.
Ю. Ф. Иванов – проведение электронно-микроскопических исследований, анализ результатов.
Р. В. Кузнецов – подготовка текста статьи, обсуждение результатов.
В. Е. Кормышев – подготовка образцов для исследований методом просвечивающей электронной микроскопии, обсуждение результатов.

Received 20.04.2022
Revised 31.10.2022
Accepted 12.12.2022

Поступила в редакцию 20.04.2022
После доработки 31.10.2022
Принята к публикации 12.12.2022

MATERIAL SCIENCE / МАТЕРИАЛОВЕДЕНИЕ

UDC 536.46:539.219
DOI 10.17073/0368-0797-2023-1-57-61

Original article
Оригинальная статья

Grain structure formation and microhardness of Ni_3Al intermetallic compound fabricated by SHS extrusion

K. O. Akimov, K. V. Ivanov, M. G. Figurko, V. E. Ovcharenko

Institute of Strength Physics and Materials Science, Siberian Branch of the Russian Academy of Sciences (2/4 Akademicheskii Ave., Tomsk, 634055, Russian Federation)

akimov_ko@ispms.ru

Abstract. In this paper we studied the possibility to enhance the microhardness of Ni_3Al intermetallic compound by reducing the average grain size and the effect of the mixture deformation during self-propagating high-temperature synthesis (SHS) on the Ni_3Al grain size and microhardness. We used an SHS extrusion test bench to continuously monitor the synthesis variables. One of the key factors affecting the grain structure and microhardness is deformation rate of the synthesis product. Increasing the extrusion nozzle diameter from 3 to 5 mm results in a longer displacement of the press plunger since it takes less force to extrude the material through the larger diameter orifice. It is assumed that the resistance to deformation under pressure decreases, while the deformation rate increases for the material in the mold, and decreases for the extruded material. As a result, the average grain size of Ni_3Al remaining in the mold after synthesis decreases by 40 % (from 7 to 5 μm), while the grain size of the extruded material is doubled (from 3 to 6 μm). Compared to Ni_3Al produced by SHS compaction, the average grain size of extruded Ni_3Al is 82 % less (17 and 3 μm, respectively). Reducing the average grain size of extruded Ni_3Al leads to a 600 MPa increase in microhardness. The results obtained may assist the development of guidelines for fine grain, high microhardness intermetallide/alloy manufacturing.

Keywords: structure, grain size, microhardness, SHS extrusion, deformation, material enhancement

Acknowledgements: The work was performed within the framework of the state assignment of the Institute of Strength Physics and Materials Science, Siberian Branch of Russian Academy of Sciences, project FWRW-2021-0004.

For citation: Akimov K.O., Ivanov K.V., Figurko M.G., Ovcharenko V.E. Grain structure formation and microhardness of Ni_3Al intermetallic compound fabricated by SHS extrusion. *Izvestiya. Ferrous Metallurgy*. 2023; 66(1): 57–61.
https://doi.org/10.17073/0368-0797-2023-1-57-61

Формирование зеренной структуры и микротвердости интерметаллического соединения Ni_3Al в результате СВС-экструзии

К. О. Акимов, К. В. Иванов, М. Г. Фигурко, В. Е. Овчаренко

Институт физики прочности и материаловедения Сибирского отделения РАН (Россия, 634055, Томск, пр. Академический, 2/4)

akimov_ko@ispms.ru

Аннотация. В рамках работы на примере микротвердости исследована возможность улучшения прочностных свойств интерметаллического соединения Ni_3Al путем уменьшения среднего размера его зерна. Исследуется влияние деформации реагирующей смеси при самораспространяющемся высокотемпературном синтезе (СВС) на размер зерна и микротвердость интерметаллического соединения Ni_3Al. СВС-экструзию проводили на экспериментальном стенде, позволяющем непрерывно контролировать параметры синтеза. Одним из ключевых факторов, влияющих на характеристики зеренной структуры и микротвердость, является степень деформации продукта синтеза. Увеличение диаметра экструзионного отверстия от 3 до 5 мм приводит к увеличению максимального линейного перемещения плунжера пресса вследствие более легкого выхода материала через отверстие большего диаметра. Предполагается, что при этом имеют место уменьшение сопротивления деформированию материала при приложении давления, увеличение степени деформации материала внутри пресс-формы и ее снижение в экструдированном материале. В результате средний размер зерна Ni_3Al, оставшегося в объеме пресс-формы после синтеза, уменьшается на 40 % (от 7 до 5 мкм), а прошедшего через экструзионное отверстие – возрастает в два раза (от 3 до 6 мкм). По сравнению с Ni_3Al, полученным методом СВС-компактирования, средний размер зерна экструдированного Ni_3Al меньше в 5,6 раза

(17 и 3 мкм соответственно). Уменьшение среднего размера зерна экструдированного Ni_3Al приводит к увеличению микротвердости на 600 МПа. Полученные результаты позволяют разработать рекомендации по получению интерметаллидов и сплавов на их основе с мелким размером зерна и высокой микротвердостью.

Ключевые слова: структура, размер зерна, микротвердость, СВС-экструзия, деформация, улучшение свойств

Благодарности: Работа выполнена в рамках государственного задания Института физики прочности и материаловедения Сибирского отделения РАН, тема № FWRW-2021-0004.

Для цитирования: Акимов К.О., Иванов К.В., Фигурко М.Г., Овчаренко В.Е. Формирование зеренной структуры и микротвердости интерметаллического соединения Ni_3Al в результате СВС-экструзии. *Известия вузов. Черная металлургия*. 2023; 66(1): 58–61. https://doi.org/10.17073/0368-0797-2023-1-57-61

Introduction

The Ni_3Al intermetallic compound is the key component of advanced nickel-based superalloys providing high strength at elevated temperatures, and creep resistance [1 – 4]. Despite the excellent mechanical properties at high temperatures, the applications of Ni_3Al are limited. This is due to its low ductility at room temperature caused by intergranular embrittlement which significantly complicates any machining [5 – 8]. As was shown in [9, 10], the ductility and strength of Ni3Al can be increased by alloying or refining the grains, for example, by severe plastic deformation [11 – 14]. Still, severe plastic deformation is suitable for small samples only such as disks ~0.5 mm thick and up to 15 mm in diameter under torsion and pressure [15], or plates less than 30 μm thick under multi-pass rolling [16].

Grain refinement in large Ni_3Al samples requires deformation at temperatures close to the melting point. Such conditions are achievable as the workpiece is crystallized during the self-propagating high-temperature synthesis and partial extrusion (SHS extrusion) [17, 18]. The phase transformations occur simultaneously in the bulk of pressed powder [19] during the volumetric exothermic reaction of Ni_3Al synthesis from the powder mixture of nickel and aluminum. Deformation of the mixture is a way to control the average grain size of the Ni_3Al compound synthesized under pressure [20, 21].

The purpose of this study was to investigate the effect of mixture deformation during SHS extrusion on the average grain size and microhardness of the Ni_3Al compound.

Materials and Methods

We used a test hydraulic press for the SHS extrusion of Ni_3Al. The press was equipped with an HF generator for inductive mold heating [22]. We processed a mixture of nickel (PNK-1L8, particle size: 1 – 5 μm) and aluminum (ASD-4, particle size: 1 – 4 μm) powders. The powder mixture was placed in a steel mold, 58 mm inner diameter, 3 to 5 mm extrusion nozzle diameter. The process temperature (inside the steel mold wall) was measured with a type *K* thermocouple, with ±7 °C accuracy. The pressure was calculated from the press instrument readings pressure and the punch area. The press plunger displacement was continuously measured using a Shahe 5403-200 digital linear scale, of ±0.6 mm accuracy.

The high-temperature synthesis of the Ni_3Al intermetallic compound from a mixture of nickel and aluminum powders under pressure consists of several steps: preloading the powder mixture (3Ni + Al) in the mold (at 115 MPa); heating the pressed powder until (Ni-Al)-eutectics is formed; melting the aluminum component; initiation of the exothermic Ni_3Al formation simultaneously with applying the specified pressure to the high-temperature synthesis product; holding the final product at the specified pressure (430 MPa).

The key process variables which control the grain structure of the synthesized intermetallide are the deformation rate of the mixture in the mold and the period of pressure applied to the thermally reacting powder mixture after the intermetallide synthesis reaction is initiated.

We manufactured Ni_3Al cylinders with concave end faces, 58 mm diameter, 16 mm height in the middle by high-temperature synthesis under pressure at different deformation rates, and partial extrusion of the synthesis product from the mold through 3, 4, and 5 mm dia. nozzles. The pressure was applied 1 s after the reaction initiation. The holding time is 1 s, in order to ensure uniform pressure distribution across the mold which has extrusion nozzles of different diameters. An increase in the extrusion nozzle diameter leads to an increase in the mixture deformation rate in the mold. After passing through the extrusion nozzle, the material was shaped as a rod up to 180 mm long.

The samples of the material remaining in the mold were cut from the middle vertical cross sections as 1 mm thick plates, in order to eliminate the edge effects which may change the structure and properties of the material. The samples of the extruded material were cut from a cross-section passing through the axial axis. The samples were mechanically ground with a diamond paste. The abrasive particle size was gradually reduced to 1 μm. Then the samples were polished with an aluminum oxide suspension (0.3 μm particle size) and cloth. In order to reveal the grain structure, we applied argon ion etching, 0.6 kV accelerating voltage. A Carl Zeiss AXIOVERT-200MAT microscope was used for metallographic analysis.

The average grain size was measured by the random plane method according to GOST 5639-82 (150 measurements). We measured the microhardness with a PMT-3 microhardness meter. The indenter load was 0.98 N, and the loading time was 15 s. The final microhardness was the mean value of at least 10 tests.

Results and Discussion

Fig. 1 shows the press plunger position vs. time curves at the mixture compression stage during the SHS extrusion through extrusion 3, 4, and 5 mm dia. nozzles.

The plunger displacement in the mold increases with the diameter of the extrusion nozzle. This indicates a decrease in the resistance to deformation under pressure. It is assumed that the deformation rate of the synthesis product within the mold increases and that of the extruded material decreases.

Fig. 2 shows that using larger nozzle diameters leads to a 40 % decrease in the average Ni_3Al grain size of the material remaining in the mold after synthesis (from 7 ± 0.4 to 5 ± 0.3 μm). With regard to the extruded material, reducing the nozzle diameter from 5 to 3 mm results in halving the average grain size (from 6 ± 0.5 to 3 ± 0.3 μm). Compared to the Ni_3Al compound made by SHS compaction, the average grain size is 82 % less (17 ± 0.5 and 3 ± 0.3 μm). SHS extrusion reduces the average grain size due to the higher deformation rate as the material exits the mold into the extrusion channel with a smaller nozzle diameter.

It should be noted that the Ni_3Al average grain size vs. extrusion nozzle diameter curve confirms the above assumption that, as the nozzle diameter increases, the deformation rate of the synthesis product remaining in the mold increases and that of the extruded material decreases.

Fig. 3 shows the hardness curves for Ni_3Al made by SHS extrusion. It can be seen that changing the extrusion nozzle diameter resulting in a decrease in the average Ni_3Al grain size leads to an increase in the intermetallide microhardness by 16, and 20 % for the material remaining

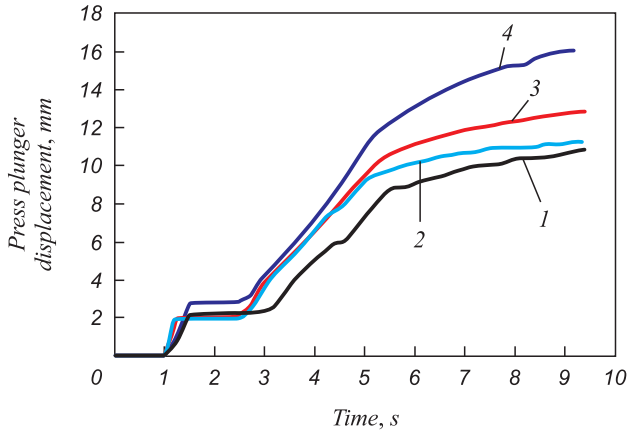

Fig. 1. Dependences of linear movement of press plunger during compression of the synthesis product in the mold without extrusion (*1*) and with partial extrusion of the product through the nozzles 3, 4 and 5 mm diameter (*2 – 4*)

Рис. 1. Зависимости линейного перемещения плунжера пресса на стадии сжатия продукта синтеза в пресс-форме без экструзии (*1*) и с частичной экструзией продукта через отверстия диаметром 3, 4 и 5 мм (*2 – 4*) от времени

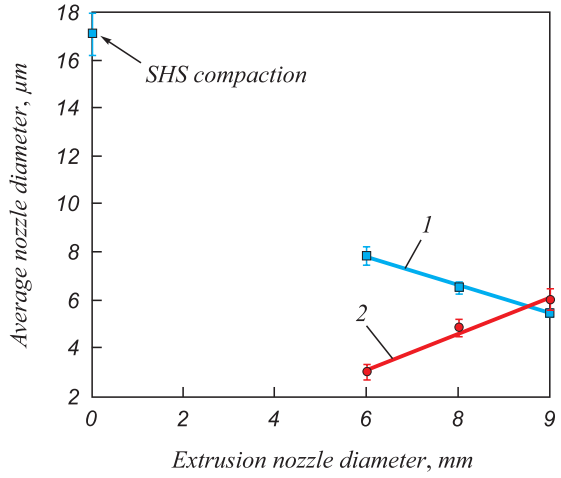

Fig. 2. Dependence of the average grain size of Ni_3Al obtained by SHS extrusion on the extrusion nozzle diameter, 1 s pressure holding period:
■ – material inside the mold; ● – extruded material

Рис. 2. Зависимость среднего размера зерна Ni_3Al, полученного методом СВС-экструзии, от диаметра экструзионного отверстия при времени задержки приложения давления 1 с:
■ – материал внутри пресс-формы;
● – экструдированный материал

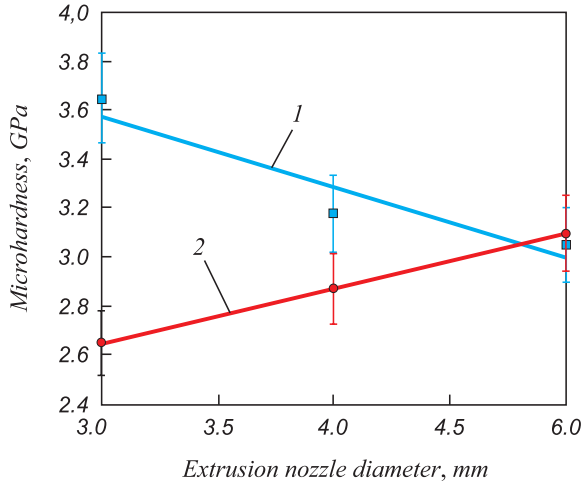

Fig. 3. Dependences of microhardness of Ni_3Al intermetallic compound obtained by SHS-extrusion, remaining in the mold (●) and extruded (■)

Рис. 3. Зависимости микротвердости интерметаллида Ni_3Al, полученного методом СВС-экструзии, оставшегося внутри пресс-формы после синтеза (●), и экструдированного (■)

inside the mold after synthesis and the extruded material, respectively.

The results are consistent with the data reported by Stolin A.M., etc. [23]. They indicate that SHS extrusion is suitable for making long products from brittle, hard-to-deform refractory materials such as Ni_3Al.

Conclusions

Deformation of the high-temperature synthesis product during SHS extrusion significantly affects the average grain size and microhardness of the Ni_3Al intermetallide (both remaining in the mold and extruded). The higher deformation rate of the material inside the mold as the extrusion nozzle diameter is increased from 3 to 5 mm, leads to a 30 % decrease in the average grain size and a 16 % increase in the microhardness. For the extruded material, as the extrusion nozzle diameter is reduced from 5 to 3 mm, the average grain size is halved, and the microhardness is increased by 20 % (600 MPa).

Our findings can be used to develop fine-grade, high-microhardness intermetallide/alloy SHS extrusion processes.

References / Список литературы

1. Liu C.T., Sikka V.K. Nickel aluminides for structural use. *Journal of Mechanical Engineering and Technology*. 1986; 38: 19–21. https://doi.org/10.1007/BF03257837
2. Taub A.I., Fleischer R.L. Intermetallic compounds for high-temperature structural use. *New Series*. 1989; 243(4891): 616–621. https://doi.org/10.1126/science.243.4891.616
3. Amrit R.P., Manidipto M., Dilpreet S. A critical review on the properties of intermetallic compounds and their application in the modern manufacturing. *Crystal Research and Technology*. 2022; 57(3): 2100159. https://doi.org/10.1002/crat.202100159
4. Tewari R., Sarkar N.K., Harish D., Vishwanadh B., Dey G.K., Banerjee S. Intermetallics and alloys for high temperature applications materials under extreme conditions. In: *Materials Under Extreme Conditions*. Tyagi A.K. ed. Amsterdam: Elsevier; 2017: 293–335. https://doi.org/10.1016/B978-0-12-801300-7.00009-7
5. Stoloff N.S., Liu C.T., Deevi S.C. Emerging application of intermetallics. *Intermetallics*. 2008; 8(9-11): 1313–1320. https://doi.org/10.1016/S0966-9795(00)00077-7
6. Sikka V.K., Deevi S.C., Viswanathan S., Swindeman R.W., Santella M.L. Advances in processing of Ni_3Al -based intermetallics and applications. *Intermetallics*. 2000; 8(9-11): 1329–1337. https://doi.org/10.1016/S0966-9795(00)00078-9
7. Pope D.P., Ezz S.S. Mechanical properties of Ni_3Al and nickel-base alloys with high volume fraction of γ′. *International Materials Reviews*. 1984; 29(1): 136–167. https://doi.org/10.1179/imtr.1984.29.1.136
8. Deevi S.C., Sikka V.K. Nickel and iron aluminides: an overview on properties, processing and applications. *Intermetallics*. 1996; 4(5): 357–375. https://doi.org/10.1016/0966-9795(95)00056-9
9. Schulson E.M., Baker I., Frost H.J. The strength and ductility of intermetallic compounds: Grain size effects. *Materials Research Society Symposia Proceedings*. 1986; 81: 195–205. https://doi.org/10.1557/PROC-81-195
10. Polkowski W., Jóźwik P., Karczewski K., Bojar Z. Evolution of crystallographic texture and strain in a fine-grained Ni_3Al (Zr, B) intermetallic alloy during cold rolling. *Archives of Civil and Mechanical Engineering*. 2014; 14(4): 550–560. https://doi.org/10.1016/j.acme.2014.04.011
11. Valiev R.Z., Estrin Y., Horita Z., Langdon T.G., Zechetbauer M.J., Zhu Y.T. Producing bulk ultrafine-grained materials by severe plastic deformation. *JOM*. 2006; 58: 33–39. https://doi.org/10.1007/s11837-006-0213-7
12. Valiev R.Z., Alexandrov I.V., Zhu Y.T., Lowe T.C. Paradox of strength and ductility in metals processed by severe plastic deformation. *Journal of Materials Research*. 2002; 17: 5–8. https://doi.org/10.1557/JMR.2002.0002
13. Jóźwik P., Bojar Z. Analysis of grain size effect on tensile properties of Ni_3Al – based intermetallic strips. *Archives of Metallurgy and Materials*. 2007; 52(2): 321–327.
14. McFadden S., Mishra R., Valiev R., Zhilyaev A.P., Mukherjee A.K. Low-temperature superplasticity in nanostructured nickel and metal alloys. *Nature*. 1998; 398: 684–686. https://doi.org/10.1038/19486
15. Korznikov A.V., Idrisova S.R., Dimitrov O., Pyshmintsev I., Sirenko A.A., Korznikova G. Structure and mechanical properties of the nanocrystalline intermetallic compound Ni_3Al. *The Physics of Metals and Metallography*. 1998; 85(5): 564–567.
16. Demura M., Kishida K., Suga Y., Takanashi M., Hirano T. Fabrication of thin Ni_3Al foils by cold rolling. *Scripta Materialia*. 2022; 47(4): 267–272. https://doi.org/10.1016/S1359-6462(02)00139-2
17. Lebrat J.P., Varma A. Self-propagating high-temperature synthesis of Ni_3Al. *Combustion Science and Technology*. 1992; 88(3-4): 211–221. https://doi.org/10.1080/00102209308947237
18. Hibino A., Matsuoka S., Kiuchi M. Synthesis and sintering of Ni_3Al intermetallic compound by combustion synthesis process. *Journal of Materials Processing Technology*. 2001; 112(1): 127–135. https://doi.org/10.1016/S0924-0136(01)00558-1
19. Merzhanov A.G. History and recent developments in SHS. *Ceramics International*. 1995; 21(5): 371–379. https://doi.org/10.1016/0272-8842(95)96211-7
20. Ovcharenko V.E., Lapshin O.V., Ramazanov I.S. Formation of the granular structure in the intermetallic compound Ni_3Al in high-temperature synthesis under compression. *Combustion, Explosion and Shock Waves*. 2006; 42(3): 302–308. https://doi.org/10.1007/s10573-006-0055-1
21. Si J., Gao F., Han P. Zhang J. Simulation on extrusion process of TiAl alloy. *Intermetallics*. 2011; 19(2): 169–174. https://doi.org/10.1016/j.intermet.2010.08.021
22. Ovcharenko V.E., Akimov K.O. Effect of deformation on the grain size of the Ni_3Al intermetallic compound synthesized under pressure. *Inorganic Materials*. 2020; 56(11): 1122–1126. https://doi.org/10.1134/S0020168520110114
23. Stolin A.M., Bazhin P.M. Manufacture of multipurpose composite and ceramic materials in the combustion regime and high-temperature deformation (SHS Extrusion). *Theoretical Foundations of Chemical Engineering*. 2014; 48(6): 751–763. https://doi.org/10.1134/S0040579514060104

Information about the Authors / Сведения об авторах

Kirill O. Akimov, *Junior Researcher of the Laboratory of Physics of Consolidation of Powder Materials,* Institute of Strength Physics and Materials Science, Siberian Branch of the Russian Academy of Sciences
ORCID: 0000-0002-3204-250X
E-mail: akimov_ko@ispms.ru

Konstantin V. Ivanov, *Dr. Sci. (Phys.-Math.), Leading Researcher of the Laboratory of Physics of Consolidation of Powder Materials,* Institute of Strength Physics and Materials Science, Siberian Branch of the Russian Academy of Sciences
ORCID: 0000-0002-8003-271X
E-mail: ikv@ispms.ru

Marina G. Figurko, *Engineer of the Laboratory of Physics of Consolidation of Powder Materials,* Institute of Strength Physics and Materials Science, Siberian Branch of the Russian Academy of Sciences
E-mail: figurko.marina@mail.ru

Vladimir E. Ovcharenko, *Dr. Sci. (Eng.), Prof., Chief Researcher of the Laboratory of Composite Materials,* Institute of Strength Physics and Materials Science, Siberian Branch of the Russian Academy of Sciences
ORCID: 0000-0003-1776-1212

Кирилл Олегович Акимов, *младший научный сотрудник лаборатории физики консолидации порошковых материалов,* Институт физики прочности и материаловедения Сибирского отделения РАН
ORCID: 0000-0002-3204-250X
E-mail: akimov_ko@ispms.ru

Константин Вениаминович Иванов, *д.ф.-м.н., ведущий научный сотрудник лаборатории физики консолидации порошковых материалов,* Институт физики прочности и материаловедения Сибирского отделения РАН
ORCID: 0000-0002-8003-271X
E-mail: ikv@ispms.ru

Марина Григорьевна Фигурко, *инженер лаборатории физики консолидации порошковых материалов,* Институт физики прочности и материаловедения Сибирского отделения РАН
E-mail: figurko.marina@mail.ru

Владимир Ефимович Овчаренко, *д.т.н., профессор, главный научный сотрудник лаборатории композиционных материалов,* Институт физики прочности и материаловедения Сибирского отделения РАН
ORCID: 0000-0003-1776-1212

Contribution of the Authors / Вклад авторов

K. O. Akimov – synthesis of the samples, experimentation, analysis of the obtained data, writing the text, preparation of graphs.

K. V. Ivanov – elaboration of the sections content, discussion of the results, correction and writing the text.
M. G. Figurko – preparation of the samples for experiments.
V. E. Ovcharenko – creation of the article idea, selection of the object and methodology of the research.

К. О. Акимов – синтез образцов, проведение экспериментов, анализ полученных данных, написание статьи, подготовка графиков.
К. В. Иванов – проработка содержания разделов, обсуждение результатов, корректировка и написание статьи.
М. Г. Фигурко – подготовка образцов для экспериментов.
В. Е. Овчаренко – создание идеи статьи, выбор объекта и методики исследования.

Received 04.08.2022
Revised 26.01.2023
Accepted 27.01.2023

Поступила в редакцию 04.08.2022
После доработки 26.01.2023
Принята к публикации 27.01.2023

MATERIAL SCIENCE / МАТЕРИАЛОВЕДЕНИЕ

UDC 539.373:669.35:539.214
DOI 10.17073/0368-0797-2023-1-62-69

Original article
Оригинальная статья

Parameters of substructure in wrought Cu – Mn alloys with FCC lattice

L. I. Trishkina [1], A. A. Klopotov [1] ✉, A. I. Potekaev [2], T. V. Cherkasova [1], V. I. Borodin [3]

[1] **Tomsk State University of Architecture and Building** (2 Solyanaya Sqr., Tomsk 634003, Russian Federation)
[2] **National Research Tomsk State University** (36 Lenina Ave., Tomsk 634050, Russian Federation)
[3] **JSC Gazprom Transgaz** (9 Frunze Ave., Tomsk 634029, Russian Federation)

✉ klopotovaa@tsuab.ru

Abstract. The development and success of the physical science of strength and plasticity allow the main aspects of dislocation physics to be proposed. This work considers the current state of this issue as part of a multilevel approach: patterns of dislocation accumulation in a material after deformation with various degrees. The main mechanism of hardening of a metal polycrystal is the accumulation of dislocations in its grains, while the main hardening parameter is the mean scalar density of dislocations. The scalar density of dislocations is divided into the following components: the density of statistically stored (ρ_S); and the density of geometrically necessary (ρ_G) dislocations. The transmission diffraction electron microscopy (TEM) is used to study the stages of dislocation substructure (DSS) types development in Cu–Mn alloys depending on the concentration of an alloying element during active plastic deformation. Polycrystal alloys are studied in a wide concentration range: from 0.4 to 25 % Mn (at.). A number of dislocation substructure parameters are measured using electron microscope images: mean scalar density of dislocations $<\rho>$; density of statistically stored (ρ_S) and geometrically necessary (ρ_G) dislocations; curvature-torsion of the crystal lattice (χ); density of microstrips (P_{strip}); and density of broken sub-boundaries ($M_{br.\ bnd.}$). A sequence of transformations of the DSS types with an increase in the deformation degree and amount of the second element to form the substructure type and parameters was established. The influence of the second element and grain size on the mean scalar density of dislocations and its components was experimentally determined. The presence of disorientations in the substructure during deformation is based on the measurement of these parameters using the TEM.

Keywords: alloys, deformation, dislocation substructures, geometric necessary dislocations, atomic volume, Zen's law

Acknowledgements: The research was carried out within the state assignment of Ministry of Science and Higher Education of the Russian Federation (theme No. FEMN-2023-0003).

For citation: Trishkina L.I., Klopotov A.A., Potekaev A.I., Cherkasova T.V., Borodin V.I. Parameters of substructure in wrought Cu – Mn alloys with FCC lattice. *Izvestiya. Ferrous Metallurgy*. 2023; 66(1): 62–69. https://doi.org/10.17073/0368-0797-2023-1-62-69

Параметры субструктуры в деформированных сплавах Cu – Mn с ГЦК решеткой

Л. И. Тришкина [1], А. А. Клопотов [1] ✉, А. И. Потекаев [2], Т. В. Черкасова [1], В. И. Бородин [3]

[1] **Томский государственный архитектурно-строительный университет** (Россия, 634003, Томск, пл. Соляная, 2)
[2] **Национальный исследовательский Томский государственный университет** (Россия, Томск, 634050, Томск, пр. Ленина, 36)
[3] **ООО «Газпром Трансгаз Томск»** (Россия, 634029, Томск, пр. Фрунзе, 9)

✉ klopotovaa@tsuab.ru

Аннотация. Развитие и успехи физической науки о прочности и пластичности позволяют сформулировать основные аспекты дислокационной физики. В настоящей работе рассмотрено современное состояние этого вопроса в рамках многоуровневого подхода: закономерности накопления дислокаций в материале после деформации с различными степенями. Основным механизмом упрочнения металлического поликристалла является накопление в его зернах дислокаций, а основным параметром упрочнения – средняя скалярная плотность дислокаций. Скалярная плотность дислокаций разделяется на компоненты: плотность статистически запасенных (ρ_S) и плотность геометрически необходимых (ρ_G) дислокаций. Методом просвечивающей дифракционной электронной микроскопии (ПЭМ) исследуются этапы развития типов дислокационной субструктуры (ДСС) в сплавах Cu – Mn в зависимости от концентрации легирующего элемента при активной пластической деформации. Исследуются поликристаллические сплавы в широком концентрационном интервале: от 0,4

до 25 % Mn (ат.). По полученным на электронном микроскопе снимкам измерен ряд параметров дислокационной субструктуры: средняя скалярная плотность дислокаций <ρ>, плотность статистически запасенных (ρ_S) и геометрически необходимых (ρ_G) дислокаций, кривизна-кручение кристаллической решетки (χ), плотность микрополос ($P_{полос.}$), плотность оборванных субграниц ($M_{об.гр}$). Установлена последовательность превращений типов ДСС при увеличении степени деформации и количества второго элемента на формирование типа субструктуры и ее параметров. Экспериментально определено влияние концентрации второго элемента и размера зерна на среднюю скалярную плотность дислокаций и ее составляющих. Наличие разориентировок в субструктуре в процессе деформации базируется на основе измерения этих параметром методом ПЭМ.

Ключевые слова: сплавы, деформация, дислокационные субструктуры, геометрические необходимые дислокации, атомный объем, закон Зена

Благодарности: Работа выполнена в рамках Государственного задания Министерства науки и высшего образования Российской Федерации (проект РФ FEMN-2023-0003).

Для цитирования: Тришкина Л.И., Клопотов А.А., Потекаев А.И., Черкасова Т.В., Бородин В.И. Параметры субструктуры в деформированных сплавах Cu – Mn с ГЦК решеткой. *Известия вузов. Черная металлургия*. 2023; 66(1): 63–69. https://doi.org/10.17073/0368-0797-2023-1-62-69

Introduction

Variation in the composition of alloys of Cu – Mn system can change the degree of short-range order and the resistance to motion of dislocations [1, 2]. At the same time, in the alloys of this system, the value of the stacking-fault energy (SFE) slightly depends on the concentration of the alloying element – manganese [3]. Variation in the concentration of the second element in the solid solution can lead to a change in the dislocation start stress and friction forces and, consequently, to a change in the resistance to the beginning of plastic deformation. An increase in the deformation degree leads to formation of a certain type of dislocation substructure, which, in turn, determines the deformation hardening of polycrystals. The nature and type of the dislocation structures formed are closely connected with the SFE value, local order parameters, and friction forces between dislocations. These parameters can significantly vary depending on the concentration of the alloying element, degree of ordering in solid solutions, as well as deformation degree [4 – 6].

For many years, the dislocation structure was characterized mainly by such a parameter as the mean scalar density of dislocations <ρ>. Further development of the dislocation study has led to the division of <ρ> into the following components which have different physical meanings: geometrically necessary (ρ_G) and statistically-stored (ρ_S) dislocations. The references show thatthe geometrically necessary dislocations are formedin the case of deformations in the polycrystal metals and alloys with deformation twins, in the dispersion-hardened materials and in other cases of functioning of strong barriers to dislocation sliding [7 – 9].

Density ρ_G is directly connected with the curvature-torsion of the crystal lattice χ [13, 14]:

$$\rho_G = \frac{1}{b}\frac{\partial\varphi}{\partial\ell} = \frac{\chi}{b} = (rb)^{-1},$$

where b is the Burgers vector; φ is the tilting angle of the crystal plane; ℓ is the distance on the plane; $\chi = \frac{\partial\varphi}{\partial\ell}$ – is the curvature-torsion of the crystal lattice; r is the radius of crystal curvature.

The formation of dislocations and dislocation reactions in the alloys after plastic deformation can be considered to be random processes. The dislocations subjected to deceleration by others formed in the course of plastic deformation are called statistically stored dislocations (SSD) [11]. Such statistically stored dislocations are formed at the very beginning of plastic deformation and are decelerated mainly by weak barriers consisting of other dislocations. When the stronger barriers (such as particles of second phases, deformation twins, or grain boundaries) are present in the alloys, the geometrically necessary dislocations (GND) accumulate in the material, and plastic deformation gradients (1) are available [11]. As a result, the mean scalar density of dislocations is determined by the following equation

$$<\rho> = \rho_S + \rho_G.$$

This work studies the influence of manganese alloying and grain size in wrought Cu – Mn alloys with FCC lattice using the transmission electron microscopy.

Study materials and methods

The study materials are polycrystal alloys of Cu – Mn system in the manganese concentration range from 0.4 to 25 % (henceforward, atomic (at.) percentage). Alloys with the mean grain size of 10, 20, 40, 60, 100, 120 and 240 μm were studied. Samples of the alloys studied were deformed by elongation at the room temperature with a rate of $2 \cdot 10^{-2}$ s^{-1}. The dislocation structure was studied by menans of transmission diffraction electron microscopy (TEM) using goniometer-equipped electron microscopes with accelerating voltage of 125 kV. The foils were examined in the microscope column at a 30,000-power magnification. The technique for measuring the dislocation structure parameters is given in [12, 13].

Results and discussion

We considered formation of the dislocation substructure (DSS) depending on the concentration of the alloying element at small ($\varepsilon_{tr} = 0.05$) deformation degrees in the copper-manganese alloys. For easy comparison of the substructures, the study results are provided for one grain size equal to 100 μm.

Fig. 1 shows the types of the dislocation substructures formed with growth of the second element. Analysis of the electron microscope images allowed us to find the following regularities in the DSS formations. With the moderate deformation degrees ($\varepsilon_{tr} = 0.05 – 0.10$) in the alloys studied (Cu + 0.4 % Mn, Cu + 8 % Mn and Cu + 19 % Mn), tangles (Fig. 1, *a*) as well as cell substructures without disorientations (Fig. 1, *b*) are formed from the dislocations. The increase in the concentration of the second component up to 8 % Mn results in transition from the cell DSS to the cell-mesh DSS (Fig. 1, *c*). The further growth of the second element concentration is accompanied by the formation of the new DSS type. In alloys Cu + 13 % Mn, Cu + 19 % Mn and Cu + 25 % Mn, we can observe the following sequence of the DSS types formation: dislocation chaos (Fig. 1, *d*); dislocation clusters and dislocation loops (Fig. 1, *e*); mesh DSS (Fig. 1, *f*) respectively.

We considered the influence of the deformation degree growth in the alloys studied, resulting in disorientations appeared in the DSS. The electron microscope images show this process as the appearance of the extinction deformation contours (Fig. 2).

In Cu – Mn alloys with a low concentration of the alloying element (up to 6 %), the disoriented cell substructure is formed with the deformation degree of 0.20 (Fig. 2, *a*). In alloys with a concentration of the alloying element higher than 8 % Mn, the disoriented cell-mesh substructure develops with further deformation increase (Fig. 2, *b*). With such deformation, clumps are formed from dislocations (Fig. 2, *b*) which riginate on the long rectilinear dislocations formed even at low deformation degrees. As a result, an increase in the density of clumps is observed, and the structure tends to become more homogeneous.

Fig. 2 provides electron microscope images of the DSS types formed with the higher deformation degrees ($\varepsilon_{tr} > 0.20$) in the alloys with different concentrations of the alloying element. The experiments established that, in the alloys with concentration of the second element equal to 0.4, 2.4 and 6 % Mn, the following substructures are observed: disoriented cell, cell-mesh, and microstrip DSS. The examples of the substructure types observed

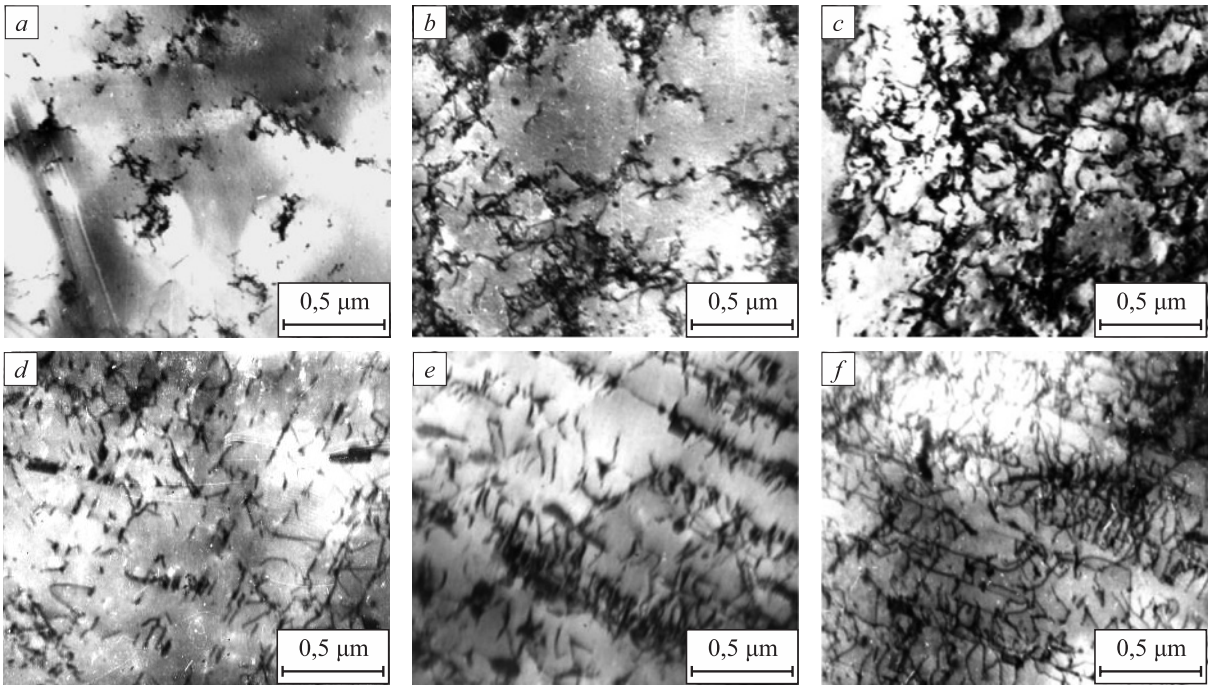

Fig. 1. Electron microscope images of DSS types formed at $\varepsilon_{tr} = 0.05 \div 0.10$
in alloys Cu – 04 % Mn (tangle (*a*), cell (*b*)); Cu + 8 % Mn (cell-mesh (*c*));
Cu + 19 % Mn, Cu + 13 % Mn (chaotic dislocation distribution (*d*)); Cu + 19 % Mn % (dislocation clusters (*e*));
Cu + 19 % Mn % (mesh (*f*))

Рис. 1. Электронно-микроскопические изображения типов ДСС, формирующихся при $\varepsilon_{ист} = 0{,}05 \div 0{,}10$
в сплавах Cu – 04 % Mn (клубковая (*a*), ячеистая (*b*)); Cu + 8 % Mn (ячеисто-сетчатая (*c*));
Cu + 19 % Mn, Cu + 13 % Mn (хаотическое распределение дислокаций (*d*)); Cu + 19 % Mn % (дислокационные скопления (*e*));
Cu + 25 % Mn (сетчатая (*f*))

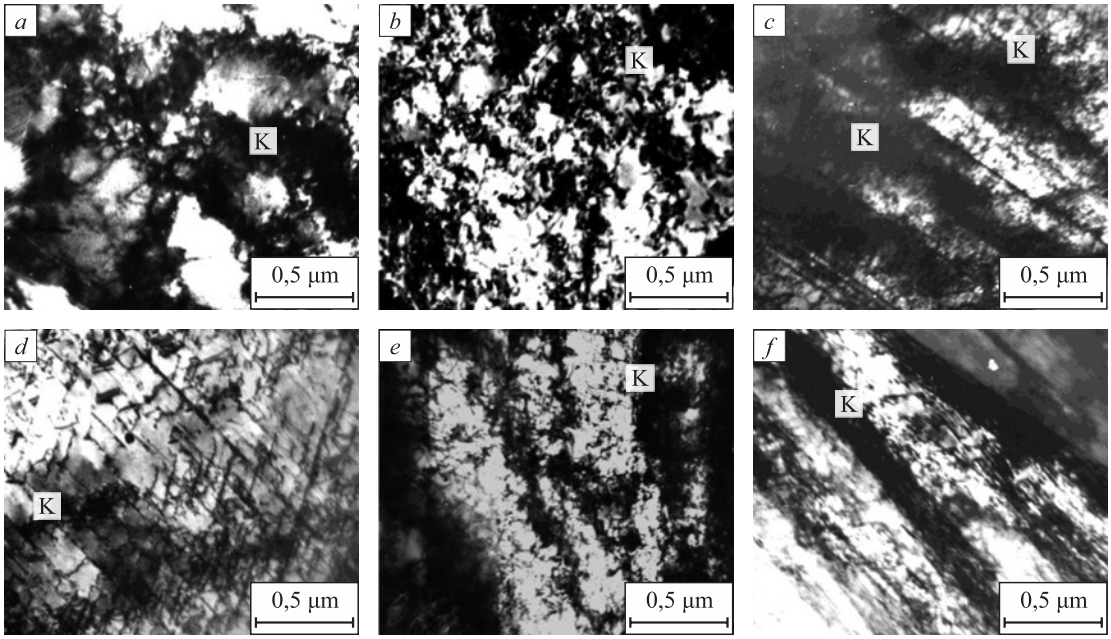

Fig. 2. Electron microscope images of DSS types formed at $\varepsilon_{tr} > 0.20$ in Cu + 0.4 % Mn alloys (disoriented cell (*a*), cell-mesh (*b*)); Cu + 6 % Mn (microstrip (*c*)); Cu + 19 % Mn (mesh (*d*), disoriented cell-mesh (*e*), microstrip (*f*)). Extinction deformation contour K

Рис. 2. Электронно-микроскопические изображения типов ДСС, формирующихся при $\varepsilon_{ист} > 0{,}20$ в сплавах Cu + 0,4 % Mn (разориентированная ячеистая (*a*), ячеисто-сетчатая (*b*)); Cu + 6 % Mn (микрополосовая (*c*)); Cu + 19 % Mn (сетчатая (*d*), разориентированная ячеисто-сетчатая (е), микрополосовая (*f*)). Экстинкционный деформационный контур K

for alloy Cu + 0.4 % Mn are provided in Fig. 2, *a* and *b*. In alloy Cu + 6 % Mn, the formation of the microstrip DSS is observed inside the grain, appearing along boundaries of the disoriented cells or from the grain boundaries (Fig. 2, *c*). It is important to note that the kinetics of the microstrip substructure formation and volume fraction growth is often connected with growth through the alloy of the broken boundaries.

It was established that, in alloys with the higher concentration of the alloying element (8, 10, 13, 19 and 25 % Mn), such substructures as disoriented mesh, disoriented cell-mesh, and microstrip DSS are present The example of the substructures observed at $\varepsilon_{tr} > 0.20$ is shown in Fig. 2, *d* – *f* for alloy Cu + 19 % Mn. Based on the analysis of the electron microscope photos, it was established that the alloy with 8 % Mn is the boundary-when transferring from the classically cell DSS to cell-mesh DSS.

The photographs were used to measure the mean scalar density of dislocations <ρ>, the density of statistically stored (ρ_S) and geometrically necessary (ρ_G) dislocations, the curvature-torsion of the crystalline lattice χ, the density of microstrips P_{strip}, as well as the density of broken boundaries Mbr.bndwith different grain sizes <*d*>. The dependencies of the mean scalar density of dislocations, density of geometrically necessary and statistically stored dislocations on the concentration of alloying element C_{Mn} at $\varepsilon_{tr} = 0.30$ and grain sizes 10 and 240 μm are provided in Fig. 3.

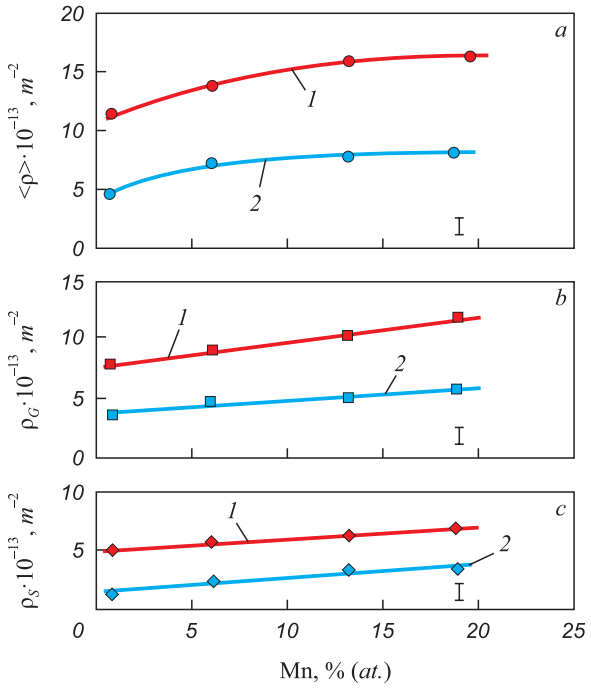

Fig. 3. Dependencies of the mean scalar density of dislocations <ρ> (*a*), density of geometrically necessary ρ_G (*b*) and statistically stored ρ_S (*c*) dislocations on the concentration of alloying element in the alloys of Cu – Mn system at $\varepsilon_{tr} = 0.30$ and grain sizes of 10 μm (*1*) and 240 μm (*2*)

Рис. 3. Зависимости средней скалярной плотности дислокаций <ρ> (*a*), плотности геометрически необходимых ρ_G (*b*) и статистически запасенных ρ_S (*c*) дислокаций от концентрации легирующего элемента в сплавах системы Cu – Mn при $\varepsilon_{ист} = 0{,}30$ и размерах зерен 10 мкм (*1*) и 240 мкм (*2*)

The growth of manganese concentration results in increase of both mean scalar density of dislocations <ρ> and its components ρ_G and ρ_S. The growth of deformation degree results in formation of disorientations in the substructure. Fig. 4 shows dependencies of the parameters which characterized is orientations in Cu – Mn alloys: the curvature-torsion of the crystal lattice, the density of microstrips, and the density of broken sub-boundaries. The values of χ, P_{strip}, and $M_{br.\ bnd.}$ increase with the increase of the concentration of the alloying element C_{Mn} more significantly in the alloys with the grain size of 10 μm compared to the alloys with the grain size of 240 μm.

We considered the features of the atomic volume change in solid solutions in the alloys of Cu – Mn system. It is believed that, in the range of existence of solid solutions of two elements, the change in the lattice period depending on the composition should be linear. This assumption was represented as the Vegard's law [14 – 16]. According to this law, the lattice period of the solid solution of two components with the same or similar structure and periods a_1 and a_2 should change linearly depending on the concentration of these components x_1 and x_2 expressed in atomic fractions:

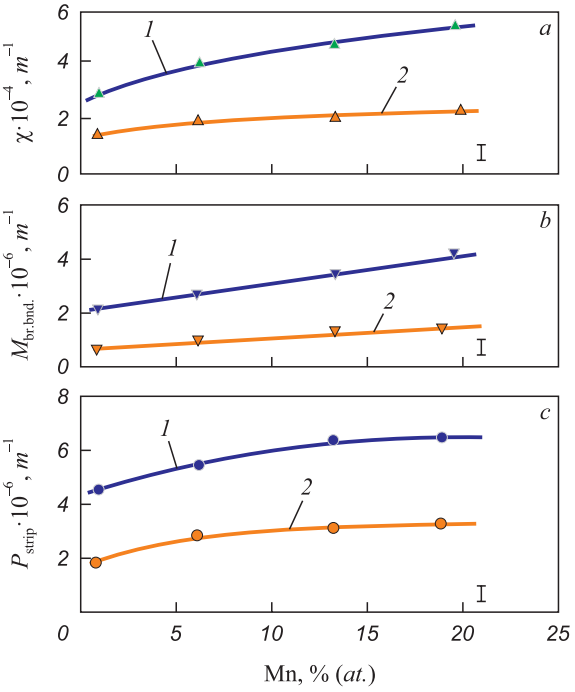

Fig. 4. Dependences of DSS curvature-torsion of crystal lattice χ (*a*), density of broken sub-boundaries $M_{br.\ bnd.}$ (*b*) and density of the microstrips P_{strip} (*c*) on concentrationof alloying element in alloys of Cu – Mn system at ε_{tr} = 0.30 and grain sizes of 10 μm (*1*) and 240 μm (*2*)

Рис. 4. Зависимости кривизны-кручения кристаллической решетки χ (*а*), плотности оборванных субграниц $M_{об.гр}$ (*b*) и плотности микрополос $P_{полос.}$ (*в*) ДСС от концентрации легирующего элемента в сплавах системы Cu – Mn при $\varepsilon_{ист}$ = 0,30 и размерах зерен 10 мкм (*1*) и 240 мкм (*2*)

$$a = x_1 a_1 + x_2 a_2.$$

On the other hand, Zen proposed the atomic volume additivity rule for ideal solid solutions [15–17]:

$$\Omega = C_A \Omega_A + C_B \Omega_B,$$

where C_A and C_B, Ω_A и Ω_B are the concentrations and atomic volumes of the pure components.

A volume fraction of the elementary cell per one atom is understood as the atomic volume, that is:

$$\Omega = \frac{V}{n}, \qquad (1)$$

where *n* is the number of atoms in the elementary cell.

Atomic volumes of pure metals Ω calculated in this way depend least of all on the crystal lattice type. The atomic volume of pure metals Ω is the more universal characteristic with respect to the parameters of elementary cell parameters pure metals and can be used to analyze the properties of compounds formed by elements with different crystal structures. This approach was successfully applied in [14] during analysis of Ti-Ni-based binary compounds.

Zen's law is true just as rare as Vegard's rule; however, it is very popular. There are many models for predicting deviations from the Zen's law, but the reliability level of these predictions is low. None of the models predicts even a deviation sign with an accuracy of more than 60 %. This suggests that the main factors of the deviation from Zen's law have not yet been identified. For the most of the known alloys where solid solutions are formed, the negative deviation of the atomic volume from Zen's rule is observed [18, 17]:

$$\Delta\Omega = \Omega_{\Gamma}^{экс} - \Omega_i^{теор} < 0. \qquad (2)$$

Fig. 5, *a* shows a phase diagram of Cu – Mn system with two concentration areas where ordered phases are formed as a result of "disorder – order" phase transitions of compositions Cu_5Mn and Cu_3Mn, as well as concentration dependencies of atomic volumes of the alloys of system Cu – Mn (Fig. 5, *b*). Within the alloys of this system, the positive deviation of the atomic volume from the Zen's law is observed. Such deviation from the Zen's law on the concentration dependency of the atomic volume occurs much less frequently than the negative deviation [20].

The above data indicates a change in the forces of interatomic interaction during formation of solid solu-

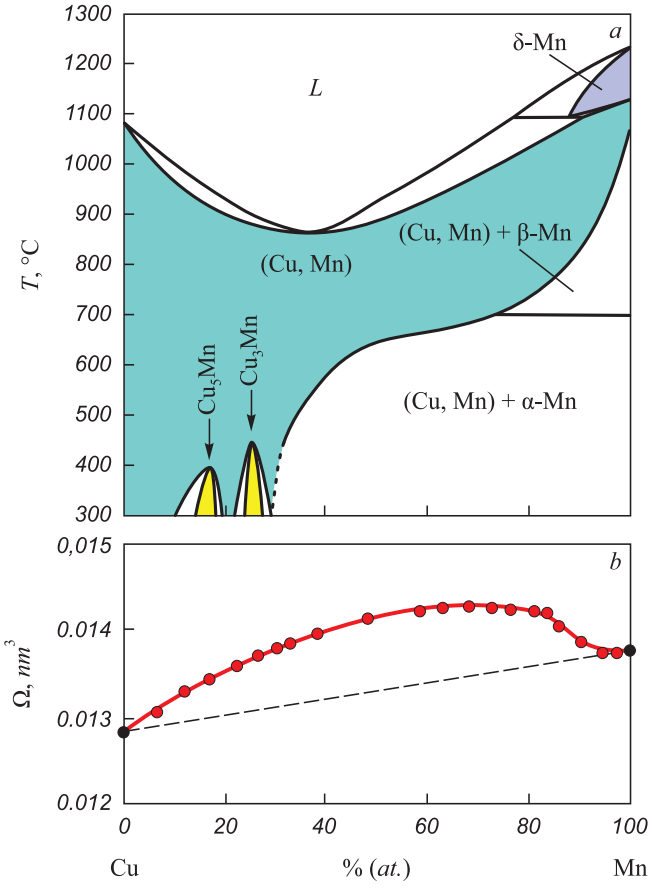

Fig. 5. Phase diagram (*a*) and atomic volume dependence (*b*) in Cu – Mn system [18, 19]

Рис. 5. Фазовая диаграмма (*a*) и зависимость атомного объема (*b*) в системе Cu – Mn [18, 19]

tions in Cu–Mn system (according to equation connecting the crystal energy and atomic volume Ω in the case of metal nature of atomic interaction [21]):

$$U = \frac{Ae^2}{\Omega^{1/3}} + \frac{B}{\Omega^{2/3}} + \frac{Ce^2}{\Omega};$$

where $\frac{Ae^2}{\Omega^{1/3}}$ and $\frac{B}{\Omega^{2/3}}$ are the potential and kinetic energies of free electrons; $\frac{Ce^2}{\Omega}$ characterizes the kinetic energy of electrons which occupy the lower energy states.

It is known that Peierls stress E_p, which is the minimum required stress for dislocation displacementin crystal bodies, depends on the interplane distance d. In this case, maximum E_p, that is the Peierls barrier value is determined as follows [22]:

$$\tau_P = \frac{G}{1-\nu}\exp\left(-\frac{2\pi\omega_д}{b}\right),$$

where $\omega_д = \frac{d}{1-\nu}$ – is the dislocation width; d is the interplane distance; G is the shear modulus; ν is the Poisson's ration; b is the Burgers vector.

Thus, the dependence of the atomic volume on the concentration for the alloys of Cu–Mn system allows us to state, according to the above analysis based on equations (1) and (2), that the increase in atomic volume contributes to the crystal energy change and the Peierls barrier height. Such changes in the atomic volume exercise significant influence over mobility of the statistically stored and geometrically necessary dislocations.

Conclusions

Based on the electron microscope study of the fine structure of wrought samples of the alloys of Cu–Mn system with FCC lattice, the parameters of the dislocation substructures are determined (mean scalar density of dislocations <ρ> and its components: density of statistically stored ρ_S and geometrically necessary ρ_G dislocations; curvature-torsion of crystal lattice χ, density of microstrips P_{strip} and density of broken sub-boundaries $M_{br.\ bnd.}$) depending on the concentration of alloying element (manganese) with different grain sizes. Features of evolution of the dislocation substructures in alloys with different manganese content are determined; and it is established that the alloy with 8 % Mn is the boundary when transferring from the classically cell DSS to cell-mesh DSS.

It was shown that the grain size decrease results in dislocation structure parameters increase. This is due to the fact that dislocation accumulation in the grains of smaller size is connected with their lower mobility.

Based on the analysis of concentration dependences of the atomic volumes in the alloys of Cu–Mn system, the positive deviation from Zen's law was established. Such an increase in atomic volume with the alloying element concentration growth contributes to the crystal energy change and, as a result, to the Peierls barrier increase. This xercises significant influence over mobility of the statistically stored and geometrically necessary dislocations. This data correlates with the results of electron microscope studies: in Cu–Mn alloys with the higher manganese content, the dislocation substructure parameters growth is observed.

It was also established that the grain size decrease has more significant effect on the dislocation substructure parameters than does the content of alloying element atoms in the alloys of Cu–Mn system with FCC lattice.

References / Список литературы

1. Dudarev E.F., Kornienko A.L., Bakach G.P. Influence of energy of packaging defect on development of dislocation structure, deformation hardening and plasticity of the HCC

of solid materials. *Izvestiya vuzov. Fizika.* 1991; 34(3): 35–46. (In Russ.).

Дударев Е.Ф., Корниенко А.Л., Бакач Г.П. Влияние энергии дефекта упаковки на развитие дислокационной структуры, деформационное упрочнение и пластичность ГЦК твердых растворов. *Известия вузов. Физика*. 1991; 34(3): 35–46.

2. Panin V.E., Dudarev E.F., Bushnev L.S. *Structure and Mechanical Properties of Solid Substitution Solutions*. Moscow: Metallurgiya; 1971: 204. (In Russ.).

Панин В.Е., Дударев Е.Ф., Бушнев Л.С. *Структура и механические свойства твердых растворов замещения*. Москва: Металлургия; 1971: 204.

3. Koneva N.A., Trishkina L.I., Cherkasova T.V. Effect of stacking-fault energy on the accumulation of dislocations during plastic deformation of copper-based polycrystalline alloys. *Letters on Materials*. 2017; 7(3): 282–286. https://doi.org/10.22226/2410-3535-2017-3-282-286

4. Koneva N.A., Kozlov E.V., Trishkina L.I., Cherkasova T.V. Evolution of dislocation structure during deformation of polycrystalline copper-based alloys and their plasticity. *Fundamental'nye problemy sovremennogo materialovedeniya.* 2016; 13(2): 162–167. (In Russ.).

Конева Н.А., Козлов Э.В., Тришкина Л.И., Черкасова Т.В. Эволюция дислокационной структуры при деформации поликристаллических сплавов на основе меди и их пластичность. *Фундаментальные проблемы современного материаловедения*. 2016; 13(2): 162–167.

5. Koneva N.A., Kozlov E.V. Physical nature of stages of plastic deformation. In: *Structural Levels of Plastic Deformation and Destruction*. Panin V.E. ed. Novosibirsk: Nauka; 1990: 123–186. (In Russ.).

Конева Н.А., Козлов Э.В. Физическая природа стадийности пластической деформации. В кн.: *Структурные уровни пластической деформации и разрушения* / Под ред. В.Е. Панина. Новосибирск: Наука; 1990: 123–186.

6. Foley D.L., Latypov M.I., Zhao X., Hestroffer J., Beyerlein I.J., Lamberson L.E., Taheri M.L. Geometrically necessary dislocation density evolution as a function of microstructure and strain rate. *Materials Science and Engineering: A*. 2022; 831; 142224. https://doi.org/10.1016/j.msea.2021.142224

7. Hansen L.T., Fullwood D.T., Homer E.R., Wagoner R.H., Lim H., Carroll J.D., Zhou G., Bong H.J. An investigation of geometrically necessary dislocations and back stress in large grained tantalum via EBSD and CPFEM. *Materials Science and Engineering: A.* 2020; 772: 138704. https://doi.org/10.1016/j.msea.2019.138704

8. Dahlberg C.F.O., Saito Y., Öztop M.S., Kysar J.W. Geometrically necessary dislocation density measurements at a grain boundary due to wedge indentation into an aluminum bicrystal. *Journal of the Mechanics and Physics of Solids*. 2017; 105: 131–149. https://doi.org/10.1016/j.jmps.2017.05.005

9. Lin P., Nie J., Liu Z., Zhuang Z. Study of two hardening mechanism caused by geometrically necessary dislocations in thin films with passivation layer. *International Journal of Solids and Structures*. 2019; 160: 59–67. https://doi.org/10.1016/j.ijsolstr.2018.10.015

10. Ashby M.F. The deformation of plastically non-homogeneous materials. *Philosophical Magazine. A Journal of Theoretical Experimental and Applied*. 1970; 21(170): 399–424. https://doi.org/10.1080/14786437008238426

11. Ashby M.F. *Strengthening Methods in Crystals*. Kelly A., Nicholson R.B. eds. London: Applied Science Publishers LTD; 1971: 137–192.

12. Saltykov S.A. *Stereometric Metallography*. Moscow: Metallurgiya; 1970: 376. (In Russ.).

Салтыков С.А. *Стереометрическая металлография*. Москва: Металлургия; 1970: 376.

13. Trishkina L.I., Cherkasova T.V., Popova N.A., etc. *Dislocation Ensemble: Scalar Dislocation Density and its Components*. Tomsk: Tomsk State University of Architecture and Building; 2019: 120. (In Russ.).

Тришкина Л.И., Черкасова Т.В., Попова Н.А. и др. *Дислокационный ансамбль: скалярная плотность дислокаций и ее компоненты*. Томск: ТГАСУ; 2019: 120.

14. Potekaev A.I., Klopotov A.A., Kozlov E.V., etc. *Weakly Stable Pre-Transition Structures in Titanium Nickelide*. Tomsk: NTL; 2004, 296 p. (In Russ.).

Тришкина Л.И., Черкасова Т.В., Попова Н.А. и др. *Дислокационный ансамбль: скалярная плотность дислокаций и ее компоненты*. Томск: ТГАСУ; 2019: 120.

15. Pearson W.B. *The Crystal Chemistry and Physics of Metals and Alloys*. New York: Wiley; 1972: 806.

Пирсон У. *Кристаллохимия и физика металлов и сплавов. Ч. 1*. Москва: Мир; 1977: 420.

16. Kozlov E.V., Dement'ev V.M., Kormin N.M., Shtern D.M. *Structures and Stability of Ordered Phases*. Tomsk: TSU; 1994, 247 p. (In Russ.).

Козлов Э.В., Дементьев В.М., Кормин Н.М., Штерн Д.М. *Структуры и стабильность упорядоченных фаз*. Томск: ТГУ; 1994: 247.

17. Zen E.-an. Validity of "Vegard's Law". *American Mineralogist*. 1956; 41(5-6): 523–524.

18. Massalski T.B. *Binary Alloy Phase Diagrams*. American Society for Metals: Metals Park, Ohio; 1986, 1987; Vols. 1, 2: 2224.

19. Barabash O.M., Koval' Yu.N. *Structure and Properties of Metals and Alloys. Crystal Structure of Metals and Alloys. Reference book*. Kiev: Naukova dumka; 1986: 600. (In Russ.).

Барабаш О.М., Коваль Ю.Н. *Структура и свойства металлов и сплавов. Кристаллическая структура металлов и сплавов. Справочник*. Киев: Наукова думка; 1986: 600.

20. Landa A., Klepeis J.E., Rudd R.E., Caspersen K.J., Young D.A. Analytic binary alloy volume-concentration relations and the deviation from Zen's law. *Applied Sciences*. 2021; 11(13): 6231. https://doi.org/10.3390/app11136231

21. Magelung O. *Festkörpertheorie III: Lokalisierte Zustände*. Berlin etc., 1973. (In Germ.).
Маделунг О. *Физика твердого тела. Локализованные состояния*. Москва: Наука; 1985: 184.

22. Fistul' V.I. *Physics and Chemistry of Solid State. Vol. 1*. Moscow: Metallurgiya; 1995: 480. (In Russ.).

Фистуль В.И. *Физика и химия твердого тела. Т. 1*. Москва: Металлургия; 1995: 480.

Information about the Authors / Сведения об авторах

Lyudmila I. Trishkina, *Dr. Sci. (Phys.-Math.), Prof. of the Chair of Physics, Chemistry, and Theoretical Mechanics,* Tomsk State University of Architecture and Building
ORCID: 0000-0002-2724-0691
E-mail: trishkina.53@mail.ru

Anatolii A. Klopotov, *Dr. Sci. (Phys.-Math.), Prof. of the Chair of Applied Mechanics and Materials Science,* Tomsk State University of Architecture and Building
ORCID: 0000-0002-3690-0436
E-mail: klopotovaa@tsuab.ru

Aleksandr I. Potekaev, *Dr. Sci. (Phys.-Math.), Prof. of the Chair of General and Experimental Physics,* National Research Tomsk State University
ORCID: 0000-0001-5330-9093
E-mail: potekaev@spti.tsu.ru

Tat'yana V. Cherkasova, *Cand. Sci. (Phys.-Math.), Assist. Prof. of the Chair of Physics, Chemistry, and Theoretical Mechanics,* Tomsk State University of Architecture and Building
ORCID: 0000-0001-5330-9093
E-mail: cherkasova_tv@mail.ru

Vladislav I. Borodin, *General Director,* JSC Gazprom Transgaz Tomsk
ORCID: 0000-0002-4111-4712
E-mail: v.borodin@gtt.gazprom.ru

Людмила Ильинична Тришкина, *д.ф.-м.н., профессор кафедры физики, химии и теоретической механики,* Томский государственный архитектурно-строительный университет
ORCID: 0000-0002-2724-0691
E-mail: trishkina.53@mail.ru

Анатолий Анатольевич Клопотов, *д.ф.-м.н., профессор кафедры прикладной механики и материаловедения,* Томский государственный архитектурно-строительный университет
ORCID: 0000-0002-3690-0436
E-mail: klopotovaa@tsuab.ru

Александр Иванович Потекаев, *д.ф.-м.н., профессор кафедры общей и экспериментальной физики,* Национальный исследовательский Томский государственный университет
ORCID: 0000-0001-5330-9093
E-mail: potekaev@spti.tsu.ru

Татьяна Викторовна Черкасова, *к.ф.-м.н., доцент кафедры физики, химии и теоретической механики,* Томский государственный архитектурно-строительный университет
ORCID: 0000-0001-5330-9093
E-mail: cherkasova_tv@mail.ru

Владислав Иванович Бородин, *генеральный директор,* ООО «Газпром Трансгаз Томск»
ORCID: 0000-0002-4111-4712
E-mail: v.borodin@gtt.gazprom.ru

Contribution of the Authors / Вклад авторов

L. I. Trishkina – analysis of the research results, complex electron microscopic examination.
A. A. Klopotov – processing of electron microscopic micrographs, analysis of the research results.
A. I. Potekaev – introduction, problem statement, calculations, analysis of the research results.
T. V. Cherkasova – mechanical testing of the samples, processing of deformation curves.
V. I. Borodin – melting of the samples, introduction, problem statement.

Л. И. Тришкина – анализ результатов, комплексное электронно-микроскопическое исследование.
А. А. Клопотов – обработка электронно-микроскопических микрофотографий, анализ результатов исследований.
А. И. Потекаев – введение, постановка задачи, результаты расчета и анализ результатов.
Т. В. Черкасова – механические испытания образцов и обработка деформационных кривых.
В. И. Бородин – плавка образцов, введение, постановка задачи.

Received 14.03.2022
Revised 04.04.2022
Accepted 11.01.2023

Поступила в редакцию 14.03.2022
После доработки 04.04.2022
Принята к публикации 11.01.2023

UDC 621.771.01
DOI 10.17073/0368-0797-2023-1-70-79

Original article
Оригинальная статья

Using machine learning tools to study flow stress of tube steels under laboratory conditions and according to industrial rolling data

A. G. Zinyagin [1, 2], A. V. Muntin [1, 2], M. O. Kryuchkova [1]

[1] **Bauman Moscow State Technical University (Bauman MSTU)** (5/1 Baumanskaya 2-ya Str., Moscow 105005, Russian Federation)
[2] **JSC "Vyksa Metallurgical Plant"** (45 Br. Batashevykh Str., Vyksa, Nizhny Novgorod Region 607060, Russian Federation)

ziniagin_ag@bmstu.ru

Abstract. Studying the flow stress of various steel grades is one of the key issues for the viable operation of automation systems which support the production of rolled products with the required precision based on geometrical properties. A knowledge of flow stress is also important for the design of rolling mill equipment. The properties of flow stress are published mainly in the form of coefficients of various equations (for instance, the Hansel–Spittel equation). However, these equations are quite often limited in terms of process variables where they provide accessible result. It also should be taken into account that the existing rolling industry fabricates tens of steel grades, the chemical composition of which can vary in wide range depending on final thickness of the rolled products, customer requirements, or on the basis of economic considerations. Studies of the rheological properties of such amount of materials under laboratory conditions is expensive, time and labor consuming and published data does not provide data completeness. This work demonstrates that, using data from industrial rolling mills and methods of machine learning, it is possible to obtain data on material rheology with satisfactory precision. This allows laboratory studies to be avoided. Similar studies are possible due to high intensity of various sensors and instrumentation in modern rolling mills. The results of industrial data were compared with flow stress measured by Gleeble. On the basis of this comparison the model was trained using gradient boosting in order to consider peculiarities of industrial production process.

Keywords: flow stress, calculation of rolling force, linear regression, machine learning, gradient boosting, Gleeble, true stress, true strain, Henzel-Spittel equation

Acknowledgements: The research was carried out within the framework of the program of strategic academic leadership of the Russian Federation "Priority-2030" aimed at supporting the development programs of educational institutions of higher education, the scientific project PRIOR/SN/NU/22/SP5/26 "Creation of innovative digital tools for the use of applied artificial intelligence and advanced statistical analysis of big data in the technological processes of production of metallurgical products" and within the framework of scientific cooperation between JSC "Vyksa Metallurgical Plant" and Bauman Moscow State Technical University.

For citation: Zinyagin A.G., Muntin A.V., Kryuchkova M.O. Using machine learning tools to study flow stress of tube steels under laboratory conditions and according to industrial rolling data. *Izvestiya. Ferrous Metallurgy*. 2023; 66(1): 59–69.
https://doi.org/10.17073/0368-0797-2023-1-70-79

Исследование сопротивления деформации трубных сталей в лабораторных условиях и по данным промышленных прокаток с использованием инструментов машинного обучения

А. Г. Зинягин [1, 2], А. В. Мунтин [1, 2], М. О. Крючкова [1]

[1] **Московский государственный технический университет им. Н.Э. Баумана (МГТУ им. Баумана)** (Россия, 105005, Москва, 2-я Бауманская ул., 5/1)
[2] **АО «Выксунский металлургический завод» (АО «ВМЗ»)** (Россия, 607060, Нижегородская обл., Выкса, ул. Бр. Баташевых, 45)

ziniagin_ag@bmstu.ru

Аннотация. Исследование сопротивления деформации различных марок стали является одним из ключевых вопросов для адекватной работы систем автоматизации, позволяющей получать прокат с требуемой точностью по геометрическим характеристикам. Кроме того, знание сопротивления деформации важно при проектировании оборудования прокатных станов. В литературе значения сопротивления деформации в подавляющем большинстве случаев приводятся в виде коэффициентов различных уравнений (например, Хензеля-Шпиттеля). Однако зачастую данные формулы имеют ограничения по диапазону технологических параметров, где они дают приемлемый результат. Следует также учитывать, что на современном прокатном производстве изготавливаются десятки марок сталей, химический состав которых может варьироваться в широком диапазоне в зависимости от конечной толщины проката, требований заказчика или исходя из экономических соображений (наиболее выгодная композиция легирования). Исследование реологических свойств такого количества материалов в лабораторных условиях дорого, долгосрочно и трудозатратно, а литературные источники не обеспечивают полноты данных. В работе показано, что, используя данные с промышленных прокатных станов и методы машинного обучения, возможно получение сведений о реологии материала с удовлетворительной точностью. Это позволяет избегать проведения лабораторных испытаний. Подобные исследования возможны благодаря высокой насыщенности современных прокатных станов различными датчиками и средствами измерений. Проведено сравнение результатов промышленных данных со значениями сопротивления деформации, полученными на установке Gleeble. На основе данного сравнения выполнялось обучение модели на основе градиентного бустинга для учета особенностей технологического процесса при промышленном производстве.

Ключевые слова: сопротивление деформации, расчет усилия прокатки, линейная регрессия, машинное обучение, градиентный бустинг, Gleeble, истинное напряжение, истинная деформация, уравнение Хензеля-Шпиттеля

Благодарности: Исследования проводились в рамках программы стратегического академического лидерства Российской Федерации «Приоритет-2030» и научного проекта ПРИОР/СН/НУ/22/СП5/26 «Создание инновационных цифровых инструментов для применения прикладного искусственного интеллекта и продвинутого статистического анализа больших данных в технологических процессах производства металлургической продукции».

Для цитирования: Зинягин А.Г., Мунтин А.В., Крючкова М.О. Исследование сопротивления деформации трубных сталей в лабораторных условиях и по данным промышленных прокаток с использованием инструментов машинного обучения. *Известия вузов. Черная металлургия*. 2023; 66(1): 71–79. https://doi.org/10.17073/0368-0797-2023-1-70-79

Introduction

The design calculations of rolling equipment and development of new process modes are based on process power parameters (PPP), mainly rolling force. In general terms, the calculation equations of contact stresses include directly the flow stress. Therefore, the precision of its detection influences directly on the PPP calculation error. Despite the available theoretical and empirical equations, which describe the influence of temperature, the strain rate and velocity on flow stress, their precision is not always acceptable during calculations for steel of new chemical composition. Therefore, the precise value of flow stress of steels and alloys of certain chemical composition should be reasonably determined by experimental means.

Several determination methods of flow stress are available, such as tension, compression, cylinder torsion, and others. Flow stress determined under compression, tension, and torsion can be used with certain assumptions in calculations of contact pressure during rolling. This is attributed to differences under deformation development, under temperature conditions, and other factors [1].

Direct determination of flow stress can be established while rolling. The method of basis pressures can be used with this aim [2]. However, such an approach is more labor intensive and requires sufficiently powerful rolling equipment. In addition, the rolling of one sample at once and the same deformation provides sufficiently less data than compression tests, which present data in the range of true strain from 0 to ~1.

A significant expansion of knowledge about flow stress of metal under actual industrial conditions can be achieved by using statistic methods of processing large data arrays obtained from sensors and control systems of rolling mills. One year of operation of sheet rolling mill provides information of about two million passes [3, 4].

Using the above-mentioned values and validating the results by compression tests (Gleeble), it is possible to develop calculation procedure of flow stress on the basis of industrial data without supplementary laboratory studies.

Modern rolling mills are intensively equipped with sensors which allow very precise detection of actual process parameters. The data obtained is collected at a high sampling rate, accumulated in files, and can be used for advanced statistical analysis. It should be mentioned that due to high scatter of parameters influencing the process, the data analysis from industrial rolling mills using classical methods is very difficult. In such cases machine learning methods are widely applied for data cleaning and highlighting of key features of the running processes. In other countries, neural networks are used for forecasting the physical properties of hot rolled thick sheet (flow stress), rolling force, and other parameters. Using such models, it is possible to significantly decrease expenses of studies during development of new products.

For example, in [5] the neural network is used as adaptation of the various calculation methods of rolling force (Sims, Tselikov) in a single rolling mill. The initial data are both the standard rolling conditions (temperature,

Table 1

Chemical composition of the considered samples, (wt. %)

Таблица 1. **Химический состав исследуемых образцов, % (по массе)**

Steel No.	C	Si	Mn	Cr	Mo	Ni	Nb	Ti	V
1*	0.110	0.55	1.630	–	–	–	–	–	–
2	0.060	0.26	1.820	0.17	–	0.27	0.034	0.016	0.031
3	0.165	1.40	0.475	–	0.025	–	–	–	0.030
4	0.090	0.21	1.690	–	–	0.20	0.059	0.023	0.022

* Reference chemical composition for simulation.

compression, rolling geometry, and so on), and the calculated forces using the aforementioned procedures.

The researchers in [6 – 8] use machine learning methods for description of curves obtained using Gleeble. This approach allows more precise data to be obtained than by classical approaches.

In [9], the use of general rolling parameters and a fully connected neural network, the authors successfully forecast rolling force and moment.

In [10 – 14] the simulation of the plastic properties of various alloys at high temperatures are considered by means of fully connected neural networks. The features of this approach are discussed here.

Machine learning is also used for forecasting phase transformations during rolling and analysis of material properties, for which analytical dependences were not developed [15 – 19].

The aim of this work is to determine the thermomechanical coefficients for calculating flow stress of selected steel on the basis of laboratory and industrial studies. In order to achieve the formulated target, various steel grades were analyzed by means of compression and rolling tests, their rheological properties were determined, and the model was proposed in accordance with machine learning methods for calculating coefficients of the Hansel–Spittel equation.

Analyzed materials, procedures and equipment

Four variants of chemical composition of steels were considered in this work used for production of rolled products for pipes, grade K52 – K60. The chemical composition of the steels considered is summarized in Table 1. Steels 1 – 4 are mentioned without grade specification in order to preserve confidentiality.

For steel 1, the tests on the Gleeble facility were carried out for basic chemical composition. However, the data from industrial rolling mill was analyzed using several variants of chemical composition, the main difference being the content of niobium.

Compression test is one of the most popular methods used to determine rheological properties. This method allows carry out tests with high strain (about 60 %) and strain rate up to 20–30 s^{-1} to be carried out. In this work the compression tests were carried out on the Gleeble facility. A typical sample was a cylinder with the diameter of 10 mm and the height of 15 mm.

One drawback of the method is changes in the sample shape upon deformation from cylindrical to barrel type. To reduce barrel distortion, a lining made of graphite and tantalum foils was used between the dies and the sample (Fig. 1). The samples were tested in the temperature range

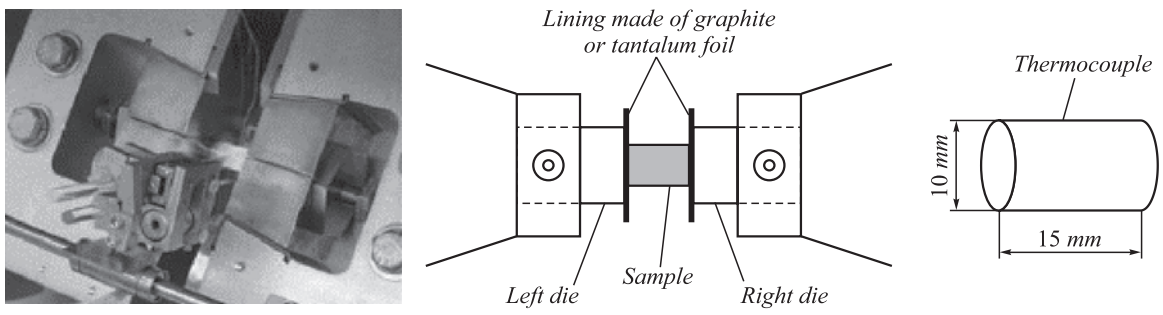

Fig. 1. External view of the Gleeble 3800 test block (*a*), strain layout (*b*) and sample for the experiment (*c*)

Рис. 1. Внешний вид испытательного блока Gleeble 3800 (*a*), схема деформации (*b*) и образец для эксперимента (*c*)

of 750 – 1150 °C (with the increment of 50 °C) at three strain rates: 0.1; 1, and 10 s^{-1}. Therefore, 30 tests were carried out for each steel grade. To obtain reliable results, a thermal cycle was applied consisting of:

– treatment for solid solution, in order to dissolve carbonitride particles;

– heating to 1150 °C;

– preliminary strain (ε = 0.1);

– holding up to complete static recrystallization;

– cooling to test temperature;

– main strain and quenching (Fig. 2).

As a consequence of tests a set of discrete curves was obtained: true strain – true stress σ(ε).

Samples for tests on the Gleeble facility were fabricated from industrial rolled products of the respective steel grades.

Results and discussion

Partial test results of uniaxial compression of samples with the diameter of 10 mm and the height of 15 mm for steels 2 and 4 at the strain rate of 1 s^{-1} are shown in Fig. 3.

The curves obtained can be subdivided into two types. The first type describe strain comprised simultaneously of strengthening and softening, and their ratio determine the form of the curve. At the same time, softening starts with very little strain dynamic. This tries to restore a previous state due to redistribution of dislocations. After achieving equilibrium, the stress remains actually the same with increase in strain degree. The curves of the first type can be observed in a significant part of the considered range of temperature and strain parameters. For example, for steel 4 in Fig. 3 – these are the curves at 1050 and 950 °C.

The curves of the second type are obtained due to low activation energy under the given strain conditions. Dynamic recrystallization starts after achieving critical density of dislocations at certain strain. If the dynamic recrystallization starts before the achievement of equilibrium state between strengthening and softening, then the following is observed decrease in stress with strain increase. The curves of the second type are observed in the region of higher temperatures and low strain rates. In Fig. 3, these are the curves at 1150 °C.

As mentioned above, the results of compression tests on the Gleeble facility are true stress as a function of true strain. However, this dependence cannot be directly applied to the calculation of flow stress in strain source upon rolling due to discreteness of the curves. For correct use it is required to convert true stress into average stress using the following equation [20]

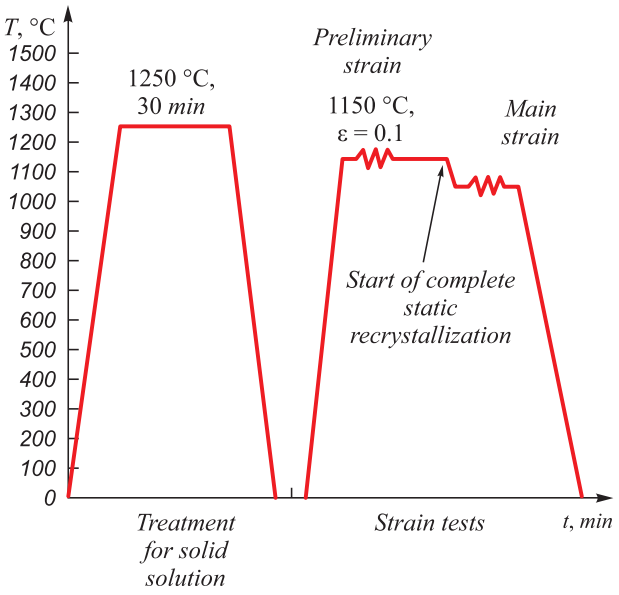

Fig. 2. Test thermal cycle

Рис. 2. Термический цикл испытания

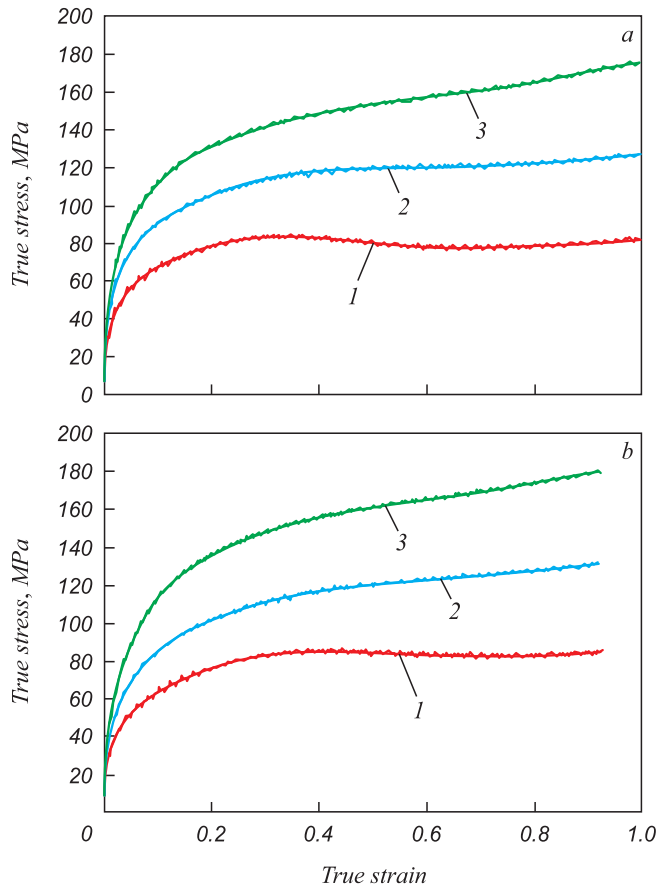

Fig. 3. Effect of temperature 1150 (*1*), 1050 (*2*), 950 °C (*3*) and true strain on true stress of steels 2 (*a*) and 4 (*b*) at a strain rate of 1 s^{-1}

Рис. 3. Влияние температуры 1150 (*1*), 1050 (*2*), 950 °C (*3*) и деформации на истинное напряжение сталей 2 (*a*) и 4 (*b*) при скорости деформации 1 $с^{-1}$

$$\sigma_c = \frac{\int_{\varepsilon_1}^{\varepsilon_2} \sigma(\varepsilon) d\varepsilon}{\varepsilon_2 - \varepsilon_1}, \quad (1)$$

where σ(ε) is the stress curve obtained on Gleeble facility; ε_1, ε_2 are the initial and final value of true strain at the segment.

Also, for ease of calculation of rolling modes, the true strain can be converted into a relative one using the following equation

$$\varepsilon_{rel} = 1 - e^{-\varepsilon}. \quad (2)$$

Figure 4 illustrates the curves before and after conversion.

The influence of strain degree, strain rate and temperature obtained in the form of curves are often described by the Hansel–Spittel equation [1]

$$\sigma = A_1 A_2 A_3 \varepsilon^{m_1} u^{m_2} e^{-m_3 T} \sigma_b, \quad (3)$$

where $A_1, A_2, A_3, m_1, m_2, m_3$ are the empirical coefficients; e is the relative strain; u is the strain rate; T is the metal temperature; σ_b is the average flow stress at basic test parameters (in this work taken equal to ε = 10 %, u = 1 s^{-1}, T = 900 °C).

To eliminate the influence of variations, all the curves were reduced to one basis in terms of strains. The conversion procedure is illustrated in Fig. 5. On the basis of the obtained data linear regression analysis was carried out for Eq. (3), and the result of the approximation was the coefficients $m_0 = \ln(A_1 A_2 A_3 \sigma_6)$, m_1, m_2, m_3

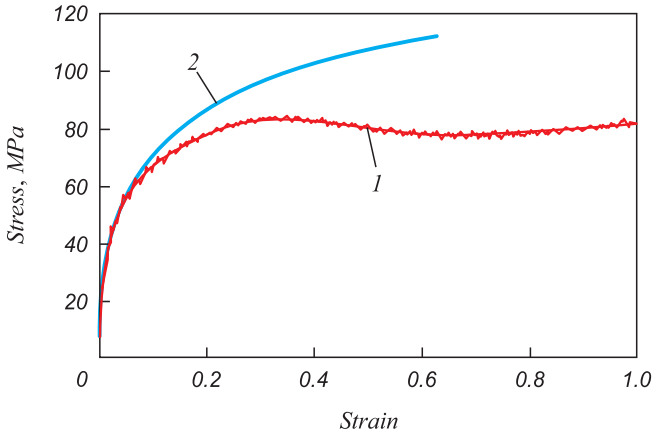

Fig. 4. Comparison of true (*1*) and average (*2*) stresses of flow of steel 2 at 1150 °C and strain rate of 1 s^{-1}

Рис. 4. Сравнение кривых истинного (*1*) и среднего (*2*) напряжения течения стали 2 при температуре 1150 °C и скорости деформации 1 $с^{-1}$

$$\ln\sigma = \ln(A_1 A_2 A_3 \varepsilon^{m_1} u^{m_2} e^{-m_3 T} \sigma_b); \quad (4)$$

$$\ln\sigma = \ln(A_1 A_2 A_3 \sigma_b) + m_1 \ln\varepsilon + m_2 \ln u - m_3 T. \quad (5)$$

As a result, the following equations were obtained for the considered steel grades:

$$\sigma_{steel\ 1} = 2245\varepsilon^{0.2864} u^{0.1001} e^{-0.00274T}; \quad (6)$$

$$\sigma_{steel\ 2} = 2827\varepsilon^{0.3334} u^{0.1097} e^{-0.00288T}; \quad (7)$$

$$\sigma_{steel\ 3} = 1818\varepsilon^{0.2544} u^{0.1119} e^{-0.00262T}; \quad (8)$$

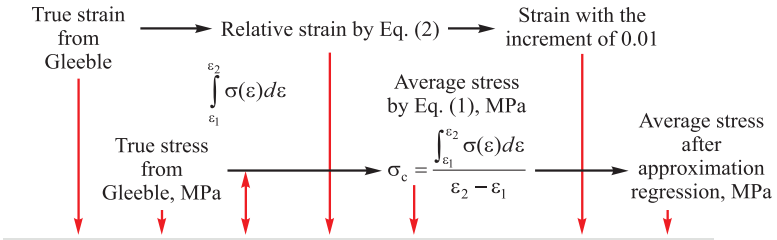

	A	B	C	D	E	F	G	H
1	0	12,12574	0	0	0		0	0
2	8E-05	12,36211	0,000980	8E-05	12,24393		0,01	49,35890
3	0,00017	11,80127	0,002067	0,00017	12,15804		0,02	59,00201
4	0,00028	12,44327	0,003400	0,00028	12,14399		0,03	65,93980
5	0,00029	11,28970	0,003519	0,00029	12,13442		0,04	70,93313
6	0,00035	11,83888	0,004213	0,00035	12,03668		0,05	74,79515
7	0,00041	11,89151	0,004925	0,00041	12,01158		0,06	77,91432
8	0,00052	11,94710	0,006236	0,00052	11,99206		0,07	80,53330
9	0,00053	11,40753	0,006353	0,00053	11,98613		0,08	82,79469
10	0,00053	11,47177	0,006353	0,00053	11,98613		0,09	84,80606
11	0,00053	12,03976	0,006353	0,00053	11,98613		0,10	86,57971
12	0,00086	11,70751	0,010271	0,00086	11,94296		0,11	87,91336
13	0,00088	11,78279	0,010506	0,00088	11,93846		0,12	89,27686
14	0,00064	12,06498	0,007644	0,00064	11,94393		0,13	90,75065

Fig. 5. Conversion algorithm of true stress – true strain to average flow stress – strain

Рис. 5. Алгоритм пересчета кривых истинное напряжение – истинная деформация в среднее напряжение течения – деформация

$$\sigma_{\text{steel 4}} = 2649\varepsilon^{0.3142}u^{0.0989}e^{-0.00285T}. \quad (9)$$

Another possible method of obtaining data on flow stress is to analyze results from industrial rolling mills. In comparison with laboratory conditions, the industrial environment can entail higher strain degrees, complicated strain–stress states, significant temperature heterogeneity with large size of workpiece, non-standard friction conditions and other factors, making obtaining of precise results more difficult.

In this paper it is proposed to use reverse calculations of flow stress from rolling force using classical approaches [2], based on data from industrial rolling mill 5000. Then, to calculate the coefficients of the equation of the Hansel–Spittel equation. The calculations were based on each separate pass (the data from more than 310 thousand passes were studied).

This work analyzed only roughing stage. The rolling width was from 2500 to 4500 mm, and the thickness was from 50 to 350 mm. The remaining parameters in the learning sampling were varied as follows: strain from 0.02 to 0.27; strain rate from 0.42 to 5.93 s^{-1}, temperature from 920 to 1150 °C.

The flow stress was calculated using the data from rolling mill (thickness, compression, diameter of rolls, temperature and other process variables). This was based on a procedure similar but inverse to calculations of rolling force according to Tselikov [2]. Based on the example of steel 1, let us consider the form of the dependence obtained in comparison with data from the Gleeble facility (Fig. 6).

At compressions more than 10 %, the properties determined by the two methods are identical, herewith, up to 10 % the flow stress from the rolling mill significantly exceed the data from Gleeble facility. We believe that this can be attributed to the features of recrystallization of the austenitic grain, as well as to errors in back calculation of flow stress when classical theories of rolling are used. It should be mentioned that this effect is observed not for all variants of steel grades but mainly for those containing niobium.

To consider this, a model was developed on the basis of gradient boosting (Catboost library). As a learning sampling, the data for steel 1 was taken for different chemical compositions (7 variants in total). 15 features were used: chemical composition, compression; time before passes; strain rate; rolling thickness; temperature and number of passes. The relative difference between the calculated flow stress from the rolling mill and the data from the Gleeble facility was taken as the targeted feature. The values obtained were subdivided into testing and learning samplings in the ratio of 75 – 25 %.

The RMSE (root mean square error) was taken as the loss function. In addition, the R2 metrics, coefficient of determination, was used for quality estimation of the obtained forecasted data.

The model was traoned by selection of optimum parameters using grid_search, and carried out as follows:

– 'learning_rate': [0.05, 0.1, 0.3];

– 'depth' (tree depth, that is, number of partitions before forecast): [4, 6, 8, 10];

– 'l2_leaf_reg' (coefficient of regularization l2): [4, 6, 8].

The best parameters were as follows: 'depth' = 8, 'learning rate' = 0.3, 'l2_leaf_reg' = 6. The obtained precision of the model by the RMSE metrics is 3.2 MPa, R2 0.97.

The most important features are illustrated in Fig. 7. As can be seen, the most important are the features directly influencing of strengthening and softening, namely: strain, niobium content, strain rate.

The model performance was then tested for steels 2 – 4. Dependences of flow stress based on data from rolling mill

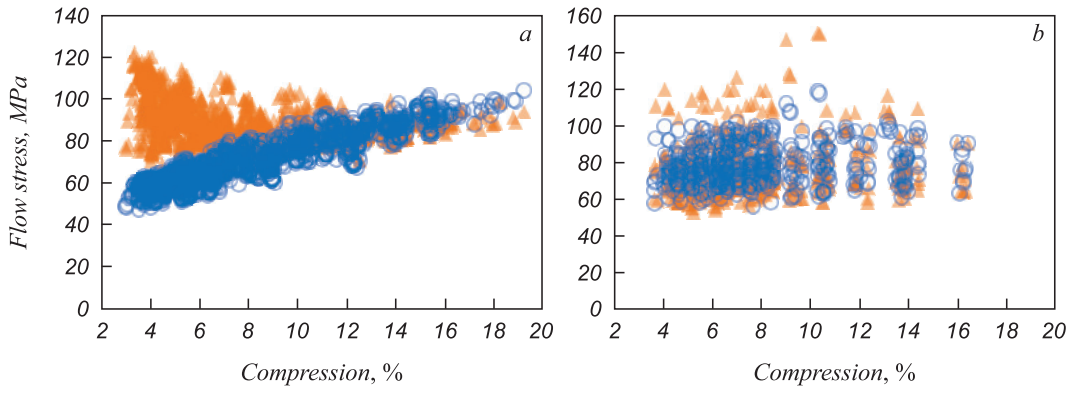

Fig. 6. Comparison of calculated flow stress using industrial data (▲)
with data from Gleeble facility (○) for steel 1 in two versions – with (*a*) and without niobium (*b*)

Рис. 6. Сравнение расчетного сопротивления деформации при помощи промышленных данных (▲)
и с установки Gleeble (○) для стали 1 в двух вариантах – с ниобием (*a*) и без ниобия (*b*)

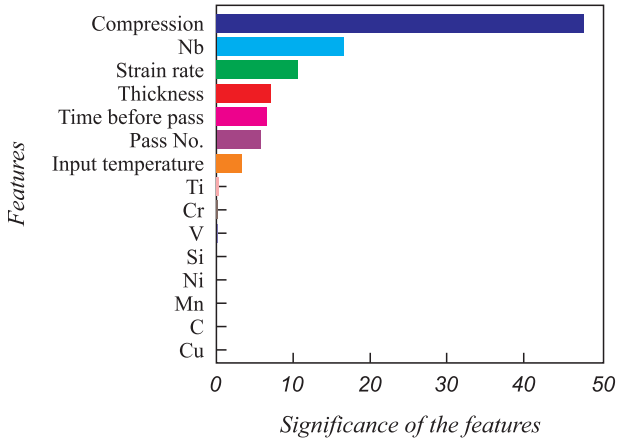

Fig. 7. Significance level of the model features

Рис. 7. Уровень значимости признаков для модели

before and after application of the model to the mentioned steels are shown below.

As can be seen in Fig. 8 and Table 2, application of the model significantly improves the accuracy of determining flow stress. For steel 2, the RMSE parameter decreased by 6.5 times, and the R2 parameter from negative value increased to 0.94. For steels 3 and 4, the result was less precise – RMSE: 5.37 and 5.88 MPa, R2: 0.89 and 0.85.

On the basis of the data obtained, the coefficients of the Hansel–Spittel equation were calculated. Comparison with the data from the Gleeble is shown in Table 3. The coefficients differ mainly due to the features of description method of stress – strain curves. Therefore, it would be reasonable to compare not single coefficients but their combined action, that is, calculated flow stress. As can be seen in Table 2, the absolute calculated values by two procedures differ by 3 – 7 %.

Therefore, application of the obtained coefficients provides satisfactory precision of determination of flow stress in the above-mentioned range of process variables. The models of flow stress obtained by statistical processing of industrial data can be applied for engineering calculations of PPP.

CONCLUSIONS

The flow stress of four steel grades with various chemical compositions measured by Gleeble was compared with the measurements at rolling mill 5000.

The discrete curves obtained in the experiments were approximated, and the coefficients of the Hansel–Spittel equation were determined.

It was demonstrated that upon calculation of flow stress on the basis of industrial data at compression less than 10 %, the data does not agree with those obtained at the Gleeble facility.

In order to account this phenomenon, it was proposed to use the machine learning model based on gradi-

Table 2

Comparison of the determination precision of flow stress before and after application of the model

Таблица 2. **Сравнение точности определения сопротивления деформации до и после использования модели**

Steel No.	Before application of the RMSE model, MPa	Before application of the R2 model	After application of the RMSE model, MPa	After application of the R2 model
2	20.40	–8.850	3.74	0.938
3	9.15	0.574	5.37	0.887
4	17.20	–2.170	5.88	0.848

Table 3

Comparison of the HenselSpittel coefficients according to the data obtained from Mill5000 and from Gleeble facility

Таблица 3. **Сравнение коэффициентов Хензеля-Шпиттеля по данным, полученным со стана 5000 и с установки Gleeble**

Steel No.	const	*k*1	*k*2	*k*3
2 (industrial data)	2607	0.345	0.143	–0.00279
2 (Gleeble data)	2827	0.333	0.109	–0.00288
3 (industrial data)	1547	0.163	0.184	–0.00275
3 (Gleeble data)	1818	0.254	0.111	–0.00262
4 (industrial data)	2321	0.276	0.166	–0.00286
4 (Gleeble data)	2649	0.314	0.098	–0.00285

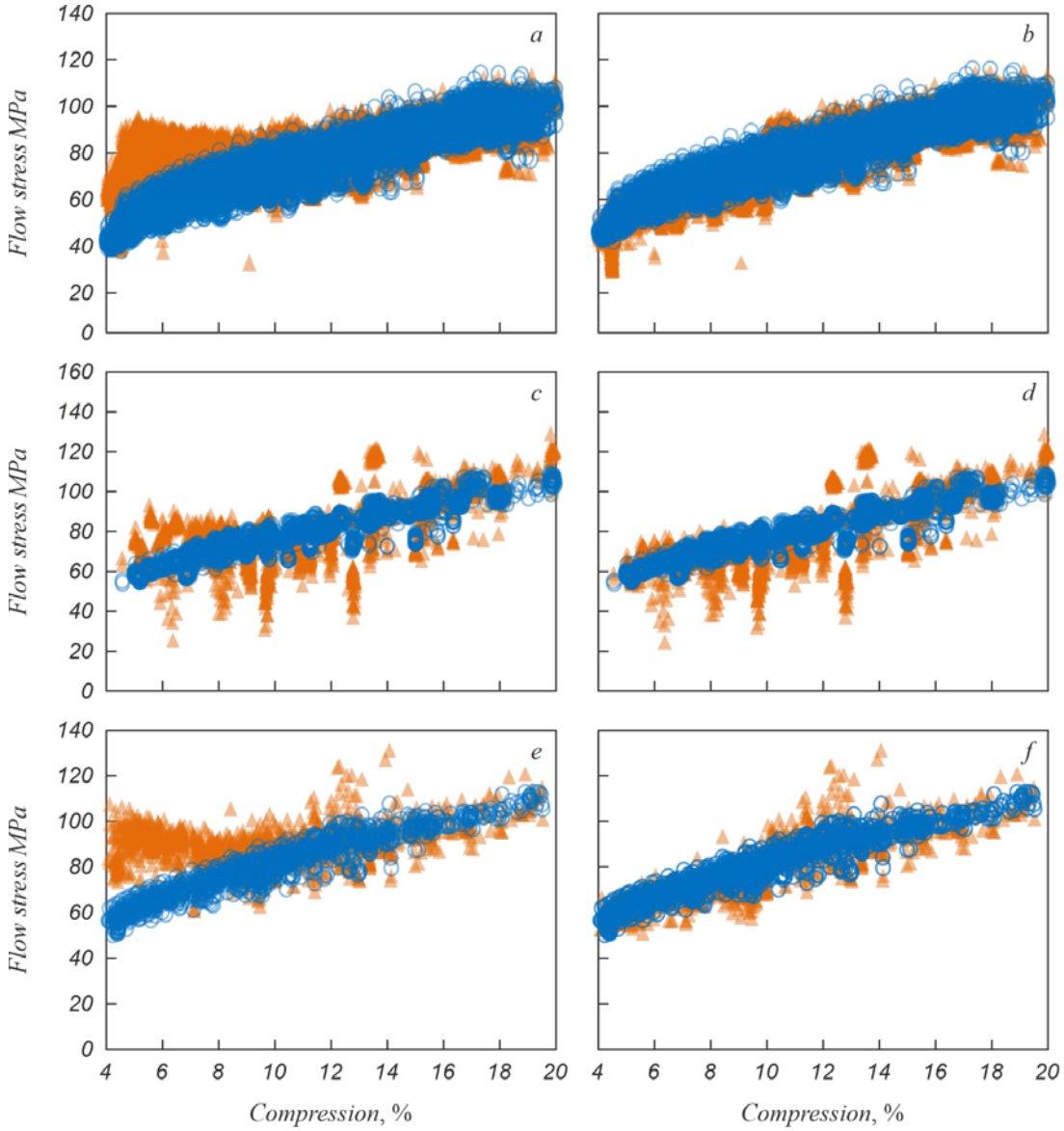

Fig. 8. Flow stress as a function of compression for steel 2 (*a*, *b*), 3 (*c*, *d*), 4 (*e*, *f*)
before (*a*, *c*, *e*) and after (*b*, *d*, *f*) application of the model:
▲ – industrial data; ○ – data from the Gleeble installation

Рис. 8. Зависимость сопротивления деформации от обжатия для стали 2 (*a*, *b*), 3 (*c*, *d*), 4 (*e*, *f*)
до (*a*, *c*, *e*) и после (*b*, *d*, *f*) применения модели:
▲ – промышленные данные; ○ – данные с установки Gleeble

ent boosting (Catboost library) . The best model parameters were as follows: 'depth' = 8, 'learning_rate' = 0.3, 'l2_leaf_reg' = 6. The model learning was based on industrial and laboratory data of one and the same steel grade with several variants of chemical composition. The obtained precision of the model with test selection by the RMSE metrics equals to 3.2 MPa, R2 is 0.97.

The use of this model allowed to achieve the precision of flow stress determination to be increased significantly. For steel 2, the RMSE parameter decreased by 6.5 times. The R2 parameter from negative, increased to 0.94. For steels 3 and 4, the results were less precise – RMSE: 5.37 and 5.88 MPa, R2: 0.89 and 0.85.

A comparison of the industrial values of flow stress with the data obtained by Gleeble demonstrated close results and the capability to use the described approach to analyze steel flow stress based on industrial data.

References / Список литературы

1. Hensel A., Spittel T. *Kraft- und Arbeitsbedarf bildsamer Formgebungsverfahren*. Leirzig: Verlag; 1978. (In Germ.).
Хензель А., Шпиттель Т. *Расчет энергосиловых параметров в процессах обработки металлов давлением*. Москва: Металлургия; 1982: 360.
2. Nikitin G.S. *Theory of Longitudinal Continuous Rolling*. Moscow: Bauman MSTU; 2009: 203. (In Russ.).

Никитин Г.С. *Теория продольной непрерывной прокатки*. Москва: МГТУ им. Баумана; 2009: 203.

3. Muntin A.V., Kurenkov Yu.M., Kolesnikov A.G. C Modern technological solutions and equipment for the production of ultra-thin hot-rolled strip. *Proizvodstvo prokata*. 2016; (8): 13–21. (In Russ.).

   Мунтин А.В., Куренков Ю.М., Колесников А.Г. Современные технологические решения и оборудование для производства ультратонкой горячекатаной полосы. *Производство проката*. 2016; (8): 13–21.
4. Muntin A.V. Advanced technology of combined thin slab continuous casting and steel strip hot rolling. *Metallurgist*. 2019; 62 (9–10): 900–910. https://doi.org/10.1007/s11015-019-00747-5

   Мунтин А.В. Передовые технологии совмещенного процесса непрерывного литья тонких слябов и горячей прокатки стальной полосы. *Металлург*. 2018; (9): 43–51.
5. Vannucci M., Colla V., Dimatteo A. Improving the estimation of mean flow stress within hot rolling of steel by means of different artificial intelligence techniques. *IFAC Proceedings Volumes*. 2013; 46(9): 945–950. https://doi.org/10.3182/20130619-3-RU-3018.00326
6. Thakur S.K., Das A.K., Jha B.K. Development of an integrated flow stress and roll force models for plate rolling of microalloyed steel. *Steel Research International*. 2022; 93(2): 2100479. https://doi.org/10.1002/srin.202100479
7. Murugesan M., Yu J., Jung K., Cho S., Bhandari K.S., ChungW., Lee C. Supervised machine learning approach for modeling hot deformation behavior of medium carbon steel. *Steel Research International*. 2023; 93(1): 2200188. https://doi.org/10.1002/srin.202200188
8. Aghasafari P., Abdi H., Salimi M. Artificial neural network modeling of flow stress in hot rolling. *ISIJ International*. 2014; 54(4): 872–879. https://doi.org/10.2355/isijinternational.54.872
9. Bagheripoor M., Bisadi H. Application of artificial neural networks for the prediction of roll force and roll torque in hot strip rolling process. *Applied Mathematical Modelling*. 2013; 37(7): 4593–4607. https://doi.org/10.1016/j.apm.2012.09.070
10. Murugesan M., Sajjad M., Jung D.W. Hybrid machine learning optimization approach to predict hot deformation behavior of medium carbon steel material. *Metals*. 2019; 9(12): 1315. https://doi.org/10.3390/met9121315
11. Moon I.Y., Jeong H.W., Lee H.W., Kim S.-J., Oh Y.-S., Jung J., Oh S., Kang S.-H. Predicting high temperature flow stress of nickel alloy A230 based on an artificial neural network. *Metals*. 2022; 12(2): 223. https://doi.org/10.3390/met12020223
12. Cao G.-M., Gao Z.-W., Gao X.-Y. Predicting flow stress of Ni steel based on machine learning algorithm. *Proceedings of the Institution of Mechanical Engineers, Part C: Journal of Mechanical Engineering Science*. 2022; 236(8): 4253–4266. https://doi.org/10.1177/09544062211048175
13. Lin Y.C., Zhang J., Zhong J. Application of neural networks to predict the elevated temperature flow behavior of a low alloy steel. *Computational Materials Science*. 2008; 43(4): 752–758. https://doi.org/10.1016/j.commatsci.2008.01.039
14. Stendal J.A., Bambach M., Eisentraut M., Sizova I., Weiß S. Applying machine learning to the phenomenological flow stress modeling of TNM-B1. *Metals*. 2019; 9(9): 220. https://doi.org/10.3390/met9020220
15. Versino D., Tonda A., Bronkhorst C.A. Data driven modeling of plastic deformation. *Computer Methods in Applied Mechanics and Engineering*. 2017; 318: 981–1004. https://doi.org/10.1016/j.cma.2017.02.016
16. Wang L.-y., Li L., Zhang Zh.-h. Accurate descriptions of hot flow behaviors across β transus of Ti-6Al-4V alloy by intelligence algorithm GA-SVR. *Journal of Materials Engineering and Performance*. 2016; 25: 3912–3923. https://doi.org/10.1007/s11665-016-2230-1
17. Zhang X., Zhi C., Wang Y., Li Y. Constitutive parameters identification of Q345E steel during hot deformation with inverse methods based on teaching–learning-based optimisation algorithm. *Materials Research Innovations*. 2015; 19(8): 634–638. https://doi.org/10.1179/1432891715Z.0000000001874
18. Santosh S., Sampath V., Mouliswar R.R. Hot deformation characteristics of NiTiV shape memory alloy and modeling using constitutive equations and artificial neural networks. *Journal of Alloys and Compounds*. 2022; 901: 163451. https://doi.org/10.1016/j.jallcom.2021.163451
19. Bambach M., Gerster S., Herty M. Online data assimilation of a hybrid flow stress model by particle filtering. *CIRP Annals.* 2021; 70(1): 255–260. https://doi.org/10.1016/j.cirp.2021.04.002
20. Zinyagin A.G. *Improving the processes of rolling and cooling of sheets from pipe steel on mill-5000: Cand. Tech. Sci. Diss*. Moscow; 2014: 159. (In Russ.).

    Зинягин А.Г. *Совершенствование процессов прокатки и охлаждения листов из трубных марки сталей на стане-5000: Диссертация ... кандидата технических наук*. Москва; 2014: 159.

Information about the Authors / Сведения об авторах

Aleksei G. Zinyagin, *Cand. Sci. (Eng.), Assist. Prof.,* Bauman Moscow State Technical University (Bauman MSTU), *Chief Innovation Specialist,* JSC "Vyksa Metallurgical Plant"
E-mail: ziniagin_ag@bmstu.ru

Aleksandr V. Muntin, *Cand. Sci. (Eng.), Assist. Prof. of the Chair "Rolling Equipment and Technologies",* Bauman Moscow State Technical University (Bauman MSTU); *Deputy Director for Research Activities,* JSC "Vyksa Metallurgical Plant"
ORCID: 0000-0002-8926-0110
E-mail: muntin_av@omk.ru

Алексей Геннадиевич Зинягин, *к.т.н., доцент,* Московский государственный технический университет им. Н.Э. Баумана (МГТУ им. Баумана); *главный специалист по инновациям,* АО «Выксунский металлургический завод»
E-mail: ziniagin_ag@bmstu.ru

Александр Вадимович Мунтин, *к.т.н., доцент кафедры «Оборудование и технологии прокатки»,* Московский государственный технический университет им. Н.Э. Баумана (МГТУ им. Баумана); *заместитель директора по научно-исследовательской деятельности,* АО «Выксунский металлургический завод»
ORCID: 0000-0002-8926-0110
E-mail: muntin_av@omk.ru

Mariya O. Kryuchkova, *Senior Lecturer,* Bauman Moscow State Technical University (Bauman MSTU)
E-mail: mariya.mironova@bmstu.ru

Мария Олеговна Крючкова, *старший преподаватель,* Московский государственный технический университет им. Н.Э. Баумана (МГТУ им. Баумана)
E-mail: mariya.mironova@bmstu.ru

Contribution of the Authors / Вклад авторов

A. G. Zinyagin – scientific guidance, conducting research.
A. V. Muntin – formation of the main idea of the work, scientific guidance.
M. O. Kryuchkova – analysis of the research results; data collection and analysis.

А. Г. Зинягин – научное руководство, проведение исследований.
А. В. Мунтин – научное руководство, идея работы.

М. О. Крючкова – поиск и анализ публикаций, сбор и анализ данных.

Received 18.08.2022
Revised 16.11.2022
Accepted 05.01.2023

Поступила в редакцию 18.08.2022
После доработки 16.11.2022
Принята к публикации 05.01.2023

METALLURGICAL TECHNOLOGIES / МЕТАЛЛУРГИЧЕСКИЕ ТЕХНОЛОГИИ

UDC 621.762:669.018.8
DOI 10.17073/0368-0797-2023-1-80-85

Original article
Оригинальная статья

Properties of spherical metal powder manufactured by plasma spraying of 03Cr17Ni10Mo2 stainless steel wire

M. A. Kaplan [1], A. D. Gorbenko [1, 2], A. Yu. Ivannikov [1], S. V. Konushkin [1], A. V. Mikhailova [1, 2], A. A. Kirsankin [1], A. S. Baikin [1], K. V. Sergienko [1], E .O. Nasakina [1], A. G. Kolmakov [1], M. A. Sevost'yanov [1, 2]

[1] **Baikov Institute of Metallurgy and Materials Science, Russian Academy of Sciences** (49 Leninskii Ave., Moscow 119991, Russian Federation)
[2] **All-Russian Research Institute of Phytopathology** (5 Institut Str., Bol'shie Vyazemy Vil., Odintsovo District, Moscow Region 143050, Russian Federation)

mkaplan@imet.ac.ru

Abstract. Stainless steel spherical powders are commonly used as additives in such manufacturing processes as selective laser melting, selective laser sintering, direct laser sintering, electron beam melting, and others. These processes require high-quality spherical powders. The purpose of this study is to develop a manufacturing process for making spherical powder by plasma spraying of a 1 mm dia. wire, stainless steel 03Cr17Ni10Mo2 (US analog: 316L steel grade) and to analyze the powder suitability for additive manufacturing. We refined the spherical powder manufacturing process and studied the spraying conditions vs. –160 μm fraction yield relationship, since this fraction is required for additive manufacturing. As the arc power gas flow rate increases, the –160 μm fraction yield increases to over 70 %. The powder has high fluidity (17.6 ± 1 s), bulk density (4.15 ± 0.1 g/cm^3), and tapped density (4.36 ± 0.2 g/cm^3). It is suitable for additive manufacturing applications. We also studied the effect of the spherical powder fraction size distribution on the fluidity, bulk density, and tapped density. The best results (fluidity: 16.64 ± 1 s; bulk density: 4.16 ± 0.1 g/cm^3; tapped density: 4.38 ± 0.2 g/cm^3) were obtained for –90 μm fraction. With these properties, the powder meets the basic additive manufacturing requirements: less than the 30 s/50 g fluidity, and bulk density exceeding 3 g/cm^3.

Keywords: stainless steel, plasma spraying, spherical powder, powder properties, grain size distribution, morphology, fluidity, bulk density

Acknowledgements: The study was carried out within the framework of the State Assignment No. 075-01176-23-00 and supported by the Presidential Scholarship SP-4955.2022.4.

For citation: Kaplan M.A., Gorbenko A.D., Ivannikov A.Yu., Konushkin S.V., Mikhailova A.V., Kirsankin A.A., Baikin A.S., Sergienko K.V., Nasakina E.O., Kolmakov A.G., Sevost'yanov M.A. Properties of spherical metal powder manufactured by plasma spraying of 03Cr17Ni10Mo2 stainless steel wire. *Izvestiya. Ferrous Metallurgy*. 2023; 66(1): 69–85. https://doi.org/10.17073/0368-0797-2023-1-80-85

Исследование характеристик сферического порошка, полученного методом плазменного распыления проволоки из коррозионностойкой стали 03Х17Н10М2

М. А. Каплан [1], А. Д. Горбенко [1, 2], А. Ю. Иванников [1], С. В. Конушкин [1], А. В. Михайлова [1, 2], А. А. Кирсанкин [1], А. С. Баикин [1], К. В. Сергиенко [1], Е .О. Насакина [1], А. Г. Колмаков [1], М. А. Севостьянов [1, 2]

[1] **Институт металлургии и материаловедения им. А.А. Байкова РАН** (Россия, 119991, Москва, Ленинский пр., 49)
[2] **Всероссийский научно-исследовательский институт фитопатологии** (Россия, 143050, Московская область, Одинцовский район, р.п. Большие Вяземы, ул. Институт, владение 5)

mkaplan@imet.ac.ru

Аннотация. В настоящее время порошок со сферическими частицами из коррозионностойких сталей используют в таких распространенных аддитивных методах, как селективное лазерное плавление, селективное лазерное спекание, прямое лазерное спекание, электронно-лучевая плавка и других. Каждый из этих методов предъявляет высокие требования к характеристикам сферических частиц порошка коррозионностойких сталей. Данная работа посвящена получению сферического порошка методом плазменного распыления проволоки диаметром 1 мм из коррозионностойкой стали 03Х17Н10М2 и исследованию характеристик порошка на пригодность для применения в аддитивных методах. Отработана технология получения сферического порошка и изучена зависимость влияния режимов распыления на выход фракции менее 160 мкм, пригодной для аддитивных методов. С увеличением мощности и расхода газа выход фракции менее 160 мкм увеличивается и достигает более 70 %. Полученный порошок обладает высокой текучестью (17,6 ± 1 с), насыпной плотностью (4,15 ± 0,1 г/см^3), плотностью после утряски (4,36 ± 0,2 г/см^3) и пригоден для применения в аддитивном производстве. Также изучена зависимость влияния фракции сферического порошка на текучесть, насыпную плотность и плотность после утряски. Наилучшие характеристики получились для фракции –90 мкм: текучесть 16,64 ± 1 с, насыпная плотность 4,16 ± 0,1 г/см^3 и плотность после утряски 4,38 ± 0,2 г/см^3. Данные показатели соответствуют требованиям, предъявляемым к порошкам, применяемым для аддитивного производства, а именно текучести 50 г порошка менее 30 с и насыпной плотности более 3 г/см^3.

Ключевые слова: коррозионностойкая сталь, плазменное диспергирование, сферический порошок, свойства порошков, гранулометрический состав, морфология, текучесть, насыпная плотность

Благодарности: Исследование выполнено в рамках Госзадания № 075-01176-23-00 при поддержке стипендии Президента СП-4955.2022.4.

Для цитирования: Каплан М.А., Горбенко А.Д., Иванников А.Ю., Конушкин С.В., Михайлова А.В., Кирсанкин А.А., Баикин А.С., Сергиенко К.В., Насакина Е.О., Колмаков А.Г., Севостьянов М.А. Исследование характеристик сферического порошка, полученного методом плазменного распыления проволоки из коррозионностойкой стали 03Х17Н10М2. *Известия вузов. Черная металлургия*. 2023; 66(1): 81–85. https://doi.org/10.17073/0368-0797-2023-1-80-85

Introduction

Stainless steels have many applications (medical equipment, agriculture, aerospace, automotive, and food industries) for their high strength, ductility, and corrosion resistance [1 – 4]. A chromium-rich oxide layer builds up on the surface and protects the steel from corrosion. 03Cr17Ni10M2 (US analog: 316L) is a popular stainless steel grade. To date, it is the most cost-efficient material for corrosive environments. The steel is widely available, easy to manufacture, and has high corrosion resistance [5 – 9].

Advanced additive manufacturing processes can make complex parts without the limitations of conventional subtractive manufacturing [10 – 13]. The raw material is metallic spherical powder. Its quality is paramount for the properties of the final product [14]. Spherical powders for additive manufacturing should have such properties as high fluidity, bulk density, homogeneous chemical composition, and particle size distribution [15 – 18]. The particle size of additive manufacturing powders is less than 160 μm. For example, melting processes use powders with particle sizes less than 60 μm, and surfacing, less than 160 μm [19]. Powders with particle sizes over 160 μm can be used in other processes such as sintering and/or hot pressing.

We refined the plasma spraying process for a higher yield of the particle size fraction suitable for additive manufacturing. We also studied the particle size distribution, morphology, fluidity, bulk, and tapped density of the spherical powder.

Materials and Methods

The powder was made from an industrial-grade wire, 1 mm dia., 03Cr17Nir10M2 (316L) steel grade. We made the spherical powder by wire spraying using a lab plasma spraying system (Russian Federation patent No. 2749403). Fig. 1 shows the system layout.

Air is evacuated from chamber *1* and then the chamber is filled with argon. Next, the plasmatron *2* is activated to generate a plasma jet, and wire feeder *3* feeds wire *4*. An electric arc is excited between the free ends of the wires, and the wire melts. The system has feeders 5 and 6 delivering power to the wires to ignite an electric arc. Spherical particles are produced by pulverizing with the plasma jet. The atomized powder particles move along chamber *1* (direction *I*). Annular nozzle *7* produces a counter flow of cooling gas which slows down and cools the powder particles (direction *II*). The powder particles are collected in bin *8*. Argon was used as the plasma-forming and atomizing gas.

After atomization, the powder was separated into fractions using an ANALYSETTE 3 SPARTAN vibratory sieve shaker (Germany). We used a JEOL JSM-IT500 scanning electron microscope (SEM) to obtain the powder particle images. An Analysette 22 NanoTec laser particle sizer was used for powder particle size analysis. The fluidity and bulk density were measured with an HFlow-1 Hall flowmeter, in accordance with the state standards GOST 20899-98 and GOST 19440-94, Part 1. The tapped density was measured in accordance with the state standard GOST 25279-93 using a BeDensi T1 analyzer.

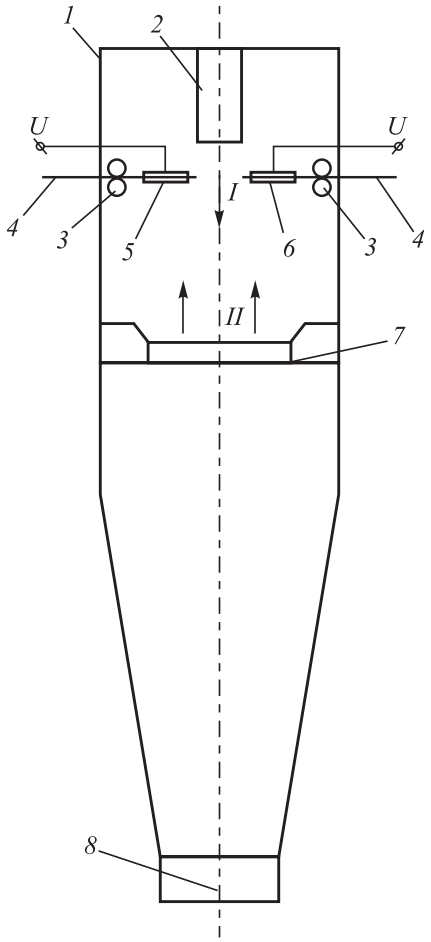

Fig. 1. Layout of wire plasma spraying system

Рис. 1. Схема установки по плазменному диспергированию проволоки

Results and Discussion

We investigated the effect of electric arc power and gas flow rate on the yield of fraction suitable additive manufacturing (less than 160 μm) using a 1 mm dia. industrial-grade wire, 03Cr17H10M2 (316L) steel grade. We selected the process variables to make spherical powder by plasma spraying. The results are shown on Fig. 2.

As the electric power and gas flow rate increase, the yield of the –160 μm fraction increases to over 70 %. When the power exceeds 4 kW, the chamber overheats rapidly, so the process has to be paused for cooling. We found the conditions (power: 4 kW; gas flow rate: 250 l/min) for continuous spherical powder manufacturing.

Then we studied the particle size distribution and morphology of the resulting spherical powder made of the 03Cr17Ni10M2 steel grade wire. It was found that 70 % of the particles are smaller than 167 μm (Fig. 3). The SEM images of the powder particles show that the shape of the particles is almost spherical with no visible defects. The powder is suitable for additive manufacturing (Fig. 4).

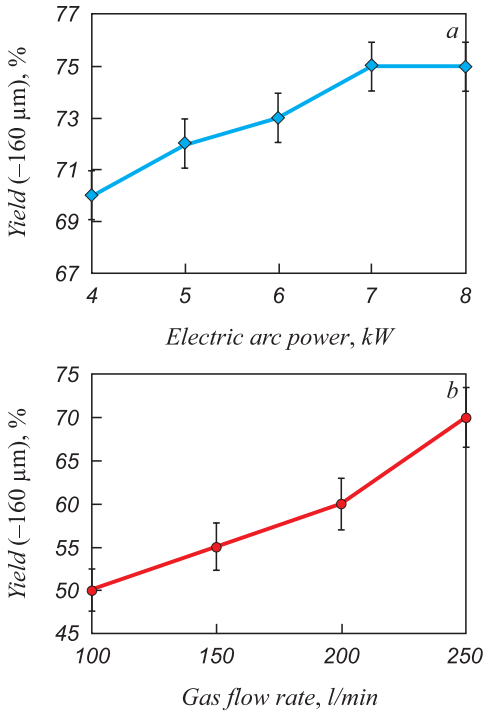

Fig. 2. Spraying conditions vs. yield (<160 μm) of particles suitable for additive manufacturing
a – electric arc power; *b* – gas flow rate

Рис. 2. Влияние режимов распыления на выход фракции менее 160 мкм, применяемой для аддитивных методов:
a – электрическая мощность дуги;
b – расход плазмообразующего и обжимного газа

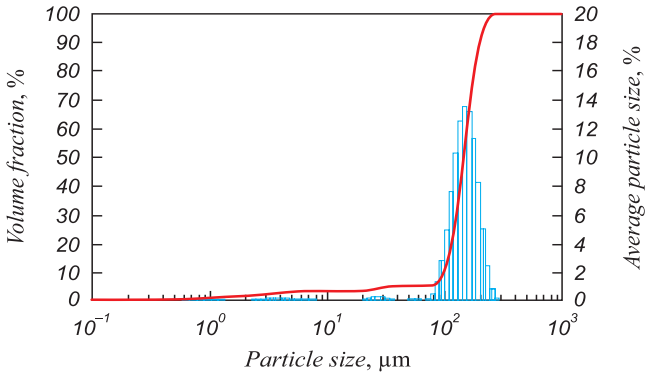

Yield, %	Particle size, μm
10	99.46
20	115.34
30	126.64
40	136.62
50	146.35
60	156.21
70	167.26
80	180.66
90	198.83

Fig. 3. Powder particle size distribution

Рис. 3. Гранулометрический состав порошка

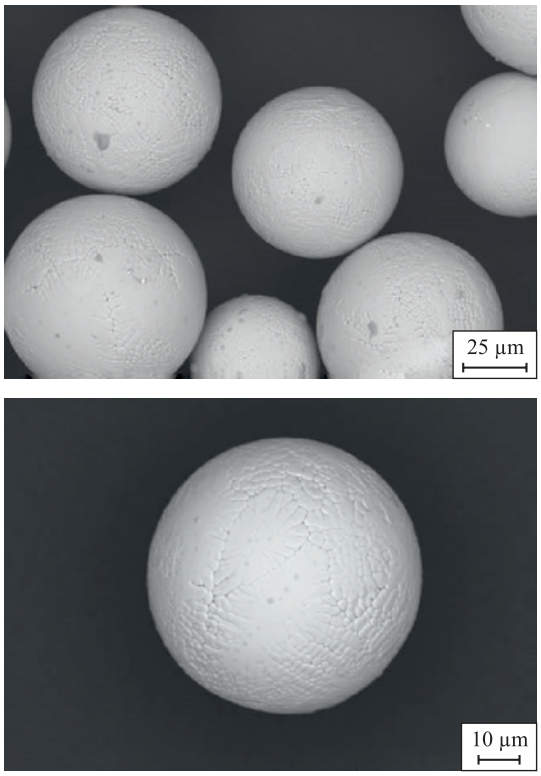

Fig. 4. SEM images of the powder particles made from the 03Ch17Ni10Mo2 (316L) wire

Рис. 4. СЭМ изображения частиц порошка, полученного из проволоки 03Х17Н10М2

We studied the bulk density, fluidity, and tapped density vs. particle size relations. The results are presented in the table.

Powder Properties

Characteristics of the powder

Particle size, μm	250 – 160	160 – 90	–90	–160
Fluidity				
t, s	22.9 ± 1.0	18.62 ± 1.0	16.64 ± 1.0	17.6 ± 1.0
Bulk density				
p, g/cm^3	4.15 ± 0.2	4.15 ± 0.2	4.16 ± 0.2	4.15 ± 0.1
Tapped density				
p, g/cm^3	4.41 ± 0.2	4.35 ± 0.2	4.38 ± 0.2	4.36 ± 0.2

It can be concluded that the smaller the particle size, the higher the fluidity (16.64 to 22.9 s), while the bulk and tapped density for all particle sizes remain unchanged (average values: 4.15 and 4.38 g/cm^3, respectively).

Conclusions

We studied the effect of spraying conditions on the yield of particles smaller than 160 μm suitable for additive manufacturing. As the arc power gas flow rate increase, the –160 μm fraction yield increases to over 70 %.

We refined the spherical powder manufacturing by plasma spraying on a 1 mm dia. industrial-grade wire, 03Cr17Ni10Mo2 (316L) steel grade. The optimum conditions are as follows: 4 kW arc power, 250 l/min gas flow rate. The yield of fractions smaller than 160 μm exceeds 70 %. The resulting powder properties are 17.6 ± 1 s fluidity, 4.15 ± 0.1 g/cm^3 bulk density, and 4.36 ± 0.2 g/cm^3 tapped density. The powder is suitable for additive manufacturing.

We also studied the effect of the spherical powder particle size on the fluidity, bulk density, and tapped density. The best results (fluidity: 16.64 ± 1 s; bulk density: 4.16 ± 0.1 g/cm^3; tapped density: 4.38 ± 0.2 g/cm^3) were obtained for a –90 μm fraction.

References / Список литературы

1. Grabco D., Shikimaka O., Pyrtsac C., Prisacaru A., Barbos Z., Bivol M., Alexandrov S., Vilotic D., Vilotic M. Microstructures generated in AISI 316L stainless steel by Vickers and Berkovich indentations. *Materials Science and Engineering: A*. 2021; 805: 140597. http://doi.org/10.1016/J.MSEA.2020.140597
2. Bekmurzayeva A., Duncanson W.J., Azevedo H.S., Kanayeva D. Surface modification of stainless steel for biomedical applications: Revisiting a century-old material. *Materials Science and Engineering: C*. 2018; 93: 1073–1089. http://doi.org/10.1016/j.msec.2018.08.049
3. Sheik S., Tirumalla A., Gurrala A.K., Mohammed R. Effect of microstructural morphology on corrosion susceptibility of austenitic and super austenitic stainless steels. *Materials Today: Proceedings*. 2022; 66(2): 514–518. http://doi.org/10.1016/j.matpr.2022.06.113
4. Feng W., Wang Z., Sun Q., He Y., Sun Y. Effect of thermo-mechanical processing via rotary swaging on grain boundary character distribution and intergranular corrosion in 304 austenitic stainless steel. *Journal of Materials Research and Technology*. 2022; 19: 2470–2482. https://doi.org/10.1016/j.jmrt.2022.06.032
5. Mehta H., Kaur G., Chaudhary G.R., Prabhakar N., Kaul S., Singhal N.K. Evaluation of corrosion resistant, antimicrobial and cytocompatible behaviour of cobalt based metallosurfactants self-assembled monolayers on 316L stainless steel surface. *Surface and Coatings Technology.* 2022; 444: 128657. https://doi.org/10.1016/j.surfcoat.2022.128657
6. Wongpanya P., Wongpinij T., Photongkam P., Siritapetawee J. Improvement in corrosion resistance of 316 L stainless steel in simulated body fluid mixed with antiplatelet drugs by coating with Ti-doped DLC films for application in biomaterials. *Corrosion Science*. 2022; 208: 110611. https://doi.org/10.1016/j.corsci.2022.110611
7. Zhang D.H., Meng X.C., Zuo G.Z., Huang M., Li L., Xu W., Li C.L., Tang Z.L., Yuan J.S., Liu Y.B., Cao X.G. Study of the corrosion characteristics of 304 and 316L stainless steel in the static liquid lithium. *Journal of Nuclear Materials*. 2021; 553: 153032. https://doi.org/10.1016/j.jnucmat.2021.153032

8. Kaplan M.A., Ivannikov A.Yu., Konushkin S.V., Nasakina E.O., Baikin A.S., Kartabaeva B.B., Gorbenko A.D., Kolmakov A.G., Sevost'yanov M.A. Study of the structure, mechanical characteristics, and antibacterial properties of corrosion-resistant steel alloyed with silver and titanium. *Doklady Chemistry.* 2022; 502(2): 37–44. https://doi.org/10.1134/S001250082202001X

Каплан М.А., Иванников А.Ю., Конушкин С.В., Насакина Е.О., Баикин А.С., Картабаева Б.Б., Горбенко А.Д., Колмаков А.Г., Севостьянов М.А. Исследование структуры, механических и антибактериальных свойств коррозионностойкой стали, легированной серебром и титаном. *Доклады Российской академии наук. Химия, науки о материалах.* 2022; 502(1): 41–49. http://doi.org/10.31857/S268695352201006X

9. Brooks E.K., Brooks R.P., Ehrensberger M.T. Effects of simulated inflammation on the corrosion of 316L stainless steel. *Materials Science and Engineering: C*. 2017; 71: 200–205. http://doi.org/10.1016/j.msec.2016.10.012

10. Singh R., Gupta A., Tripathi O., Srivastava S., Singh B., Awasthi A., Rajput S.K., Sonia P., Singhal P., Saxena K.K. Powder bed fusion process in additive manufacturing: An overview. *Materials Today: Proceedings*. 2020; 26(2): 3058–3070. http://doi.org/10.1016/j.matpr.2020.02.635

11. Ngo T.D., Kashani A., Imbalzano G., Nguyen K.T.Q., Hui D. Additive manufacturing (3D printing): A review of materials, methods, applications and challenges. *Composites Part B: Engineering.* 2018; 143: 172–196. http://doi.org/10.1016/j.compositesb.2018.02.012

12. Haselhuhn A.S., Wijnen B., Anzalone G.C., Sanders P.G., Pearce J.M. In situ formation of substrate release mechanisms for gas metal arc weld metal 3-D printing. *Journal of Materials Processing Technology*. 2015; 226: 50–59. http://doi.org/10.1016/j.jmatprotec.2015.06.038

13. Yap C.Y., Chua C.K., Dong Z.L., Liu Z.H., Zhang D.Q., Loh L.E., Sing S.L. Review of selective laser melting: Materials and applications. *Applied Physics Reviews.* 2015; 2(4): 241101. http://doi.org/10.1063/1.4935926

14. Chen Q., Thouas G.A. Metallic implant biomaterials. *Materials Science and Engineering: R: Reports*. 2015; 87: 1–57. http://doi.org/10.1016/j.mser.2014.10.001

15. Egger G., Gygax P.E., Glardon R., Karapatis N.P. Optimization of powder layer density in selective laser sintering. In: *10th Int. Solid Freeform Fabrication Symp*. 1999: 255–263. http://doi.org/10.26153/tsw/746

16. Sing S.L., An J., Yeong W.Y., Wiria F.E. Laser and electron-beam powder-bed additive manufacturing of metallic implants: A review on processes, materials and designs. *Journal of Orthopedic Research*. 2016; 34(3): 369–385. http://doi.org/10.1002/jor.23075

17. Ganesan V.V., Amerinatanzi A., Jain A. Discrete Element Modeling (DEM) simulations of powder bed densification using horizontal compactors in metal additive manufacturing. *Powder Technology*. 2022; 405: 117557. http://doi.org/10.1016/j.powtec.2022.117557

18. Zhai W., Zhou W., Nai S.M.L., Wei J. Characterization of nanoparticle mixed 316 L powder for additive manufacturing. *Journal of Materials Science & Technology*. 2020; 47:162–168. http://doi.org/10.1016/j.jmst.2020.02.019

19. Kolmakov A.G., Ivannikov A.Yu., Kaplan M.A., Kirsankin A.A., Sevost'yanov M.A. Corrosion-resistant steels in additive manufacturing. *Izvestiya. Ferrous Metallurgy*. 2021; 64(9): 619–650. https://doi.org/10.17073/0368-0797-2021-9-619-650

Колмаков А.Г., Иванников А.Ю., Каплан М.А., Кирсанкин А.А., Севостьянов М.А. Коррозионностойкие стали в аддитивном производстве. *Известия вузов. Черная металлургия.* 2021; 64(9): 619–650. https://doi.org/10.17073/0368-0797-2021-9-619-650

Information about the Authors / Сведения об авторах

Mikhail A. Kaplan, *Junior Researcher,* Baikov Institute of Metallurgy and Materials Science, Russian Academy of Sciences
ORCID: 0000-0002-8635-0719
E-mail: mkaplan@imet.ac.ru

Artem D. Gorbenko, *Research Engineer,* Baikov Institute of Metallurgy and Materials Science, Russian Academy of Sciences; *Research Engineer,* All-Russian Research Institute of Phytopathology
E-mail: artemgorbenk@yandex.ru

Aleksandr Yu. Ivannikov, *Cand. Sci. (Eng.), Senior Researcher,* Baikov Institute of Metallurgy and Materials Science, Russian Academy of Sciences
ORCID: 0000-0003-1113-391X
E-mail: aivannikov@imet.ac.ru

Sergei V. Konushkin, *Junior Researcher,* Baikov Institute of Metallurgy and Materials Science, Russian Academy of Sciences
ORCID: 0000-0002-9574-1957
E-mail: venev.55@mail.ru

Anna V. Mikhailova, *Research Engineer,* Baikov Institute of Metallurgy and Materials Science, Russian Academy of Sciences; *Research Engineer,* All-Russian Research Institute of Phytopathology
E-mail: mikhannavlad@gmail.com

Михаил Александрович Каплан, *младший научный сотрудник,* Институт металлургии и материаловедения им. А.А. Байкова РАН
ORCID: 0000-0002-8635-0719
E-mail: mkaplan@imet.ac.ru

Артем Дмитриевич Горбенко, *инженер-исследователь,* Институт металлургии и материаловедения им. А.А. Байкова РАН; *инженер-исследователь,* Всероссийский научно-исследовательский институт фитопатологии
E-mail: artemgorbenk@yandex.ru

Александр Юрьевич Иванников, *к.т.н., старший научный сотрудник,* Институт металлургии и материаловедения им. А.А. Байкова РАН
ORCID: 0000-0003-1113-391X
E-mail: aivannikov@imet.ac.ru

Сергей Викторович Конушкин, *младший научный сотрудник,* Институт металлургии и материаловедения им. А.А. Байкова РАН
ORCID: 0000-0002-9574-1957
E-mail: venev.55@mail.ru

Анна Владимировна Михайлова, *инженер-исследователь,* Институт металлургии и материаловедения им. А.А. Байкова РАН; *инженер-исследователь,* Всероссийский научно-исследовательский институт фитопатологии
E-mail: mikhannavlad@gmail.com

***Andrei A. Kirsankin*,** *Cand. Sci. (Phys.-Math.), Senior Researcher,* Baikov Institute of Metallurgy and Materials Science, Russian Academy of Sciences
ORCID: 0000-0002-9206-7805
E-mail: akirsankin@imet.ac.ru

***Aleksandr S. Baikin*,** *Research Associate,* Baikov Institute of Metallurgy and Materials Science, Russian Academy of Sciences
E-mail: baikinas@mail.ru

***Konstantin V. Sergienko*,** *Junior Researcher,* Baikov Institute of Metallurgy and Materials Science, Russian Academy of Sciences
E-mail: shulf@yandex.ru

***Elena O. Nasakina*,** *Senior Researcher,* Baikov Institute of Metallurgy and Materials Science, Russian Academy of Sciences
ORCID: 0000-0002-0783-1558
E-mail: nacakina@mail.ru

***Aleksei G. Kolmakov*,** *Corresponding Member of RAS, Dr. Sci. (Eng.), Head of the Laboratory,* Baikov Institute of Metallurgy and Materials Science, Russian Academy of Sciences
ORCID: 0000-0002-4907-951X
E-mail: akolmakov@imet.ac.ru

***Mikhail A. Sevost'yanov*,** *Cand. Sci. (Eng.), Leading Researcher,* Baikov Institute of Metallurgy and Materials Science, Russian Academy of Sciences; *Head of the Center,* All-Russian Research Institute of Phytopathology
ORCID: 0000-0003-2652-8711
E-mail: msevostyanov@imet.ac.ru

***Андрей Александрович Кирсанкин*,** *к.ф-м.н, старший научный сотрудник,* Институт металлургии и материаловедения им. А.А. Байкова РАН
ORCID: 0000-0002-9206-7805
E-mail: akirsankin@imet.ac.ru

***Александр Сергеевич Баикин*,** *научный сотрудник,* Институт металлургии и материаловедения им. А.А. Байкова РАН
E-mail: baikinas@mail.ru

***Константин Владимирович Сергиенко*,** *младший научный сотрудник,* Институт металлургии и материаловедения им. А.А. Байкова РАН
E-mail: shulf@yandex.ru

***Елена Олеговна Насакина*,** *старший научный сотрудник,* Институт металлургии и материаловедения им. А.А. Байкова РАН
ORCID: 0000-0002-0783-1558
E-mail: nacakina@mail.ru

***Алексей Георгиевич Колмаков*,** *член-корреспондент РАН, д.т.н., заведующий лабораторией,* Институт металлургии и материаловедения им. А.А. Байкова РАН
ORCID: 0000-0002-4907-951X
E-mail: akolmakov@imet.ac.ru

***Михаил Анатольевич Севостьянов*,** *к.т.н, ведущий научный сотрудник,* Институт металлургии и материаловедения им. А.А. Байкова РАН; *руководитель центра,* Всероссийский научно-исследовательский институт фитопатологии
ORCID: 0000-0003-2652-8711
E-mail: msevostyanov@imet.ac.ru

Contribution of the Authors / Вклад авторов

M. A. Kaplan – writing the text, processing of the results.

A. D. Gorbenko – assistance in obtaining powders, working out spray modes).
A. Yu. Ivannikov – obtaining powders, setting up and adjusting equipment, obtaining the final powder for waste spray modes.

S. V. Konushkin – literary review, selection of the research methods.

A. V. Mikhailova – conducting the SEM research.
A. A. Kirsankin – study of the powder characteristics.
A. S. Baikin – study of the particle size distribution.
K. V. Sergienko – figures processing.
E .O. Nasakina – consulting in the research and writing the article.

A. G. Kolmakov – revision of the text, correction of the conclusions.
M. A. Sevost'yanov – scientific guidance, article analysis.

М. А. Каплан – подготовка текста статьи и обработка результатов.
А. Д. Горбенко – помощь в получении порошков, отработка режимов распыления.
А. Ю. Иванников – получение порошков, настройка и наладка оборудования, получение финального порошка по отработанным режимам распыления.
С. В. Конушкин – изучение литературы, подбор методик для исследования.
А. В. Михайлова – проведение исследований на СЭМ.
А. А. Кирсанкин – исследование характеристики порошка.
А. С. Баикин – исследование гранулометрического состава.
К. В. Сергиенко – обработка рисунков.
Е .О. Насакина – консультация в исследованиях и написании работы.
А. Г. Колмаков – доработка текста, корректировка выводов.
М. А. Севостьянов – научное руководство, анализ статьи.

Received 19.10.2022
Revised 27.11.2022
Accepted 30.12.2022

Поступила в редакцию 19.10.2022
После доработки 27.11.2022
Принята к публикации 30.12.2022

UDC 622.788
DOI 10.17073/0368-0797-2023-1-86-88

Short report
Краткое сообщение

Cracking in MgO briquettes

N. A. Babailov[1], Yu. N. Loginov[2], L. I. Polyanskii[3]

[1] **Institute of Engineering Science, Ural Branch of the Russian Academy of Sciences** (34 Komsomol'skaya Str., Yekaterinburg 620049, Russian Federation)
[2] **Ural Federal University named after the first President of Russia B.N.Yeltsin** (19 Mira Str., Yekaterinburg 620002, Russian Federation)
[3] **LLC "Spaidermash"** (54 Studencheskaya Str., Yekaterinburg 620912, Russian Federation)

fupi_vs@e1.ru

Abstract. This paper examines the crack geometry of briquettes in magnesium oxide (MgO), a slagging material widely used in iron and steel making applications. Geometry measurement data and crack layout in briquettes are produced by roll briquetteizing. Cracking in briquettes is likely due to the workflow of roll briquetteizing. This defect affects the strength of briquettes and yield ratio (plus productivity rate) during briquetteizing using roll baling presses. A number and angles of cracks in respect to the briquetteizing direction were identified in accordance with photos of briquette side surfaces using graphical software.

Keywords: briquette, roll mill briquetteizing, MgO, cracks, crack angle, briquette strength, maximum tangential stress

For citation: Babailov N.A., Loginov Yu.N., Polyanskii L.I. Cracking in MgO briquettes. *Izvestiya. Ferrous Metallurgy*. 2023; 66(1): 86–88. https://doi.org/10.17073/0368-0797-2023-1-86-88

Трещинообразование в брикетах из оксида магния

Н. А. Бабайлов[1], Ю. Н. Логинов[2], Л. И. Полянский[3]

[1] **Институт машиноведения имени Э.С. Горкунова Уральского отделения РАН** (Россия, 620049, Екатеринбург, ул. Комсомольская, 34)
[2] **Уральский федеральный университет имени первого Президента России Б.Н. Ельцина** (Россия, 620002, Екатеринбург, ул. Мира, 19)
[3] **ООО «Спайдермаш»** (Россия, 620049, Екатеринбург, ул. Студенческая, 54)

fupi_vs@e1.ru

Аннотация. В работе рассмотрена геометрия трещин в объеме брикетов из шлакообразующего материала, широко используемого в черной металлургии – оксида магния MgO. Представлены результаты измерения геометрии и расположения трещин в объеме брикетов, полученных методом валкового брикетирования. Возможность появления трещин в объеме брикетов является технологической особенностью валкового брикетирования. Этот дефект влияет на прочность брикетов, а также на выход годного (и производительность) в процессе брикетирования на валковых брикетировочных прессах. Количество и угол наклона трещин относительно направления брикетирования определено по фотографиям боковой поверхности брикета с использованием графических программ.

Ключевые слова: брикет, валковое брикетирование, оксид магния, трещины, угол наклона трещины, прочность брикетов, максимальное касательное напряжение

Для цитирования: Бабайлов Н.А., Логинов Ю.Н., Полянский Л.И. Трещинообразование в брикетах из оксида магния. *Известия вузов. Черная металлургия*. 2023; 66(1): 86–88. https://doi.org/10.17073/0368-0797-2023-1-86-88

MgO (its content in slag varies from 10 to 20 %) is a mandatory component for steelmaking slags. Quantities of MgO in slag control its viscosity. MgO enhances slag sulphur-scavaging capabilities, as well as the lining strength of steel-making furnaces and ladles.

Roll pressing techniques are commonly used [1, 2] in order to prepare powdered materials for metallurrgical processing. Roll presses have rolls equipped with cells of one shape or another [3]. Transverse and diagonal cracks are formed when pressing and rolling powder-metallur-

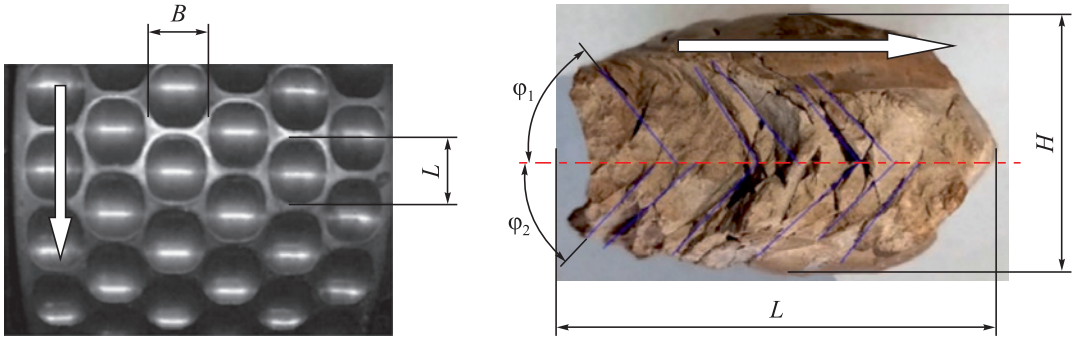

a *b*

External view of cells on the roll (*a*) and magnesian briquette (*b*) (the image is rotated), arrow shows briquetting direction

Внешний вид ячеек на валке (*a*) и вид магнезиального брикета (*b*) (изображение повернуто), стрелка показывает направление брикетирования

gical materials. This defect is commonly seen in powder metallurgy [4, 5]. The strength properties of products are governed by this defect.

The aim of this work is to define the geometry and layout of the cracks subject to formation at high pressing pressure in the event of dry briquetteizing of cryolite, aluminium fluoride, MgO, etc.

Ten magnesian briquettes were studied after briquetteizing using roll presses in rolls (or bands) with mechanically processed cells (Fig. *a*). The particle-size composition varies from 0 to 1 mm. Briquette density is 2,100 kg/m^3. Falling strength of briquettes ranges from 75 to 92 %. The briquette dimensions are as follows: length $L = 32 \pm 1$ mm; height $H = 19.5 \pm 0.5$ mm; breadth $B = 29 \pm 1$ mm. In this paper the so-called "dry briquetteizing" method (i. e. briquetteization with no binder or water) is applied. During briquetteizing the baling press roll gap is 5 mm. Fig. *b* shows an image of the MgO briquette side surface which demonstrates clearly visible cracking.

As seen in the figure, the cracks are positioned close to the rear portion of the briquette. It was previously shown that the roll mill cell has a pressurizing side and an opposing side of the process circuit. Whereas high pressure is created on the pressurizing side, this side is involved in creating the rear portion of the briquette. In this specific case, cracking was formed in the high pressure area, i.e. these cracks are induced by over-pressure.

Using our graphical software, we calculated average crack angles in the top and bottom of a briquette ($\varphi_1 = 49.2°$ and $\varphi_2 = 48.4°$). The visible cracks in briquettes amount to 5 – 6 pcs. Average crack angle in a briquette is 48.8° (this value is within 45 – 60°.) Normally, the formation of cracks with an angle of approx. 45° to the = axis is associated with maximum tangential stresses in place.

Conclusions

The findings reveal that cracks in briquettes are formed in the rear portion of a briquette i. e. where high pressure exists. One recommendation for the remedying of such defects (over-pressing induced cracking) obtained is to increase the gap between rolls of briquetting press.

References / Список литературы

1. Dec R.T., Zavaliangos A., Cunningham J.C. Comparison of various modeling methods for analysis of powder compaction in roller press. *Powder Technology*. 2003; 130(1–3): 265–271. http://doi.org/10.1016/S0032-5910(02)00203-6
2. Simonov K.V., Luzin A.G., Bocharov L.D., Fleer S.A., Gol'dberg I.A., Timofeev N.N., Shumeiko R.M. Briquetting caustic magnesite on industrial type smooth rollers. *Refractories*. 1974; 15: 185–193. https://doi.org/10.1007/BF01286260
3. Bayul K.V. Effect of the geometrical parameters of roll press forming elements on the briquetting process: Analytical study. *Powder Metallurgy and Metal Ceramics*. 2012; 51: 157–164. https://doi.org/10.1007/s11106-012-9411-8
4. Eremin A.Ya., Babanin V.I., Kozlova S.Ya. Establishing the requirements for indices characterizing the mechanical strength of briquets with binders. *Metallurgist*. 2003; 47(11–12): 437–446. https://doi.org/10.1023/B:MELL.0000019002.95148.fa
5. Barsukov V.G., Krupicz B., Barsukov V.V. Tribomechanical analysis of interlayer shear and surface crack nucleation processes in compacted disperse materials. *Journal of Friction and Wear*. 2015; 36: 112–117. https://doi.org/10.3103/S1068366615020026
6. Babailov N.A., Loginov Yu.N., Polyansky L.I. Influence of the gap between the rolls on parameters of the roll briquetting of metallurgical lime and magnesium oxide. *Chernye Metally*. 2022; (6): 9–14. https://doi.org/10.17580/chm.2022.06.02
Бабайлов Н.А., Логинов Ю.Н., Полянский Л.И. Влияние зазора между валками на параметры валкового брикетирования металлургической извести и оксида магния. *Черные металлы*. 2022; (6): 9–14. https://doi.org/10.17580/chm.2022.06.02

Information about the Authors

Nikolai A. Babailov, *Cand. Sci. (Eng.), Senior Researcher of the Laboratory of Applied Mechanics,* Institute of Engineering Science, Ural Branch of the Russian Academy of Sciences
ORCID: 0000-0002-6245-2841
E-mail: fupi_vs@e1.ru

Yurii N. Loginov, *Dr. Sci. (Eng.), Prof. of the Chair "Metal Forming",* Ural Federal University named after the first President of Russia B.N. Yeltsin
ORCID: 0000-0002-7222-2521
E-mail: j.n.loginov@urfu.ru

Leonid I. Polyanskii, *Director,* LLC "Spaidermash"
E-mail: info@spidermash.ru

Сведения об авторах

Николай Александрович Бабайлов, *к.т.н., старший научный сотрудник лаборатории прикладной механики,* Институт машиноведения имени Э.С. Горкунова Уральского отделения РАН
ORCID: 0000-0002-6245-2841
E-mail: fupi_vs@e1.ru

Юрий Николаевич Логинов, *д.т.н., профессор кафедры «Обработка металлов давлением»,* Уральский федеральный университет имени первого Президента России Б.Н. Ельцина
ORCID: 0000-0002-7222-2521
E-mail: j.n.loginov@urfu.ru

Леонид Иванович Полянский, *директор,* ООО «Спайдермаш»
E-mail: info@spidermash.ru

Contribution of the Authors

N. A. Babailov – determining the angle of inclination of cracks in briquettes.
Yu. N. Loginov – review and method for determining the angle of inclination of crack in briquettes.
L. I. Polyanskii – conducting experiments on roller briquetting.

Вклад авторов

Н. А. Бабайлов – проведение работ по определению угла наклона трещин в брикетах.
Ю. Н. Логинов – обзор и методика определения угла наклона трещины в брикетах.
Л. И. Полянский – проведение экспериментальных работ по валковому брикетированию.

Received 16.01.2023
Revised 20.01.2023
Accepted 20.01.2023

Поступила в редакцию 16.01.2023
После доработки 20.01.2023
Принята к публикации 20.01.2023

PHYSICO-CHEMICAL BASICS OF METALLURGICAL PROCESSES / ФИЗИКО-ХИМИЧЕСКИЕ ОСНОВЫ МЕТАЛЛУРГИЧЕСКИХ ПРОЦЕССОВ

UDC 669.162.275.2
DOI 10.17073/0368-0797-2023-1-89-96

Original article
Оригинальная статья

Effect of B_2O_3 on viscosity of high-magnesia blast furnace slag

A. S. Vusikhis [1] ✉, L. I. Leont'ev [1, 2, 3], R. I. Gulyaeva [1], S. V. Sergeeva [1], S. N. Tyushnyakov [1]

[1] **Institute of Metallurgy, Ural Branch of the Russian Academy of Science** (101 Amundsena Str., Yekaterinburg 620016, Russian Federation)
[2] **National University of Science and Technology "MISIS"** (4 Leninskii Ave., Moscow 119049, Russian Federation)
[3] **Scientific Council on Metallurgy and Metal Science of Russian Academy of Sciences (Department of Chemistry and Material Sciences)** (32a Leninskii Ave., Moscow 119991, Russian Federation)

✉ vas58@mail.ru

Abstract. Smelters in the Urals procure only 50 – 60 % of raw materials from local sources. The rest is imported from Central Russia, the Kola Peninsula, and Kazakhstan. Switching to local raw materials would increase the competitiveness of the Urals metals, so local alternatives should be considered, such as siderite ore from the Bakal deposit. The ore is in low demand due to its low iron content and high magnesium content. The higher the siderite content in the charge, the higher the magnesium oxide content in the slag. This affects the slag viscosity, so for siderite content exceeding 20%, melting is difficult or impossible. We proposed the addition of boric oxide to liquefy the slag. The simulated slag (CaO 26.8 %; SiO_2 38.1 %; Al_2O_3 11.8 %; MgO 23.6 %) identical to that produced by the Magnitogorsk Metallurgical Plant (MMK) blast furnaces with the addition of 30 % of calcined siderite is short and unstable. The temperature when the slag viscosity is equal to that at the blast furnace taphole (0.5 Pa·s) is 1390 °C, while the melting point (2.5 Pa·s viscosity) is 1367 °C. The addition of boric anhydride makes the slag long and stable. As the B_2O_3 content is increased from 0 to 12 %, the temperatures at which the slag viscosity is 0.5 and 2.5 Pa·s decrease to 1260 and 1100 °C, respectively. The study shows it is possible to significantly increase the siderite content in blast furnace charge.

Keywords: iron-ore raw materials, Bakal siderites, viscosity, slag, boron oxide, magnesium oxide, melting temperature

Acknowledgements: The work was supported by the Russian Science Foundation, project No. 22-29-00400.

For citation: Vusikhis A.S., Leont'ev L.I., Gulyaeva R.I., Sergeeva S.V., Tyushnyakov S.N. Effect of B_2O_3 on viscosity of high-magnesia blast furnace slag. *Izvestiya. Ferrous Metallurgy*. 2023; 66(1): 89–96. https://doi.org/10.17073/0368-0797-2023-1-89-96

Влияние B_2O_3 на вязкость высокомагнезиальных доменных шлаков

А. С. Вусихис [1] ✉, Л. И. Леонтьев [1, 2, 3], Р. И. Гуляева [1], С. В. Сергеева [1], С. Н. Тюшняков [1]

[1] **Институт металлургии Уральского отделения РАН** (Россия, 620016, Екатеринбург, ул. Амундсена, 101)
[2] **Национальный исследовательский технологический университет «МИСИС»** (Россия, 119049, Москва, Ленинский пр., 4)
[3] **Президиум РАН** (Россия, 119991, Москва, Ленинский пр., 32а)

✉ vas58@mail.ru

Аннотация. На металлургических предприятиях Урала доля местного сырья составляет 50 – 60 %. Его дефицит компенсируется использованием материалов, завозимых из Центральной России, Кольского полуострова и Казахстана. Замена их на местное сырье увеличит конкурентоспособность производимого на Урале металла, поэтому вопрос оценки возможности замены привозного сырья на местное является весьма актуальным. Таким сырьем могут быть сидеритовые руды Бакальского месторождения. Они не пользуются спросом у металлургов из-за низкого содержания железа и высокого содержания магния. С ростом количества сидеритов в шихте увеличивается содержание оксида магния в шлаке, что влияет на его вязкость и делает затруднительным или невозможным плавку с использованием более 20 % сидеритов. Для разжижения шлака предложено использовать оксид бора. Синтетический шлак, содержащий 26,8 % CaO, 38,1 % SiO_2, 11,8 % Al_2O_3, 23,6 % MgO, моделирующий состав шлака доменной плавки Магнитогорского

металлургического комбината с добавкой 30 % обожженных сидеритов, является коротким и неустойчивым. Температура, при которой его вязкость соответствует вязкости на выпуске (0,5 Па·с), составляет 1390 °С, а температура, соответствующая температуре плавления (вязкость 2,5 Па·с), составляет 1367 °С. Если в такой шлак добавить борный ангидрид, он становится длинным и устойчивым. В расплавах при увеличении доли B_2O_3 от 0 до 12 % температура, при которой вязкость шлака составляет 0,5 и 2,5 Па·с, снижается до 1260 и 1100 °С соответственно. Это делает возможным значительное увеличение доли сидеритов в доменной шихте.

Ключевые слова: железорудное сырье, бакальские сидериты, вязкость, шлак, оксид бора, оксид магния, температура плавления

Благодарности: Работа выполнена при поддержке Российского научного фонда по проекту №22-29-00400.

Для цитирования: Вусихис А.С., Леонтьев Л.И., Гуляева Р.И., Сергеева С.В., Тюшняков С.Н. Влияние B_2O_3 на вязкость высокомагнезиальных доменных шлаков. *Известия вузов. Черная металлургия*. 2023; 66(1): 90–96. https://doi.org/10.17073/0368-0797-2023-1-89-96

Smelters in the Urals procure only 50 – 60 % of the raw materials from local sources. The rest comes from the central and northwestern regions of Russia and Kazakhstan, since less than half of the 50 iron ore deposits in the Urals region are in operation [1 – 5], and the production rate does not match demand. There are several reasons for that. The siderite iron ore extraction volume at the Bakal deposit (Southern Urals) with its about 1 bln. ton reserves are far less than the deposit capacity due to low demand for low-grade ore. The magnesium oxide content in the mining waste is about 40 – 50 % [6 – 8]. For this reason, siderites can be used only as additives to blast furnace charges or sinter cakes. Bakal siderite is unsuitable as the key component of the blast furnace charge, since the slag will have a very high melting point [9].

Slags are melted in a certain temperature range, so the melting point (T_{mp}) is not constant. It is either the liquidus temperature (T_l) above which the slag is completely liquid or the temperature at which the slag begins to freely flow from the coke packing (the required viscosity should be less than 2.5 Pa·s).

Also, the slag melting point should be below 1400 °C for smooth, safe smelting, and the slag should have sufficient mobility in the 1400 to 1500 °C temperature range [10 – 13].

The viscosity of acidic slags grows slowly over a relatively wide range of temperatures. That is why such slags are called “long slags”. Basic slags become thicker as the temperature drops below the crystallization point due to heterogenization and solid phase formation. The thickening occurs in a narrow temperature range. Such slags are called “short slags”.

Both slag temperature and fluidity are important variables in the blast furnace smelting process. Indeed, the viscosity of melted slag is the key property affecting blast furnace stability and efficiency and the entire smelting process. Many researchers [14 – 21] have studied the correlation between the slag component (e.g, magnesium oxide) content, melting point, and viscosity. Authors [14 – 16] studied the effects of slag composition on its properties over a wide range of component contents. The results are in good agreement with the studies of a narrower range of contents [17 – 21].

Any blast furnace slag consists of four basic components: $CaO–SiO_2–MgO–Al_2O_3$. For such melts containing less than 15 % of alumina, an increase in the base-to-silica ratio (R) from 0.6 to 1.5, and the magnesium oxide content from 0 to 20 % leads to the melting point increase to 1350 – 1400 °C and narrowing the solidification temperature range. The slags become “shorter”. Any amount of magnesium oxide can be added. Slags containing more than 25 % MgO are not flowable below 1400 °C.

Raising the MgO content from 0 to 25 % in the slag with 0.6 – 1.5 the base-to-silica ratio results in a viscosity drop to a minimum. The minimum value depends on the alumina content and temperature. Acidic slags show higher viscosity drop rates than basic ones.

Slags containing 5 % of Al_2O_3 have a minimum viscosity (0.15 Pa·s) at 1500 °C; R ~ 0.9 – 1.1; 17 – 20 % MgO; 36 – 38 % SiO_2. Reducing the temperature to 1400 °C increases the minimum viscosity to 0.35 Pa·s. Now the minimum viscosity exists in a wider MgO content range of up to 13 – 20 % with a shift towards more acidic slags containing 39 – 41 % of SiO_2.

The alumina content increase to 10 % increases the minimum viscosity. As the temperature drops from 1500 to 1400 °C, the minimum viscosity increases from 0.2 to 0.3 Pa·s. The composition ranges where the minimum viscosity occurs are narrowed from R ~ 0.8 – 1.2; 13 – 24 % MgO; 35 – 40 % SiO_2 (at 1500 °C) to R ~ 1.05 – 1.2; 14 – 16 % MgO; 39 – 41 % SiO_2 (1400 °C), respectively.

For the 15 % Al_2O_3 content, the minimum viscosity increases from 0.30 to 0.55 Pa·s. The content ranges change from R ~ 0.9 – 1.2; 15 – 26 % MgO; 30 – 33 % SiO_2 to R ~ 0.80 – 1.05; 18 – 22 % MgO, 33 – 35 % SiO_2, as the temperature drops from 1500 to 1400 °C. The higher magnesium oxide content leads to a dramatic viscosity reduction in acid slags containing 25 – 35 % of CaO. Such slags with R ~ 0.5 – 0.8, containing 13 – 18 % Al_2O_3 and 16 – 25 % MgO, are quite fluid at 1350 – 1400 °C.

The melting point of slags containing 20 % Al_2O_3 (R ~ 1.2 – 1.5) exceeds 1500 °C for any magnesium oxide content. When R ~ 1.1 – 1.2, the crystallization occurs at >16 % MgO. As R decreases to 0.6, the criti-

cal content of magnesium oxide increases to 20 %. When $MgO/Al_2O_3 \sim 0.5$, for $R \sim 1.1 – 1.2$ T_l is about 1450 °C. As R decreases to 0.6, T_l drops to 1350 °C. the minimum viscosity of such slags varies from 0.4 Pa·s (at 1500 °C) to 1.0 Pa·s (at 1400 °C) for 34 – 36 % SiO_2 content.

The above data indicates that in slags with less than 1.0 MgO base-to-silica ratio, the MgO content can reach 15 – 20 %, with no significant smelting issues. Such slags are sufficiently fluid. They melt at temperatures below 1350 °C. When the MgO content is above 25 %, the melting point raises drastically making the slag short and unstable. The analysis [22] shows that such slags are formed when the blast furnace charge contains about 30 % of siderite. The conclusion is that such a charge is difficult or impossible to use.

As it is known [23 – 25], the addition of boric oxide to blast furnace slag reduces its viscosity over the entire temperature range and makes slags longer.

The purpose of this study is to identify the effect of adding boric oxide on the viscosity and melting point of high-magnesia blast furnace slags.

We produced simulated slag containing 26.8 % CaO, 38.1 % SiO_2, 11.8 % Al_2O_3, and 23.6 % MgO. Its composition was similar to the estimated [22] composition of the slag produced by blast furnace No. 9, MMK when the charge was a mixture of in-house sinter and pellets from Sokolovo-Sarbai Mining and Concentrating Facility in the 2:1 ratio, and 30 % of calcined siderite concentrate.

The calcium oxide (AR grade) we used was calcinated in a muffle furnace at 910 °C for 6 h. The boric anhydride (B_2O_3) was calcinated at 170 °C for 2 h. The latter was subsequently melted in a resistance furnace at 900 °C for 4 h.

The samples were prepared by heating and melting an oxide mixture ($CaO – SiO_2 – MgO – Al_2O_3$) in a graphite pot at 1500 – 1550 °C (30 min holding time). The melt was poured into the mold and cooled.

After cooling the material was crushed and mixed with boric anhydride to achieve 3, 6, 9, and 12 % B_2O_3 content. Then the sample was placed in a molybdenum pot, heated to 1550 °C, and its viscosity was measured. We used a forced-oscillation vibrating viscometer [26, 27]. The melt temperature was measured with a tungsten-rhenium thermocouple. The probe was made of molybdenum, in order to avoid its reaction with the melt. The cooling rate was 5 – 7 °C/min.

For combined thermogravimetry and differential scanning calorimetry (DSC), we used a Netzsch STA 449C Jupiter simultaneous thermal analyzer. The experimental data was processed using NETZSCH Proteus Thermal Analysis [28] in its standard configuration (±3 °C temperature accuracy). The samples were heated to 1430 °C and then cooled to 500 °C at the 20 °C/min rate in pure blanketing argon (99.998 % Ar). The pots were made of Pt-Rh; the lids and inserts were made of aluminum oxide. The samples weighing 23 – 30 mg were made from crushed, pre-sintered slag. The sample slags contained the key components ($SiO_2 – CaO – MgO – Al_2O_3$), and 0.6 and 12 % of boric oxide.

We used an XRD-7000 Maxima (Shimadzu) diffractometer (CuK_α radiation). The 2θ scattering angle range was 15 – 65°.

Data analysis (Fig. 1) resulted in the following findings. The slag viscosity vs. temperature curve is similar to the polytherm of a similar slag presented in [15]. The slag viscosity is less than 0.5 Pa·s at temperatures

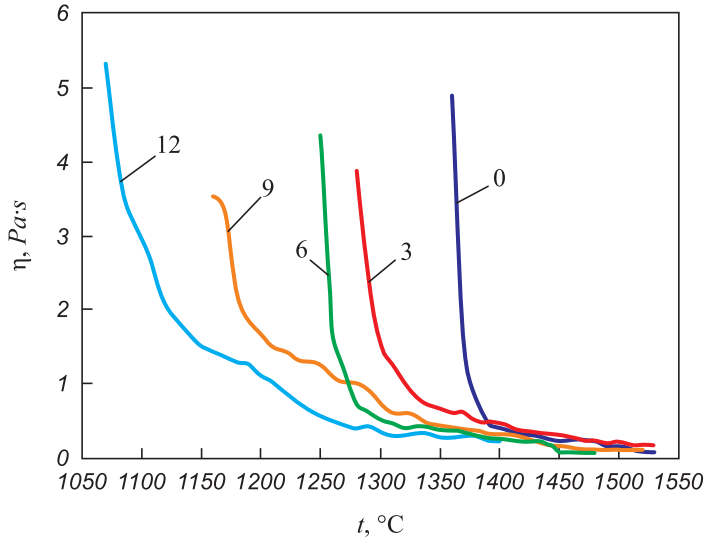

Fig. 1. Viscosity polyterms for $CaO – SiO_2 – MgO – Al_2O_3 – B_2O_3$ melts (the numbers indicate B_2O_3 content)

Рис. 1. Политермы вязкости расплавов $CaO – SiO_2 – MgO – Al_2O_3 – B_2O_3$ (цифры у кривых – содержание B_2O_3)

above 1390 °C. The viscosity increases to 2.5 Pa·s at about 1370 °C (T_{mp}). After that, the slag thickening rate rises sharply. Adding boric anhydride reduces the temperature at which the slag viscosity is less than 0.5 Pa·s. The slag thickening temperature range is extended to T_{mp}. The higher the boric oxide content, the lower the solidification temperature.

The thermal analysis results are slightly different from the viscosity measurements (Fig. 2). As sample No. 1 (Fig. 2, *a*) without any B_2O_3 was heated, the DSC curve

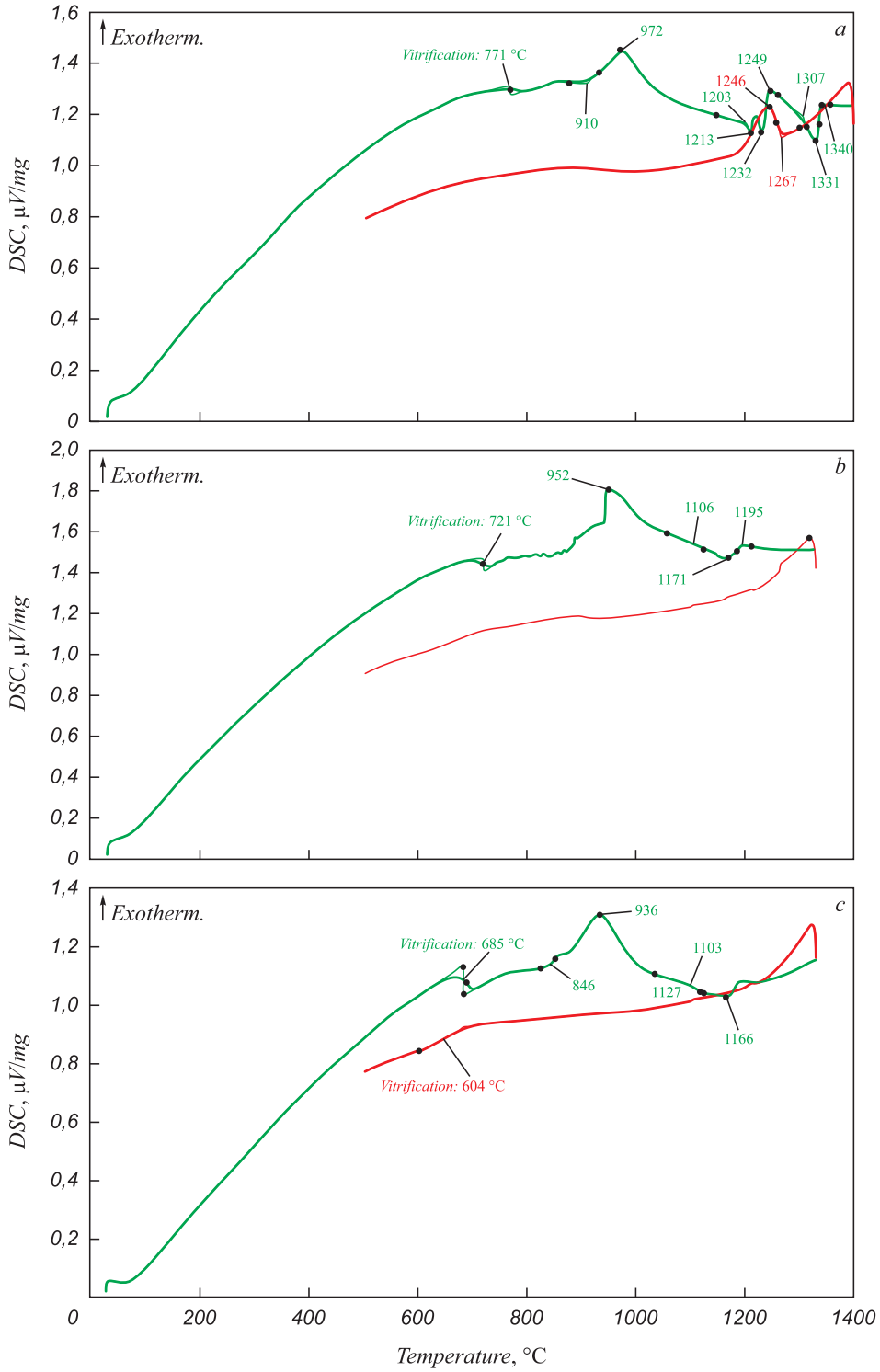

Fig. 2. DSC curves for heating and cooling of the SiO_2 – CaO – MgO – Al_2O_3 slag samples (*a*) 6 % B_2O_3 (*b*) and 12 % B_2O_3 (*c*)

Рис. 2. ДСК линии, полученные при нагревании и охлаждении образцов шлака системы SiO_2 – CaO – MgO – Al_2O_3 (*a*) с добавлением 6 (*b*) и 12 (*c*) % B_2O_3

indicates devitrification at 771 °C, as well as the exothermic effect of "cold" crystallization beginning at 910 °C and reaching the maximum at 972 °C. It also shows three endothermic effects with their maximums at 1213, 1232, and 1331 °C, apparently caused by the melting of the slag phase components. The liquidus temperature was 1340 °C. The DSC cooling curve shows an exothermic effect of the slag crystallization with its beginning/maximum at 1267/1246 °C.

The thermal analysis of sample No. 2 (Fig. 2, *b*) containing 6 % B_2O_3 showed the devitrification effect at 721 °C, and the effects of "cold" crystallization (952 °C) and melting (1106/1171 °C). The slag liquidus temperature was 1195 °C. As the slag was cooled, the DSC curve did not show any effects which indicates the slag's amorphous structure is preserved.

Increasing the B_2O_3 content to 12 % (Fig. 2, *c*) does not significantly change the DSC curves. We found a slight decrease in the devitrification temperature (t_g = 685 °C) during heating, and vitrification effects during cooling (604 °C). The effects of "cold" crystallization and melting were observed at 936 °C and 1103/1166 °C. It is slightly lower than the temperatures found in samples No. 1 and 2. Generally, the addition of B_2O_3 to a $SiO_2 – CaO – MgO – Al_2O_3$ slag reduces the devitrification, "cold" crystallization, and melting temperatures and facilitates the formation and stabilization of the amorphous phase. This was also confirmed by the *X*-ray phase

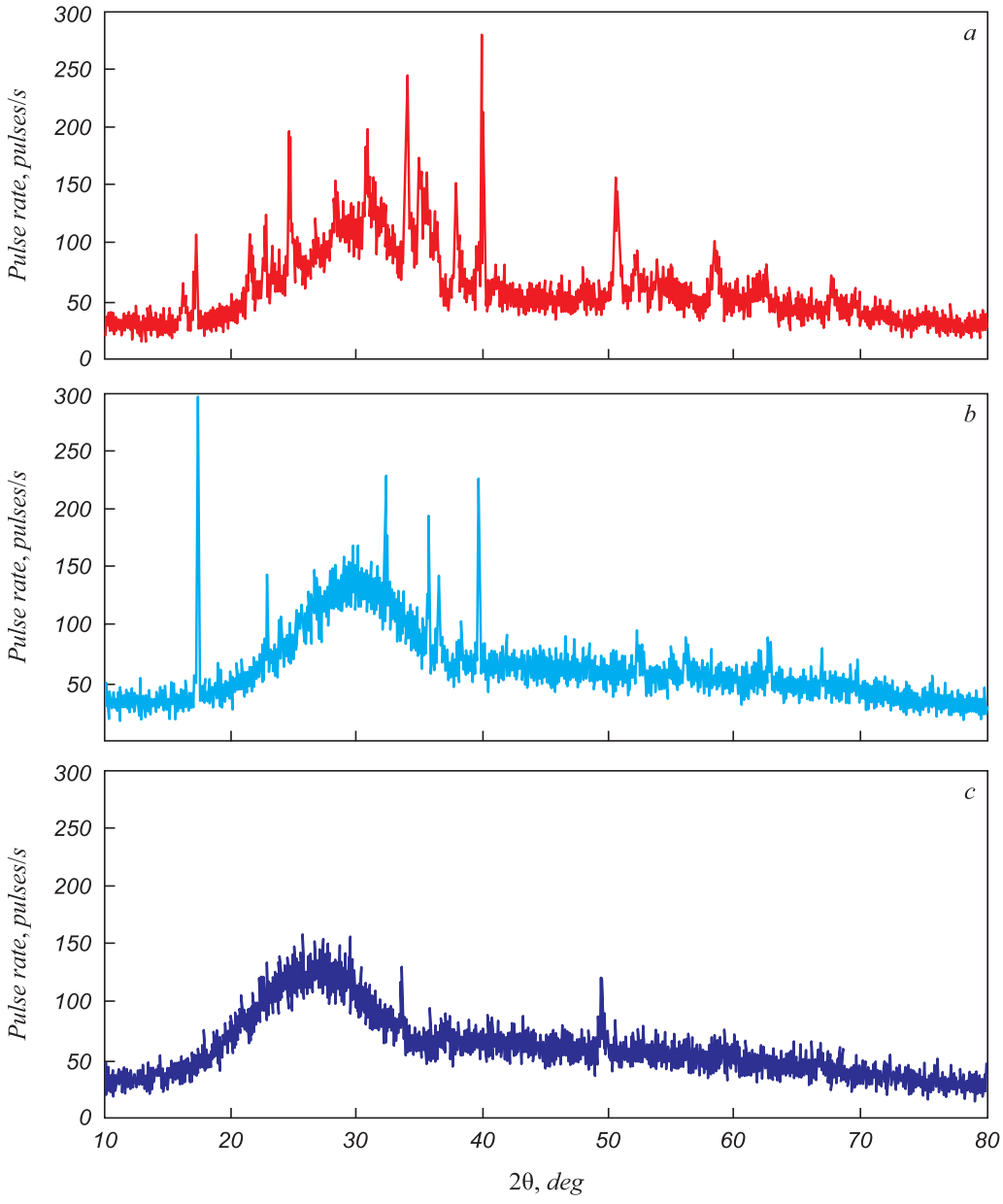

Fig. 3. Diffractograms of the of $SiO_2 – CaO – MgO – Al_2O_3$ slag samples (*a*) with addition of 6 % B_2O_3 (*b*) and 12 % B_2O_3 (*c*)

Рис. 3. Дифрактограммы образцов шлака системы $SiO_2 – CaO – MgO – Al_2O_3$ (*a*) с добавлением 6 (*b*) и 12 (*c*) % B_2O_3

analysis (Fig. 3). Without boric anhydride when the slag is cooled, it crystallizes, and calcium and magnesium aluminosilicates are formed. When boric anhydride is added during cooling, slag vitrification occurs. As a result, the borate component is added to the aluminosilicates.

Conclusions

Siderites (as raw ore, after calcination and concentration, or pelleting) are currently used as additives to blast furnace charges. Their content in the charge is selected in such a way that the magnesium oxide content in the resulting slag does not exceed 15 – 20 %. Such slags are liquid above 1400 °C. Further magnesium oxide content increases, making the slag short and refractory. Melting a charge containing more than 30 % of siderite, which results in a high-magnesia slag (>25 % MgO), is difficult. The addition of boric anhydride to the charge reduces the melting temperature of the slag. For a melt with a 23.6 % magnesium oxide content, adding 0 to 12 % of boric anhydride reduces the temperature at which the slag viscosity is 0.5 Pa·s from 1390 to 1260 °C, and from 1367 to 1100 °C for the 2.5 Pa·s viscosity. This makes it possible to significantly increase the siderite content in the charge.

References / Список литературы

1. Volkov Yu.V., Sokolov I.V., Smirnov A.A. Strategy for development of raw material resources in the Urals. *Gornaya promyshlennost'*. 2006: (4): 57–62. (In Russ.).

   Волков Ю.В., Соколов И.В., Смирнов А.А. Стратегия освоения сырьевых ресурсов Урала. *Горная промышленность*. 2006; (4): 57–62.
2. Volkov Yu.V., Slavikovskii O.V., Sokolov I.V., Smirnov A.A. Prospects for development of raw material base of mining and metallurgical enterprises in the Urals. *Gornyi informatsionno-analiticheskii byulleten'*. 2007; (5): 286–290. (In Russ.).

   Волков Ю.В., Славиковский О.В., Соколов И.В., Смирнов А.А. Перспективы развития сырьевой базы горно-металлургических предприятий Урала. *Горный информационно-аналитический бюллетень*. 2007; (5): 286–290.
3. Pakhomov V.P., Dushin A.V. Analysis of the mineral-raw material safety in the Ural Federation District. *Ekonomika regiona*. 2008; (3): 129–143. (In Russ.).

   Пахомов В.П., Душин А.В. Оценка минерально-сырьевой безопасности УрФО. *Экономика региона*. 2008; (3): 129–143.
4. Valiev N.G., Slavikovskii O.V., Slavikovskaya Yu.O. Peculiarities of development of mineral resource base in the Urals urbanised territories. *Gornyi informatsionno-analiticheskii byulleten' (nauchno-tekhnicheskii zhurnal)*. 2012; (6): 344–347. (In Russ.).

   Валиев Н.Г., Славиковский О.В., Славиковская Ю.О. Особенности освоения минерально-сырьевой базы на урбанизированных территориях Урала. *Горный информационно-аналитический бюллетень (научно-технический журнал)*. 2012; (6): 344–347.
5. Kornilkov S.V., Kantemirov V.D. Iron ore deposits of the Nether-Polar Urals as a prospective raw materials base of the Urals metallurgy. *Izvestiya vuzov. Gornyi zhurnal*. 2015; (8): 22–28. (In Russ.).

   Корнилков С.В., Кантемиров В.Д. Железорудные месторождения Приполярного Урала как перспективная сырьевая база уральской металлургии. *Известия вузов. Горный журнал*. 2015; (8): 22–28.
6. Krasnoborov V.A., Yaroshevskii S.L., Denisov A.A., Rudin V.S., Biryuchev V.I., Polushkin M.F. *Efficiency and Prospects of Using Siderite Ores in Blast Furnace Smelting*. Donetsk; 1996: 88. (In Russ.).

   Красноборов В.Я., Ярошевский С.Л., Денисов А.А., Рудин В.С., Бирючев В.И., Полушкин М.Ф. *Эффективность и перспективы применения сидеритовых руд в доменной плавке*. Донецк; 1996: 88.
7. Yur'ev B.P., Melamud S.G., Spirin N.A., Shatsillo V.V. *Technological and Thermal Engineering Bases of Siderite Ore Preparation for Metallurgical Processing: Monograph*. Yekaterinburg: Den' RA; 2016: 428. (In Russ.).

   Юрьев Б.П., Меламуд С.Г., Спирин Н.А., Шацилло В.В. *Технологические и теплотехнические основы подготовки сидеритовых руд к металлургическим переделам*. Екатеринбург: ООО АМК «День РА»; 2016: 428.
8. Vusikhis A.S., Leont'ev L.I. *The Use of Siderite Ores in Production of Iron and Steel: Monograph*. Moscow, Vologda: Infra-Inzheneriya; 2022: 116. (In Russ.).

   Вусихис А.С., Леонтьев Л.И. *Применение сидеритовых руд при производстве чугуна и стали*. Москва, Вологда: Инфра-Инженерия; 2022: 116.
9. *Slag Atlas*. Düsseldorf, Verlag Stahlissen GmbH; 1995: 616.
10. Gotlib A.D. *Blast Furnace Process*. Moscow: Metallurgiya; 1966: 503. (In Russ.).

    Готлиб А.Д. *Доменный процесс*. Москва: Металлургия; 1966: 503.
11. Efimenko G.G., Gimmel'farb A.A., Levchenko V.E. *Ironmaking*. Kiev: Vyshcha shkola; 1988: 351. (In Russ.).

    Ефименко Г.Г., Гиммельфарб А.А., Левченко В.Е. *Металлургия чугуна*. Киев: Выща школа; 1988: 351.
12. Vegman E.F., Zherebin B.N., Pokhvisnev A.N., etc. *Ironmaking*. Moscow: Akademkniga; 2004: 774. (In Russ.).

    Вегман Е.Ф., Жеребин Б.Н., Похвиснев А.Н., Юсфин Ю.С., Курунов И.Ф., Паренько А.Е., Черноусов П.И. *Металлургия чугуна*. Москва: ИКЦ «Академкнига»; 2004: 774.
13. Badich A., Senk D., Gudenau H.W., Mavrommatis K.Th. *Ironmaking*. Aahen, RWTH Aahen University; 2008: 402.
14. Bol'shakova L.I., Zhilo N.L. Physical properties of high-magnesia blast furnace slags during smelting of Bakal siderites. In: *Slag Mode in Blast Furnaces*. Moscow: Metallurgiya; 1967: 173–185. (In Russ.).

    Большакова Л.И., Жило Н.Л. Физические свойства высокомагнезиальных доменных шлаков при выплавке бакальских сидеритов. В кн.: *Шлаковый режим доменных печей* / Под ред. Н.Л. Жило, М.Я. Остроухова. Москва: Металлургия; 1967: 173–185.
15. Zhilo N.L. *Formation and Properties of Blast Furnace Slag*. Moscow: Metallurgiya; 1974: 120. (In Russ.).

    Жило Н.Л. *Формирование и свойства доменных шлаков*. Москва: Металлургия; 1974: 120.

16. Voskoboinikov V.G., Dunaev N.E., Mikhalevich A.G., etc. *Properties of Liquid Blast Furnace Slags: Manual*. Moscow: Metallurgiya; 1975: 182. (In Russ.).

Воскобойников В.Г., Дунаев Н.Е., Михалевич А.Г. и др. *Свойства жидких доменных шлаков: Справочное пособие*. Москва: Металлургия; 1975: 182.

17. Saito N., Hori N., Nakashima K., Mori K. Viscosity of blast furnace type slags. *Metallurgical and Materials Transactions B*. 2003; 34(5): 509–516. https://doi.org/10.1007/s11663-003-0018-9

18. Kou M., Wu S., Ma X., Wang L., Chen M., Cai Q., Zhao B. Phase equilibrium studies of CaO–SiO_2–MgO–Al_2O_3 system with binary basicity of 1.5 related to blast furnace slag. *Metallurgical and Materials Transactions B*. 2016; 47(2): 1093–1102. https://doi.org/10.1007/s11663-016-0584-2

19. Liu Y., Lu X.W., Li B., Bai C.G. Relationship between structure and viscosity of CaO–SiO_2–MgO–30.00 wt.% Al_2O_3 slag by molecular dynamics simulation with FT-IR and Raman spectroscopy. *Ironmaking & Steelmaking*. 2018; 45(6): 492–501. https://doi.org/10.1080/03019233.2017.1288309

20. Shen F., Hu X., Zheng H., Jiang X., Gao Q., Han H., Long F. Proper MgO/Al_2O_3 ratio in blast-furnace slag: Analysis of proper MgO/Al_2O_3 ratio based on observed data. *Metals*. 2020; 10(6): 784. https://doi.org/10.3390/met10060784

21. Das K., Agrawal A., Reddy A.S., Ramna R.V. FactSage studies to identify the optimum slag regime for blast furnace operation. *Transactions of the Indian Institute of Metals*. 2021; 74: 419–428. https://doi.org/10.1007/s12666-020-02144-y

22. Vusikhis A.S., Leont'ev L.I., Agafonov S.N. Assessment of the efficiency of the use of Bakal siderites in blast furnace smelting. *Izvestiya. Ferrous Metallurgy*. 2022; 65(7): 504–510. (In Russ.). https://doi.org/10.17073/0368-0797-2022-7-504-510

Вусихис А.С., Леонтьев Л.И., Агафонов С.Н. Оценка эффективности использования бакальских сидеритов в доменной плавке. *Известия вузов. Черная металлургия*. 2022; 65(7): 504–510. https://doi.org/10.17073/0368-0797-2022-7-504-510

23. Ren S., Zhang J., Wu L. Influence of B_2O_3 on viscosity of high Ti-bearing blast furnace slag. *ISIJ International*. 2012; 52(6): 984–991. https://doi.org/10.2355/isijinternational.52.984

24. Kim G.H., Sohn I. Role of B_2O_3 on the viscosity and structure in the CaO–Al_2O_3–Na_2O-based system. *Metallurgical and Materials Transactions B*. 2014; 45(2): 86–95. https://doi.org/10.1007/s11663-013-9953-2

25. Wang G., Wang J.-S., Xue Q.-G. Properties of boron-rich slag separated from boron-bearing iron concentrate. *Journal of Central South University*. 2018; 25(4): 783–794. https://doi.org/10.1007/s11771-018-3783-y

26. Selivanov E.N., Gulyaeva R.I., Istomin S.A., Belyaev V., Tyushnyakov S., Bykov A. Viscosity and thermal properties of slag in the process of autogenous smelting of copper–zinc concentrates. *Mineral Processing and Extractive Metallurgy*. 2015; 124(2): 88–95. https://doi.org/10.1179/1743285514Y.0000000078

27. Vusikhis A.S., Selivanov E.N., Dmitriev A.N., Chentsov V.P., Ryabov V.V. Structure sensitive properties of system B_2O_3–CaO melts. *Defect and Diffusion Forum*. 2020; 400: 186–192. https://doi.org/10.4028/www.scientific.net/DDF.400.186

28. *NETZSCH Proteus Software. Thermal Analysis*. Version 4.8.3.

Information about the Authors / Сведения об авторах

Aleksandr S. Vusikhis, *Cand. Sci. (Eng.), Senior Researcher of the Laboratory of Pyrometallurgy of Non-Ferrous Metals,* Institute of Metallurgy, Ural Branch of the Russian Academy of Science
ORCID: 0000-0002-6395-0834
E-mail: vas58@mail.ru

Александр Семенович Вусихис, *к.т.н., старший научный сотрудник лаборатории пирометаллургии цветных металлов,* Институт металлургии Уральского отделения РАН
ORCID: 0000-0002-6395-0834
E-mail: vas58@mail.ru

Leopol'd I. Leont'ev, *Academician, Adviser,* Russian Academy of Sciences, *Dr. Sci. (Eng.), Prof.,* National University of Science and Technology "MISIS", *Chief Researcher,* Institute of Metallurgy, Ural Branch of the Russian Academy of Science
ORCID: 0000-0002-4343-914X
E-mail: leo@presidium.ras.ru

Леопольд Игоревич Леонтьев, *академик, советник,* Президиум РАН, *д.т.н., профессор,* Национальный исследовательский технологический университет «МИСиС», *главный научный сотрудник,* Институт металлургии Уральского отделения РАН
ORCID: 0000-0002-4343-914X
E-mail: leo@presidium.ras.ru

Roza I. Gulyaeva, *Cand. Sci. (Chem.), Senior Researcher of the Laboratory of Pyrometallurgy of Nonferrous Metals,* Institute of Metallurgy, Ural Branch of the Russian Academy of Sciences
ORCID: 0000-0003-2860-0377
E-mail: gulroza@mail.ru

Роза Иосифовна Гуляева, *к.х.н., старший научный сотрудник лаборатории пирометаллургии цветных металлов,* Институт металлургии Уральского отделения РАН
ORCID: 0000-0003-2860-0377
E-mail: gulroza@mail.ru

Svetlana V. Sergeeva, *Cand. Sci. (Eng.), Senior Researcher of the Laboratory of Pyrometallurgy of Nonferrous Metals,* Institute of Metallurgy, Ural Branch of the Russian Academy of Sciences
ORCID: 0000-0002-1310-7670
E-mail: lazarevasv@mail.ru

Светлана Владимировна Сергеева, *к.т.н., старший научный сотрудник лаборатории пирометаллургии цветных металлов,* Институт металлургии Уральского отделения РАН
ORCID: 0000-0002-1310-7670
E-mail: lazarevasv@mail.ru

Stanislav N. Tyushnyakov, *Cand. Sci. (Eng.), Senior Researcher of the Laboratory of Pyrometallurgy of Non-Ferrous Metals,* Institute of Metallurgy, Ural Branch of the Russian Academy of Sciences
ORCID: 0000-0002-0864-0462
E-mail: tyushnyakov.sn@gmail.com

Станислав Николаевич Тюшняков, *к.т.н., старший научный сотрудник лаборатории пирометаллургии цветных металлов,* Институт металлургии Уральского отделения РАН
ORCID: 0000-0002-0864-0462
E-mail: tyushnyakov.sn@gmail.com

Contribution of the Authors

A. S. Vusikhis – setting the research goal, literary review, writing the text, forming the conclusions.
L. I. Leont'ev – scientific guidance, analysis of the research results, editing the article.
R. I. Gulyaeva – conducting experiments, processing results.

S. V. Sergeeva – conducting experiments, processing results.

S. N. Tyushnyakov – carrying out calculations, conducting experiments.

Вклад авторов

А. С. Вусихис – постановка задачи исследования, литературный обзор, подготовка текста, формирование выводов.
Л. И. Леонтьев – научное руководство, анализ результатов исследований, редактирование статьи.
Р. И. Гуляева – проведение экспериментов, обработка результатов.
С. В. Сергеева – проведение экспериментов, обработка результатов.
С. Н. Тюшняков – проведение расчетов, проведение экспериментов.

Received 06.12.2022
Revised 14.12.2022
Accepted 30.12.2022

Поступила в редакцию 06.12.2022
После доработки 14.12.2022
Принята к публикации 30.12.2022

Materials of the Conference
«PHYSICO-CHEMICAL FOUNDATIONS
OF METALLURGICAL PROCESSES"
named after Academician A.M. Samarin – 2022

По материалам конференции
«ФИЗИКО-ХИМИЧЕСКИЕ ОСНОВЫ
МЕТАЛЛУРГИЧЕСКИХ ПРОЦЕССОВ»
им. академика А.М. Самарина – 2022

UDC 669.046.516.4
DOI 10.17073/0368-0797-2023-1-97-104

Original article
Оригинальная статья

Influence of barium and strontium on calcium recovery degree upon ladle treatment of steel by complex modifiers with alkaline earth metals

I. V. Bakin [1, 2], A. N. Shapovalov [3], A. V. Kalyaskin [1], M. S. Kuznetsov [4]

[1] **South Ural State University** (76 Lenina Ave., Chelyabinsk 454080, Russian Federation)
[2] **LLC RPE "Technology"** (25 Vodrem Vil. - 40, Chelyabinsk 454901, Russian Federation)
[3] **Novotroitsk Branch of the National University of Science and Technology "MISIS"** (8 Frunze Str., Novotroitsk, Orenburg Region 426359, Russian Federation)
[4] **JSC "Ural Steel"** (1 Zavodskaya Str., Novotroitsk, Orenburg Region 462356, Russian Federation)

igor.npp.bakin@gmail.com

Abstract. Increasingly rigid requirements in terms of the steel products quality are forcing the metallurgy technologists to search for innovative solutions to stabilize the steel quality. Much attention is paid to ladle treatment of melt and selection of rational composition of modifiers, which enables the content of non-metallic inclusions to be reduced. In order to solve the formulated problem, complex modifiers are used containing both calcium and other alkaline earth metals (barium and strontium). This article presents the results of a pilot campaign on metal ladle treatment by complex modifiers with alkaline earth metals (calcium, barium, strontium) upon production of steel with higher requirements for non-metallic inclusions under conditions of electric-furnace melting at JSC "Ural Steel". In the course of experimental activities, the maximum level of inclusions content of sheet rolled products from pipe steel grades was decreased in terms of brittle silicates (according to State Standard GOST 1778) from 4.0 to 1.5 – 2.5, and in terms of non-deforming silicates from 4.0 to 3.0 – 3.5. Substitution of silicocalcium, grade SK40, with experimental modifiers resulted in improvement of strength properties of rolled products both during tension tests and during impact bending tests at lower temperatures. This influence was observed in all variants of consumption of the experimental modifiers. With increase in the consumption of modifiers positive influence on steel mechanical properties also increased. As a consequence of substitution of silicocalcium with experimental modifiers, the calcium recovery with the use of Si – Ca – Ba increased in average by 1.6 times, and with the use of Si – Ca – Ba – Sr in average by 2.4 times. The use of the complex modifiers enabled the targeted value of residual calcium in steel sample from tundish to be obtained at significantly lower calcium consumption.

Keywords: pipe steel, ladle treatment, non-metallic inclusions, non-deformed silicates, steel modification, silicocalcium, microcrystalline complex modifiers, calcium recovery

For citation: Bakin I.V., Shapovalov A.N., Kalyaskin A.V., Kuznetsov M.S. Influence of barium and strontium on calcium recovery degree upon ladle treatment of steel by complex modifiers with alkaline earth metals. *Izvestiya. Ferrous Metallurgy*. 2023; 66(1): 97–104.
https://doi.org/10.17073/0368-0797-2023-1-97-104

Влияние бария и стронция на степень усвоения кальция при внепечной обработке стали комплексными модификаторами с щелочноземельными металлами

И. В. Бакин [1, 2], А. Н. Шаповалов [3], А. В. Каляскин [1], М. С. Кузнецов [4]

[1] **Южно-Уральский государственный университет** (Россия, 454080, Челябинск, пр. Ленина, 76)
[2] **ООО НПП «Технология»** (Россия, 454901, Челябинск, пос. Водрем-40, 25)
[3] **Новотроицкий филиал НИТУ «МИСИС»** (Россия, 426359, Оренбургская обл., Новотроицк, ул. Фрунзе, 8)
[4] **АО «Уральская сталь»** (Россия, 462356, Оренбургская обл., Новотроицк, ул. Заводская, 1)

igor.npp.bakin@gmail.com

Аннотация. Ужесточающиеся требования к качеству металлопродукции вынуждают технологов металлургического производства искать новые решения, позволяющие стабилизировать качество металла. Большое внимание уделяется технологиям внепечной обработки расплава и подбору рационального состава модификаторов, позволяющих снизить загрязненность металла по неметаллическим включениям. Для решения поставленной задачи применяются комплексные модификаторы, содержащие как кальций, так и другие щелочноземельные металлы (барий и стронций). Представлены результаты опытно-промышленной компании по внепечной обработке металла комплексными модификаторами с щелочноземельными металлами (кальций, барий, стронций) при производстве стали с повышенными требованиями к неметаллическим включениям в условиях электросталеплавильного цеха АО «Уральская Сталь». В ходе экспериментальных работ удалось снизить максимальный балл загрязненности листового проката из трубных марок стали по силикатам хрупким (по ГОСТ 1778) с 4,0 до 1,5 – 2,5, по силикатам недеформирующимся с 4,0 до 3,0 – 3,5. Замена силикокальция марки СК40 на опытные модификаторы привела к улучшению прочностных свойств проката как при испытаниях на растяжение, так и при испытаниях на ударный изгиб при пониженных температурах. Указанное влияние наблюдалось при всех вариантах расходов опытных модификаторов. Отмечено, что с увеличением расхода модификаторов положительное влияние на механические свойства стали усиливалось. В результате замены силикокальция на опытные варианты модификаторов усвоение кальция при использовании Si – Ca – Ba повысилось в среднем в 1,6 раза, а при использовании Si – Ca – Ba – Sr – в среднем в 2,4 раза. Применение комплексных модификаторов позволило при существенно меньшем расходе кальция получить целевое значение остаточного кальция в маркировочной пробе.

Ключевые слова: трубная сталь, ковшевая обработка, неметаллические включения, силикаты недеформирующиеся, модифицирование стали, силикокальций, микрокристаллические комплексные модификаторы, усвоение кальция

Для цитирования: Бакин И.В., Шаповалов А.Н., Каляскин А.В., Кузнецов М.С. Влияние бария и стронция на степень усвоения кальция при внепечной обработке стали комплексными модификаторами с щелочноземельными металлами. *Известия вузов. Черная металлургия*. 2023; 66(1): 98–104. https://doi.org/10.17073/0368-0797-2023-1-97-104

Introduction

The continuously tightening of requirements with regard to the quality of metal products has lead metallurgy technologists to search for innovative solutions which enable a steady high quality of metal to be obtained. In particular, much attention is paid to ladle treatment of melt and selection of rational composition of modifiers which enables the content of non-metallic inclusions (NMI) to be reduced. The general principles of decreasing the NMI level of steel deoxidized by aluminum are known [1 – 4]. Treatment of steel by calcium containing materials is a common practice which allows metal to be refined from the products by aluminium deoxidizing [5 – 8]. In this respect, good results are also steadily achieved with the use of complex modifiers with alkaline earth metals (AEM) both in Russia [9 – 12] and abroad [13 – 14]. Nowadays much attention is paid to the use of strontium as a component of complex alloy with AEM together with calcium and barium. The promising potentials of this element are confirmed both by the theoretical studies [15], and by results of the pilot projects [16, 17].

The execution of certain contracts for pipe steel grades at JSC "Ural Steel" requires compliance with higher specifications (State Standard GOST 1778-70) in terms of NMI points:

– in terms of oxides, sulfides, and brittle silicates (BS) – not higher than 2.5 points regarding average level and not higher than 3.0 points regarding maximum level;

– in terms of non-deformed silicates (NDS) – not higher than 3.0 points regarding average level and not higher than 3.5 points regarding maximum level.

However, upon steel treatment by conventionally used silicocalcium SK40, the achieved performance of steel quality in terms of content of various NMI does not always comply with the targeted values. Thus, in terms of non-deformed silicates the inclusions content in the metal equals in average 2.5 points, the maximum content being 4.5 points. These NMI are calcium aluminates of complex composition. In order to decrease their sizes and content, industrial tests of complex modifiers were performed (Table 1). The technological parameters were verified providing maximum efficiency of their use.

The modifiers mentioned proved to be successful in production of corrosion resistance, high carbon (wheel steel), and structural steels under conditions of Taganrog Iron & Steel Factory [18], OMZ Special Steel plant, as well as in the course of R&D project of development of production technology of sheet rolled products with normalized level of corrosion active NMI in the electric-furnace melting shop of JSC "Ural Steel" [19, 20].

The aim of this work is to develop a set of recommendations on the technology of the ladle treatment of melt, in order to reduce the content of non-deformed silicates

Table 1

Properties of experimental modifiers

Таблица 1. **Характеристика опытных модификаторов**

Name	Description	Influence
INSTEEL®1.5	Ca – Ba modifier on iron silicon base	Decrease in NMI content, improvement of mechanical properties
INSTEEL®9.4	Ca – Ba – Sr modifier on iron silicon base	Decrease in NMI content, preventing submerged entry nozzle clogging with aluminum silicates

(in terms of maximum level) lower than 3.5 points and achieve targeted content of residual calcium together with reduction of cumulative production expenses.

Experimental

In order to solve the formulated problems, a series of pilot experiments were performed on production of steel, grade K52 – K60, using complex modifiers with AEM in comparison with standard silicocalcium, grade SK40. Chemical composition of the modifiers with AEM is summarized in Table 2. The composition of test alloys with AEM was selected by the results of positive experience of their use under various production conditions, including those of the electric-furnace melting shop of JSC "Ural Steel" [20]. Consumption of the modifiers was determined on the basis of analysis of large scale laboratory and commercial tests of alloys with AEM.

Table 2

Actual chemical composition of modifiers (cored wire fillers), %

Таблица 2. **Химический состав модификаторов (наполнителей порошковой проволоки), %**

Element	Modifier		
	SK40	INSTEEL®1.5	INSTEEL®9.4
Mg	–	0.1	0.1
Al	1.0	1.0	1.1
Si	42.2	36.5	46.8
Ca	39.9	31.2	18.4
Ba	–	22.8	10.4
Sr	–	–	11.2

In accordance with the pilot experiment plan, each modifier was used for the treatment of more than 20 melt heats of steel, grade K52 – K60. Melting and ladle treatment of comparative and test melt heats were carried out in comparison with valid process specifications. The steel was modified at steel vacuum degasser (SVD) after deoxidizing by aluminum. Consumption of modifiers in test melt heats was varied in the range of 80 – 100 % (of comparative variant with SK40) in terms of overall AEM [20].

Sampling and assessment of NMI content in steel were carried out in accordance with State Standard GOST 1778-70 (method Sh6). Spectral microanalysis and NMI assessment in sheet rolled products from steel of test and comparative melt heats were carried out using a JSM- 6490LV scanning electron microscope in combination with an INCA Energy 250 energy dispersion analyzer at 200× magnification.

Results and discussion

The main parameters of modification in comparative and test melts are summarized in Table 3.

As can be seen from Table 3, the consumption of INSTEEL®1.5 modifier according to several variants, provided for the addition of AEM from 82 % (variant *1*) to 103 % (variant *3*) of the basic technology with SK40. In the case of INSTEEL®9.4 modifier the amount of AEM supplied with the wire varied from 79 % to 90 %, respectively. Therefore, the modifier consumption provides the calcium addition:

– for INSTEEL®1.5: from 47.7 % (variant *1*) to 59.6 % (variant *3*) with respect to the basic technology;

Table 3

Average parameters of steel modifying treatment

Таблица 3. **Усредненные параметры модифицирования стали**

Modifier	Variant	Number of heats	Modifying parameters (per melt heat)*			
			consumption, m	filler consumption, kg	Ca supply, kg	AEM supply, kg
SK40	Existing technology	24	147.0	37.8	15.1	15.1
INSTEEL®1.5	*1*	6	104.0	23.1	7.2	12.5
	2	15	113.0	25.1	7.8	13.5
	3	4	130.0	28.9	9.0	15.6
INSTEEL®9.4	*1*	7	123.0	30.0	5.5	12.0
	2	9	131.0	32.0	5.9	12.8
	3	6	140.0	34.2	6.3	13.7

* Melt heat weight: 120 t.

Table 4

Assessment of contamination with nonmetallic inclusions of sheet metal according to State Standard GOST 1778 (method Sh6)

Таблица 4. **Результаты оценки загрязненности листового проката НВ по ГОСТ 1778 (метод Ш6)**

Modifier	Variant	Sheet thickness, mm	NMI level, points, (min – max)/average		
			1D oxides	brittle silicates (BS)	non-deformed silicates (NDS)
SK40	Existing technology	10 – 11 / 10.8	0.5 – 0.5 / 0.5	0 – 4.0 / 0.5	1.0 – 4.0 / 1.5
INSTEEL®1.5	*1*	10 – 12 / 11.0	0.5 – 0.5 / 0.5	0 – 2.5 / 0.5	1.0 – 4.0 / 1.5
	2	11 – 12 / 11.1	0.5 – 0.5 / 0.5	0 – 2.5 / 0.5	1.0 – 3.0 / 1.5
	3	11 – 13.4 / 12.1	0.5 – 0.5 / 0.5	0 – 2.0 / 0.5	1.0 – 3.0 / 1.5
INSTEEL®9.4	*1*	11 – 11 / 11.0	0.5 – 0.5 / 0.5	0 – 2.0 / 0.5	1.0 – 3.5 / 1.5
	2	11 – 16 / 12.1	0.5 – 0.5 / 0.5	0 – 2.0 / 0.5	1.0 – 3.5 / 1.5
	3	11 – 20 / 12.5	0.5 – 0.5 / 0.5	0 – 1.5 / 0.5	1.0 – 3.0 / 1.5

R e m a r k: other NMI types were not detected.

– for INSTEEL®9.4: from 36.4 % (variant *1*) to 41.7 % (variant *3*) with respect to the basic technology.

The contents of NMI in sheet rolled products obtained from slabs after comparative and test melt heats according to several variants are summarized in Table 4.

Analysis of NMI content in metal (Table 4) demonstrated the following:

– substitution of silicocalcium with test variants of modifiers decreases the maximum points in terms of BS from 4.0 to 1.5 – 2.5;

– maximum inclusions content of NDS decreased from 4.0 points for standard technology to 3.5 points with the use of INSTEEL®9.4 modifiers according to variants *1* and *2*; and to 3.0 points with the use of INSTEEL®1.5 modifier according to variants *2* and *3*, as well as with the maximum consumption of INSTEEL®9.4 modifier (variant *3*).

Therefore, the results of test melt heats and integrated studies of metal rolled products demonstrated that the metal produced with the use of INSTEEL® modifiers was characterized by lower NMI content, in comparison with the rolled products manufactured by standard technology with the use of silicocalcium SK40.

As a final result of decrease in NMI content in steel with the use of test modifiers, the main physical properties of metal rolled products were improved. The results of mechanical tests of samples after comparative and test melt heats are summarized in Table 5.

Table 5 shows that substitution of silicocalcium with the test modifiers resulted in improvement of strength prop-

Table 5

Mechanical properties (State Standards GOST 149784 and GOST 945478) of sheet metal

Таблица 5. **Механические свойства (по ГОСТ 1497-84 и ГОСТ 9454-78) листового проката**

Modifier	Variant	Yield strength (σ_y), N/mm^2	Ultimate strength (σ_u), N/mm^2	Impact toughness (KCU^{-60}), MJ/m^2
SK40	Existing technology	435 – 510/479.5	520 – 584/553.6	110 – 335/227.3
INSTEEL®1.5	*1*	455 – 510/483.3	550 – 630/589.2	133 – 270/217.4
	2	450 – 580/505.4	550 – 650/596.3	200 – 348/259.3
	3	464 – 530/507.0	555 – 630/586.1	195 – 498/300.6
INSTEEL®9.4	*1*	450 – 525/478.8	530 – 600/560.0	165 – 353/288.8
	2	450 – 540/505.0	530 – 610/573.6	193 – 353/274.5
	3	455 – 550/523.3	540 – 630/590.6	240 – 358/289.5

erties of rolled products both upon static tension tests, and upon dynamic impact bending tests at lower temperatures. The influence was observed in all variants of consumption of the test modifiers. The increased consumption of modifiers showing positive influence on mechanical properties of steel has been also increased. However, the mentioned improvement of properties can be attributed not only with the use of the test materials, but also with other simultaneously acting factors. Therefore, it should be verified on larger array of melt heats.

In addition to a decrease in NMI content, an important parameter is the content of residual calcium after treatment by the modifier. It is precisely this parameter that is critical upon express assessment of the efficiency of this or that composition of modifier under production conditions. The content of residual calcium is an important factor in providing stable conditions of casting (with minimum submerged entry nozzle clogging), as well as the favorable form and position of NMI in the structure of a workpiece, especially with consideration of the possible reoxidation process and decrease in oxygen solubility.

In this regard an important issue is the selection of consumption of complex modifier, which allows metal from NMI to be refined with high quality, in order to obtain the required content of residual calcium without increased expenses for steel treatment. In addition, a disputable issue is whether the influence mechanism of calcium and other AEM is more modifying or deoxidizing.

In the course of pilot experiments, in order to assess the deoxidizing action of calcium during modifying treatment, the content of active oxygen was measured before and after metal treatment by silicocalcium using Heraeus Electro-Nite equipment. The results demonstrated that during high quality deoxidizing of melt by aluminum the treatment by silicocalcium slightly decrease the content of active oxygen (by 1 – 2 ppm). This is an indirect evidence that calcium works to a higher extent as a modifier than a deoxidizing agent.

Table 6 summarizes averaged contents of main elements in test and comparative metals.

Table 6 shows that the chemical compositions of steel in comparative and test melt heats in terms of main elements are comparable. The calcium content of steel sample from tundish corresponded to targeted values approved upon production of steel of these grades. Herewith, the content of added calcium with the use of comparative and test modifiers differed several times (Table 3). Steel casting was carried out according to standard procedure at normalized parameters of temperature and rate. No violations were revealed upon casting and rolling of steel of comparative and test melt heats. No submerged entry nozzle clogging was observed.

It is known that calcium recovery significantly depends on slag composition before modification. Average basicity and FeO content in slag before addition of powdered wire in comparative and test melt heats were comparable. Furthermore, the slag parameters varied in wide range, which allowed their influence on calcium recovery to be analyzed (Figure).

Comparative and test melt heats with increase in the slag basicity demonstrate a steady trend towards the increase in calcium recovery degree (Figure, *a*). As for the influence of slag oxidation degree (Figure, *b*) generally characterized by FeO content in slag, then, in the region of normal oxidation degree of 0.5 – 0.6 % FeO, the influence of this parameter on calcium recovery was not statistically noticeable. This can be observed in comparative melt heats. In tests melts, there were cases of higher FeO content in excess of 0.6 %, which influenced the decrease in calcium recovery (Figure, *b*). However, even under such unfavorable conditions, the calcium recovery in test melts was higher than the results of comparative melt heats. Therefore, FeO content in slag melt before modification should not exceed 0.6 %. The confidence of the dependences characterized by coefficients of determination (R^2) is at a sufficiently low level. This is related to the moderate sample size and simultaneous influence of numerous factors. However, the dependences obtained qualitatively confirm the known theoretical regularities.

It should be mentioned that both average and maximum temperature of treatment at SVD with the use of complex alloys was higher than upon treatment by silicocalcium SK40: SK40 – 1569 – 1633 °C (average: 1606.4 °C); INSTEEL®1,5 – 1599 – 1648 °C (average: 1619 °C); INSTEEL®9.4 – 1593 – 1650 °C (average: 1617.6 °C). Comparative data analysis for melt heats at higher temperature demonstrated that in this case the specific flow rate of argon is higher, which can be attributed to the need for adjustment of metal temperature before ladle transfer

Table 6

Content of the main chemical elements in the steel samples from tundish, %

Таблица 6. **Содержание основных элементов в маркировочных пробах металла, %**

Element	Modifier		
	SK40	INSTEEL®1.5	INSTEEL®9.4
C	0.0900	0.0900	0.0800
Si	0.3600	0.3600	0.3800
Mn	1.5600	1.5700	1.5300
P	0.0100	0.0110	0.0100
S	0.0020	0.0020	0.0020
Ti	0.0150	0.0140	0.0150
Al	0.0400	0.0360	0.0390
Ca	0.0011	0.0010	0.0011

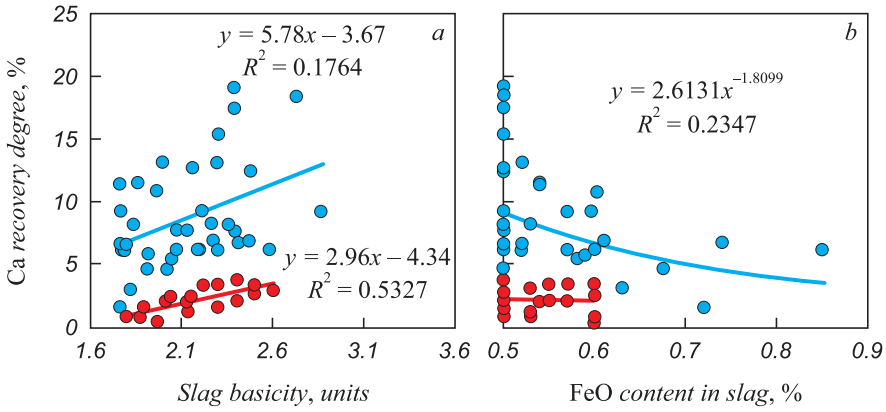

Ca recovery degree as a function of slag basicity (*a*) and FeO (*b*) content in slag in comparative (●) and test (●) melts

Влияние основности (*a*) и содержания FeO (*b*) в шлаке на степень усвоения кальция на сравнительных (●) и опытных (●) плавках

to continuous-casting machine. As a consequence, during melt heats at higher temperatures, it is required to blow metal after the end of modification with a higher intensity and inevitable exposure of metal, accompanied by additional waste of calcium. The analysis of the data on pilot campaign, shows a trend towards a decrease in calcium recovery degree with increase in argon flow rate at SVD from 0.08 to 0.10 m^3/t and higher. Furthermore, blowing by argon with a normal flow rate (up to 0.08 m^3/t) and intensity not causing excessive metal exposure and reoxidation promotes the removal of NMI from metal. This is further demonstrated by a decrease in the content of non-deformed silicates in rolled products.

Therefore, despite the significantly lower content of calcium added to metal with test modifiers and non-optimum treatment parameters of SVD, the content of residual calcium in metal was at the level of comparative melt heats. The mechanical properties of metal rolled products were improved and the NMI content was decreased.

Conclusions

The use of complex modifiers with AEM allows the problems of modification at the consumption to be resolved, thus providing cumulative addition of AEM of 80 – 90 % of calcium content predefined according to regular technology.

In the course of pilot activities, the calcium recovery from Si – Ca – Ba modifier was by 1.6 times and from Si – Ca – Ba – Sr modifier by 2.4 times higher in comparison with the use of conventional silicocalcium SK40.

The use of complex modifiers allowed the content of non-deformed silicates in steel to be reduced (in terms of maximum rank) to a level lower than 3.5 points under conditions of the electric-furnace melting shop of JSC “Ural Steel”.

In the case of the use of complex alloys with AEM the mechanical properties of sheet rolled products were improved both during tension tests and during impact bending tests at lower temperatures.

References / Список литературы

1. Emi T. Improving steelmaking and steel properties. In: *Fundamentals of Metallurgy. Seetharaman S. ed. Woodhead Publishing,* Cambridge UK Inst. of Materials, Minerals & Mining; 2005: 503–554.
2. Turkdogan E.T. *Fundamentals of Steelmaking*. London: The institute of materials; 1996: 331.
3. Dyudkin D.A., Kisilenko V.V. *Modern Technology of Steelmaking*. Moscow: Teplotekhnik; 2007: 529. (In Russ.).

   Дюдкин Д.А., Кисиленко В.В. *Современная технология производства стали*. Москва: Теплотехник; 2007: 529.
4. Gulyaev A.P. *Clean Steel*. Moscow: Metallurgiya; 1975: 184. (In Russ.).

   Гуляев А.П. *Чистая сталь*. Москва: Металлургия; 1975: 184.
5. Ren Y., Zhang L., Li S. Transient evolution of inclusions during calcium modification in linepipe steels. *ISIJ International*. 2014; 54(12): 2772–2779. https://doi.org/10.2355/isijinternational.54.2772
6. Zhao D., Li H., Cui Y., Yang J. Control of inclusion composition in calcium treated aluminum killed steels. *ISIJ International*. 2016; 56(7): 1181–1187. https://doi.org/10.2355/isijinternational.ISIJINT-2016-123
7. Veerababu Gollapalli, Venkata Rao M.S., Phani S. Karamched, Chenna Rao Borra, Gour G. Roy, Prakash Srirangam. Modification of oxide inclusions in calcium-treated al-killed high sulphur steels. *Ironmaking and Steelmaking*. 2019; 46(7): 663–670. https://doi.org/10.1080/03019233.2018.1443382
8. Liu C., Kumar D., Webler B.A., Pistorius P.C. Calcium modification of inclusions via slag/metal reactions. *Metallurgical and Materials Transactions B*. 2020; 51: 529–542. https://doi.org/10.1007/s11663-020-01774-3
9. Ryabchikov I.V., Golubtsov V.A., Usmanov R.G., Lunev V.V. Effect of complex alloys with alkaline-earth metals on characteristics of steel castings for transport applications. *Liteinoe proizvodstvo*. 2016; (5): 4–7. (In Russ.).

   Рябчиков И.В., Голубцов В.А., Усманов Р.Г., Лунев В.В. Влияние комплексных сплавов с ЩЗМ на характерис-

тики стальных железнодорожных отливок. *Литейное производство*. 2016; (5): 4–7.

10. Rozhikhina I.D., Nokhrina O.I., Dmitrienko V.I., Platonov M.A. Modification of steel by barium and strontium. *Izvestiya. Ferrous Metallurgy*. 2015; 58(12): 871–876. (In Russ.) https://doi.org/10.17073/0368-0797-2015-12-871-876

Рожихина И.Д., Нохрина О.И., Дмитриенко В.И., Платонов М.А. Модифицирование стали барием и стронцием. *Известия вузов. Черная металлургия*. 2015; 58(12): 871–876. https://doi.org/10.17073/0368-0797-2015-12-871-876

11. Morozov S.S., Kuznetsov A.A., Boldyrev D.A. Improving service durability for tooling made of heat resistant austenitic steel by barium-strontium carbonatite treatment. *Steel in Translation*. 2020; 50(4): 266–269. https://doi.org/10.3103/S0967091220040051

Морозов С.С., Кузнецов А.А., Болдырев Д.А. Повышение эксплуатационной стойкости оснастки из жаропрочной аустенитной стали обработкой барий-стронциевыми карбонатитами. *Сталь*. 2020; (4): 41–43.

12. Grigorovich K.V., Demin K.Yu., Arsenkin A.M., Garber A.K. Prospects for application of barium-bearing alloys for deoxidation and modification of transport metal. *Metally*. 2011; (5): 146–156. (In Russ.).

Григорович К.В., Демин К.Ю., Арсенкин А.М., Гарбер А.К. Перспективы применения барийсодержащих лигатур для раскисления и модифицирования транспортного металла. *Металлы*. 2011; (5): 146–156.

13. Irons G.A., Tong X.-P. Treatment of steel with alkaline-earth elements. *ISIJ International*. 1995; 35(7): 838–844. https://doi.org/10.2355/isijinternational.35.838

14. Mukai K., Han Q. Application of barium-bearing alloys in steelmaking. *ISIJ International*. 1999; 39(7): 625–636. https://doi.org/10.2355/isijinternational.39.625

15. Makrovets L.A., Samoilova O.V., Mikhailov G.G., Bakin I.V. Phase equilibrium occurring during low-carbon iron-based melt deoxidation with silicostrontium. *Izvestiya. Ferrous Metallurgy*. 2021; 64(6): 413–419. (In Russ.) https://doi.org/10.17073/0368-0797-2021-6-413-419

Макровец Л.А., Самойлова О.В., Михайлов Г.Г., Бакин И.В. Фазовые равновесия, реализующиеся при раскислении силикостронцием низкоуглеродистого расплава на основе железа. *Известия вузов. Черная металлургия*. 2021; 64(6): 413–419. https://doi.org/10.17073/0368-0797-2021-6-413-419

16. Bakin I.V., Shaburova N.A., Ryabchikov I.V., Mizin V.G., Belov B.F., Mikhailov G.G., Senin A.V. Experimental study of refining and modification of steel with Si–Ca, Si–Sr and Si–Ba alloys. *Steel in Translation*. 2019; 49(8): 543–547. https://doi.org/10.3103/S0967091219080023

Бакин И.В., Шабурова Н.А., Рябчиков И.В., Мизин В.Г., Белов Б.Ф., Михайлов Г.Г., Сенин А.В. Экспериментальное исследование рафинирования и модифицирования стали сплавами Si–Ca, Si–Sr и Si–Ba. *Сталь*. 2019; (8): 14–18.

17. Ryabchikov I.V., Bakin I.V., Mizin V.G., Novokreshchenov V.V., Golubtsov V.A. Secondary steelmaking with compound alloys with AEMs – an economically feasible approach to improve steel quality. *Steel in Translation*. 2021; 51(5): 324–329. https://doi.org/10.3103/S0967091221050107

Рябчиков И.В., Бакин И.В., Мизин В.Г., Новокрещенов В.В., Голубцов В.А. Внепечная обработка комплексными сплавами с ЩЗМ – экономичный способ улучшения качества стали. *Сталь*. 2021; (5): 11–15.

18. Golubtsov V.A., Milyuts V.G., Tsukanov V.V. Impact of complex modifying treatment for non-metallic inclusions contamination of shipbuilding steel. *Tyazheloe mashinostroenie*. 2013; (1): 2–5. (In Russ.).

Голубцов В.А., Милюц В.Г., Цуканов В.В. Влияние комплексного модифицирования на загрязненность неметаллическими включениями судостроительной стали. *Тяжелое машиностроение*. 2013; (1): 2–5.

19. Bakin I.V., Shapovalov A.N., Kuznetsov M.S., Shaburova N.A., Usmanov R.G., Golubtsov V.A., Ryabchikov I.V., Mizin V.G., Panov V.N. Industrial tests of microcrystalline complex alkaline earth metal alloys when casting pipe steel. *Steel in Translation*. 2020; 50(11): 795–800. https://doi.org/10.3103/S0967091220110030

Бакин И.В., Шаповалов А.Н., Кузнецов М.С., Шабурова Н.А., Усманов Р.Г., Голубцов В.А., Рябчиков И.В., Мизин В.Г., Панов В.Н. Промышленные испытания микрокристаллических комплексных сплавов с ЩЗМ при выплавке трубной стали. *Сталь*. 2020; (11): 21–25.

20. Kunitsyn G.A., Kuznetsov M.S., Shapovalov A.N., Bakin I.V. Application of complex modifiers in the production of steel with increased requirements for non-ferrous metallic inclusions. *Chernye Metally*. 2022; (5): 9–16. (In Russ.). https://doi.org/10.17580/chm.2022.05.02

Куницын Г.А., Кузнецов М.С., Шаповалов А.Н., Бакин И.В. Применение комплексных модификаторов при производстве стали с повышенными требованиями по неметаллическим включениям. *Черные металлы*. 2022; (5): 9–16. https://doi.org/10.17580/chm.2022.05.02

Information about the Authors / Сведения об авторах

Igor' V. Bakin, *Cand. Sci. (Eng.), Lecturer of the Chair of Materials Science and Physical Chemistry of Materials,* South Ural State University; *Head of the Division of Innovation, Modernization and Technical Development,* LLC RPE "Technology"
ORCID: 0000-0003-0825-717X
E-mail: igor.npp.bakin@gmail.com

Aleksei N. Shapovalov, *Cand. Sci. (Eng.), Assist. Prof. of the Chair "Metallurgical Technology and Equipment",* Novotroitsk Branch of the National University of Science and Technology "MISIS"
E-mail: alshapo@yandex.ru

Игорь Валерьевич Бакин, *к.т.н., преподаватель кафедры материаловедения и физико-химии материалов,* Южно-Уральский государственный университет; *начальник отдела инновации, модернизации и технического развития,* ООО НПП «Технология»
ORCID: 0000-0003-0825-717X
E-mail: igor.npp.bakin@gmail.com

Алексей Николаевич Шаповалов, *к.т.н., доцент кафедры металлургических технологий и оборудования,* Новотроицкий филиал НИТУ «МИСИС»
E-mail: alshapo@yandex.ru

Artem V. Kalyaskin, *Postgraduate of the Chair of Pyrometallurgical and Foundry Technologies,* South Ural State University
E-mail: 155@nppgroup.ru

Maksim S. Kuznetsov, *Cand. Sci. (Eng.), Deputy Head of the Workshop,* JSC "Ural Steel"
E-mail: m.kuznetsov@uralsteel.com

Артем Владимирович Каляскин, *аспирант кафедры пирометаллургических и литейных технологий,* Южно-Уральский государственный университет
E-mail: 155@nppgroup.ru

Максим Сергеевич Кузнецов, *к.т.н., заместитель начальника электросталеплавильного цеха по совершенствованию технологии,* АО «Уральская Сталь»
E-mail: m.kuznetsov@uralsteel.com

Contribution of the Authors / Вклад авторов

I. V. Bakin – formation of the concept of pilot work; setting the goal and objectives of the study; performing calculations and substantiating the required number of modifiers to obtain the required result; conducting the industrial experiment; collecting and analyzing data.

A. N. Shapovalov – setting the goals of the study; formation of the concept of pilot work; processing and analyzing the data obtained during the pilot work.
A. V. Kalyaskin – participation in a pilot experiment, writing the text, formation of conclusions, presentation of the results, structuring and design of the article.

M. S. Kuznetsov – setting the goals of the study, organization of the industrial experiment process, collecting data, organization of sampling, chemical analysis and metallographic studies of the metal samples.

И. В. Бакин – формирование основной концепции опытно-промышленной работы, постановка цели и задачи исследования, проведение расчетов и обоснование необходимого количества модификаторов для получения требуемого результата, руководство проведением промышленного эксперимента, сбор и анализ данных.
А. Н. Шаповалов – постановка задач, формирование концепции опытно-промышленной работы, обработка и анализ полученных в ходе проведения опытной работы данных.
А. В. Каляскин – участие в опытно-промышленном эксперименте, подготовка текста, формирование выводов и оформление результатов исследования, структурирование и оформление статьи.
М. С. Кузнецов – постановка задач, организация процесса промышленного эксперимента в производственных условиях, сбор данных, организация работ по отбору проб, проведению химического анализа и металлографических исследований образцов металла.

Received 01.11.2022
Revised 09.11.2022
Accepted 10.01.2023

Поступила в редакцию 01.11.2022
После доработки 09.11.2022
Принята к публикации 10.01.2023

Materials of the Conference «PHYSICO-CHEMICAL FOUNDATIONS OF METALLURGICAL PROCESSES" named after Academician A.M. Samarin – 2022

По материалам конференции «ФИЗИКО-ХИМИЧЕСКИЕ ОСНОВЫ МЕТАЛЛУРГИЧЕСКИХ ПРОЦЕССОВ» им. академика А.М. Самарина – 2022

UDC 669.1: 620.186.8:620.192.43
DOI 10.17073/0368-0797-2023-1-105-111

Original article
Оригинальная статья

Metallographic analysis of structural peculiarities of thin slab and rolled products manufactured thereof

E. L. Vorozheva [1], K. S. Smetanin [1], V. V. Kislitsa [1], D. V. Kudashov [1, 2]

[1] **JSC "Vyksa Metallurgical Plant"** (45 Br. Batashevykh Str., Vyksa, Nizhny Novgorod Region 607060, Russian Federation)
[2] **Vyksa Branch of the National University of Science and Technology "MISIS"** (206 Kalinina Str., Shimorskoe, Vyksa District, Nizhny Novgorod Region 607060, Russian Federation)

vorozheva_el@vsw.ru

Abstract. The article describes the determination of level of zonal and dendritic segregations in slabs cast by thin slab technology. The calculated coefficients of variation of content of main and impurity chemical elements over slab cross-section do not exceed 10 %, while the zonal segregation are moderate. The content of manganese measured by the surface area occupied by dendritic axes and interdendritic spaces determines the level of dendritic segregation. The manganese concentration varies from 0.6 to 1.1 %, respectively. It was established that the dynamic soft reduction during solidification allows the primary dendritic structure to be refined, in order to form additional centers upon phase transformation of δ ferrite into austenite. The sizes of initial austenite grains formed accounting for the primary dendritic structure are 3 times lower in a thin slab than in a slab with the thickness of more than 200 mm. Transformations of dendritic structure during reductions demonstrate the high level of conditioning required for the formation of uniform austenite grains in semifinished rolled stock before finish rolling. The studies did not confirm the hypothesis that bainite of coarse morphology in the microstructure of hot rolled products is formed in segregation sites. The inherited influence of the primary dendritic structure on structure formation during rolling was detected. The manganese concentration varies between bainite and neighboring structure from 0.68% to 1.01% similarly to the level in initial dendritic segregation. The difference in the content of chemical elements influences on recrystallization of austenite grains during high temperature roughing. Bainite was formed in the frames of chemically depleted coarse austenite grains steady upon phase transformation.

Keywords: slab, segregation, dendritic structure, rolled, microstructure, bainite

For citation: Vorozheva E.L., Smetanin K.S., Kislitsa V.V., Kudashov D.V. Metallographic analysis of structural peculiarities of thin slab and rolled products manufactured thereof. *Izvestiya. Ferrous Metallurgy*. 2023; 66(1): 105–111. https://doi.org/10.17073/0368-0797-2023-1-105-111

Металлографическое исследование особенностей строения тонкого сляба и произведенного из него проката

Е. Л. Ворожева [1], К. С. Сметанин [1], В. В. Кислица [1], Д. В. Кудашов [1, 2]

[1] **АО «Выксунский металлургический завод»** (Россия, 607060, Нижегородская обл., Выкса, ул. Бр. Баташевых, 45)
[2] **Выксунский филиал НИТУ «МИСиС»** (Россия, 607060, Нижегородская обл., Выксунский район, п.г.т. Шиморское, ул. Калинина, 206)

vorozheva_el@vsw.ru

Аннотация. Определен уровень зональных и дендритных сегрегаций в слябах, разлитых по тонкослябовой технологии. Рассчитанные коэффициенты вариации содержания основных и примесных химических элементов по сечению слябов не превышают 10 %, зональные сегрегации невысокие. Содержание марганца, измеренное по площади, занимаемой дендритными осями и междендритными промежутками, показало уровень дендритной сегрегации. Концентрация марганца изменяется от 0,6 до 1,1 % соответственно. Установлено, что использование динамического мягкого обжатия в процессе затвердевания позволяет измельчить первичную дендритную структуру для образования дополнительных центров при фазовом превращении δ-феррита в аустенит. Размеры исходных аустенитных зерен, сформированных с учетом первичной дендритной структуры, в тонком слябе в 3 раза меньше, чем в слябе толщиной более 200 мм. Преобразования дендритной структуры в ходе обжатий показывают высокую прорабатываемость, необходимую для формирования равномерных аустенитных зерен в подкате перед чистовой прокаткой. Исследованием не подтверждена гипотеза о том, что бейнит

грубой морфологии в микроструктуре горячекатаного проката образуется в сегрегационных участках. Выявлено наследственное влияние первичной дендритной структуры на структурообразование в ходе прокатки. Концентрация марганца изменяется между бейнитом и «соседней» структурой от 0,68 до 1,01 % подобно уровню исходной дендритной сегрегации. Различие в содержании химических элементов влияет на процессы рекристаллизации аустенитных зерен в ходе высокотемпературной черновой прокатки. Бейнит сформировался в рамках химически «обедненных» крупных аустенитных зерен, устойчивых при фазовом превращении.

Ключевые слова: сляб, сегрегация, дендритная структура, прокат, микроструктура, бейнит

Для цитирования: Ворожева Е.Л., Сметанин К.С., Кислица В.В., Кудашов Д.В. Металлографическое исследование особенностей строения тонкого сляба и произведенного из него проката. *Известия вузов. Черная металлургия*. 2023; 66(1): 106–111. https://doi.org/10.17073/0368-0797-2023-1-105-111

Introduction

The rolling production of various steel grades was implemented at the casting and rolling facility (CRF), JSC "Vyksa Metallurgical Plant", including cold and corrosion resistant versions. The continuous improvement of product quality allows the properties of hot rolled product [1 – 5] to be enhanced. Thus the increase in the slab thickness from 90 to 105 mm resulted in increase in the facility efficiency [6]. In thin slab technology without recrystallization of austenite grains before rolling and restricted cumulative deformation, the initial cast structure exerts inherited influence on formation of final structure of rolled products [7]. The slab austenite structure before the start of rolling is determined by the cast metal structure previously formed during crystallization. The boundaries of initial cast grains are propagated along the interdendritic spaces. The grain shape and sizes depend on the solidifying conditions. The dispersity of cast structure changes from the surface to the middle of the slab thickness: consecutively the zones of fine crystals are formed, oriented columnar crystals and crystals of equiaxial shape. According to the results in [8 – 12], the distances between the dendritic axes of the second order increase from the surface to the center from 20 to 180 – 250 μm in thin slabs, respectively. This parameter in dendritic structure of classical thick slab is higher: 50 μm near surface, 350 μm in the middle of thickness.

It was experimentally established that under conditions of CRF in the course of blistering slab from micro-alloyed steel in tunnel furnace at 1150 – 1170 °C, about 60 % of dispersed particles are dissolved. The size of initial austenite grain in slab changes insignificantly [4]. Therefore, in order to achieve superior properties in rolled products, more disperse initial cast structure must be obtained before slab rolling by controlling metal solidifying [13]. In addition to the sizes of cast grains, the microstructure formation during rolling can be also influenced by chemical segregations stipulated by conditions of melt presence in liquid solid two phase region. During solidification there occurs subdivision of elements at macrolevel with formation zonal segregations. The dendritic character of solidification leads to microsegregations.

Generally, the main consequence of segregations can be the formation of structural heterogeneity in rolled metal negatively influencing on mechanical properties [14]. The aim of this work was to analyse the internal chemical and structural properties formed at the stages of solidification of thin slab and as a consequence of $\delta \rightarrow \gamma$ transformation, and to determine their influence on the formation of microstructure during hot deformation.

Experimental

The research material was an array of ten industrial thin slabs of low carbon micro-alloyed steels, Grade K52, and respective rolled products.

The zonal chemical segregation was determined by slab thickness using atomic emission spectral analysis [15]. Five to seven measurements were made at each considered site: at least 30 burnings over the thickness of each slab. The dissipation of chemical elements over the slab cross section was estimated by the coefficient of variation calculated as the ratio of standard deviation in the data array to average value [11]. The distribution of chemical elements over the dendrite axes and interaxial spaces was estimated by manganese content [16; 17]. The cast structure was analyzed using a Carl Zeiss Axio Observer Dlm optical microscope on metallographic polished cross sections made from rapidly cooled slabs. The diameter of former austenite grains highlighted by ferrite was measured in the cross sections parallel to the slab wide faces. In these cross-sections, the grains are of equiaxial shape. Therefore, it was sufficient to measure the diameter without adjusting coefficients [18; 19]. The microstructure of rolled products was analyzed by reflected electron diffraction (RED) using Ultra 55 electron microscope equipped with HKL Channel 5 analytical system. The RED maps were plotted as 1/4 thickness of rolled products at 125× and 500× magnifications with scanning step of 0.5 and 0.1 μm, respectively. In the maps obtained, the low angle boundaries (LAB) were plotted at the grain boundary angle from 2 to 15°, and the high angle boundaries (HAB) at the angle boundaries of higher than 15°. The grain sizes were estimated by the sizes of sites restricted by HAB [20].

Results and discussion

The calculated coefficients of array variation together with the data of spectral analysis (Table 1) demonstrate

Table 1

Variation coefficients

Таблица 1. **Коэффициенты вариации**

Variation coefficient (ratio of standard deviation to average value), %						
C	Mn	Si	P	S	V	Nb
5.6 – 6.6	0.5 – 0.8	0.6 – 1.0	5.2 – 9.4	2.6 – 3.4	0.8	3.7 – 5.1

that the dissipation chemical elements over the cross section of thin slabs from low carbon micro-alloyed steel is insignificant. The variation coefficients of the main and impurity elements are lower than 10 %. In comparison with these results in a classical slab with the thickness of 250 mm of identical chemical composition, the coefficient of variation of carbon reaches 25.7 %. The dissipation of other elements is the same as in a thin slab. Therefore, the casting conditions of thin slabs allows metal close to chemically homogenous metal to be obtained.

The zonal segregations are insignificant. Analysis of dendritic segregation demonstrated that the manganese content over the area occupied by dendritic axes and interdendritic spaces varies from 0.6 to 1.1 %. The manganese distribution map illustrates primary solidified state and dendritic segregation in a slab from low carbon steel (Fig. 1).

The classic tree structure in a thin slab of low carbon steel is violated. One of the reasons of destruction of the dendritic structure is the dynamic soft reduction during solidification, leading to breakage and refining

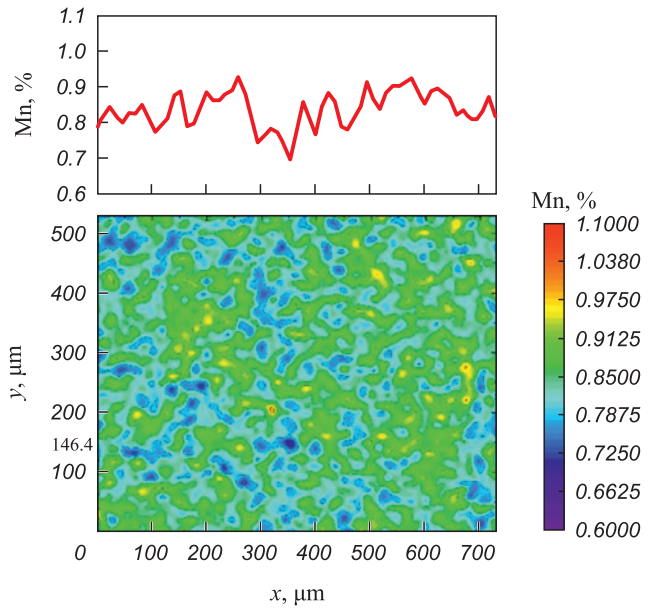

Fig. 1. Map of manganese distribution over the cross section of dendrites and inter-dendritic spaces

Рис. 1. Карта распределения марганца по сечению дендритов и междендритных пространств

of growing dendrites. Additional centers are formed for nucleation of austenite grains during phase transformation δ → γ [13], providing structure dispersity before hot rolling.

The size of initial austenite grains formed with accounting for primary dendritic structure is in the range from 0.5 to 1.5 mm. In the aims of comparison, in a classic slab with the thickness of higher than 200 mm before rolling preheating the grain size near the surface is 1.5 mm and increases to 4.5 mm in the middle of the thickness. The grains highlighted by ferrite in cross section parallel to wide faces of slabs with the thickness of 90 and 105 mm are illustrated in Fig. 2.

In the course of thermomechanical treatment, the structural heterogeneity is minimized due to correctly selected microalloying and significant reductions of slab in roughing train [1 – 5]. The deformation distribution curve plotted by relative changes of dendritic structure [21] in a slab during roughing demonstrated that actual reductions in the CRF roughing train provide uniform local deformations (Fig. 3), which are required for obtaining of homogeneous fine grain structure before roughing.

The maps of grain boundary and microstructure of final hot rolled products in the form of Kikuchi diffraction patterns are illustrated in Fig. 4. It can be seen that the structure is comprised mainly of polygonal ferrite (Fig. 4, *a*), the matrix of which contains bainite regions with predominant granular morphology (Fig. 4, *b*) and, to a lower extent, of rack morphology. The structure of granular bainite contains to a higher extent large angle boundaries [20], which can be observed in the grain boundary maps.

The maps are plotted to give a better demonstration of grain sizes in the structure of the considered samples (Fig. 5). Each site bounded by HAB is colored from blue to red. Blue corresponds to the finest grains, red corresponds to the coarsest sites. The structure is mainly homogenous in terms of grain sizes.

The grain measurements are summarized in Table 2. The fraction of large sizes of bainite of low temperature modification of rack morphology with LAB, formed in the frames of initial austenite grains, does not exceed 10 %.

The map of manganese distribution over bainite surface area does not confirm the hypothesis that bainite

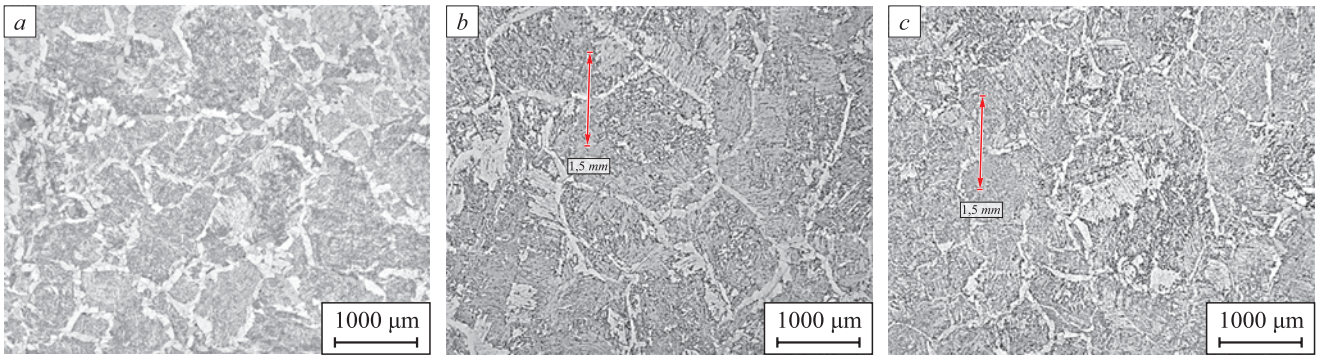

Fig. 2. View of grains in the planes parallel to the wide face of thin slabs:
a – 5 mm from the surface, d_{av} = 0.5 mm; *b* – quarter of slab thickness, d_{av} = 1.5 mm; *c* – middle of the slab thickness, d_{av} = 1.0 mm

Рис. 2. Вид зерен в плоскостях, параллельных широкой грани тонких слябов:
a – 5 мм от поверхности, $d_{ср}$ = 0,5 мм; *b* – четверть толщины сляба, $d_{ср}$ = 1,5 мм; *c* – середина толщины сляба, $d_{ср}$ = 1,0 мм

of coarse morphology in the microstructure of hot rolled products is formed in segregation sites (Fig. 6). This figure demonstrates that it is identical with dendritic segregation. The manganese content in the surface area occupied by bainite and neighboring structure varies from 0.68 to 1.01 %, respectively. Bainite with LAB was formed in the frames of austenite grains steady upon phase transformation [22].

The difference in content of chemical elements between dendrite frames and in interdendritic spaces can influence on recrystallization of austenite grains during high temperature roughing. At a chemically pure site, the barrier action for prevention of growth of recrystallized austenite grains is weakened, in comparison with chemically enriched spaces. The determined regularity indicates that minimization of bainite fraction of coarse morphology in rolling is possible due to decrease in the initial dendritic segregation during solidification of liquid steel. The studies established that a decrease in the distance between dendritic axes of the second order by 30 μm in

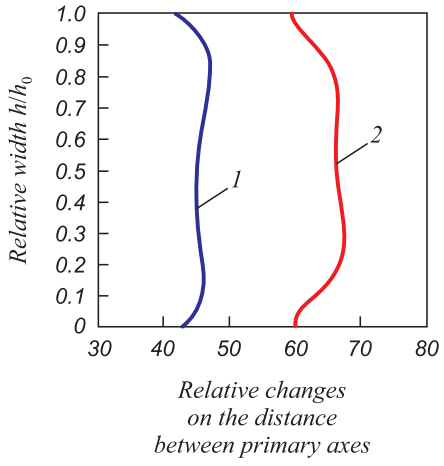

Fig. 3. Influence of deformation on dendrite transformation along the slabs thickness:
1 – 45 – 50 %; *2* – 65 – 70 %

Рис. 3. Влияние деформации на трансформацию дендритов по толщине слябов:
1 – 45 – 50 %; *2* – 65 – 70 %

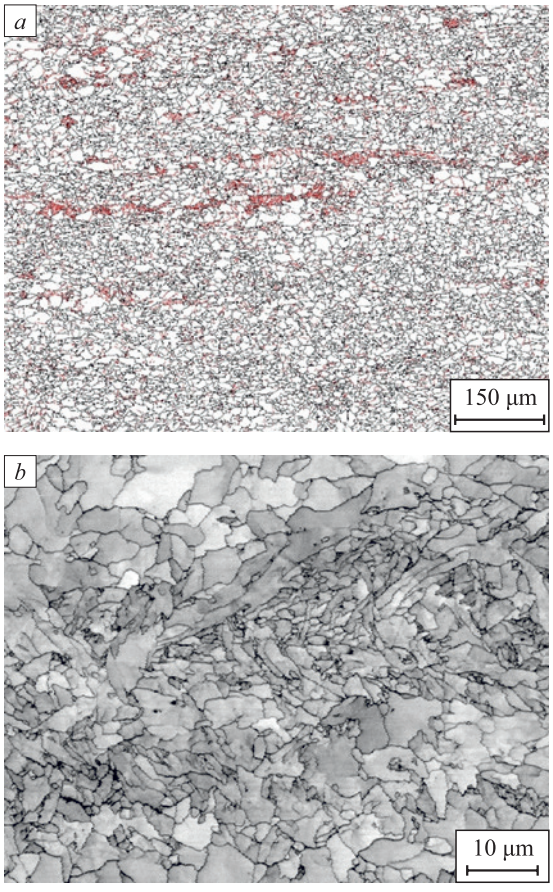

Fig. 4. Microstructure of hot rolled products:
a – grid of large-angle (black) and small-angle (red) borders;
b – structure of bainite areas

Рис. 4. Микроструктура горячекатаного проката:
a – сетка большеугловых (черные) и малоугловых (красные) границ; *b* – структура бейнитных участков

Table 2

Grain size estimation based on the maps of reflected electron diffraction

Таблица 2. **Результаты оценки размеров зерна на основе ДОЭ-карт**

Weighted average grain diameter, μm	Maximum grain diameter, μm	Maximum grain surface area, μm^2	Coefficient of grain size non-homogeneity
13.4	48.7	1864	5.4

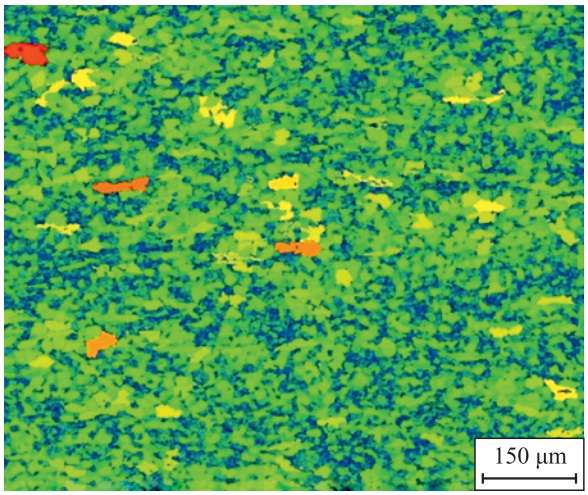

Fig. 5. Grain size maps

Рис. 5. Карты размеров зерна

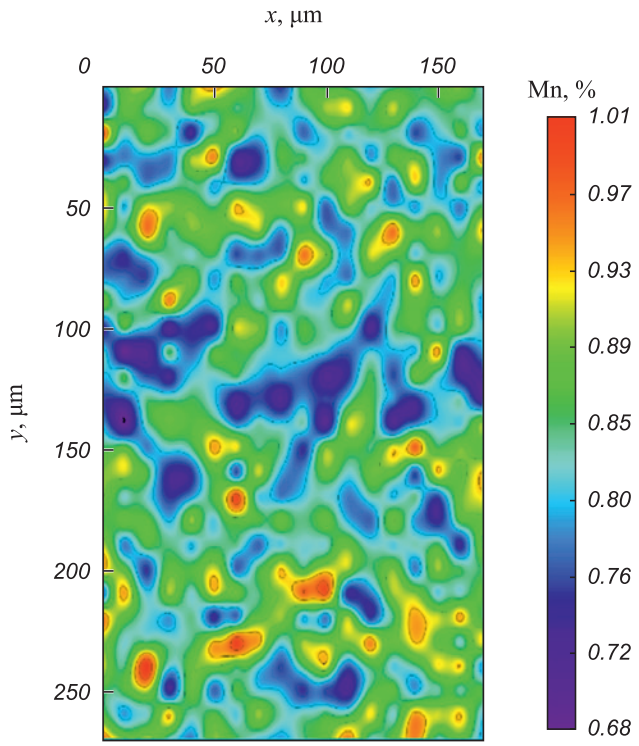

Fig. 6. Mn content at the site of bainite and "neighboring" microstructure areas

Рис. 6. Содержание Mn по месту бейнита и «соседних» участков микроструктуры

average results in a decrease in the dendritic segregation by 20 % [23]. The disperse primary dendritic structure is a prerequisite for formation of uniform recrystallized austenite structure during rolling in roughing train.

Conclusions

Estimation of zonal segregations demonstrated that dissipation of chemical elements over the cross section of thin slabs from low carbon micro-alloyed steel is insignificant. The coefficients of variation are less than 10 %. In comparison with these results in slab with the thickness of more than 200 mm the variation coefficient of carbon reaches 25.7 %.

The dendritic segregation illustrated by the map of manganese distribution demonstrated the primary solidified state of low carbon steel with violated structure of dendrite. The refining of growing dendrites in the course of solidification by dynamic reduction of slab provided additional centers for the nucleation of austenite grains upon phase transformation $\delta \rightarrow \gamma$. The sizes of initial austenite grains in the cast structure of thin slab are three times lower than in a slab with the thickness of higher than 200 mm.

The calculation of relative changes in the sizes of dendritic structure during roughing demonstrated uniform structural transformations required for obtaining of uniform austenite grain before entry into finishing train.

It was established that the nature of bainite with a higher density of low angle boundaries in final microstructure of rolled products is stipulated by the inherited influence of dendritic segregation during rolling. Decrease in the dendritic segregation is a prerequisite for formation of uniform recrystallized austenite structure during roughing.

References / Список литературы

1. Muntin A.V., Chastukhin A.V., Chervonnyi A.V., Naumenko V.V., Efron L.I., Ringinen D.A. Development of technology for production of rolled products of K60 strength class in conditions of casting and rolling complex. *Problemy chernoi metallurgii i materialovedeniya*. 2016; (3): 17–25. (In Russ.).

Мунтин А.В., Частухин А.В., Червонный А.В., Науменко В.В., Эфрон Л.И., Рингинен Д.А. Разработка технологии производства рулонного проката трубного назначения класса прочности К60 в условиях литейно-прокатного комплекса. *Проблемы черной металлургии и материаловедения*. 2016; (3): 17–25.

2. Muntin A.V. Advanced technologies of combined process of thin slabs continuous casting and hot strip rolling. *Metallurgist*. 2019; 62(9-10): 900–910. https://doi.org/10.1007/s11015-019-00747-5

Мунтин А.В. Передовые технологии совмещенного процесса непрерывного литья тонких слябов и горячей прокатки. *Металлург*. 2018; (9): 43–51.

3. Chervonnyi A.V., Ringinen D.A., Chastukhin A.V., Efron L.I., Muntin A.V., Naumenko V.V., Bagmet O.A. Structure and property formation for pipe coiled rolled product during manufacture under casting and rolling complex conditions. *Metallurgist*. 2019; 62(9-10): 1012–1021. https://doi.org/10.1007/s11015-019-00748-4

Червонный А.В., Рингинен Д.А., Частухин А.В., Эфрон Л.И., Мунтин А.В., Науменко В.В., Багмет О.А. Формирование структуры и свойств рулонного проката трубного назначения при производстве в условиях литейно-прокатного комплекса. *Металлург*. 2018; (10): 40–47.

4. Chervonnyi A.V. *Development of microalloyed steel compositions for electro-welded pipes of strength classes K56-K60 and their controlled rolling modes in the conditions of casting and rolling complex: Extended Abstract of Cand. Sci. Diss*. Moscow; 2021: 16. (In Russ.).

Червонный А.В. *Разработка составов микролегированных сталей для электросварных труб классов прочности К56-К60 и режимов их контролируемой прокатки в условиях литейно-прокатного комплекса: Автореферат диссертации ... кандидата технических наук*. Москва; 2021: 16.

5. Barykov A.M., Stepanov P.P. *Development of Technologies for the Production of Steel, Rolled Products and Pipes at the Vyksa Production Site: Coll. of Papers*. Barykov A.M. ed. Moscow: Metallurgizdat; 2016: 203. (In Russ.).

Барыков А.М., Степанов П.П. *Развитие технологий производства стали, проката и труб на выксунской производственной площадке: Сборник трудов*. Под общ. ред. А.М. Барыкова. Москва: Металлургиздат; 2016: 203.

6. Kislitsa V.V., Maksaev E.N., Boiko A.S., Vorozheva E.L., Smetanin K.S. Evaluation of quality indices of slabs and rolled products with an increase in thickness of continuously cast billets. *Steel in Translation*. 2021; 51(8): 548–553. https://doi.org/10.3103/S0967091221080076

Кислица В.В., Максаев Е.Н., Бойко А.С., Ворожева Е.Л., Сметанин К.С. Оценка качественных показателей сляба и проката при повышении толщины непрерывнолитой заготовки. *Сталь*. 2021; (8): 17–21.

7. Efron L.I. *Metal Science in "Big" Metallurgy. Pipe Steels.* Moscow: Metallurgizdat; 2012: 696. (In Russ.).

Эфрон Л.И. *Металловедение в «большой» металлургии. Трубные стали*. Москва: Металлургиздат; 2012: 696.

8. Ruiz-Aparicio A. *Evolution of Microstructure in Nb-Bearing Microalloyed Steels Produced by the Compact Strip Production Process: Master's Thesis*. University of Pittsburg; 2004: 162.

9. Garcia C.I., Ruiz-Aparicio A., Cho K., Ma Y.P, Graham C., Vazquez M., Ruiz-Aparicio L., DeArdo A.J. Microstructural characterization of the solidification and equilibrated microstructures of Nb-bearing microalloyed steels produced by the compact strip processing. *Int. Symp. on Thin Slab Casting and Rolling (TSCR'2002), December 3–5,2002, Guangzhou, China.* URL: https://www.researchgate.net/publication/304900786

10. Garcia C.I., Torkaz C., Graham C., DeArdo A.J. Physical metallurgy of high strength low alloy strip steel production using compact strip processing. *Ironmaking and Steelmaking*. 2005; 32(4): 314–318. https://doi.org/10.1179/174328105X48052

11. Vorozheva E.L., Kudashov D.V., Khlybov A.A., Smetanin K.S. Methods for studying the structural state of continuously cast slabs and the hot-rolled metal produced at the casting and rolling complex. *Russian Metallurgy (Metally)*. 2022; (5): 496–494. http://doi.org/10.1134/S003602952205010X

Ворожева Е.Л., Кудашов Д.В., Хлыбов А.А., Сметанин К.С. Методы изучения структурного состояния непрерывнолитых слябов и горячекатаного металла, произведенного на литейно-прокатном комплексе. *Металлы*. 2022; (3): 40–48.

12. Khlybov A., Vorozheva E. Studying on the internal quality of steel at various stages of production: Slab-rolled metall. *Materials Science Forum*. 2022; 1052: 377–383. https://doi.org/10.4028/p-0skw5n

13. Zhou T., O'Malley R.J., Zurob H.S., Subramanian M., Cho S.-H., Zhang P. Control of upstream austenite grain coarsening during the thin-slab cast direct-rolling (TSCDR) process. *Metals*. 2019; 9(158): 1–18. https://doi.org/10.3390/met9020158

14. Verhoven J.D. A review of microsegregation induced banding phenomena in steels. *Journal of Materials Engineering and Performance*. 2000; 9(3): 286–296. https://doi.org/10.1361/105994900770345935

15. *GOST R 54153-2010. Steel. The method of atomic emission spectral analysis*. Moscow: Standartinform; 2012: 28.

ГОСТ Р 54153-2010 «Сталь. Метод атомно-эмиссионного спектрального анализа». Москва: Стандартинформ; 2012: 28.

16. Presslinger H., Mayr M., Tragl E., Bernhard C. Assessment of the primary structure of slabs and the influence on hot- and cold-rolled strip structure. *Steel Research International*. 2006; 77(2): 107–115. https://doi.org/10.1002/srin.200606362

17. Yan C., Ju X., Meng Y., Shi X. Quantification of manganese dendritic segregation in 380CL steel billet by electron probe microanalysis. *SN Applied Sciences*. 2019; 1: 623. https://doi.org/10.1007/s42452-019-0612-3

18. Bernhard C., Reiter J., Presslinger H. A model for predicting the austenite grain size at the surface of continuously-cast slabs. *Metallurgical and Materials Transactions B*. 2008; 39(6): 885–895. https://doi.org/10.1007/s11663-008-9197-8

19. *GOST 5639-82. Steels and alloys. Methods of detection and determination of grain size*. Moscow: IPK Izdatel'stvo standartov; 2003: 16.

ГОСТ 5639-82 «Стали и сплавы. Методы выявления и определения величины зерна». Москва: ИПК «Издательство стандартов»; 2003: 16.

20. Efron L.I., Stepanov P.P., Vorkachev K.G., Kantor M.M., Bozhenov V.A., Smetanin K.S. Questioning the effect of bainite morphology on the impact viscosity of low-carbon steels. *Steel in Translation*. 2021; 51(9): 670–676. https://doi.org/10.3103/S0967091221090035

Эфрон Л.И., Степанов П.П., Воркачев К.Г., Кантор М.М., Боженов В.А., Сметанин К.С. К вопросу о влиянии морфологии бейнита на ударную вязкость низкоуглеродистых сталей. *Сталь*. 2021; (9): 45–50.

21. Levchenko G.V., Vorobei S.A., Demina E.G., Dement'eva Zh.A. Development of a method for assessing the workability of structural steel structure during hot deformation. In: *VIII Int. Conf. "Deformation and Destruction of Materials and Nanomaterials". Moscow. November 19–22, 2019: Coll. of Papers*. Moscow: IMET RAS; 2019: 42–43.

Левченко Г.В., Воробей С.А., Демина Е.Г., Дементьева Ж.А. Развитие метода оценки прорабатываемости структуры конструкционной стали в процессе горячей деформации. *VIII Международная конференция «Деформация и разрушение материалов и наноматериалов». Москва. 19–22 ноября 2019 г.: Сборник материалов*. Москва: ИМЕТ РАН; 2019: 42–43.

22. Jayanti S. *Austenitic grain size of steel. Engineering Notes*. URL: https://www.engineeringenotes.com/metallurgy/steel/austenitic-grain-size-of-steel-metallurgy/25901

23. Vorozheva E.L., Kudashov D.V, Khlybov A.A., Smetanin K.S. Features of formation of the structure of thin slabs cast at different speeds, their influence on the structure and properties of hot-rolled steel. *Chernye metally*. 2022; (7): 27–34. https://doi.org/10.17580/chm.2022.07.05

Ворожева Е.Л., Кудашов Д.В, Хлыбов А.А., Сметанин К.С. Особенности формирования структуры тонких слябов, разлитых с разными скоростями, их влияние на структуру и свойства горячекатаного проката. *Черные металлы*. 2022; (7): 27–34. https://doi.org/10.17580/chm.2022.07.05

Information about the Authors / Сведения об авторах

Evgeniya L. Vorozheva, *Chief Specialist,* JSC "Vyksa Metallurgical Plant"
E-mail: vorozheva_el@vsw.ru

Kirill S. Smetanin, *Chief Specialist on Electron Microscopy and Radiography of the Laboratory of Metal Science,* JSC "Vyksa Metallurgical Plant"
E-mail: smetanin_ks@vsw.ru

Vyacheslav V. Kislitsa, *Cand. Sci. (Eng.), Head of the Department of Metallurgical Processes,* JSC "Vyksa Metallurgical Plant"
E-mail: kislica_vv@vsw.ru

Dmitrii V. Kudashov, *Cand. Sci. (Eng.), Chief Innovation Specialist,* JSC "Vyksa Metallurgical Plant"; *Director,* Vyksa Branch of the National University of Science and Technology "MISIS"
E-mail: kudashov_dv@vsw.ru

Евгения Львовна Ворожева, *главный специалист,* АО «Выксунский металлургический завод»
E-mail: vorozheva_el@vsw.ru

Кирилл Сергеевич Сметанин, *главный специалист по электронной микроскопии и рентгенографии лаборатории металловедения,* АО «Выксунский металлургический завод»
E-mail: smetanin_ks@vsw.ru

Вячеслав Владимирович Кислица, *к.т.н., начальник управления по металлургическим процессам,* АО «Выксунский металлургический завод»
E-mail: kislica_vv@vsw.ru

Дмитрий Викторович Кудашов, *к.т.н., главный специалист по инновациям,* АО «Выксунский металлургический завод»; *директор,* Выксунский филиал НИТУ «МИСиС»
E-mail: kudashov_dv@vsw.ru

Contribution of the Authors / Вклад авторов

E. L. Vorozheva – review of literary data, research planning, preparation and etching of the samples, metallographic research using optical microscopy, analysis of the research results, writing the text, formation of the conclusions.

K. S. Smetanin – metallographic research using electron microscopy, calculations.
V. V. Kislitsa – formation of the main concept, goals and objectives of the study; approval of the article final version.
D. V. Kudashov – scientific guidance, analysis of the research results, editing the text, correction of the conclusions.

Е. Л. Ворожева – обзор литературных данных, планирование исследования, подготовка и травление образцов, металлографическое исследование с применением оптической микроскопии, анализ полученных результатов, подготовка текста, формирование выводов.
К. С. Сметанин – металлографическое исследование с применением электронной микроскопии, выполнение расчетов.
В. В. Кислица – формирование основной концепции, цели и задачи исследования, утверждение последней версии статьи.
Д. В. Кудашов – научное руководство, анализ результатов исследований, редактирование текста, корректировка выводов.

Received 25.11.2022
Revised 02.12.2022
Accepted 30.12.2022

Поступила в редакцию 25.11.2022
После доработки 02.12.2022
Принята к публикации 30.12.2022

Информационные технологии и автоматизация в черной металлургии

UDC 621.78.013
DOI 10.17073/0368-0797-2023-1-112-118

Original article
Оригинальная статья

Simulation of slab heating in a walking beam furnace

I. B. Abdukodirov [1], A. V. Vargin [2], I. A. Levitskii [2]

[1] **Subsidiary Foundry and Mechanical Plant of the "O'ztemiryo'lmashta'mir" Unitary Enterprise** (41 Kh. Baikaro Str., Tashkent 100213, Republic of Uzbekistan)
[2] **National University of Science and Technology "MISIS"** (4 Leninskii Ave., Moscow 119049, Russian Federation)

ilhomabdukadirov@mail.ru

Abstract. Slabs are preheated before hot rolling to achieve the required metal plasticity. Walking beam furnace is the most efficient form of equipment since it heats the slab from all sides. Nevertheless, the bottom surfaces in contact with the water-cooled support beams are shielded from the heat radiated by the lower part of the furnace, and their heat is transferred to the beams. We developed and implemented by means of software a simulation model to study the non-uniformity of the temperature distribution across the slab and how the slab transportation system design affects it. Thesimulation model includes a numerical solution of a 3D thermal conductivity problem with piecewise defined boundary conditions on the slab bottom surface. Identical boundary conditions were applied to both the top surface and the open areas of the slab bottom surface. For the areas of contact with the beams, we applied modified boundary conditions to account for the duration of the contact. We numerically solved the system of difference equations with the layer-by-layer method, in order to obtain a system defined by a tridiagonal matrix. The slab-to-beam contact heat transfer was assumed to be adiabatic during the entire contact period. The calculations produced the temperature fields at different cross-sections of the slab. As a result, we discovered a significant non-uniformity of the temperature field on the lower surface of the slab leading to the entire temperature field non-uniformity of the slab. We developed simulation and visualization software to study the slab temperature field under various heating conditions. The simulation model is refined from the experimental data available.

Keywords: mathematical simulation, slab heating, walking-beam furnace, 3D heat transfer problem, boundary conditions, finite difference method, heat transfer coefficient

For citation: Abdukodirov I.B., Vargin A.V., Levitskii I.A. Mathematical model of slab heating in a furnace with walking beams. *Izvestiya. Ferrous Metallurgy*. 2023; 66(1): 112–118. https://doi.org/10.17073/0368-0797-2023-1-112-118

Математическая модель нагрева сляба в печи с шагающими балками

И. Б. Абдукодиров [1], А. В. Варгин [2], И. А. Левицкий [2]

[1] **Дочернее предприятие «Литейно-механический завод» Унитарного предприятия «O'ztemiryo'lmashta'mir»** (Республика Узбекистан, 100213, Ташкент, ул. Х. Байкаро, 41)
[2] **Национальный исследовательский технологический университет «МИСИС»** (Россия, 119049, Москва, Ленинский пр., 4)

ilhomabdukadirov@mail.ru

Аннотация. Нагрев слябов перед горячей прокаткой необходим для придания металлу требуемых пластических свойств. Наиболее эффективны для этого печи с шагающими балками, обеспечивающие подачу теплоты со всех сторон сляба. Однако области нижних поверхностей слябов, контактирующие с водоохлаждаемыми балками, экранированы от излучения нижних зон обогрева печи и отдают теплоту балкам. Для исследования неоднородности температурного поля слябов и ее зависимости от особенностей конструкции системы транспортировки разработана и программно реализована математическая модель нагрева сляба в печи с шагающими балками. Модель основана на численном решении трехмерной задачи теплопроводности с кусочно-определенными граничными условиями на нижней поверхности сляба. Для открытых областей нижней поверхности сляба задавались такие же граничные условия, как на верхней поверхности, а для областей контакта с балками – модифицированные граничные условия, учитывающие продолжительность этого контакта. Для численного решения системы разностных уравнений применен послойный метод, позволяющий получить систему с трехдиагональной матрицей коэффициентов. Проведенные расчеты в приближении адиабатности участков контакта сляба с балками в период контакта позволили получить температурные поля для различных сечений сляба. В результате выявлена существенная неоднородность температурного поля нижней поверхности сляба, влияющая на неоднородность температурного поля всего сляба. Разработанная программа расчета и визуализации результатов может быть использована для изучения температурного поля сляба при различных режимах его нагрева в случае наличия экспериментальной информации, позволяющей уточнить настроечные параметры модели.

Ключевые слова: математическое моделирование, нагрев сляба, печь с шагающими балками, трехмерная задача теплопроводности, граничные условия, метод конечных разностей, коэффициент теплоотдачи

Для цитирования: Абдукодиров И.Б., Вargин А.В., Левицкий И.А. Математическая модель нагрева сляба в печи с шагающими балками. *Известия вузов. Черная металлургия*. 2023; 66(1): 113–118. https://doi.org/10.17073/0368-0797-2023-1-112-118

Introduction

The walking beam furnace providing slab heating from four sides is a state-of-the-art piece of equipment. It preheats slabs before hot rolling [1]. The slab movement system in such furnaces contains fixed and movable beams which partially shield the contact areas of the bottom surface of the slab from the thermal radiation of the combustion products coming from the lower heating area. It leads to partial heat outflow through heat conduction in the contact areas. The experimental study of heat transfer in industrial conditions is challenging, so we used simulation instead. The models simulating metal heating in furnaces [2, 3] can be divided into statistical [4, 5], analytical [6], and numerical [7 – 10]. Both direct and inverse heat conduction problems are considered in some articles [6, 11]. Simulation of in-furnace processes is extensively used to solve optimization problems [11 – 15] or to employ the capabilities of with advanced CFD software [16, 17].

The purpose of this study is to build a simulation model of slab heating in a walking beam furnace that accounts for the effect of these beams on the heating and apply the model to analyze the temperature field of the slab.

Methods and Materials

The simulation model addresses a 3D unsteady heat conduction problem in the Cartesian coordinate system. The computational domain is a parallelepiped without any internal heat sources. Its thermophysical properties are temperature-dependent. The model uses asymmetric boundary conditions of the third kind. These conditions are piecewise on the bottom surface of the computational domain.

With the above assumptions, the heat conduction equation is nonlinear:

$$\frac{\partial T}{\partial t} = \frac{1}{\rho c}\left[\frac{\partial}{\partial x}\left(\lambda\frac{\partial T}{\partial x}\right)+\frac{\partial}{\partial y}\left(\lambda\frac{\partial T}{\partial y}\right)+\frac{\partial}{\partial z}\left(\lambda\frac{\partial T}{\partial z}\right)\right],$$
$$\left\{0 < x < \delta_x,\ 0 < y < \delta_y,\ 0 < z < \delta_z\right\}. \quad (1)$$

The initial temperature field is homogeneous

$$T(x, y, z) = T_b. \quad (2)$$

Then the boundary conditions can be expressed as:

$$-\left(\lambda\frac{\partial T}{\partial x}\right)\Big|_{x=0} = \alpha_x^{\uparrow}\left(T_g - T_{x=0}\right),$$
$$\left(\lambda\frac{\partial T}{\partial x}\right)\Big|_{x=\delta_x} = \alpha_x^{\downarrow}\left(T_g - T_{x=\delta_x}\right); \quad (3)$$

$$-\left(\lambda\frac{\partial T}{\partial y}\right)\Big|_{y=0} = \alpha_y^{\uparrow}(z)\left(T_g^{\uparrow}(z) - T_{y=0}\right),$$
$$\left(\lambda\frac{\partial T}{\partial y}\right)\Big|_{y=\delta_y} = \alpha_y^{\downarrow}\left(T_g - T_{y=\delta_y}\right); \quad (4)$$

$$-\left(\lambda\frac{\partial T}{\partial z}\right)\Big|_{z=0} = \alpha_z^{\uparrow}\left(T_g - T_{z=0}\right),$$
$$\left(\lambda\frac{\partial T}{\partial z}\right)\Big|_{z=\delta_z} = \alpha_z^{\downarrow}\left(T_g - T_{z=\delta_z}\right); \quad (5)$$

Eq. (1) – (5) is a complete formulation of the differential heat conduction problem. The notations are defined as follows: $T(x, y, z, t)$ is the slab temperature, K; δ_x, δ_y, δ_z are the slab dimensions (width, thickness, length), m; ρ is the slab material density, kg/m^3; c is slab material specific heat capacity, J/(kg·K); λ is the slab material thermal conductivity, W/(m·K); $\alpha_x^{\uparrow}$ and $\alpha_x^{\downarrow}$ are the heat transfer coefficients on the rear and front vertical surfaces of the slab, respectively, W/(m^2·K); $\alpha_y^{\uparrow}$ and $\alpha_y^{\downarrow}$ are the heat transfer coefficients on the bottom and top surfaces of the slab, respectively, W/(m^2·K); $\alpha_z^{\uparrow}$ and $\alpha_z^{\downarrow}$ are the heat transfer coefficients on the left and right end surfaces of the slab, respectively, W/(m^2·K); T_g is the heating medium temperature, K; T_b is initial slab temerature, K.

The equations are expressed in the coordinate system attached to the slab. For this reason, the design features of a specific furnace affect the boundary conditions. First, in order to account for different heating conditions in various furnace areas, the heat transfer coefficients and the temperature of the heating medium are described as a piecewise function of time. Secondly, the properties are specified individually for each slab surface to take into account the furnace geometry in the simulation model. For example, if the furnace hearth is solid (which is common in walking hearth and pusher furnaces), the respective heat transfer coefficient $\alpha_y^{\uparrow}$ is set to zero. In this way, we expressed the adiabatic condition on the slab bottom surface. For walking beam furnaces, the boundary conditions at the slab top and bottom surfaces must be consistent with the different heat input rates in the lower and upper areas of the furnace chamber. Although the combustion occurs

in both lower and upper areas, the slab bottom surface is significantly shielded by the slab transport components. Moreover, the slab bottom surface has contact areas with riders on the movable and fixed beams. For this reason, the boundary conditions should be different for the three types of bottom surface areas:

– areas between the beams (type 0);

– areas that periodically come into contact with the movable beams (type 1);

– areas in permanent contact with the fixed beams (type 2).

This means that $\alpha_y^{\uparrow}(z)$ and $T_g^{\uparrow}(z)$ – members of the boundary conditions on the slab bottom surface – are piecewise functions of the coordinate along the slab's length. They are piecewise functions of time in the same way as the other boundary conditions. We also should remember that as the slab is walked (moved) through the furnace, both the contact conditions with the beams and the intensity of the slab bottom surface shielding vary. The simulation model describes the heat transfer on the slab bottom surface as it comes into contact with the cooled beam by the conditional heat transfer coefficients $\tilde{\alpha}_s$ and $\tilde{\alpha}_m$, W/(m^2·K). The heat is transferred to the medium at a temperature $\tilde{T}_s$ or $\tilde{T}_m$, K, which circulates in the beam cooling system. In most cases, the coolant is water or steam. For open-flame furnaces (they also include walking beam furnaces), the heat transfer coefficients describe both convective and radiative heat transfer (linearization of the (3) – (5) boundary conditions is beneficial to accelerate the numerical solution convergence).

The walking cycle consists of individual stages. We used the stage names and approximate durations specified in the datasheet of a furnace operated in Casthouse No. 2, Severstal. The walk beam system specifications are listed in Table 1.

Note that the information in Table 1 is insufficient to estimate the slab-to-beam contact time. We need to know the slab feed cycle time τ, s (its minimum value is equal to the total duration of walking, but in real-life applications, the value is usually several times greater), and the spacing between the slabs in the furnace L, m (sum of the slab width and the slab-to-slab gap). Then during the feed cycle τ, the time of contact with the movable beams is [7]:

$$\tau_m = \frac{L}{l}\left(\tau_{\uparrow} + \tau_{\rightarrow} + \tau_{\downarrow}\right), \quad (6)$$

and the time of contact with the stationary beams is

$$\tau_s = \tau - \frac{L}{l}\left(\tau_{\uparrow} + \tau_{\rightarrow} + \tau_{\downarrow}\right). \quad (7)$$

For heating simulation, modifying the boundary conditions at each walking stage is impractical, because it would require extremely small time steps ($\Delta t \le 1$ c). It is advisable to specify the boundary conditions for the areas in contact with the beams as a weighted average result to account for the share of total contact time. This approach does not require the time steps to be multiples of the walking stage durations. Then the effective heat transfer coefficient, specified as a boundary condition on an area of the lower surface of an i^{th} type, is estimated as

$$\alpha_y^{\uparrow}(z_i) = \begin{cases} \alpha^{\uparrow}, & i = 0 \\ \alpha^{\uparrow}(1-\xi) + \xi\tilde{\alpha}_m, & i = 1, \\ \alpha^{\uparrow}\xi + \tilde{\alpha}_m(1-\xi), & i = 2 \end{cases} \quad (8)$$

the effective temperature of the medium in contact with the lower surface area of the i^{th} type is

$$T_g^{\uparrow}(z_i) = \begin{cases} T_g, & i = 0 \\ \dfrac{\xi\tilde{\alpha}_m\tilde{T}_m + (1-\xi)\alpha^{\uparrow}T_g}{\xi\tilde{\alpha}_m + (1-\xi)\alpha^{\uparrow}}, & i = 1 \\ \dfrac{(1-\xi)\tilde{\alpha}_s\tilde{T}_s + \xi\alpha^{\uparrow}T_g}{(1-\xi)\tilde{\alpha}_s + \xi\alpha^{\uparrow}}, & i = 2 \end{cases}, \quad (9)$$

the auxiliary coefficient ξ characterizes the share of time when the slab is in contact with the movable beams:

$$\xi = \frac{\tau_m}{\tau} = \frac{L}{l}\frac{\tau_{\uparrow} + \tau_{\rightarrow} + \tau_{\downarrow}}{\tau}. \quad (10)$$

The non-linear problem (1) – (5) has no analytical solution, so we had to resolve it by the finite difference method [7, 18, 19].

This method introduces a discrete time variable $t_k = k\Delta t$ (k = 1, 2, ...) with the constant step Δt and dis-

Table 1

Example of the walking mechanism characteristics

Таблица 1. **Пример характеристик работы механизма шагания**

Stage	Lifting	Move forward	Lowering	Reverse	Push rod stroke, mm
Designation	$\tau_{\uparrow}$	$\tau_{\rightarrow}$	$\tau_{\downarrow}$	$\tau_{\leftarrow}$	l
Duration, s	16	12	19	9	480

crete coordinates $x_i = i\Delta x$ $(i = 0, 1, 2, .., n_x)$, $y_j = j\Delta y$ $(j = 0, 1, 2, .., n_y)$, $z_l = l\Delta z$ $(l = 0, 1, 2, .., n_z)$. For the simple geometry under consideration, the coordinate also changes with the constant steps Δx, Δy and Δz. The n_x, n_y and n_z values are the numbers of partitions along each coordinate axis.

As a result, the computational domain is partitioned into elementary volumes. Their number is equal to $(n_x + 1)$ $(n_y + 1)(n_z + 1)$. Each of these elementary volumes contains one node of the 3D grid. Each node is denoted with three indices (i, j, l). At each time step increment, the heat balance equations are formulated for each elementary volume. They form a quasi-linear system of equations where the temperatures at the nodes at the end of each time step are unknown quantities. Solving the system with general methods is not advisable [19, 20].

Results

We implemented the simulation model as a Builder C++ ver. 6.0 application. The software supports three algorithms for solving the system of difference equations:

– the split method (applicable to linear problems only);

– the simple iteration method (low memory requirements, but slow to converge);

– the layer-by-layer method (direct solution for heat propagation along the slab thickness with an iterative refinement of its propagation along the length and width).

The $\tilde{\alpha}_s$, $\tilde{\alpha}_m$, $\tilde{T}_s$ and $\tilde{T}_m$ values can be found only from test data using a model of heat transfer between the slab bottom surface and the slab transport components. For our software implementation, these values are input data. So far we proposed to take into account only the shielding effect of the slab transport components by setting $\tilde{\alpha}_s$ and $\tilde{\alpha}_m$ to zero. Fig. 1 shows the initial data for the simulation, and Table 2 lists the slab heating conditions in a five zone heating furnace.

The heat balance of the slab is verified at each time step and globally (max error does not exceed 0.001). Fig. 2 shows the final temperature profiles for the bottom (*a*) and top (*b*) surfaces (temperature variation along the longitudinal axis of the surface) of a 250×500×6000 mm slab heated in a furnace with four fixed and two movable beams. For comparison, Fig. 2, *c* shows the temperature profile along the axis of the bottom surface heated under uniform boundary conditions obtained by averaging of conditions at this surface.

Discussion

The results indicate that at the slab end faces, the temperature on the axis of the top and bottom surfaces increases by about 20 – 25 °C regardless of the type of boundary conditions. This can be explained by the effect of heat supply to the slab ends. In terms of the uniform boundary conditions on the bottom surface, the temperature profile in the rest of the bottom surface axis of the slab is vir-

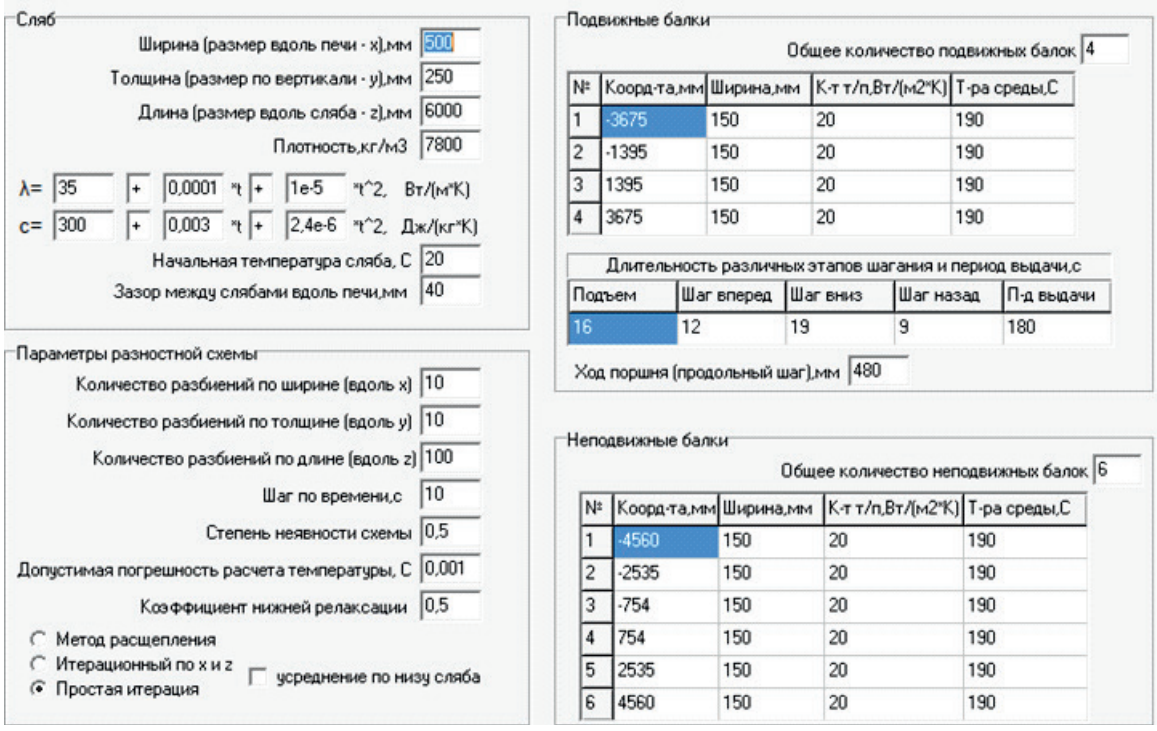

Fig. 1. Input data for simulation

Рис. 1. Снимок экрана программы с исходными данными для моделирования

Table 2

Simulated heating conditions

Таблица 2. **Параметры режима нагрева при моделировании**

Heating zone number	Duration, min	Medium temperature, °C		Heat transfer coefficient at the slab face, W/(m²·K)					
		start	end	bottom	top	left	right	rear	front
1	40	700	1000	30	40	30	30	35	45
2	35	1000	1100	40	50	30	30	45	55
3	35	1100	1200	50	60	60	60	55	65
4	35	1200	1250	90	100	100	100	95	105
5	35	1250	1250	110	120	110	110	105	115

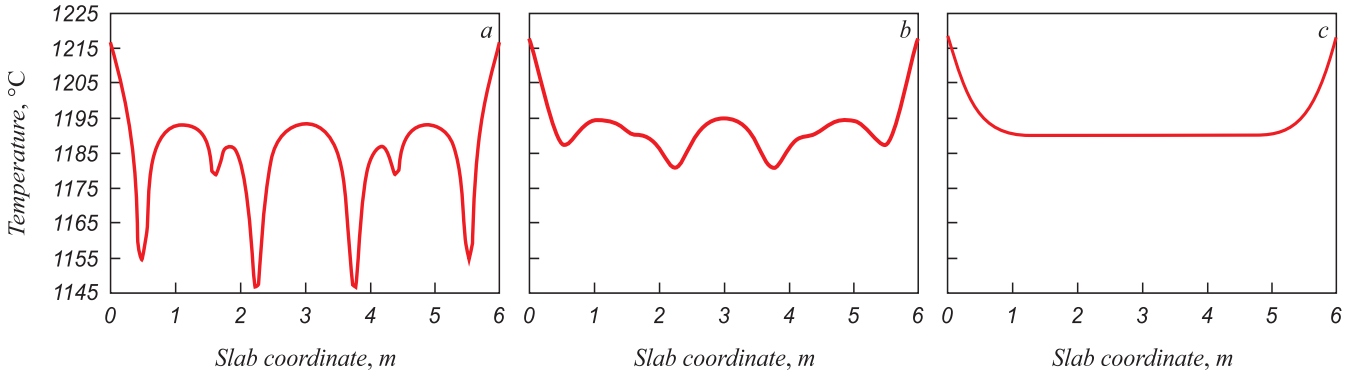

Fig. 2. Temperature profile along the axis of the top (*a*) and bottom (*б*) slab surfaces for piecewise-defined and averaged (*в*) boundary conditions at the bottom surface

Рис. 2. Температурный профиль вдоль оси нижней (*а*) и верхней (*б*) поверхностей сляба при кусочном задании граничных условий на нижней поверхности и их усреднении (*в*)

tually uniform (Fig. 2, *c*), while for piecewise boundary conditions, the temperature field non-uniformity in this area reaches 48 °C (Fig. 2, *a*). The non-uniformity of the temperature field can also be seen at the slab top face, but it is significantly lower (about 15 °C away from the slab ends, refer to Fig. 2, *b*). It should also be noted that for stationary beams, the "impact spot" is deeper and wider than for movable beams (Fig. 2, *a*). This is because the contact time of the slab bottom surface with the stationary beams is longer than with the movable beams.

The software can be used to study the slab temperature field in various heating conditions from available experimental data used to specify the model tuning parameters $\tilde{\alpha}_s$, $\tilde{\alpha}_m$, $\tilde{T}_s$ and $\tilde{T}_m$. The results of analysis when only the shielding effect of the beams is accounted for should be considered as a lower-bound estimate of the slab temperature field non-uniformity.

Conclusions

We developed and implemented a simulation model of the slab heating in a walking beam furnace which accounts for the effect of the beams on the slab bottom surface.

The model is a 3D unsteady thermal conductivity problem with boundary conditions of the third kind. These conditions are piecewise on the slab bottom surface.

For a furnace with four fixed and two movable beams, we simulated the heating of a 250×500×6000 mm slab under standard conditions and accounting for only the shielding effect of the beams on the slab bottom surface. The temperature non-uniformity on the slab bottom surface away from its ends was about 48 °C, while on the top surface – about 15 °C.

Список литературы / References

1. Gusovskii V.L., Lifshits A.E. *Methods of Heating and Thermal Furnaces Design: Reference Textbook*. Moscow: Teplotechnik; 2004: 400. (In Russ.).

   Гусовский В.Л., Лифшиц А.Е. *Методики расчета нагревательных и термических печей: Учебно-справочное издание*. М.: Теплотехник; 2004: 400.
2. Timoshpol'skii V.I., Trusova I.A., Mendeleev D.V., Ratnikov P.E. Analysis of mathematical modeling methods of heat transfer in industrial furnaces for metal heating. *Lit'e i metallurgiya*. 2012; 2(65): 102–107. (In Russ.).

Тимошпольский В.И., Трусова И.А., Менделеев Д.В., Ратников П.Э. Анализ методов математического моделирования процессов теплообмена в промышленных печах для нагрева металла. *Литье и металлургия*. 2012; 2(65): 102–107.

3. Singh V.K., Talukdar P. Comparisons of different heat transfer models of a walking beam type reheat furnace. *International Communications in Heat and Mass Transfer*. 2013; 47: 20–26. https://doi.org/10.1016/j.icheatmasstransfer.2013.06.004
4. Belen'kiy A.M., Bogatova M.Zh., Chibizova S.I. Statistical modeling of metal heating in furnaces with walking beams. *Chernye Metally*. 2021; 8: 32–37. (In Russ.). https://doi.org/10.17580/chm.2021.08.06

   Беленький А.М., Богатова М.Ж., Чибизова С.И. Статическое моделирование нагрева металла в печах с шагающими балками. *Черные металлы*. 2021; 8: 32–37. https://doi.org/10.17580/chm.2021.08.06
5. Bogatova M.Zh., Chibizova S.I. Statistical modeling of temperature operating modes of heating furnaces for hot strip mills. *Izvestiya. Ferrous Metallurgy*. 2021; 64(5): 374–381. (In Russ.). https://doi.org/10.17073/0368-0797-2021-5-374-381

   Богатова М.Ж., Чибизова С.И. Статистическое моделирование температурных режимов работы нагревательных печей листовых станов горячей прокатки. *Известия вузов. Черная металлургия*. 2021; 64(5): 374–381. https://doi.org/10.17073/0368-0797-2021-5-374-381
6. Levitskiy I.A. The linear heat conduction problem for bodies with a regular shape under boundary conditions of the third kind. *Chernye Metally*. 2019; 10: 67–72. (In Russ.).

   Левицкий И.А. Линейная задача теплопроводности для тел правильной формы при граничных условиях третьего рода. *Черные металлы*. 2019; 10: 67–72.
7. Abdukodirov I.B. *Mathematical model of slab heating in a furnace with walking beams: Mag. Diss*. Moscow; 2020: 68. (In Russ.).

   Абдукодиров И.Б. *Математическая модель нагрева сляба в печи с шагающими балками: дис. магистра:* 22.04.02. Москва; 2020: 68.
8. Han S.H., Chang D., Kim C.Y. A numerical analysis of slab heating characteristics in a walking beam type reheating furnace. *International Journal of Heat and Mass Transfer*. 2010; 53(19-20): 3855–3861. https://doi.org/10.1016/j.ijheatmasstransfer.2010.05.002
9. Kurnosov V.V., Levitskii I.A., Pribytkov I.A. Massive billets different rates heating in batch furnaces study. *Izvestiya. Ferrous Metallurgy*. 2012; 55(9): 27–31. (In Russ.). https://doi.org/10.17073/0368-0797-2012-9-27-31

   Курносов В.В., Левицкий И.А., Прибытков И.А. Исследование нагрева массивных заготовок с различными скоростями в печах периодического действия. *Известия вузов. Черная металлургия*. 2012; 55(9): 27–31. https://doi.org/10.17073/0368-0797-2012-9-27-31
10. Landfahrer M., Schluck C. Numerical and experimental investigation of scale formation on steel tubes in a real-size reheating furnace. *International Journal of Heat and Mass Transfer.* 2019; 129: 460–467. https://doi.org/10.1016/j.ijheatmasstransfer.2018.09.110
11. Kurnosov V.V., Levitskii I.A. Mathematic simulation of workpieces heating with variable thermal characteristics and thermal condition, corresponding to a given heating curve. *Izvestiya. Ferrous Metallurgy*. 2012; 55(7): 19–22. (In Russ.). https://doi.org/10.17073/0368-0797-2012-7-19-22

    Курносов В.В., Левицкий И.А. Математическое моделирование нагрева заготовок с переменными теплофизическими характеристиками и теплового режима, соответствующего заданному графику нагрева. *Известия вузов. Черная металлургия*. 2012; 55(7): 19–22. https://doi.org/10.17073/0368-0797-2012-7-19-22
12. Jang J.-Y., Huang J.-B. Optimization of a slab heating pattern for minimum energy consumption in a walking-beam type reheating furnace. *Applied Thermal Engineering*. 2015; 85: 313–321. https://doi.org/10.1016/J.APPLTHERMALENG.2015.04.029
13. Tang G., Wu B., Bai D., Wang Y., Bodnar R., Zhou C.Q. Modeling of the slab heating process in a walking beam reheating furnace for process optimization. *International Journal of Heat and Mass Transfer*. 2017; 113: 1142–1151. https://doi.org/10.1016/j.ijheatmasstransfer.2017.06.026
14. Ding J.G., Kong L.P., Guo J.H., Song M.X., Jiao Z.J. Multi-objective optimization of slab heating process in walking beam reheating furnace based on particle swarm optimization algorithm. *Steel Research International*. 2021; 92(3): 2000382. https://doi.org/10.1002/srin.202000382
15. Tang L., Liu J., Rong A., Yang Z. An effective heuristic algorithm to minimise stack shuffles in selecting steel slabs from the slab yard for heating and rolling. *Journal of the Operational Research Society*. 2001; 52(10): 1091–1097. https://doi.org/10.1057/palgrave.jors.2601143
16. Tang G., Wu B., Wang Y., Bodnar R., Zhou C. CFD modeling and validation of a dynamic slab heating process in an industrial walking beam reheating furnace. *Applied Thermal Engineering*. 2018; 132: 779–789. https://doi.org/10.1016/j.applthermaleng.2018.01.017
17. Mayr B., Prieler R., Demuth M., Moderer L., Hochenauer C. CFD analysis of a pusher type reheating furnace and the billet heating characteristic. *Applied Thermal Engineering*. 2017; 115: 986–994. https://doi.org/10.1016/j.applthermaleng.2017.01.028
18. Arutyunov V.A., Bukhmirov V.V., Krupennikov S.A. *Mathematical Modeling of Industrial Furnaces Thermal Operation*. Moscow: Metallurgiya; 1990: 239. (In Russ.).

    Арутюнов В.А., Бухмиров В.В., Крупенников С.А. *Математическое моделирование тепловой работы промышленных печей*. М.: Металлургия; 1990: 239.
19. Kudinov V.A., Kudinov I.V. *Methods for Solving Parabolic and Hyperbolic Equations of Heat Conduction*. Moscow: Librokom; 2012: 280. (In Russ.).

    Кудинов В.А., Кудинов И.В. *Методы решения параболических и гиперболических уравнений теплопроводности*. М.: Книжный дом «Либроком»; 2012: 280.
20. Mathews J.H. Computer derivations of numerical differentiation formulae. *International Journal of Mathematics Education in Science and Technology*. 2003; 34(2): 280–287. https://doi.org/10.1080/0020739031000158317

Information about the Authors

Ilkhomzhon B. Abdukodirov, *Deputy Head of the Section of Metal Preparation and Sorting,* Subsidiary Foundry and Mechanical Plant
E-mail: ilhomabdukadirov@mail.ru

Aleksandr V. Vargin, *Postgraduate of the Chair "Energy-Efficient and Resource-Saving Industrial Technologies",* National University of Science and Technology "MISIS"
ORCID: 0000-0001-8657-8716
E-mail: mr.vargin@yandex.ru

Igor' A. Levitskii, *Cand. Sci. (Eng.), Assist. Prof. of the Chair "Energy-Efficient and Resource-Saving Industrial Technologies",* National University of Science and Technology "MISIS"
ORCID: 0000-0002-9345-3628
E-mail: lewwwis@mail.ru

Сведения об авторах

Илхомжон Бахтиерович Абдукодиров, *заместитель начальника участка заготовки и сортировки металла,* Дочернее предприятие «Литейно-механический завод»
E-mail: ilhomabdukadirov@mail.ru

Александр Вячеславович Варгин, *аспирант кафедры энергоэффективных и ресурсосберегающих промышленных технологий,* Национальный исследовательский технологический университет «МИСИС»
ORCID: 0000-0001-8657-8716
E-mail: mr.vargin@yandex.ru

Игорь Анисимович Левицкий, *к.т.н., доцент кафедры энергоэффективных и ресурсосберегающих промышленных технологий,* Национальный исследовательский технологический университет «МИСИС»
ORCID: 0000-0002-9345-3628
E-mail: lewwwis@mail.ru

Contribution of the Authors

I. B. Abdukodirov – development of the mathematical model.
A. V. Vargin – clarification of the mathematical model, carrying out variant calculations.
I. A. Levitskii – scientific guidance, software implementation.

Вклад авторов

И. Б. Абдукодиров – разработка математической модели.
А. В. Варгин – уточнение математической модели, проведение вариантных расчетов.
И. А. Левицкий – общее руководство, программная реализация.

Received 15.07.2022
Revised 10.10.2022
Accepted 22.10.2022

Поступила в редакцию 15.07.2022
После доработки 10.10.2022
Принята к публикации 22.10.2022

УДК 004.942
DOI 10.17073/0368-0797-2023-1-119-126

Оригинальная статья
Original article

Mathematical modelling system for metallurgical enterprise: Operation and usability enhancement

A. S. Leont'ev, I. A. Rybenko

Siberian State Industrial University (42 Kirova Str., Novokuznetsk, Kemerovo Region – Kuzbass 654007, Russian Federation)

rybenkoi@mail.ru

Abstract. Metallurgical plants (smelters) adjust their production plans to match changing global demand. EVRAZ West Siberian Metallurgical Combine JSC (EVRAZ ZSMK) employs furnace charges and pellets containing 110 components, with a product range exceeding 2000 items that vary from month to month. The production plan is optimized individually for each manufacturing process, with the goal of minimizing costs and maximizing output. This paper discusses the development and deployment of the smelter simulation system currently in use at EVRAZ ZSMK. Unlike other solutions, this system performs concurrent, end-to-end optimization of all smelter processes, with the ultimate goal of maximizing the company's profit. During the system's operation from 2019 to 2020, users encountered tedious and time-consuming tasks, such as creating 60 production plans per year, conducting 10,000 test iterations, and analyzing 30 scenarios. To gather statistical data, a feedback form was used, which identified several issues. Firstly, the mathematical model fails with incorrect input data. Secondly, repeated analyses are required to identify and interpret the plan/actual cost discrepancies. Thirdly, data validation errors, such as incorrect chemical composition or model settings unsuitable for the specific timeframe, were observed. To address these shortcomings, several measures were developed: an input data validator (before and after analysis) was introduced; sensitivity and factor analysis modules were developed to aid in identifying and interpreting cost discrepancies; a chemical composition uploading tool was developed to ensure data validation. Finally, the system was retrained on historical datasets to improve its accuracy.

Keywords: simulation, optimization, mathematical model, production planning

For citation: Leont'ev A.S., Rybenko I.A. Mathematical modelling system for metallurgical enterprise: Operation and usability enhancement. *Izvestiya. Ferrous Metallurgy*. 2023; 66(1): 119–126. https://doi.org/10.17073/0368-0797-2023-1-119-126

Опыт использования и повышения юзабилити системы математического моделирования производства на металлургическом предприятии

А. С. Леонтьев, И. А. Рыбенко

Сибирский государственный индустриальный университет (Россия, 654007, Кемеровская обл. – Кузбасс, Новокузнецк, ул. Кирова, 42)

rybenkoi@mail.ru

Аннотация. В связи с развитием мировой торговли у металлургических комбинатов появилась большая вариативность при составлении производственного плана. На АО «ЕВРАЗ Западно-Сибирский металлургический комбинат» (АО «ЕВРАЗ ЗСМК») шихту оптимизируют из 110 компонентов только в части агломерационного и доменного производств. Номенклатура выпускаемой продукции состоит более чем из 2000 единиц и меняется от месяца к месяцу. Обычно производственный план оптимизируют только внутри отдельных переделов. Целью оптимизации является минимизация себестоимости передела и максимизация производства. В работе представлены разработка и внедрение системы математического моделирования производства всего металлургического комбината на примере АО «ЕВРАЗ ЗСМК». В отличие от существующих систем моделирования переделов целью системы является единовременная сквозная оптимизация всех переделов комбината. Конечная цель – максимизация прибыли всего комбината. В процессе эксплуатации новой системы в 2019 – 2020 гг. были обнаружены высокие трудозатраты при работе пользователей. Например, совершается более 10 000 тестовых итераций расчетов для выпуска 60 планов за год и расчета 30 экономических кейсов. Разработана и проанализирована форма статистики, которая показала следующие основные проблемы: неразрешимость модели из-за ввода математически некорректных данных; повторные расчеты экономических кейсов для

выделения и интерпретации отдельных изменившихся факторов плана от бюджета; ошибки на этапе верификации данных из-за некорректного химического состава элементов или неверных настроек модели под конкретный период работы. Для устранения недостатков системы разработаны системы валидации вводимых данных на этапе до и после расчетов, модули анализа чувствительности и факторный расчет, система автоматического заполнения химического состава, а также добавлена возможность переобучения модели на исторических данных.

Ключевые слова: математическое моделирование, оптимизация, математическая модель, планирование производства

Для цитирования: Леонтьев А.С., Рыбенко И.А. Опыт использования и повышения юзабилити системы математического моделирования производства на металлургическом предприятии. *Известия вузов. Черная металлургия*. 2023; 66(1): 120–126. https://doi.org/10.17073/0368-0797-2023-1-119-126

Introduction

Nowadays, steelmakers mostly use the sintering and blast furnace process [1]. Usually, iron is reduced from ore in blast furnaces as pig iron and then the impurities are oxidized in steelmaking converters or electric furnaces with subsequent ladle refining [2].

The metallurgical industry consumes a lot of resources and energy. Smelters introduce both investment-based and zero-cost initiatives to reduce costs through optimal production planning. Planning is essentially an optimal allocation of expensive (purchased) or insufficient (in-house) resources to maximize profit. It is a pressing problem for smelters buying raw materials from third-party suppliers. The key challenge is that the charge for each furnace may consist of hundreds of components in various combinations. For example, EVRAZ ZSMK makes the charge for cast iron production from more than 110 components [3]. Planning cannot be done manually because it is so complicated and includes the following concurrent processes:

– optimizing the charge composition for cost;

– optimizing the recycling content [4];

– analyzing the production processes [5].

Process simulation models became commercially available worldwide in 2010. Such models should be highly flexible [6] which is exactly what the Russian smelter needs in the current situation.

This paper covers the deployment of a production planning system at EVRAZ ZSMK, and new tools improving the system's efficiency.

Currently, the sintering and blast furnace process is the predominant method used by steelmakers [1]. This process involves reducing iron from ore in blast furnaces to produce pig iron, which is then further processed in steelmaking converters or electric furnaces, followed by ladle refining to remove impurities [2]. However, the metallurgical industry is known for its high consumption of resources and energy. In order to reduce costs and achieve optimal production planning, smelters are introducing investment-based and zero-cost initiatives. Production planning involves the optimal allocation of expensive (purchased) or insufficient (in-house) resources to maximize profit. This is particularly challenging for smelters that purchase raw materials from third-party suppliers, as the charge for each furnace may consist of hundreds of components in various combinations.

For example, EVRAZ ZSMK uses more than 110 components in the charge for cast iron production [3]. Manual planning is not feasible due to the complexity of concurrent processes, which include optimizing the charge composition for cost, optimizing the recycling content [4], and analyzing production processes [5]. Since 2010, commercially available process simulation models have been used worldwide to address this challenge. To be effective, these models should be highly flexible, which is precisely what is needed by the Russian smelter in the current situation [6]. This paper discusses the implementation of a production planning system at EVRAZ ZSMK, as well as new tools that improve the system's efficiency.

Mathematical Model Summary

In 2019, EVRAZ ZSMK successfully deployed a mathematical model that covers every production stage from ore mining to steel rolling. The system offers easy integration with third-party analysis modules. Fig. 1 shows the main window of the Forecast process simulation system (PSS). Initially, the system was developed to optimize the production plan in financial terms at each site and at the corporate level.

However, the optimization results were challenging to interpret. For example, in cases where the system suggests 100 % of composition *1* pellets instead of composition *2* and *3* pellets, it is not clear why such a switch would lead to cost savings or if it would even be advantageous. Therefore a new option was added to the system to enable users to select either planning or scenario analysis mode. In the planning mode, the system suggests an optimal production plan that meets constraints, while in the scenario mode, the system estimates costs for various possible scenarios. This enhanced the system's efficiency but increased user effort.

A detailed analysis of system usage statistics was conducted to identify bottlenecks, which revealed that only 30 out of 3000 scenarios analyzed in 2020 were implemented. Moreover, the new scenario mode considerably increased user efforts and the number of simulation runs. The total number of analysis cases run was more than 11,545, indicating that each scenario had to undergo

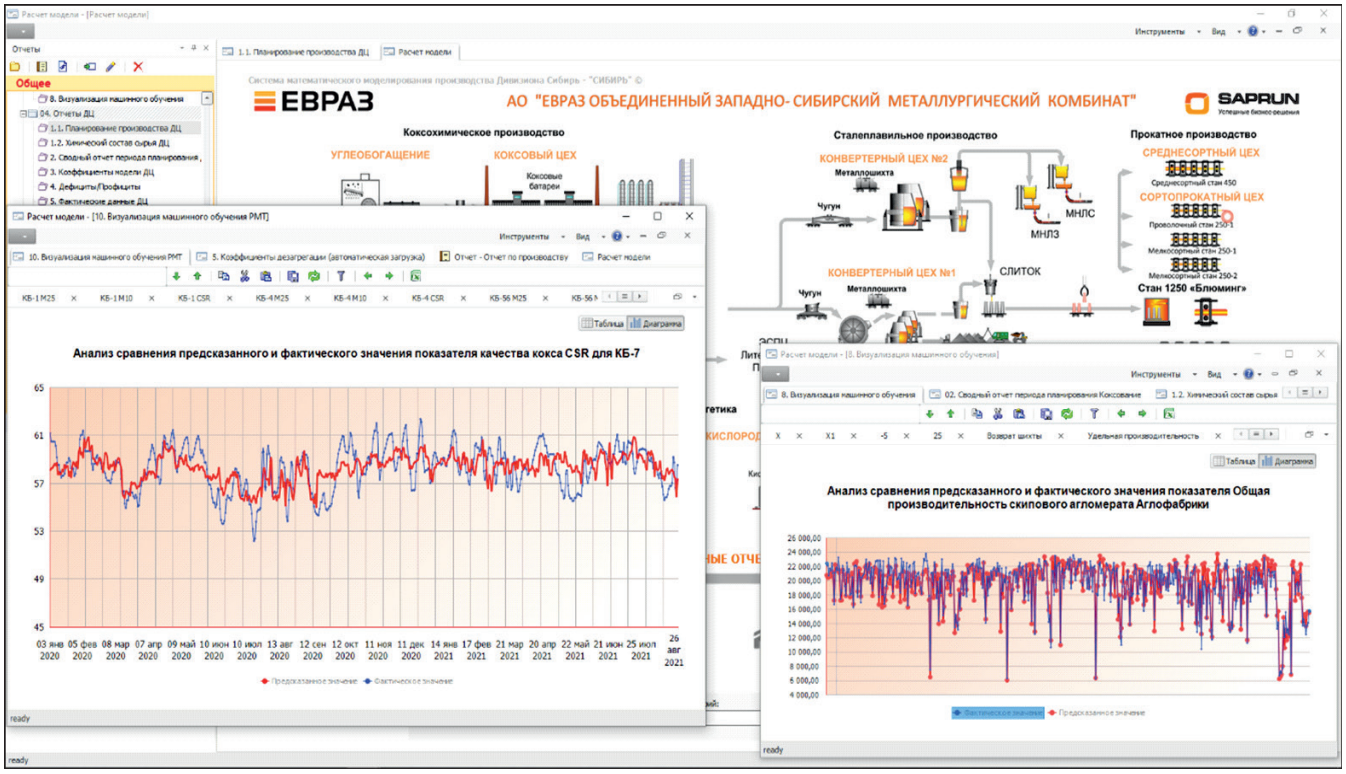

Fig. 1. Main window of the "Forecast" process simulation system

Рис. 1. Рабочее окно СММ «Прогноз»

3 – 4 runs to ensure error-free results. The study results are illustrated in Fig. 2.

After analyzing the results, we developed special productivity-boosting tools for the system users. In addition, we added a simulation experiment capability to the system. With the rise of resource-saving technologies, computational experiments have become necessary to analyze processes and system behavior. As such, the company required a simulation tool for such experiments.

A computational experiment typically involves several steps. First, the input data is entered and validated. Following this, physical experiments are conducted to fine-tune the mathematical model [7].

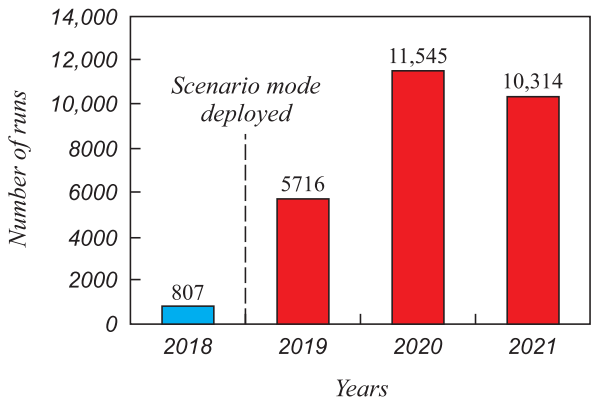

Fig. 2. System use statistics

Рис. 2. Анализ статистики работы системы

Input Data Validation

"Data Validation" tool

The input data is validated before running the solver to identify any incorrect values. For user convenience, the validation tool is programmed to start automatically before each simulation run, providing brief explanations and displaying the input data status.

Consider the report from the Abagursk Concentration Facility (Fig. 3). The report is checked against the following rules applied to concentration facility reports:

– the minimum reconcentrate intake should be less than or equal to the maximum intake;

– if the maximum intake value is non-zero, the ore preparability tables should report non-zero values;

– if the maximum intake value is non-zero, the preconcentrate price should be non-zero.

"Checklist" tool

The "Checklist" tool is launched after successfully simulating a model. It displays the solution to the optimization problem and checks it for compliance with pro-

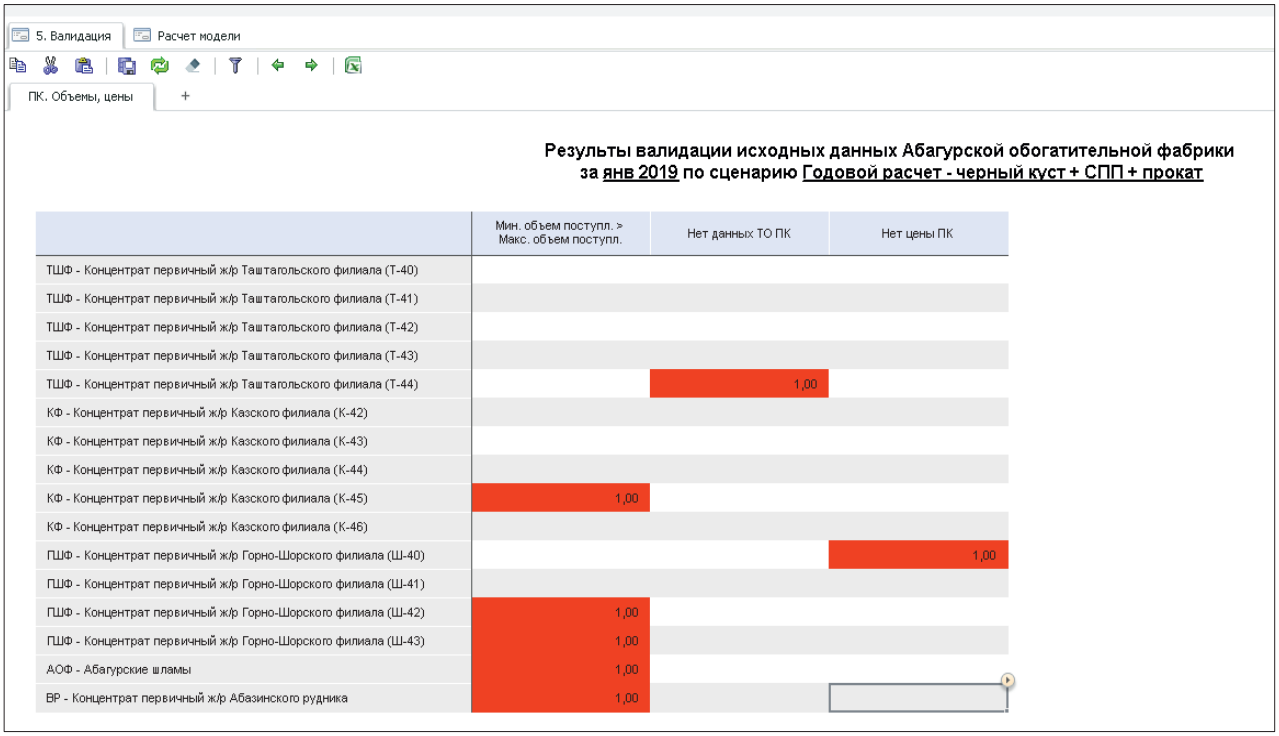

Fig. 3. Report on validation results for Abagur concentrating plant

Рис. 3. Отчет по результатам валидации для АОФ

cess constraints. The solution is then checked against the checklist as a post-processing stage. If a rule is not satisfied and the solution fails to meet process requirements, it is highlighted in red. Some of the rules checked by the tool are:

– whether the raw o re stock is underutilized. This rule checks for unused ore resources since in-house ore stock should be used first;

– the sinter cake output is less than the production capacity. This rule checks if the sinter production plan underutilizes the available equipment capacity;

– whether the pig iron output is less than the production capacity. This rule checks if the pig iron production plan underutilizes the available equipment capacity.

"Chemical Composition Uploading" Tool

Entering the raw chemical composition into the system was a time-consuming process. The mathematical model requires an extended chemical composition for each charge component (e.g., TiO_2, ZnO, etc.). However, extended analysis incurs higher costs and is often outsourced. Therefore, the in-house lab can only provide incomplete analysis and updates the record once a quarter or upon request.

The chemical composition data is sourced from both lab test reports and raw material data sheets. Lab reports are given priority, and if they are unavailable, data sheets are used instead. Consequently, the chemical compositions for all materials over the planning period (scenario) are uploaded into the system. If a chemical composition is updated, the new data overwrites the old values.

These tools have significantly reduced potential data entry errors as more than 10,000 values are entered every month.

Result Analysis Tools

"Price Sensitivity Analysis" Tool

Price sensitivity analysis aims to identify the relationship between raw material prices and purchase volume. To conduct this analysis, the user specifies the material of interest, along with lower and upper price limits. The user also specifies the number of increments in the price sensitivity analysis window.

Once the price sensitivity analysis is completed, the results are presented in the form of a table and diagram, as shown in Fig. 4. The user can export the results to Excel by clicking on the "Export to Excel" button.

"Pipeline Processing" Tool

The batch scenario simulation tool allows for multiple simulations to be run with varying input data within speci-

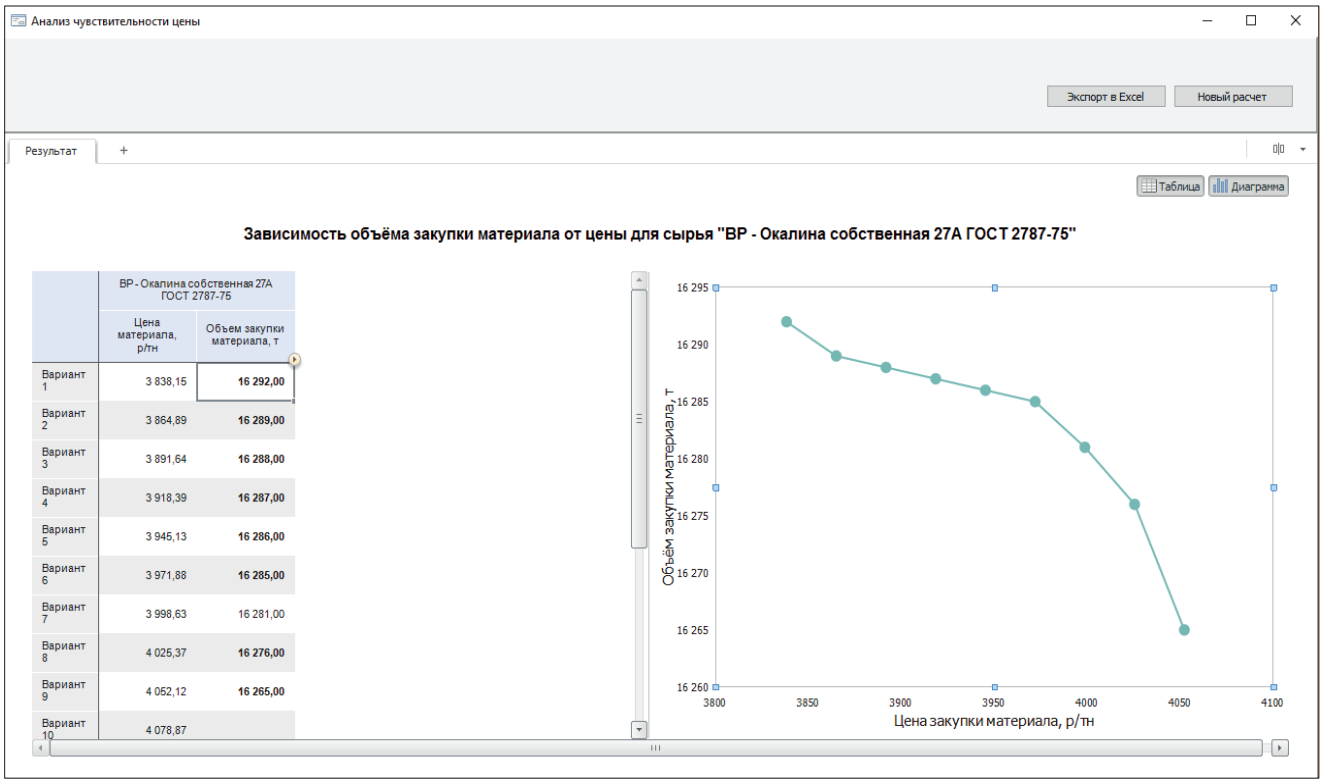

Fig. 4. Results of price sensitivity analysis

Рис. 4. Окно с результатами расчета анализа чувствительности

fied ranges and increments. The tool window is displayed in Fig. 5.

The results of the simulations are presented in the form of a standard Production Report and can be exported to Excel by clicking on the "Export to Excel" button and specifying the path and file name. The user also has the option to save the configuration for later use.

"Model Factor Calculation" Tool

This tool is designed to recalculate the factors utilized in several plant models, including the sinter plant, byproduct coke-making plant, melt shop, and LD plant models. These factors are estimated based on historical data. In this discussion, we will specifically focus on the factor estimation process for the sinter plant model.

The blast furnace process is responsible for the production of pig iron from sinter, pellets, and briquettes. In order to ensure high-performance blast furnace operation, fine ore and concentrate are converted into larger fragments, which provide better gas permeability [8].

This is typically accomplished through one of three processes: briquetting, agglomeration sintering, or pelletizing. Agglomeration sintering is the most commonly used process due to its significant advantages over the other options. For instance, agglomeration sintering makes it possible to utilize by-products and in-house waste, such as sludge and furnace dust, resulting in water savings and reduced air pollution [9].

One challenge of sinter plants is the inconsistent composition of the ore concentrate, furnace fuel, and flux, as well as varying base-to-silica ratios. Estimating sinter machine capacity based solely on ore concentrate and factor recalculation is insufficient to achieve the required simulation accuracy. Instead, only machine learning on historical datasets can effectively estimate every factor that affects the sinter machine's capacity and sinter cake quality. Market price analysis over the last five years has shown that the price of sinter cake made from purchased ore concentrate is lower than that of purchased pellets. To increase sinter cake output, several options exist, including:

– increasing plant capacity;

– intensifying the sintering process;

– increasing yield through better sinter quality or reducing fines;

– and using substandard sinter in the blast furnace as a compromise [10, 11].

Charge optimization [12 – 15] is the key factor for the sinter quality and sinter machine capacity [16 – 19]. It is a zero-cost profit booster [12].

A regression model for the sinter plant output is as follows:

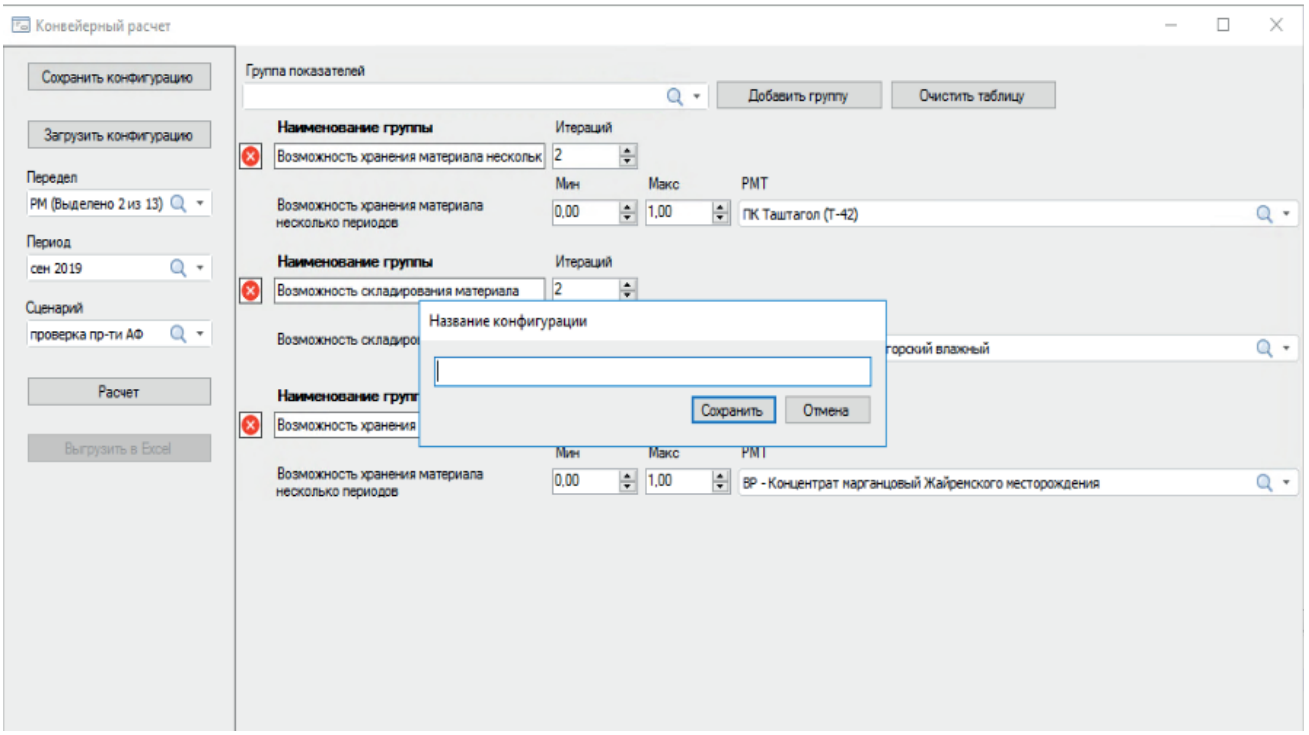

Fig. 5. Pipeline processing tool

Рис. 5. Инструмент «Конвейерный расчет»

$$y = b_0 + b_1 x_1 + b_2 x_2 + ... + b_n x_n,$$

where y is the expected sinter output, tons; b_0 is the intercept term; b_1, b_2, ... b_n are the regression coefficients; x_1, x_2, ... x_n are the factors affecting the sinter output.

To estimate sinter quality, the *Random Forest* method was utilized due to its higher prediction accuracy when compared to regression. The *Random Forest* method is an ensemble learning method that was proposed by Leo Breiman and Adele Cutler. It utilizes multiple decision trees to generate predictions. The algorithm combines two key concepts: Breiman's bagging and the random subspace method by Tin Kam Ho. This method can be applied to classification, regression, and clustering problems. The core idea behind this method is to use a large ensemble of decision trees, where each individual tree may produce a poor classification quality but the collective output of many trees produces more accurate and reliable results[1].

Conclusions

In modern times, user experience has become the most critical aspect of simulation and optimization tools. Even the most accurate and flexible solution can be rejected by users due to its confusing user interface. To overcome this issue, we applied system analysis and software adoption rate assessment to identify and rectify any bottlenecks in the software's usability.

[1] Random Forest. Wikipedia. URL: https://en.wikipedia.org/wiki/Random_forest (Last accessed: 16.11.2021).

References / Список литературы

1. Lisienko V.G., Solov'eva N.V., Trofimova O.G. *Alternative Metallurgy: Problem of Alloying, Model Efficiency Estimates*. Moscow: Izd. Teplotekhnik; 2007: 440. (In Russ.).

Лисиенко В.Г., Соловьева Н.В., Трофимова О.Г. *Альтернативная металлургия: проблема легирования, модельные оценки эффективности*. Москва: изд. Теплотехник; 2007: 440.

2. Protopopov E.V., Kalinogorskii A.N., Ganzer A.A. Steelmaking production: Current state and directions of development. In: *Metallurgy: Technologies, Innovations, Quality. Proceedings of the XX Int. Sci. and Pract. Conf. Part 1*. Novokuznetsk: ITs SibSIU; 2019: 9–14. (In Russ.).

Протопопов Е.В., Калиногорский А.Н., Ганзер А.А. Сталеплавильное производство: современное состояние и направления развития. В кн.: *Металлургия: технологии, инновации, качество. Труды XX междунар. науч.-практ. конф. Ч. 1*. Новокузнецк: ИЦ СибГИУ; 2019: 9–14.

3. Leont'ev A.S., Rybenko I.A., Borisov A.S., Volkova I.V. Experience in development and application of a mathematical modeling system at JSC "EVRAZ ZSMK". In: *Modeling and High-Tech Information Technologies in Technical and Socio-Economic Systems. Proceedings of the V All-Russ. Sci. and Pract. Conf. with Int. Participation*. Novokuznetsk: ITs SibSIU; 2021: 250–255. (In Russ.).

Леонтьев А.С., Рыбенко И.А., Борисов А.С., Волкова И.В. Опыт разработки и применения системы математичес-

кого моделирования на «ЕВРАЗ ЗСМК». В кн.: *Моделирование и наукоемкие информационные технологии в технических и социально-экономических системах. Труды V всерос. науч.-практ. конф. с международным участием*. Новокузнецк: ИЦ СибГИУ; 2021: 250–255.

4. Golodova M.A., Dmitrienko V.I., Rozhikhina I.D., Nokhrina O.I., Rybenko I.A. Study of process conditions for vanadium and iron reduction from vanadium converter slag. *Izvestiya. Ferrous Metallurgy*. 2011; 54(4): 3–5. (In Russ.).

   Голодова М.А., Дмитриенко В.И., Рожихина И.Д., Нохрина О.И., Рыбенко И.А. Исследование условий процесса восстановления ванадия и железа из конвертерного ванадиевого шлака. *Известия вузов. Черная металлургия*. 2011; 54(4): 3–5.

5. Rybenko I.A., Mochalov S.P. *Modeling and Optimization of Stationary Modes of Metallurgical Processes*. Novokuznetsk: ITs SibSIU; 2015: 168. (In Russ.).

   Рыбенко И.А., Мочалов С.П. *Моделирование и оптимизация стационарных режимов металлургических процессов*. Новокузнецк: ИЦ СибГИУ; 2015: 168.

6. Cech M., Lenort R., Tolstykh T., Shkarupeta E. Modeling metallurgical supply chain resilience using Markov process. In: *Proceedings of 28th Int. Conf. on Metallurgy and Materials*. 2019: 1798–1803. https://doi.org/10.37904/metal.2019.782

7. Rybenko I.A. Solving problems of optimization of metallurgical processes using the instrumental system "Engineering-Metallurgy". *Ferrous Metallurgy. Bulletin of Scientific, Technical and Economic Information*. 2018; 1(3): 42–47. (In Russ.).

   Рыбенко И.А. Решение задач оптимизации металлургических процессов с использованием инструментальной системы «Инжиниринг-Металлургия». *Черная металлургия. Бюллетень научно-технической и экономической информации*. 2018; 1(3): 42–47.

8. Spirin N.A., Ovchinnikov Yu.N., Shvydkii V.S., Yaroshenko Yu.G. *Heat Exchange and Efficiency Improvement of Blast Furnace Smelting*. Yekaterinburg: USTU; 1995: 243. (In Russ.).

   Теплообмен и повышение эффективности доменной плавки / Н.А. Спирин, Ю.Н. Овчинников, В.С. Швыдкий, Ю.Г. Ярошенко. Екатеринбург: УГТУ; 1995: 243.

9. Frolov Yu.A. *Agglomeration. Technology, Heat Engineering*. Moscow: Metallurgiya; 2006: 600. (In Russ.).

   Фролов Ю.А. *Агломерация. Технология, теплотехника*. Москва: Металлургия; 2006: 600.

10. Bizhanov A., Chizhikova V. *Agglomeration in Metallurgy*. Springer; 2020: 453. https://doi.org/10.1007/978-3-030-26025-5

11. Majumder A., Biswas C., Saugata Dhar, Rajib Dey, Das G.C. Use of artificial neural network to predict the yield of sinter plant as a function of production parameters. In: *International Conference on Innovative Computing and Cutting-edge Technologies*. 2020: 13–26. https://doi.org/10.1007/978-3-030-65407-8_2

12. Kumar V., Sairam S.D.S.S., Kumar S., Singh A., Nayak D., Sah R., Mahapatra P.C. Prediction of iron ore sinter properties using statistical technique. *Transactions of the Indian Institute of Metals*. 2017; 70: 1661–1670. https://doi.org/10.1007/s12666-016-0964-y

13. Mochón J., Ruiz-Bustinza I., Cores A., Verdeja L., etc. Iron ore sintering. Part 2. Quality indices and productivity. In: *Network of Non-Commercial Academy-Owned Open Access Scientific Journals*. 2014: 168–177. http://doi.org/10.15446/dyna.v81n183.41568

14. Shao H., Yi Z., Chen Z., Zhou Z., Deng Z. Application of artificial neural networks for prediction of sinter quality based on process parameters control. *Transactions of the Institute of Measurement and Control*. 2019; 42(3): 422–429. http://doi.org/10.1177/0142331219883501

15. Mallick A., Dhara S., Rath S. Application of machine learning algorithms for prediction of sinter machine productivity. *Machine Learning with Applications*. 2021; 6: 100186. http://doi.org/10.1016/j.mlwa.2021.100186

16. Song L., Qing L., Xiaojie L., Yanqin S. Synthetically predicting the quality index of sinter using machine learning model. *Ironmaking & Steelmaking*. 2020; 47(7): 828–836. http://doi.org/10.1080/03019233.2019.1617573

17. Mitterlehner J., Loeffler G., Winter F., Hofbauer H., Schmid H., Zwittag E., Buergler T.H., Pammer O., Stiasny H. Modeling and simulation of heat front propagation in the iron ore sintering process. *ISIJ International*. 2004; 44(1): 11–20. http://doi.org/10.2355/isijinternational.44.11

18. Yang W., Rui C., Choi S., Choi E., Lee D., Huh W. Modeling of combustion and heat transfer in an iron ore sintering bed with considerations of multiple solid phases. *ISIJ International*. 2004; 44(3): 492–499. http://doi.org/10.2355/isijinternational.44.492

19. Calhoun P., Su X., Spoon K.M., Levine R.A., Fan J. Random forest. *Wiley StatsRef: Statistics Reference Online*. 2021: 1–20. http://doi.org/10.1002/9781118445112.stat08287

Information about the Authors / Сведения об авторах

Aleksei S. Leont'ev, *Postgraduate of the Chair of Applied Information Technologies and Programming,* Siberian State Industrial University
E-mail: aleksey.leontiev@evraz.com

Inna A. Rybenko, *Dr. Sci. (Eng.), Prof., Head of the Chair of Applied Information Technologies and Programming,* Siberian State Industrial University
ORCID: 0000-0003-1679-0839
E-mail: rybenkoi@mail.ru

Алексей Сергеевич Леонтьев, *аспирант кафедры прикладных информационных технологий и программирования,* Сибирский государственный индустриальный университет
E-mail: aleksey.leontiev@evraz.com

Инна Анатольевна Рыбенко, *д.т.н., профессор, заведующий кафедрой прикладных информационных технологий и программирования,* Сибирский государственный индустриальный университет
ORCID: 0000-0003-1679-0839
E-mail: rybenkoi@mail.ru

Contribution of the Authors

A. S. Leont'ev – theoretical analysis, calculations, analysis of the research results, drawing conclusions, literary review, writing the text.
I. A. Rybenko – scientific guidance, analysis of the research results, revision of the text, correction of conclusions.

Вклад авторов

А. С. Леонтьев – теоретический анализ, проведение расчетов, анализ результатов исследований, формирование выводов, обзор литературы, подготовка текста.
И. А. Рыбенко – научное руководство, анализ результатов исследований, доработка текста, корректировка выводов.

Received 04.04.2022
Revised 25.04.2022
Accepted 18.12.2022

Поступила в редакцию 04.04.2022
После доработки 25.04.2022
Принята к публикации 18.12.2022

In the order of discussion / **В порядке дискуссии**

UDC 622.7
DOI 10.17073/0368-0797-2023-1-127-132

Оригинальная статья
Original article

Composition of tailings after selective reduction of laterite

F. Bahfie [1, 2], A. Manaf [2], W. Astuti [1], F. Nurjaman [1], S. Suharto [1], U. Herlina [1], W. A. Adi [3], M. Manawan [4]

[1] **Research Center of Mining Technology, National Research and Innovation Agency of Indonesia** (Jalan Ir. Sutami Km. 15, South Lampung, Lampung 35361, Indonesia)
[2] **University of Indonesia** (Pondok Cina, Beji, Depok City, West Java 16424, Indonesia)
[3] **Center for Advanced Materials Science and Technology, National Research and Innovation Agency of Indonesia** (Indonesia, 15310, South Tangerang, West Java, PUSPIPTEK Serpong Area, Bld 43)
[4] **Indonesia Defense University** (Kawasan IPSC Sentul, Bogor, West Java 16810, Indonesia)

fath007@brin.go.id/azwar@ui.ac.id

Abstract. The selective reduction process generates products in the form of concentrates and tailing/by-products. There is high percentage of iron and other elements in the tailings that are not extracted in selective reduction process. Properties of by-products of selective reduction were investigated using X-ray diffraction (XRD), inductively coupled plasma optical emission spectroscopy (ICP–OES), ultraviolet-visible (UV–VIS), and scanning electron microscopy energy dispersion spectroscopy (SEM–EDS). Based on the results of this study, the properties of iron-sulfur, iron-magnesium-aluminium, and silica phases in the tailings can be interpreted experimentally. For future research, it can be the reference for such processes as acid and base leaching. Pure iron extracted from tailings can be used for metal fuel in the future. The tailings composition data will help future researchers to find optimal processes for the tailings.

Keywords: composition, tailings, phase, microstructure

Acknowledgements: The work was supported by the Ministry of Education, Culture, Research, and Technology-Directorate of Higher Education, Research, and Technology under research project PDD 2022 and contract No. NKB-968/UN2.RST/HKP.05.00/2022.
The authors express their gratitude to the Materials Science University of Indonesia and the Research Center of Mining Technology – National Research and Innovation Agency of Indonesia for support and research facilities.

For citation: Bahfie F., Manaf A., Astuti W., Nurjaman F., Suharto S., Herlina U., Adi W.A., Manawan M. Composition of tailings after selective reduction of laterite. *Izvestiya. Ferrous Metallurgy*. 2023; 66(1): 127–132. https://doi.org/10.17073/0368-0797-2023-1-127-132

Состав хвостов при избирательном восстановлении латерита

Ф. Бахфи [1, 2], А. Манаф [2], В. Астути [1], Ф. Нурьаман [1], С. Сухарто [1], У. Херлина [1], В. А. Ади [3], М. Манаван [4]

[1] **Научно-исследовательский центр горных технологий, Национальное агентство исследований и инноваций Индонезии** (Индонезия, 35361, Лампунг, Южный Лампунг)
[2] **Университет Индонезии** (Индонезия, 16424, Западная Ява, Депок, Беджи)
[3] **Центр материаловедения и передовых технологий, Национальное агентство исследований и инноваций Индонезии** (Индонезия, 15310, Западная Ява, Южный Тангеранг)
[4] **Военный университет Индонезии** (Индонезия, 16810, Западная Ява, Богор, Кавасан ИПЦС Сентул)

fath007@brin.go.id/azwar@ui.ac.id

Аннотация. В результате избирательного восстановления образуются концентраты и пустая порода (хвосты). В хвостах содержится высокий процент железа и других элементов, которые не извлекаются в процессе селективного восстановления. Свойства хвостов после избирательного восстановления исследовались методами рентгеноструктурного анализа, оптико-эмиссионной спектрометрии с индуктивно связанной плазмой, оптической, УФ- и сканирующей электронной микроскопии, а также энергодисперсионного микроанализа на растровом

электронном микроскопе. Экспериментально установлено, что хвосты содержат сульфиды железа, соединения железа с алюминием и магнием, а также диоксид кремния. На основании полученных данных в дальнейшем возможна разработка технологий кислотного и щелочного экстрагирования минералов с целью получения чистого оксида железа, применяемого в качестве металлического топлива.

Ключевые слова: состав, хвосты, фаза, микроструктура

Благодарности: Работа выполнена при поддержке Министерства образования, культуры, исследований и технологий – Дирекции высшего образования, исследований и технологий в рамках исследовательского проекта PDD 2022 и договора № NKB-968/UN2.RST/HKP.05.00/2022. Авторы выражают благодарность Университету материаловедения Индонезии и Исследовательскому центру горных технологий – Национальному агентству исследований и инноваций Индонезии за поддержку и исследовательские возможности.

Для цитирования: Бахфи Ф., Манаф А., Астути В., Нурджаман Ф., Сухарто С., Херлина У., Ади В.А., Манаван М. Состав хвостов при избирательном восстановлении латерита. *Известия вузов. Черная металлургия*. 2023; 66(1): 108–132.
https://doi.org/10.17073/0368-0797-2023-1-127-132

Introduction

Extraction of nickel from the widely occurring laterite ores has become an important task of research [1 – 9]. Previous studies have shown that direct reduction roasting process followed by magnetic separation is an effective method for recovering nickel from laterite nickel ores [10 – 17]. To obtain nickel alloy powder with high nickel content, iron reduction needs to be controlled in the direct reduction roasting process. Selective reduction can be achieved by adjusting the reducing atmosphere [18 – 19] and the number of additives [20 – 22]. Li et al. [10] found that FeS is produced by direct reduction with the Na_2SO_4 additive. The formation of the Fe/FeS eutectic promotes the growth of Ni/Fe particles; simultaneously, in the magnetic separation process the nonmagnetic FeS will go to the tailings thus achieving the purpose of selective reduction. Also, the formation of FeS promotes the growth of metal particles. Jiang et al. [25] found that Na_2SO_4 reacts with silicates producing low melting point nepheline and suppressing FeO reduction by inhibiting the diffusion of the reducing gas; it can also promote the growth of nickel-iron particles through the formation of FeS. In the FeO reduction process, the diffusion of the reducing gas was impeded due to the increase in the amount of liquid phase in the roasting system. All of the above studies found that FeS plays an important role in the selective reduction of laterite nickel ore. In direct selective reduction of laterite nickel ore, FeS also serves as a paramagnetic film covering the FeO surfaces. That thin layer blocks the contact between the reducing gas and FeO suppressing the reduction process. Iron-rich, it can be used as a nanoparticle's precursor in food technology, biomedicine, energy and fuel production, etc. [26, 27]. The best possible application of the iron nanoparticles precursor is for metal fuel which is illustrated in Fig. 1 [27]. Iron-rich by-product shall be seen as a primary source for the extraction processes to be used in the future.

Material and Methods

Data on tailings/by-products is taken from selective reduction process at the Research Unit for Mineral Technology, National Research and Innovation Agency of Indonesia, South Lampung, Lampung, Indonesia. First, the by-product was brought through a 200-mesh shaker sieve. After that the sample was dissolved in aqua regia for 5 days, diluted 50 and 1000 times, and analysed first by the ICP-OES Analytika Jena PQ9000 (with the resulting data converted in excel from ppm to weigh percent); and then by the XRD PANalytical X'Pert3 Powder (in the 200 mesh sample size, the 2θ is in the range of 10 – 80°, step size 0.05, and analysis data by High Score Plus) (Fig. 3). For SEM–EDS Thermo-scientific Quatro 6 with magnification 5000× was used and Bruker for EDS.

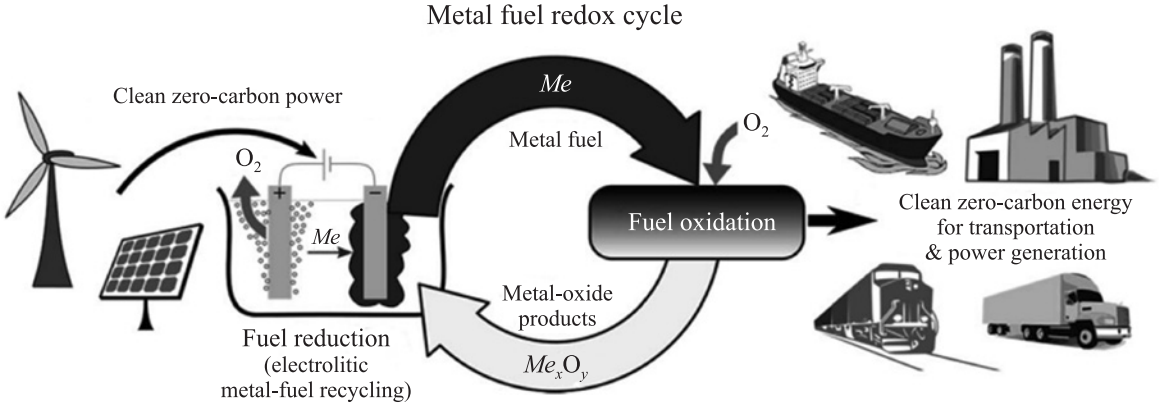

Fig. 1. Metal fuel in the future [27]

Рис. 1. Примеры применения металлического горючего в будущем [22]

Results

ICP and UV–VIS Study

Table 1 gives tailing specific chemical composition: 0.74 wt% Ni, 39.45 wt% Fe, 5.1 wt% Mg. Fig. 2 gives Fe, Ni, Mg, Mn, Al, and Co ratios in the tailings according to their absorbance and wave lengths [28]; therefore, the same elements are detected by UV–VIS and ICP. The agreement of the ICP and UV–VIS result shows that the aggregate amounts of components in both tests are the same; for example, iron is the greatest ingredient while cobalt, nickel, and manganese are the least ones.

XRD Study

In the sulfide phase, iron occurs in a higher percentage than in magnesioferrite, forsterite, and quartz phases, where there is less iron which occurs together with constituent elements magnesium or aluminium. The Rietveld refinement calculation results agree with the XRD results in Table 2. Significantly, it is the first time that the tailing product is addressed as raw material.

SEM–EDS Study

This study gives the same results for the elements and phases of the tailings which can be further identified in microstructure. The morphology of tailings, as shown in Fig. 4, convincingly proves that the major elements in the tailing are iron-sulfur, iron-magnesium-silica-oxide, natrium, and quartz extracted in selective reduction with sulfur appearing in XRD. From Table 3, the magnesium-iron-aluminium is appearing in spots *2* and *4* indicating the magnesioferrite and forsterite phases.

Table 1

Chemical composition of tailing

Таблица 1. **Химический состав хвостов**

Element	Fe	Ni	Mg	Mn	Al	Co
Amount, wt%	39.45	0.74	5.1	0.55	2.63	0.074

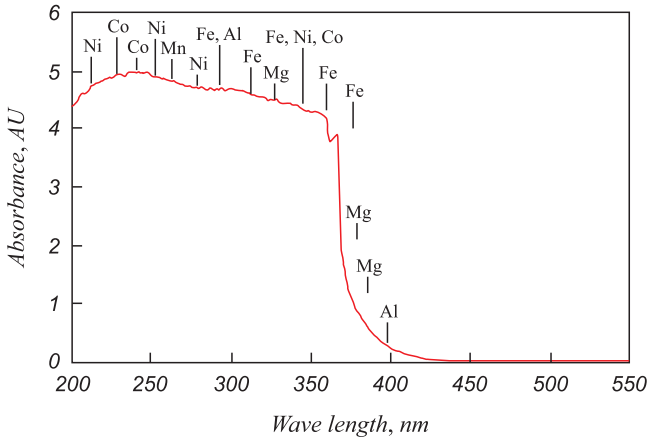

Fig. 2. UV–VIS analysis of tailing

Рис. 2 Результаты УФ- и оптической микроскопии хвостов

Table 2

Rietveld refinement calculations of tailing

Таблица 2. **Фазовый состав хвостов по Ритвельду**

Compound	Total, %
Pyrite	32.5
Wuestite	24.3
Magnesioferrite	21.5
Forsterite	16.3
Quartz	5.4

Table 3

Chemical composition of tailing in EDS

Таблица 3. **Химический состав хвостов, полученный с помощью энергодисперсионного микроанализа**

Sampling spots	Element (%wt)					
	Fe	Ni	Mg	Al	Mn	Co
1	57.48	–	1.37	–	0.63	–
2	47.77	–	3.77	1.70	0.97	–
3	37.64	–	1.99	5.13	1.03	–
4	20.45	–	6.47	14.50	1.01	–
5	0.98	–	–	–	–	–

Conclusions

Based on the results, the tailing includes such phases as iron-sulfur, iron-magnesium-aluminium, and silica which can be interpreted so that the tailing is iron-rich and not

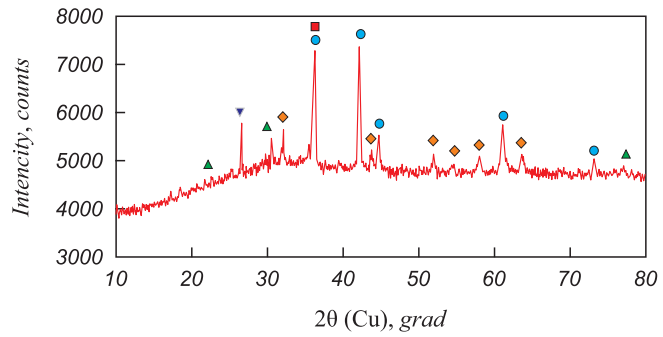

Fig. 3. XRD analysis of tailing:
● – pyrite, ■ – wuestite, ◆ – magnesioferrite, ▲ – forsterite, ▼ – quartz

Рис. 3. Результаты рентгеноструктурного анализа хвостов:
● – пирит; ■ – вюстит; ◆ – магнезиоферрит; ▲ – форстерит; ▼ – кварц

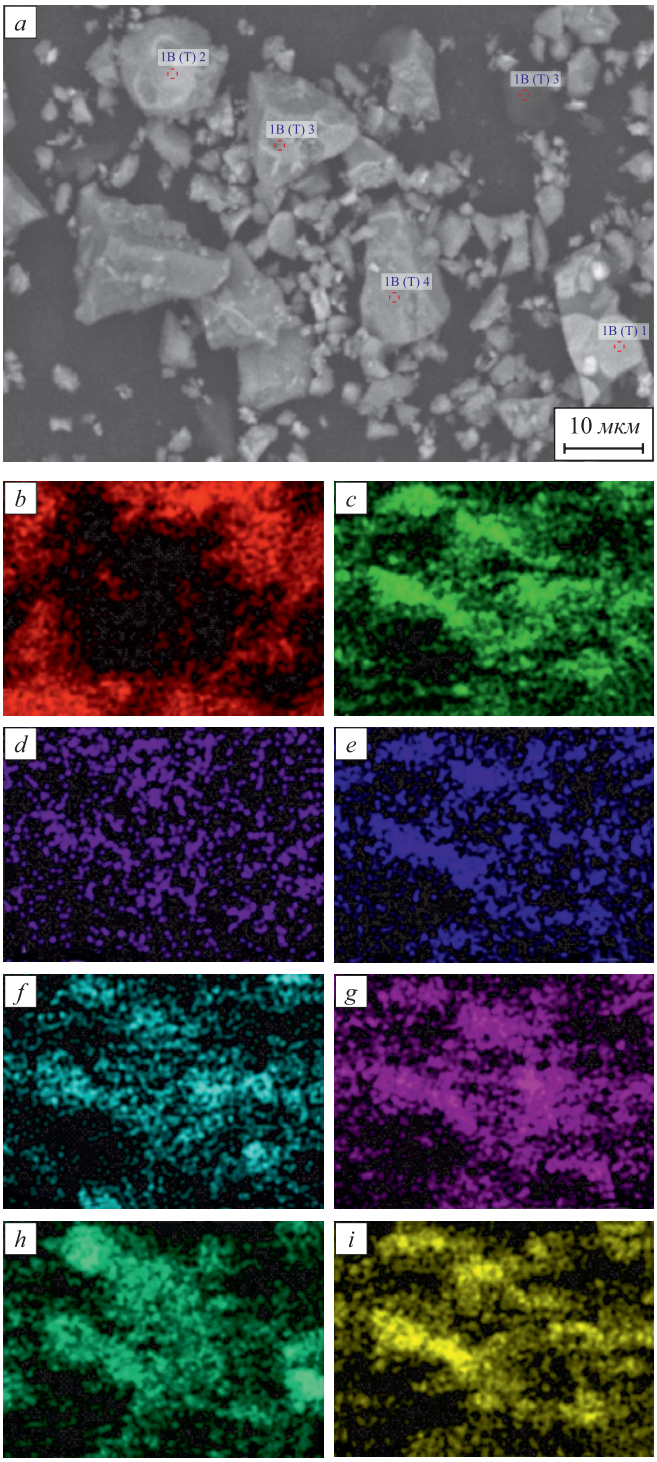

Fig. 4. SEM EDS of tailing in ×5000 (*a*) area magnification mode: *b* – carbon, *c* – oxygen, *d* – sulfur, *e* – natrium, *f* – magnesium, *g* – aluminium, *h* – silica, *i* – iron

Рис. 4. Результаты энергодисперсионного микроанализа хвостов на растровом электронном микроскопе: *a* – ×5000; *b* – углерод; *c* – кислород; *d* – сера; *e* – натрий; *f* – магний; *g* – алюминий; *h* – двуокись кремния; *i* – железо

usable after process. The process under consideration can serve as reference for further processes such as acid and base leaching. Pure iron extracted from tailings can be used for metal fuel in the future.

References / Список литературы

1. Li Y.J., Yu H.C., Wang D.Q., Yin W.X., Bai Y.S. The current status of laterite ore resources and its processing technology. *Jinshu Kuangshan/Metal Mine*. 2010; 11: 5–9.
2. Rao M.J., Li G.H., Jiang T., Luo J., Zhang Y.B., Fan X.H. Carbothermic reduction of nickeliferous laterite ores for nickel pig iron production in China: a review. *JOM*. 2013; 65(11): 1573–1583. https://doi.org/10.1007/s11837-013-0760-7
3. Wang C.Y., Yin F., Chen Y.Q., Wang Z., Wang J. Worldwide processing technologies and progress of nickel laterites. *Chinese Journal of Nonferrous Metals*. 2008; 18(S1): 1–8.
4. Dalvi A.D., Bacon W.G., Osborne R.C. The past and the future of nickel laterites. *PDAC 2004 Int. Conf. Trade Show and Investors Exchange, Toronto, 7-10 March, 2004*: 1–27.
5. Bahfie F., Manaf A., Astuti W., Nurjaman F., Prasetyo E., Sumardi S. Characterization of thermal upgrading of nickel from limonite by selective reduction. *Izvestiya. Ferrous Metallurgy*. 2022; 65(7): 471–478. https://doi.org/10.17073/0368-0797-2022-7-471-478

   Бахфи Ф., Манаф А., Астути В., Нурджаман Ф., Прасетио Э., Сумарди С. Термическое обогащение никеля из лимонита методом селективного восстановления. *Известия вузов. Черная металлургия*. 2022; 65(7): 471–478. https://doi.org/10.17073/0368-0797-2022-7-471-478
6. Bahfie F., Manaf A., Astuti W., Nurjaman F. Studies on reduction characteristics of limonite and effect of sodium sulphate on the selective reduction to nickel. *Journal of the Institution of Engineers (India): Series D*. 2020; 102(1): 149–157. https://doi.org/10.1007/s40033-020-00240-3
7. Bahfie F., Manaf A., Astuti W., Nurjaman F., Prasetyo E. Studies of carbon percentage variation and mixing saprolite-limonite in selective reduction. *Materials Today: Proceedings*. 2022; 62: 4156–4160. https://doi.org/10.1016/j.matpr.2022.04.679
8. Bahfie F., Murti D.U., Nuryaman A., Astuti W., Nurjaman F., Prasetyo E., Sudibyo S., Susanti D. Kinetic properties of nickel leaching by ANOVA method. *Progress in Physics of Metals*. 2022; 23(3): 476–88. https://doi.org/10.15407/ufm.23.03.476
9. Nurjaman F., Handoko A.S., Bahfie F., Astuti W., Suharno B. Effect of modified basicity in selective reduction process of limonitic nickel ore. *Journal of Materials Research and Technology*. 2021; 15: 6476–6490. https://doi.org/10.1016/j.jmrt.2021.11.052
10. Li G.H., Shi T.M., Rao M.J., Jiang T., Zhang Y.B. Beneficiation of nickeliferous laterite by reduction roasting in the presence of sodium sulphate. *Minerals Engineering*. 2012; 32: 119–26. https://doi.org/10.1016/j.mineng.2012.03.012
11. Kim J., Dodbiba G., Tanno H., Okaya K., Matsuo S., FujitaT. Calcination of low-grade laterite for concentration of Ni by magnetic separation. *Minerals Engineering*. 2010; 23: 282–288. https://doi.org/10.1016/j.mineng.2010.01.005
12. Zheng G.L., Zhu D.Q., Pan J., Li Q.H., An Y.M., Zhu J.H., Liu Z.H. Pilot scale test of producing nickel concentrate from low-grade saprolitic laterite by direct reduction-magnetic separation. *Journal of Central South University*. 2014; 21: 1771–1777. https://doi.org/10.1007/s11771-014-2123-0

13. Li B., Wang H., Wei Y.G., The reduction of nickel from low-grade nickel laterite ore using a solid-state deoxidisation method. *Minerals Engineering*. 2011; 24: 1556–1562. https://doi.org/10.1016/j.mineng.2011.08.006

14. Liang W., Wang H., Fu J.G., He Z.X. High recovery of ferro-nickel from low grade nickel laterite ore. *Journal Central South University (Science and Technology)*. 2011; 42(8): 2173–2177.

15. Li G.H., Rao M.J., Jiang T., Huang Q.Q., Tang T.M., Zhang Y.B. Innovative process for preparing ferronickel materials from laterite ore by reduction roasting-magnetic separation. *The Chinese Journal of Nonferrous Metals*. 2011; 21(12): 3137–3142.

16. Huang D.H., Zhang J.L., Lin C.C., Mao R. Production of ferro-nickel granules from nickel laterite ore/coal composite briquettes by direct reduction. *Chinese Journal of Engineering*. 2011; 33(12): 1442–1447. https://doi.org/10.13374/j.issn1001-053x.2011.12.015

17. Cao Z.C., Sun T.C., Yang H.F., Wang J.J., Wu X.D. Recovery of iron and nickel from nickel laterite ore by direct reduction roasting and magnetic separation. *Chinese Journal of Engineering*. 2010; 32(6): 708–712. https://doi.org/10.13374/j.issn1001-053x.2010.06.004

18. Sun T.C., Ji Y.N., Jiang M. Influence mechanism of different types of coal on selective nickel reduction in nickel laterite reduction roasting. *Chinese Journal of Engineering*. 2011; 33(10): 1197–1203. https://doi.org/10.13374/j.issn1001-053x.2011.10.015

19. Jiang M., Sun T.C., Liu Z.G., Kou J., Liu N., Cao Y.Y., Zhang S.Y. Effects of coal types and additives on selective direct reduction of nickel laterite. *Mining and Metallurgical Engineering*. 2012; 32(5): 77–81.

20. Li G.H., Rao M.J., Jiang T., Shi T.M., Huang Q.Q. Reduction roasting-magnetic separation mechanisms of nickelferous laterite ore in presence of sodium salts. *The Chinese Journal of Nonferrous Metals*. 2012; 22(1): 274–278.

21. Sun T.C., Jiang M., Liu Z.G., Liu N., Zhang S.Y., Kou J., Xu C.Y. Research on the effect of additive on selective reduction of the laterite ores with low nickel and high iron content. *Zhongguo Kuangye Daxue Xuebao/Journal of China University of Mining and Technology*. 2013; 42(5): 838–844.

22. Zhu D.Q., Cui Y., Vining K., Hapugoda S., Douglas J., Pan J., Zheng G.L. Upgrading low nickel content laterite ores using selective reduction followed by magnetic separation. *International Journal of Mineral Processing*. 2012; 106–109: 1–7. https://doi.org/10.1016/j.minpro.2012.01.003

23. Valix M., Cheung W.H. Effect of sulphur on the mineral phases of laterite ores at high temperature reduction. *Minerals Engineering*. 2002; 15: 523–530. https://doi.org/10.1016/S0892-6875(02)00069-9

24. Lu J., Liu S.J., Shangguan J., Du W.G., Pan F., Yang S. The effect of sodium sulphate on the hydrogen reduction process of nickel laterite ore. *Minerals Engineering*. 2013; 49: 154–164. https://doi.org/10.1016/j.mineng.2013.05.023

25. Jiang M., Sun T.C., Liu Z.G., Kou J., Liu N., Zhang S.Y. Mechanism of sodium sulfate in promoting selective reduction of nickel laterite ore during reduction roasting process. *International Journal of Mineral Processing*. 2013; 123: 32–38. https://doi.org/10.1016/j.minpro.2013.04.005

26. Ali A., Zafar H., Zia M., ul Haq I., Phull A. R., Ali J. S., Hussain A. Synthesis, characterization, applications, and challenges of iron oxide nanoparticles. *Nanotechnology, Science and Applications*. 2016; 2016(9): 49–67. https://doi.org/10.2147/NSA.S99986

27. Julien P., Bergthorson J. M. Enabling the metal fuel economy: green recycling of metal fuels. *Sustainable Energy & Fuels*. 2017; 3: 1–11. https://doi.org/10.1039/C7SE00004A

28. William F. M., Charles H. C., Bourdon F. *Tables of Spectral-Line Intensities. Part I: Arranged by Elements*. U.S. Department of Commerce-National Bureau of Standards; 1975: 456.

Information about the Authors / Сведения об авторах

Fathan Bahfie, *Researcher,* Research Center of Mining Technology, National Research and Innovation Agency of Indonesia*; Postgraduate,* University of Indonesia
ORCID: 0000-0003-3460-469X
E-mail: fathanbahfie@gmail.com

Azwar Manaf, *PhD, Prof. of the Chair of Physics, Faculty of Mathematics and Science,* University of Indonesia
ORCID: 0000-0002-6142-3918
E-mail: azwar@ui.ac.id

Widi Astuti, *PhD, Researcher,* Research Center of Mining Technology, National Research and Innovation Agency of Indonesia
ORCID: 0000-0001-9364-4291
E-mail: widi.mineral@gmail.com

Fajar Nurjaman, *PhD, Researcher,* Research Center of Mining Technology, National Research and Innovation Agency of Indonesia
ORCID: 0000-0002-1329-5296
E-mail: nurjaman_80@yahoo.com

Suharto Suharto, *Researcher,* Research Center of Mining Technology, National Research and Innovation Agency of Indonesia
ORCID: 0000-0002-8105-2528
E-mail: harto_berg@yahoo.com

Фатхан Бахфи, *научный сотрудник,* Научно-исследовательский центр горных технологий, Национальное агентство исследований и инноваций Индонезии; *аспирант*, Университет Индонезии
ORCID: 0000-0003-3460-469X
E-mail: fathanbahfie@gmail.com

Азвар Манаф, *д.н., профессор кафедры физики факультета математики и естественных наук,* Университет Индонезии
ORCID: 0000-0002-6142-3918
E-mail: azwar@ui.ac.id

Види Астути, *д.т.н., научный сотрудник,* Научно-исследовательский центр горных технологий, Национальное агентство исследований и инноваций Индонезии
ORCID: 0000-0001-9364-4291
E-mail: widi.mineral@gmail.com

Фаджар Нурджаман, *д.н., научный сотрудник,* Научно-исследовательский центр горных технологий, Национальное агентство исследований и инноваций Индонезии
ORCID: 0000-0002-1329-5296
E-mail: nurjaman_80@yahoo.com

Сухарто Сухарто, *научный сотрудник,* Научно-исследовательский центр горных технологий, Национальное агентство исследований и инноваций Индонезии
ORCID: 0000-0002-8105-2528
E-mail: harto_berg@yahoo.com

***Ulin Herlina*,** *Researcher,* Research Center of Mining Technology, National Research and Innovation Agency of Indonesia
E-mail: ulin_herlina@yahoo.com

***Wisnu Ari Adi*,** *PhD, Prof.,* Center for Advanced Materials Science and Technology, National Research and Innovation Agency of Indonesia
E-mail: wisnu.ari.adi@brin.go.id

***Maykel Manawan*,** *Lecturer of Defense Technology Faculty,* Indonesia Defense University
E-mail: maykeltem@gmail.com

***Улин Херлина*,** *научный сотрудник,* Научно-исследовательский центр горных технологий, Национальное агентство исследований и инноваций Индонезии
E-mail: ulin_herlina@yahoo.com

***Вишну Ари Ади*,** *д.н., профессор,* Центр материаловедения и передовых технологий, Национальное агентство исследований и инноваций Индонезии
E-mail: wisnu.ari.adi@brin.go.id

***Мейкель Манаван*,** *преподаватель факультета оборонных технологий,* Военный университет Индонезии
E-mail: maykeltem@gmail.com

Received 17.05.2022
Revised 27.05.2022
Accepted 22.10.2022

Поступила в редакцию 17.05.2022
После доработки 27.05.2022
Принята к публикации 22.10.2022

Наукометрические показатели журнала

В 2017 году международная база данных Scopus возобновила индексирование журнала «Известия ВУЗов. Черная металлургия». На инфографике отражены текущие показатели.

Данные предоставлены сайтами https://www.scopus.com, https://www.scimagojr.com и https://www.scival.com

Над номером работали:

Л.И. Леонтьев, *главный редактор*

Е.В. Протопопов, *заместитель главного редактора*

Е.А. Ивани, *заместитель главного редактора*

Л.П. Бащенко, *заместитель ответственного секретаря*

Е.Ю. Потапова, *заместитель главного редактора по развитию*

О.А. Долицкая, *научный редактор*

Е.М. Запольская, *ведущий редактор*

Н.Н. Киселева, *ведущий редактор*

В.В. Расенець, *верстка, иллюстрации*

Г.Ю. Острогорская, *менеджер по работе с клиентами*

Подписано в печать 25.02.2023. Формат 60×90 $^{1}/_{8}$. Бум. офсетная № 1.
Печать цифровая. Усл. печ. л. 16,5. Заказ 16872. Цена свободная.

Отпечатано в типографии Издательского Дома МИСИС.
119049, Москва, Ленинский пр-кт, д. 4, стр. 1.
Тел./факс: (499) 236-76-17

Corrosion-resistant steels based on Fe – ~13 % Cr: Heat treatment, corrosion- and wear resistance. Review

Spraying wear-resistant coatings from clad powders TiB_2/Ti and HfB_2/Ti

Preliminary assessment of the possibility to use large-diameter pipes of X52 steel for transportation of pure gaseous hydrogen under pressure

Influence of silicon carbides on the structure and properties of composite nickel-phosphorus coating

Transformation of fine structure of lamellar pearlite under deformation of rail steel

Formation of grain structure and microhardness of Ni_3Al intermetallic compound as a result of SHS extrusion

Substructure parameters in deformed Cu – Mn alloys with a FCC lattice

Study of pipe steel resistance to deformation in laboratory conditions and on the data from industrial rolling with the use of machine learning tools

Investigation of spherical powder obtained by plasma spraying of wire from corrosion-resistant steel 03Kh17N10M2

Cracking in magnesium oxide briquettes

Effect of B_2O_3 on viscosity of high-magnesia blast furnace slag

Impact of barium and strontium on calcium recovery level in ladle treatment of steel by complex modifiers with alkaline-earth metals

Metallographic study on the structural features of thin slab and rolled products made from it

Mathematical model of slab heating in a furnace with walking beams

Experience in using and improving the usability of mathematical modeling system of production at a metallurgical enterprise

Composition of tailings after selective reduction of laterite

Зарегистрирован Федеральной службой по надзору в сфере связи, информационных технологий и массовых коммуникаций. Свидетельство о регистрации ПИ № ФС77-35456.

Подписной индекс 70383.